Imperial College London

Medical Robots for MRI Guided Diagnosis and Therapy

by Tsz Ho Tse

Submitted for the degree of Doctor of Philosophy and the Diploma of Imperial College London

London, June 2009

Mechatronics In Medicine Laboratory
Department of Mechanical Engineering

Abstract

Magnetic Resonance Imaging (MRI) provides the capability of imaging tissue with fine resolution and superior soft tissue contrast, when compared with conventional ultrasound and CT imaging, which makes it an important tool for clinicians to perform more accurate diagnosis and image guided therapy. Medical robotic devices combining the high resolution anatomical images with real-time navigation, are ideal for precise and repeatable interventions. Despite these advantages, the MR environment imposes constraints on mechatronic devices operating within it. This thesis presents a study on the design and development of robotic systems for particular MR interventions, in which the issue of testing the MR compatibility of mechatronic components, actuation control, kinematics and workspace analysis, and mechanical and electrical design of the robot have been investigated. Two types of robotic systems have therefore been developed and evaluated along the above aspects.

(i) A device for MR guided transrectal prostate biopsy: The system was designed from components which are proven to be MR compatible, actuated by pneumatic motors and ultrasonic motors, and tracked by optical position sensors and fiducial markers. Clinical trials have been performed with the device on three patients, and the results reported have demonstrated its capability to perform needle positioning under MR guidance, with a procedure time of around 40mins and with no compromised image quality, which achieved our system specifications.

(ii) Limb positioning devices to facilitate the magic angle effect for diagnosis of tendinous injuries: Two systems were designed particularly for lower and upper limb positioning, which are actuated and tracked by the similar methods as the first device. A group of volunteers were recruited to conduct tests to verify the functionality of the systems. The results demonstrate the clear enhancement of the image quality with an increase in signal intensity up to 24 times in the tendon tissue caused by the magic angle effect, showing the feasibility of the proposed devices to be applied in clinical diagnosis.

Acknowledgments

This thesis is the result of my research work at Imperial College London where I have been accompanied and supported by many people. It is a pleasure that I now have the opportunity to express my gratitude to all, who gave me the motivation and inspiration to complete this thesis. First of all, I owe my most sincere thanks to my supervisors, Dr. Michael Lamperth, Prof. Ian Young and Dr. Mihailo Ristic who introduced me to the field of MRI robotics and gave me the most important guidance throughout my PhD studies. Their wide knowledge and insightful thinking have been of great value to me. I would have never reached new heights without their stimulating suggestions and great encouragement during the period of the research and writing of this thesis. Secondly, I wish to express my warm thanks to my colleagues in the Mechatronics in Medicine Laboratory who I have worked with for the last few years. Special thanks go to Abbi Hamed, Haytham Elhawary, Marc Rea and Aleksandar Zivanovic for their enormous guidance during my first steps into medical robotics. I also owe my thanks to my lab mates Luca Frasson, Tassanai Parittotokkaporn, Yaroslav Tencer, Andy Turner, Seong Young Ko and Gorkem Dogangil for the enormous amount of technical discussions and support that I have received from them and also for providing me such a pleasant and enjoyable working environment to conduct my research. I am also thankful to Prof. Brian Davies, Dr. Ferdinando Rodriguez Y Baena, Prof Colin Besant and Prof. Nandita deSouza for sharing with me their perceptiveness and knowledge on diverse areas of medical robotics. Thirdly, I am indeed grateful to all my friends for being like a surrogate family during the years I stayed in London and for always standing by me in good and bad times. Their moral support and encouragement has made my experience more enriching and valuable than I expected it to be. Lastly, and most importantly, I wish to thank my parents. They raised me, supported me, taught me, and loved me. To them I dedicate this thesis.

Contents

Abstract **1**

Acknowledgements **2**

Contents **3**

List of Figures **7**

List of Tables **15**

Abbreviations **16**

1 Introduction, Aims and Objectives **19**
1.1 Introduction . . . 19
1.2 Motivation for Research . . . 19
1.2.1 MR guided Prostate Biopsy . . . 19
1.2.2 Diagnostic Imaging using the Magic Angle Effect . . . 21
1.3 Research Objectives . . . 23
1.4 Structure of the Thesis . . . 24

2 Literature Survey of MRI Robotics **26**
2.1 Introduction . . . 26
2.2 MRI System . . . 26
2.2.1 Magnetic Resonance Imaging . . . 26
2.2.2 MRI Scanner Structure . . . 27
2.2.3 Scanner Types . . . 29
2.3 Challenges in MRI Environment . . . 29
2.3.1 Magnetically Induced Force and Torque . . . 29
2.3.2 Image Artifact and Geometric Distortion . . . 31
2.3.3 Degradation of Signal to Noise Ratio . . . 31
2.3.4 Magnetically Induced Thermal Effect . . . 32
2.3.5 Workspace Limitation . . . 32
2.4 MRI Compatible Robot . . . 33
2.4.1 Actuation Technology . . . 34

2.4.2 Position Sensing Technology . . . 40
2.4.3 Force Sensing Technology . . . 41
2.4.4 Medical Robots for Percutaneous Interventions . . . 46
2.5 Conclusion . . . 51

3 Testing MR Compatibility of Mechatronic Components 52
3.1 Introduction . . . 52
3.2 MRI Safety and Compatibility . . . 52
3.3 Susceptibility and Design Guidelines . . . 53
3.4 Testing MR Compatibility . . . 55
3.4.1 Preliminary Screening . . . 55
3.4.2 Tests for Magnetically Induced Force and Torque . . . 58
3.4.3 Tests for Signal to Noise Ratio Reduction . . . 59
3.4.4 Tests for Artifact Generation . . . 63
3.4.5 Tests for Image Geometrical Distortion . . . 64
3.4.6 Tests for Thermal Effect . . . 66
3.5 Conclusion . . . 68

4 Actuation Control and Evaluation 70
4.1 Introduction . . . 70
4.2 Actuation Specifications . . . 71
4.3 Ultrasonic motor . . . 71
4.3.1 Principle of the Ultrasonic Motor . . . 71
4.3.2 Control Electronics for Motor Synchronisation . . . 73
4.3.3 Characteristics of the Piezoleg . . . 75
4.3.4 Haptic Control . . . 79
4.3.5 Specifications of a Master-Slave Test Unit . . . 82
4.3.6 Discussion . . . 84
4.3.7 Summary . . . 86
4.4 Pneumatic Rotary Motor . . . 86
4.4.1 Principle of the Pneumatic Motor . . . 86
4.4.2 Control Electronics . . . 87
4.4.3 Control Performance and Characteristics . . . 89
4.4.4 Summary . . . 94
4.5 Conclusion . . . 96

5 System for MR Guided Prostate Biopsy 97
5.1 Introduction . . . 97
5.2 Design Specifications and Guidelines . . . 97
5.2.1 General Objectives . . . 98
5.2.2 Acceptable Level of MR Compatibility . . . 98
5.2.3 Required Workspace . . . 98

5.2.4 Spatial Availability for Robot Movement . . . 99
5.2.5 Robot kinematics . . . 100
5.2.6 Robot Control and Tracking . . . 100
5.3 Design Overview . . . 102
5.4 Robot Kinematic Analysis . . . 102
5.4.1 Forward Kinematics . . . 102
5.4.2 Robot-Scanner Registration . . . 108
5.4.3 Inverse Kinematics . . . 112
5.4.4 Workspace Analysis . . . 112
5.4.5 Real-Time Tracking . . . 116
5.5 Engineering Design . . . 116
5.5.1 Cartesian Robot . . . 116
5.5.2 Haptic Needle Firing Unit . . . 117
5.6 System Electronics . . . 117
5.6.1 Faraday Cage . . . 117
5.6.2 Touch Screen Control PC . . . 120
5.7 Scanner, Robot and Control PC Communications . . . 121
5.8 Conclusion . . . 122

6 Evaluation and Clinical Experience of the Prostate System 125
6.1 Introduction . . . 125
6.2 MR Compatibility of the System . . . 125
6.3 User Control . . . 126
6.3.1 Auto Needle Alignment . . . 127
6.3.2 Manual Needle Alignment . . . 127
6.3.3 Control Setting . . . 130
6.4 Functional Hazard Assessment and Safety Measures . . . 130
6.5 Clinical Trial with Patients . . . 131
6.5.1 Trial Procedure . . . 131
6.5.2 Results and Discussion . . . 136
6.6 Conclusion . . . 141

7 System for Magic Angle Study in Man and its Evaluation 142
7.1 Introduction . . . 142
7.2 Design Objectives and Guidelines . . . 143
7.3 Kinematics for Limb Positioning . . . 143
7.3.1 Kinematics of a Lower Extremity Structure . . . 145
7.4 Mechanical Design . . . 156
7.5 Control Hardware and Electronics . . . 159
7.6 Movement Trajectory in Lower Limb Positioning . . . 159
7.7 Signal to Noise Degradation Test . . . 162
7.8 Functional Hazard Assessment and Safety Measures . . . 164

7.9 Preliminary Trials . . . 165
7.9.1 Procedure . . . 165
7.9.2 Results and Discussion . . . 165
7.10 Conclusion . . . 172

8 Conclusions and Future Work **175**
8.1 Introduction . . . 175
8.2 Chapter Summary . . . 175
8.3 Conclusions . . . 178
8.3.1 MR Compatibility Evaluation . . . 178
8.3.2 Control Strategies of MR Compatible Actuators . . . 179
8.3.3 Prostate Biopsy System . . . 180
8.3.4 Magic Angle Positioning Devices . . . 180
8.4 Future Work . . . 181
8.4.1 Adaptation in 3Tesla Scanners . . . 181
8.4.2 Investigations into Position and Force Control Strategies . . . 181
8.4.3 Improved Prostate Biopsy System . . . 182
8.4.4 Improved Magic Angle Positioning Devices . . . 182
8.5 Publication Output . . . 183

List of Figures

1.1 Male reproductive system showing the prostate gland located immediately inferior to the urinary bladder . . . 20
1.2 A doctor inserts a lubricated finger into rectum for Digital Rectal Examination [Line, 2005]. . . . 20
1.3 TRUS guided prostate biopsy [Line, 2005]. . . . 21
1.4 Large part of spin-spin interaction is proportional to a factor of $3\cos^2\theta - 1$ and the magic angle effect occurs when θ is equal to 54.7degrees where $3\cos^2\theta - 1 = 0$. . . . 22
1.5 MR images of an Achilles tendon (a) at 0degrees with respect to the main field and (b) at 55degrees. Tendons with a dark colour in the image represent very weak or no signals, and vice versa. . . . 23

2.1 Cross section of an MRI scanner , shown its principal components . . . 28
2.2 Schematic diagram of key components of a typical MRI machine. . . . 29
2.3 (a) Conventional closed bore scanner (3T Siemens Trio MRI scanner) [Siemens, 2009] . 30
2.4 Open bore scanners: (a) Philips Mid-Field Open MRI system Panorama, 0.6T [Hamstring, 2009]. (b) ESAOTE Hologic scanner, 0.2T permanent magnet [Dotmed, 2009]. (c) East Brunswick Open Upright MRI scanner, 0.6T [Brunswick, 2009]. . . . 30
2.5 (left) Commercial optical encoder (HP HEDL-5540) (right) Image artifact caused by the magnetic metal component in the encoder. . . . 31
2.6 (a) MR image of a patient prostate taken when an electronic amplifier placed near to the scanner bore entrance was not powered. (b) Image taken when the amplifier was powered. . . . 32
2.7 Workspace of a scanner with diameter of 60cm [Sie, 2005] . . . 33
2.8 Cross sectional view of the scanner with a patient's profile, showing a very limited workspace for image guided procedures and even for the location of the device [Tsekos, 2008]. . . . 33
2.9 Life size mock-up of an MRI scanner with a human subject placed in the left lateral decubitus position (a common position for transrectal biopsy). The space available for the manipulator is displayed. . . . 34
2.10 Cross sectional view of a magnetism free USB60 ultrasonic motor [Shinsei Corporation Inc., 2004] . . . 35

2.11 A robot for general purpose image guided inventions was develop by Chinzei and integrated with an open intraoperative scanner. Ultrasonic motor USR60, motor drives, and all necessary electronics are placed at a meter away from the imaging volume and mounted to the top of the scanner. 36
2.12 A 5DOF robot designed for transperineal prostate biopsy under MR image guidance and actuated by custom design double action pneumatic cylinders [DiMaio, 2006]. . . . 36
2.13 (a) PneuStep, an MR compatible stepper motor driven by compressed air (b) CAD drawing of the motor showing the central nut-shaped gear head connected to a screw threaded rod to convert a rotary motion to a linear motion. 37
2.14 Schematic diagram of the pneumatic stepper motor, showing the sequential airflow to the three linear actuators individually. 38
2.15 Control electronics of the pneumatic stepper motor: a custom optical encoder is embedded into the motor for position tracking, adapter to convert optical signals to electrical signals, a stepper motion control cards to generate sequential control signals, and pneumatic valves to regulate airflow to the motor. 38
2.16 (a) Single unit of electromagnetic driver. (b) A MRE motion generator for mechanical excitation of human breast [Rossman, 1999]. 39
2.17 (a) A general purpose MRE motion generator, in which piezoelectric actuation is used with a simple level mechanism to amplify the vibration magnitude up to 1mm. (b) 250mm long piezoelectric stack from PI [PI, 2009]. 39
2.18 Optical position encoder [Avago, 2003]. 41
2.19 Schematic diagram of an MRI compatible absolute position encoder design: optical signals are transmitted to and from the LED and photo detector placed outside the scanner room to avoid EM interference [Virtanen, 2003]. 42
2.20 Device based on a MR compatible sensor where optical signals are transmitted to and from LED and photo detected based in control with optical fibres [Chapuis, 2004]. . . . 42
2.21 Principle of force sensing by detection of the displacement of the hinge spring with light-intensity measurement [Moser, 2003]. 43
2.22 Configurations of (a) a force sensor based on a hinge spring and (b) a torque sensor based on a torsional spring [Gassert, 2006a]. 44
2.23 (a) A haptic interface mounted on a large aluminum frame, which was developed to investigate the neuromuscular response in human brains [Gassert, 2006a]. (b) The system setup. 44
2.24 An optical 2DOF force sensor [Tada, 2002]. 45
2.25 Principle of the two-dimensional optical micrometry. The 2DOF sensor consists of emitting and receiving electronics, fibre optics and lenses. Electronics are located outside of the scanner room [Tada, 2004]. 45
2.26 (a) MR compatible robot for liver biopsy with the ability of real-time liver tracking. (b) Needle alignment is performed according to the information from the liver tracking. . . 47

2.27 (a) A general proposal MRI interventional robot consists of a Cartesian gantry for gross position and an extension arm with 3DOF in Euler angles for targeting. (b) The system was placed at the front entrance of the scanner with the extension arm toward the image volume above the patient. 48
2.28 The master handle (hardware user interface) is used for control the robot in master/slave mode where the extension arm replicates the motion of the master handle. The master handle and the extension arm have the same kinematics for ease of control. 48
2.29 (a) CAD rendering of MR-Bot performing prostate biopsy on a patient and (b) its photo [Muntener, 2006]. 49
2.30 (a) A manual actuated transrectal prostate biopsy manipulator consists of two ball joints and one linear rail to allow the workspace to target the suspected tissue. (b) Inside the rectal sheath is a needle channel which allows the channel movement for needle alignment with no shear stress exerted to the prostate [Krieger, 2007]. 50

3.1 Full range of magnetic susceptibility value in susceptibility Spectrum (Top). The region of MR compatibility (bottom) [Schenck, 1996] 55
3.2 (a) Piezoleg, a type of ultrasonic motor based on the piezoelectric technology for actuation. The motor body is made from non-magnetic stainless steel, and the linear rotor is made from a ceramic material [Piezoleg, 2009]. 56
3.3 (a) The pneumatic rotary motor consists of an air turbine and a set of modular gearboxes. The rotor and the motor housing are manufactured by rapid prototyping. (b) CAD drawing of the air turbine. 57
3.4 (a) A quadrature optical position encoder (left), the encoder surface mounted on a custom design PCB board to form a robust unit (right) (b) piezoresistive force sensor. 57
3.5 Schematic diagram of the test for assessment of the magnetically induced force experienced by the test subject. F is the induced force, mg is the gravitational force of the component, and B_0 is the static magnetic field strength [ASTM-F2052, 2004a]. 58
3.6 Schematic diagram of the torsional pendulum method [ASTM-F2052, 2004b] 59
3.7 Calculation of signal to noise ratio: $SNR = \frac{P_{Centre}}{SD_{Corner}}$, where P_{Centre} is the mean signal of a 40×40 pixel region at the centre of the phantom (Region 1), and SD_{Corner} is the standard deviation of the signal at a 40×40 pixel region at a corner of the image (Region 2) [Chinzei, 2000a]. 60
3.8 (a) The aluminium enclosure acts as a Faraday cage to electrically isolate the noise source from the scanner room. (b) Its internal view. 62
3.9 (a) A group of low-pass filters mounted at the wall of the aluminum enclosure to attenuate RF interference at the Larmor frequency of 64MHz. (b) Attenuation characteristics of the low-pass filters 62
3.10 Artifact measurement suggested by the ASTM standard F2119. The artifact width is measured from the subject body to the artifact fringe where there is a 30% change of pixel intensity relative to the reference image where the subject is absent [ASTM-F2119, 2004]. 64

3.11 MR images showing size of image artifacts generated by: (a) pneumatic motor (14mm), (b) ultrasonic motor (39mm), (c) piezoresistive force sensor (42mm), and (d) encoder (20mm). The sizes of artifact were quantified by the ASTM F2119 standard. All the largest artifacts appeared in the True FISP image sequence. 65
3.12 A phantom with geometric patterns and filled with $CuSO_4$ fluid was used to quantify geometry distortion, if any, induced by a test subject. 66
3.13 (a) TSE control image with fine geometrical patterns shown, (b) TSE image with the force sensor introduced and actuated with load applied to the force sensor, and (c) subtraction image between (a) and (b). Images (d)-(f) are the same images but with the True FISP image sequence 67
3.14 Temperature variation of the endorectal probe during a 30min scan with FLASH 2D image sequence, demonstrating no noticeable thermal effect recorded. 68

4.1 A cross section of a general structure of a ultrasonic motor. The stator (piezoelectric ceramic) generates ultrasonic vibration to push the rotor [Shinsei Corporation Inc., 2008]. 72
4.2 (a) CAD rending of the Piezoleg, showing its components including a well polished ceramic rod, a pair of brass bearings, a adjustable brass spring, and four piezoelectric ceramic legs. (b) Its photo. 73
4.3 (a) Schematic drawings of the Piezoleg working principle [Piezoleg, 2008]. (b) Motion is achieved by exciting the four ceramic legs with repeated waveforms 1, 2, 3 and 4. The speed of the linear motion can be controlled by the amplitudes, the frequency and the phase difference of the voltage waveforms to the ceramic legs. 74
4.4 CAD drawing of a pair of Piezoleg connected together to form a stronger actuation link 75
4.5 The synchronisation circuit mounted on a motor drive (four-channel signal generator). 76
4.6 Diagram of a synchronisation circuit with magnification $\left(1+\frac{R2}{R1}\right)$for signal supplies to a group of Piezoleg motors. 77
4.7 (a) the speed-frequency relationship of the Piezoleg motor under different load conditions and (b) under a load of 2N, showing its nonlinear characteristics. Polynomial regressions from 2nd to 5th orders do not fit well the nonlinear range of the curve from 80kHz onward in (b) 78
4.8 The Architecture of the Neural Network with $n = 30$ neurons in the log-sigmoid layer and a single linear neuron in the linear layer. 79
4.9 Block diagram of admittance control implemented in the master-slave master 81
4.10 Speed model consists of a neural network model of the Piezoleg motor 81
4.11 Master control interface 82
4.12 Slave prototype and its CAD drawing 83
4.13 Open loop velocity control of the ultrasonic motor with the neural network model: (i) under low load conditions of 2N and 4N (b), with a controlled speed of 10mm/s (a). The computed driving frequencies are shown in (c) and is in the nonlinear speed range; (ii) under high load conditions of 10N and 12N (e), with a controlled speed of 2mm/s (d). The computed driving frequencies are shown in (f) and is in the linear speed range. 85

4.14 Force and displacement responses in the master-slave system with (a) no speed model, and (b) with the speed model 85
4.15 (a) CAD rendering of the pneumatic air motor. (b) Photo of the air motor with its components. 87
4.16 (a) Schematic diagram of the working principle in the pneumatic turbine. (b) CAD drawing of the turbine shaft assembly. 88
4.17 (a) CAD drawing of the planetary gearbox and pneumatic turbine assembly [ServoCity, 2009]. (b) Its side view [Tamiya, 2009] 88
4.18 Block diagram of a simple close loop control in the pneumatic motor 89
4.19 Test unit consists of a pneumatic motor with gear ratio 2000: 1, and an optical quadrature encoder with its code-disc. 89
4.20 Step response of the pneumatic motor at 100% duty cycle at an operating pressure of 1.3bar 90
4.21 Relationship between speed and duty cycle under different periods for pulse width modulation of air supply (No load, operating pressure of 1.3bar) 91
4.22 Relationship between torque and speed under different operating pressures. 92
4.23 Test unit II consists of a pneumatic motor, optical position encoder, and plastic wheel and limb platform. The platform, base board, wheel plastic and the plastic linkage forms a four bar linkage system. 94
4.24 Step response of the closed loop PID control in the pneumatic system under the condition of no load, a palm and load of 25N at the operation pressure of 1.3bar. The PID parameters were kept unchanged in each condition. 94
4.25 Step response of the closed loop PID control in the load conditions of 0N, 10N, 20N, 30N, 40N and 50N (1.3bar). The PID parameters were auto-tuned in each condition. . . 95
4.26 Variation of PID parameters under the load conditions of 0N, 10N, 20N, 30N, 40N and 50N. The parameters were tuned by Ziegler–Nichols method based on the function of Auto-tuning PID in LabView®. 95

5.1 Schematic diagrams of (a) posterior-anterior view and (b) foot-head view, showing the required workspace covering the prostate. 99
5.2 MR images of (a) posterior-anterior view and (b) foot-head view, showing the adenocarcinomas area in the periphery of the capsule. 100
5.3 Robot kinematics for transrectal prostate biopsy: at least 4 actuated DOF for the needle alignment and insertion, and a support frame to place the end effector close to the patient anus. [Blue, 2009, Harald H. Quick, 2005]. 101
5.4 (a) CAD drawing of the robot design consisting of a Cartesian positioning robot, an extension arm, a gimbals mechanism and a haptic needle firing unit with an endorectal probe attached. (b) The setup of the biopsy robot with its control interface. 103
5.5 Kinematic diagram of the prostate robot design. 104
5.6 (a) Side view and (b) top view of the gimbals, showing the geometric relationship between the pitch angle θ_P, the yaw Angle θ_Y of the gimbals, the centre of the gimbals, and the position of the rectal sphincter. 109

5.7 Three passive fiducial markers were embedded in the robot base for registration. The process for registration involves localisation of the markers in scanner coordinates and maps the points to the robot coordinates which were pre-obtained with the use of Microscribe®, a digital measurement device with a maximum error of 0.05mm. 110
5.8 MR image of the three fiducial markers localised for registration. A modified 2D sequence was adapted to process the coordinates with accuracy of 0.2mm [Rea, 2008]. . . 111
5.9 A 3mm×3mm fiducial micro-coil marker with Spenco® embedded as a signal generating material. The LC circuit was tuned to resonate at 63.6MHz. 111
5.10 (a) CAD model of the prostate biopsy robot placed according to the position of the patient. Workspace analysis of the prostate robot in (b) Y_0Z_0 and (c) X_0Z_0 plane (robot frame 0). The contour of the needle notch workspace is presented in blue, showing the space covering the whole prostate. 114
5.11 Potential workspace constraint of the prostate robot: patient with the biopsy target at the far anterior side ($+Y_0$ direction). 115
5.12 Potential workspace constraint of the prostate robot: patient with a small hip and therefore with his rectal sphincter at a lower position. 115
5.13 (a) Endorectal probe with a receive coil and two fiducial markers embedded. (b) Fiducial markers appear as bright points in the MR image for localisation of the position of the biopsy needle notch (yellow box). 116
5.14 (a) A Cartesian robot formulated by interconnecting three modules. Each module is incorperated with a rack and pinion mechanism, a pneumatic air motor and an optical encoder. (b) Its side view. (c) The robot integrated with a haptic needle firing mechanism for transrectal prostate biopsy which is linked with the use of gimbals and an extension arm. 118
5.15 The side view (a) and (b), and the top view (c) of the prostate biopsy robot mounted onto the scanner table. 119
5.16 (a) CAD model of the haptic unit carrying a biopsy needle coupled with an endorectal probe. (b) Its zoom view: a pair of force sensors embedded for force measurement in two directions for push and pull. The biopsy needle mounted on the needle housing is moved by the ultrasonic motor along the plastic linear rails. 120
5.17 Electronics components used within the aluminium enclosure. 121
5.18 (a) 15inch touch screen for graphic user interface in the aluminum enclosure for the image tracking display and robot control interface, and (b) the flash disk PC embedded. 122
5.19 Standard shielded Ethernet cables connecting the robot to its supporting electronics in the control enclosure (Faraday cage) and the signals pass though a group of low-pass filter with cut-off frequency of 64MHz to suppress the RF interference. (a) Back view of the control enclosure showing the electrical and optical cables connectors. (b) Low-pass filter group. (c) Ethernet optical signal converter connecting the control PC in the enclosure to the host PC in the control room. 123

6.1 The movement sequence of the prostate biopsy: in/out direction (Z module), pitch direction (Y module), and yaw direction (X module) to minimise friction exerted to the rectum wall and to reduce prostate deformation caused by the endorectal probe. 128
6.2 Schematic diagram of an angular movement of the needle projection in (a) yaw direction and (b) pitch direction 129
6.3 The acquired prostate image shows clear the suspected cancerous target. 132
6.4 Robot and integrated hardware panel setup 133
6.5 Endorectal probe inserted in a patient rectum. 133
6.6 (a) Fiducial markers embedded in the robot base for registration. (b) MR image taken for robot-scanner registration where fiducial markers appears as bright spots for localisation. 134
6.7 Sagittal plane, fiducial plane and needle plane in the endorectal probe 135
6.8 MR Tracking images showing the needle aligned step by step towards the target point. The tracking sequence kept the two fiducial always at the centre of the Field of View. . 136
6.9 (a) MR image of the prostate showing the target tissue. (b) Images taken in two perpendicular planes showing the needle alignment before a biopsy sample was taken. . 139

7.1 Schematic diagram showing the required DOF for: (a) low extremity positioning and (b) upper extremity positioning. 144
7.2 (a) Anatomy of musculoskeletal structure in the ankle joint [HuAnat, 2009] and (b) its MR image. 147
7.3 (a) Geometric view of the knee in a transverse view of the scanner bore, and (b) geometric view of a patient's leg in the scanner coronal view. 147
7.4 Constraint I: The knee collides with the scanner wall before the angle of the femur is optimised. In this case, orientating the ankle tendon to a larger β can be achieved only by rotating the tibia about the knee which is kept in touch with the wall. 151
7.5 (a) Anatomy of musculoskeletal structure in the knee and (b) its MR image in a lateral view. 152
7.6 The ankle collides with the scanner wall before the angle of the femur α is optimised in constraint I. In this case, the ankle is kept in touch with the wall and slides along to orientate the tibia and to achieve a larger β. 153
7.7 The femur is kept parallel to the main field to avoid any collision of the ankle to the scanner wall at a small angle of femur α and to provide maximum space for the knee movement. 155
7.8 (a) CAD rendering of the low limb system. (b) The underside view of the platform. (c) Photo of the system. (d) The system is mounted on a scanner table and the patient is placed with left position and has his leg strapped on the limb fixture of the system. . . . 157
7.9 (a) CAD rendering of the upper limb system (setup for left hand positioning). (b) Photo of the system mounted on a scanner table with the patient placed in supine position and his arm strapped on the arm holder of the system (setup for right hand positioning). (c) A four bar linkage mechanism connecting the linear motion in the rack and pinion mechanism to the rotational movement in the arm holders about the pivot point. 158

7.10 Block diagram of the control scheme in the both limb positioning system. 159
7.11 (a) Auxiliary equipment in the control room. (b) Hardware devices inside the electronics box: FPGA processor (NI CompartRIO 9004), solenoid valves and circuitry to converts optical pulses from the position encoders into electrical pulses. Optical pulses are transmitted via optic fibres through the wave guide to the control room. 160
7.12 A custom design electrical-optical converter capable of dealing with six channels (two for each encoder), (b) its circuit diagram in one channel. The device converts electrical pulses from the encoders to optical pulses and transmits the signals to the receiver in the control room via optical fibres. (c) The circuit diagram of the optical-electrical converter (receiver) in one channel. 161
7.13 (a) Block diagram of the trajectory control in the low extremity positioning system. Cubic Segment method is adapted to ensure the joint movement smoothness and synchronisation of each actuated axis. (b) Measured position for all three axes following a defined trajectory. 163
7.14 Average signals in the region of interest RIO1 at the tendon is normalized with that at a proximal structure RIO2 which is only subject to magnetisation (such as bone marrow). 166
7.15 The 3DOF lower limb system with patients set up for scans of: (a) the Achilles tendons, (b) the patellar tendons and quadriceps tendons. (c) The 1DOF upper limb system for scans of elbow tendons and vincula brevia tendons in forefinger. 167
7.16 Signal intensity at the Achilles tendons from four volunteers normalised to bone marror. Increase in the signal is observed from around 40degrees, peaks at around 55degrees, and then decreases rapidly. Subjects had their knee in touch with the scanner wall at different angles when the experiments ended, but all were at greater than 65degrees. The final angle γ_f is subject to the size of patients. 168
7.17 (a) and (b) respectively show the 0degrees and 55degrees images of a slice through the Achilles tendon of a volunteer acquired using the 3DOF system. 168
7.18 Signal enhancement ratios of different tendons at the magic angle. Comparison between the signal intensity at magic angle and that at their initial orientation γ_0. 169
7.19 Normalised signal intensity at the patellar tendon, quadriceps tendon, elbow tendon and vincula brevia tendon in forefinger plotted against their orientation to the main field. . . 170
7.20 (a) and (b) respectively show the 0degrees and 55degrees images of a slice through the patellar tendon of a volunteer, acquired using the 3DOF system. 170
7.21 (a) and (b) respectively show the 0degrees and 55degrees images of a slice through the quadriceps tendon of a volunteer, acquired using the 3DOF system. 171
7.22 (a) and (b) respectively show the 0degrees and 55degrees images of a slice through the elbow tendon of a volunteer, acquired using the 1DOF system. 171
7.23 (a) and (b) respectively show the 0degrees and 55degrees images of a slice through the vincula brevia tendon in forefinger of a volunteer, acquired using the 1DOF system. . . 172
7.24 MR images of an vincula brevia tendon taken from 0degrees to 59degrees 173
7.25 Time taken for hardware setup and image acquisition for different tendinous imaging studies 174

List of Tables

3.1 Description of ferromagnetic, paramagnetic, and diamagnetic materials [Schenck, 1996] . 54
3.2 Procedures for calculation of signal to noise ratio Reduction 61
3.3 Details of the image sequences 61
3.4 SNR degradation under different test conditions 63
3.5 Artifact size measured from different orientations according to the ASTM standard F2119 65

4.1 List of symbols in the neural network 78
4.2 List of symbols used in the haptic control 80
4.3 Specifications of the system 83
4.4 Speed errors of the model under different load conditions 84
4.5 Tuning formula under PID control 93

5.1 Definition of symbols in the kinematics calculation 105
5.2 DH transformation matrices for each connected link in the prostate robot 106
5.3 DH transformation matrices from frame 0 to frame N: 107

6.1 SNR degradation under different test conditions 126
6.2 Summary of the procedure time in each task 138
6.3 Details of biopsy procedures on three patients. Needle notch projection refers to the expected position of the needle notch after it is inserted to the prostate, and it is shown as the centre of the yellow box in Figure 6.9. 140

7.1 List of symbol definitions 146
7.2 Kinematics equations for positioning Achilles tendons 150
7.3 Kinematics equations for positioning patellar tendons 154
7.4 Kinematics equations for positioning quadriceps tendons 155
7.5 Accuracies of the two systems as measured on the bench in the laboratory using conventional metrology equipment and in the MRI scanner using fiducial markers 156
7.6 Details of the image sequences 163
7.7 SNR reductions in image sequences of TSE and True FISP 164
7.8 Details of the TSE image sequence 166

List of Abbreviations

2D	Two Dimensions
3D	Three Dimensions
ASTM	American Society for Testing and Materials
BW	BandWidth
CAD	Computer Aided Design
CT	Computer Tomography
DC	Direct Current
DICOM	Digital Imaging and COmmunications in Medicine
DOF	Degrees Of Freedom
DRE	Digital Rectal Examination
DSV	Diameter of Spherical Volume
EM	ElectroMagnetic
FA	Flip Angle
FDA	Food and Drug Association
FISP	Fast Imaging with Steady Precession
FLASH	Fast Low Angle SHot
FOV	Field Of View
FPGA	Field Programmable Gate Array
GE	General Electric
GUI	Graphical User Interface
HIFU	High Intensity Focused Ultrasound

IC	Integrated Circuit
IMechE	Institute of Mechanical Engineers
LCD	Liquid Crystal Display
MRI	Magnetic Resonance Imaging
NI	National Instruments
NMR	Nuclear Magnetic Resonance
PAN	PolyAcryloNitrile
PC	Personal Computer
PCB	Printed Circuit Board
PID	Proportional, Integral, Derivative
PPM	Parts Per Million
PSA	Prostate Specific Antigen
PTFE	PolyTetraFluoroEthylene
PWM	Pulse Width Modulation
RF	Radio Frequency
RIO	Reconfigurable Input Output
RMS	Root Mean Square
ROI	Region Of Interest
RP	Rapid Prototyping
RT	Real Time
SAR	Specific Absorption Rate
SD	Standard Deviation
SNR	Signal to Noise Ration
T	Tesla
T1	Longitudinal (or Spin-Lattice) Relaxation Time
T2	Transverse (or Spin-Spin) Relaxation Time
TE	Time to Echo
TR	Time to Repeat

TrueFISP	TRUe Fast Induction Steady-state Potential
TRUS	TransRectal UltraSound
TSE	Turbo Spin Echo

Chapter 1

Introduction, Aims and Objectives

1.1 Introduction

The precise spatial information and high resolution three dimensional anatomical images provided by Magnetic Resonance Imaging (MRI), has motivated the research of combining the high repeatability and precision of medical robots with MRI for image guided therapy. Despite the advantages of MRI bringing benefits in diagnostic accuracy by presenting higher soft tissue contrast and imaging of any cross section of a patient body without the need for repositioning; the strong magnetic field and the RF environment impose challenges on the development of MR compatible medical robots which is still an ongoing research area. This chapter starts with two clinical motivations for the development of compatible robots: (i) to perform better prostate biopsy for cancer diagnosis and (ii) to facilitate the magic angle effect for tendinous diagnosis, followed by the objective of the research work, and an outline of the thesis structure.

1.2 Motivation for Research

1.2.1 MR guided Prostate Biopsy

Pathology of Prostate Cancer

The prostate shown in Figure 1.1 is a gland in the male reproductive system. Prostate cancer is a disease in which cancer develops in the gland, and cells of the prostate mutate and multiply abnormally. Related diseases can happen in bones, lymph nodes and other parts of the body to which cells have metastasized from the prostate. Pain and difficultly in urinating and erectile dysfunction are the general symptoms for prostate cancers.

Prostate cancer is the most common form of cancer in men and is second only to lung cancer in terms of mortality rates in the UK. As of 2008, there are approximately 27000 men in the UK diagnosed with prostate cancer and 10000 people die of it annually [UKCancerResearch, 2008]. Prostate cancer develops most frequently in men over fifty and 80% of the diagnosed cases are men over the age of 65 [UKCancerResearch, 2008]. The occurrence of cancer becomes greater with increasing age.

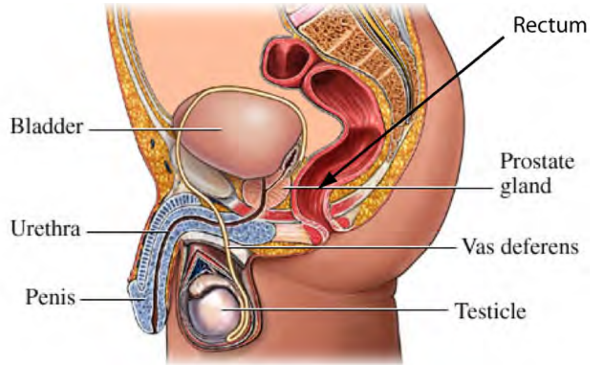


Figure 1.1: Male reproductive system showing the prostate gland located immediately inferior to the urinary bladder

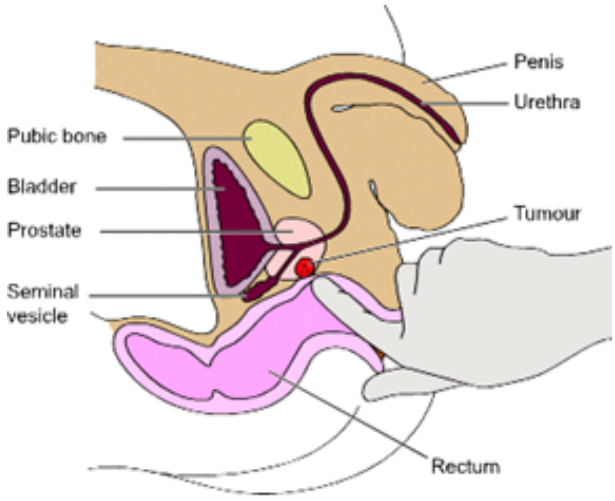


Figure 1.2: A doctor inserts a lubricated finger into rectum for Digital Rectal Examination [Line, 2005].

Examination Methods of Prostate Cancer

Regular prostate examination is imperative to prevent death from the disease. Two of the most common examination methods are to test the amount of Prostate Specific Antigen (PSA) in the blood (which is a substance released by the prostate gland) and to conduct a Digital Rectal Examination (DRE), as indicated in Figure 1.2, in which a doctor inserts a lubricated finger into the rectum and feels for any irregularities on the prostate [Line, 2005, ACS, 2005]. Prostate biopsy would be recommended if the results of either of the two tests are positive in order to confirm whether the suspicious tissue is malignant or benign and what the current stage is.

Transrectal Ultrasound (TRUS) guided biopsy is a frequently used modality for image guided prostate biopsy. An ultrasound probe is inserted into the rectum, next to the prostate, to capture images there. With the help of real-time ultrasound imaging, a hollow core biopsy needle is pierced through into the prostate to extract samples of the tissue for pathological analysis as shown in Figure 1.3

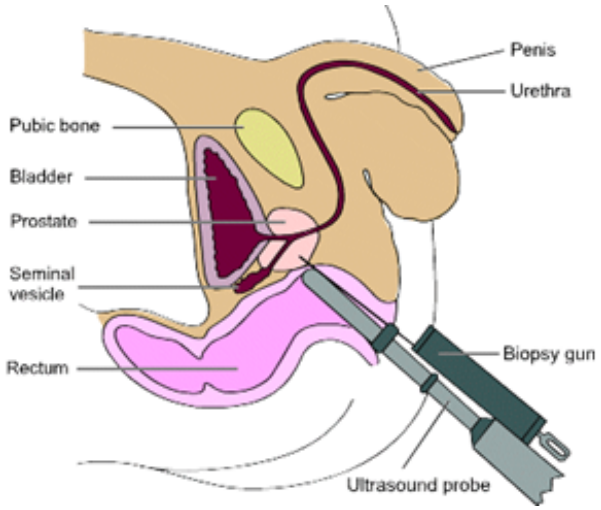


Figure 1.3: TRUS guided prostate biopsy [Line, 2005].

[Line, 2005, Norberg, 1997]. However, the limited image resolution of ultrasound, results in diagnostic inaccuracies and a number of biopsies have to be repeated on the patient in different areas of the prostate in order that cancerous tissue, if any, is more likely to be hit. Literature indicates that 15-31% of prostate cancers are undetected in TRUS guided biopsy [D'Amico, 2000]. Also, as no anesthesia is applied during the repeated biopsies, patients generally experience moderate to severe pain, with immediate complications of feeling faint, rectal bleeding and hematuria.

The limitations of TRUS guided prostate biopsy have provoked interest for using MRI for tumour diagnosis and image guided interventions. Compared with ultrasound scanning, MRI scans present a superior image quality with no radiation exposure on patient bodies and no contrast agents required [Gassert, 2006, Stark, 1999]. Organs of a patient can be rendered in three dimensions for preoperative planning, pathological analysis and image guided surgery [Tseng, 2000]. MRI with use of an endorectal coil can give a more precise image of the prostate and hence improve the accuracy of cancer diagnosis during biopsy.

1.2.2 Diagnostic Imaging using the Magic Angle Effect

Conventional MR sequences using available Time to Echo (TE), produce images that exhibit tissue with a tightly bound structure, with very little or no signal intensity. Dense structure of tissue, such as in a tendon, restricts the motion of water protons and hence increases spin-spin interactions between excited nuclei [Marshall, 2002]. Spin-spin relaxation controls the decay of the signal in the transverse plane and its characteristic time constant is called the spin-spin relaxation time. T2 is the notation for spin-spin relaxation time, and different tissue types have different T2s. Technically, T2 is a decay constant for the transverse magnetisation vector of the excited protons to drop to 37% of its original magnitude [McRobbie, 2003]. Strong dipolar interactions in densely structured tissue, shorten the T2 relaxation time, causing a direct reduction of the signal intensity in an MR image [Erickson, 1993].

In nuclear magnetic resonance (NMR) spectroscopy, one of the factors governing the magnitude of the spin-spin interaction is the orientation of the internuclear vector with respect to the main magnetic

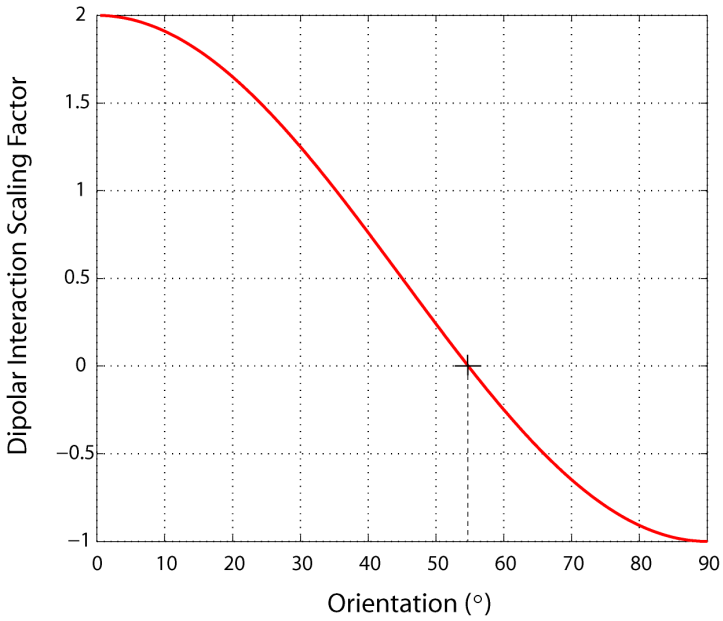
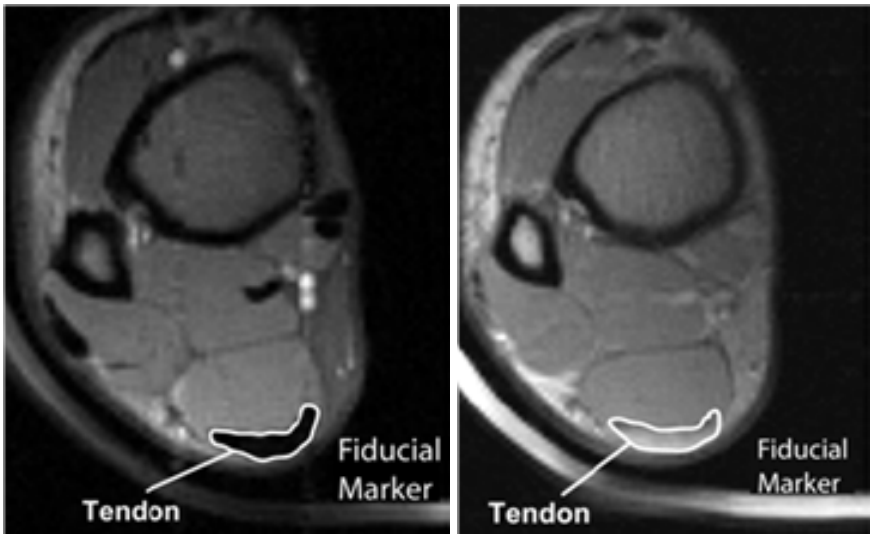


Figure 1.4: Large part of spin-spin interaction is proportional to a factor of $3\cos^2\theta - 1$ and the magic angle effect occurs when θ is equal to 54.7degrees where $3\cos^2\theta - 1 = 0$.

field B_0, such that a large part of the interaction is proportional to a factor of $3\cos^2\theta - 1$, where θ is the angle between the main field and the direction along which the spins are coupled in the structure in which they are held; for example a tendon [Erickson, 1993]. From Figure 1.4, the factor becomes zero at $\theta = 54.7$ degrees and the dipolar interactions are then minimised. This particular orientation is named the "Magic Angle" and the phenomenon is coined the "Magic Angle Effect", which refers to the increased signal in MR images of a target tissue with a tightly bound structure in one direction, such as tendon or articular hyaline cartilage [Xia, 2000]. The magic angle effect occurs when the orientation of the fibers concerned is set to approximately $\theta = 55$degrees relative to the magnetic field, at which point the T2 relaxation time can then increase about 100 fold [Ballinger, 1996], resulting in the tendons being visible in images generated using ordinary pulse sequences. A bright signal from this effect is commonly seen in the rotator cuff, Achilles tendon and occasionally in the patellar tendon [Ballinger, 1996]. Figure 1.5 demonstrates the magic angle effect in the Achilles tendon at 55degrees with respect to the main field and compares it with the signal at 0degrees.

Recently research has been conducted on the application of the magic angle effect on musculoskeletal MR images [Hayes, 1996] and MR neurography [Chappell, 2004]. It is found that signal intensity of the target tissue changes with orientation to B_0, as a result of the magic angle effect from the highly ordered, linearly orientated collagen within these areas. The enhanced image quality can assist the accuracy of diagnosis; however, exploration of the magic angle effect for tendinous related diagnosis is a difficult task in the clinical environment. This arises from the spatial limitations of a closed bore MRI scanner, the motion of a patient body during scans, and the difficulty in setting a target tendon precisely at 55degrees considering that some tendons are not completely aligned in parallel with the limb. A dialog with radiologists of MRI diagnosis has revealed the motivation of designing an MRI



(a) (b)

Figure 1.5: MR images of an Achilles tendon (a) at 0degrees with respect to the main field and (b) at 55degrees. Tendons with a dark colour in the image represent very weak or no signals, and vice versa.

mechatronic system to automate magic angle related experiments and tendinous related diagnosis.

1.3 Research Objectives

The objective of this research work is to provide a technological base for MR compatible robotics, and this requires a literature survey and research into the area of testing the MR compatibility, special actuator and sensor development or adaptation, system control and kinematic analysis. Driven by the clinical motivations, two types of MR compatible systems will hence be developed for the specific applications; one for MR guided prostate biopsy and the other for tendinous related diagnosis using the magic angle effect. Thus, the objectives of the research work comprises of the following main points:

- Research will be conducted to evaluate the MR compatibility of mechatronic components with a series of tests to characterise their effect on the MR environment. The selected components will then adapted to develop MR robots with particular specifications. This testing process is necessary and must be conducted to quantify the interference between the scanner and the robot components before the robots are designed.

- Research will be conducted to develop control strategies for two selected actuators; one is with high force and speed output, suitable for positioning with heavy loads such as limb; another with high positional accuracy and fast response, suitable for accurate positioning and implementation of force control related functions. Both actuators will be then characterised for their control performance and usability for MR robots.

- Research will be conducted to design and develop a robotic system to perform transrectal prostate biopsy. This device will assist clinicians to perform real-time image guided biopsy and target a

suspected target tissue inside a 1.5Tesla (T) closed bore MRI scanner. This system will be used on three recruited patients for clinical trials to verify its functionality.

- Research will be conducted to design and develop limb positioning devices to assist tendinous related diagnosis inside a 1.5T closed bore MRI scanner. These devices are capable of orientating and positioning tendons of upper or lower limbs to any location within the imaging volume to assist magic angle related diagnosis and experiments.

The designed robotic systems have to be MR compatible to ensure that they can be used inside or very near to the isocentre of a scanner. Image distortion and generated artifacts of each component need to be concisely quantified. The systems should fit alongside the patient inside the cylindrical bore of a 1.5T closed bore MRI scanner, and provide an intuitive user interface. The procedures should be performable without producing discomfort to the patient, and the systems should be safe for patients, staff and the MRI scanner.

1.4 Structure of the Thesis

Following the introduction of this thesis, a survey of the literature concerning the research area is given in Chapter 2. It begins with a brief introduction of Magnetic Resonance Imaging, including the principal components of an MRI scanner and a description of the different types of MRI scanners available. Following that is an overview about different types of actuation methods implemented in MRI devices in literature. To measure the position and force of the device, MR compatible sensing technology is required and the current state of sensing technology found in literature is laid out. Chapter 2 also provides a review of the state of the art in the research area of MRI robotics, where engineering challenges imposed by the MR environment are addressed for particular interventions and the solutions appearing in literature serve as a starting point for this thesis.

Chapter 3 discusses one of the most necessary criteria for the MRI robot design, i.e. MRI compatibility. Some important terminologies concerning MR safety are explained in this chapter with five different types of interferences due to the MR environment, affecting the usability of a device in the MR environment, i.e. (i) magnetically induced force and torque, (ii) artifact generation, (iii) signal to noise ratio reduction, (iv) image geometrical distortion, and (iv) thermal effect. Suitable mechatronic components including actuators, position sensors and force sensors are selected and their capability demonstrated with a detailed analysis in terms of those five aspects. The selected components are a pneumatic rotary motor, a linear ultrasonic motor, an optical quadrature position sensor and a piezoresistive force sensor.

Chapter 4 focuses on the engineering evaluation of the pneumatic and the ultrasonic motor actuation control. The chapter starts with an introduction to the motor concepts and a description of the corresponding hardware and electronics. Designs of test rigs are presented for proof of concept and their functionality are then evaluated. The control issue of accurate positioning by a pneumatic motor is discussed and the feasibility of the implementation of master-slave haptic control in the ultrasonic motor is also studied.

Chapter 5 is a complete description of a robot for transrectal prostate biopsy under MR image guidance. It starts with the system specifications and kinematic analysis of a conceptual robot design,

followed by the mechanical design, prototype, and its control electronics and hardware. Integration of an MRI tracking algorithm based on passive fiducial markers on the robot is discussed as well.

Chapter 6 is a detailed report of three clinical trials performed by the prostate biopsy robot and discussions on them. It comprises of the evaluation of the MR compatibility of the whole system, the control schemes for needle alignment to target lesion, descriptions of the graphical user interface, and the clinical procedures, and three clinical cases reported.

Chapter 7 describes two limb positioning robots to facilitate tendinous related diagnosis using the magic angle effect; one for tendons in the upper limb; and the other for tendons in the lower limb. Design specifications are first summarised and the kinematics for tendon positioning in the lower limb, including for the Achilles tendon, patellar tendon, and quadriceps tendon are deduced, followed by the mechanical and control hardware design of the system. The pneumatic motors are used to provide sufficiently high power for limb positioning. The same approach is applied for designing the upper limb positioning device with the prototypes presented. This Chapter also reports the MRI compatibility of the two limb positioning robots, followed by a series of preliminary trials on different tendons from volunteers to verify its functionality. The data is then analysed, with results demonstrating the capability of the two systems to enhance magic angle related tendinous study by way of their accurate positioning.

The final Chapter of this thesis is about the conclusions and future work in relation to this research topic.

Chapter 2

Literature Survey of MRI Robotics

2.1 Introduction

Computer-aided robotic systems combined with high resolution image quality from MRI not only provide clinicians with detailed preoperative planning, but also increase the accuracy and safety of an operation. This has driven the development of MRI compatible robots and the technology required for mechatronic components working in MR environments without mutual interference.

In this Chapter, a brief introduction of MRI principles, scanner structure, and the key components in a scanner are presented to equip readers from different backgrounds with a fundamental knowledge in MRI and so be able to understand the engineering challenges in MRI robotics which is the objective of this research work to overcome. After that, a review of the state-of-the-art technology for MR compatible actuation, position sensing and force sensing are presented; as they are the fundamental components for general MRI robots. Followed is an overview of MRI robots designed for percutaneous interventions.

2.2 MRI System

The engineering challenge and the constraints of the MRI environment have led to different technologies, developed and adapted for MRI robot designs. The general principle of magnetic resonance imaging and the scanner structure are first presented, which then leads onto the issue of the constraints in mechatronic components due to its imaging principles.

2.2.1 Magnetic Resonance Imaging

MRI is a complicated technique involving the combination of advanced science in quantum physics, classical mechanics, cryogenics, superconductivity, electromagnetism and computer technology as well as other special areas of knowledge [McRobbie, 2003]. A complete description of this technique would exceed the pages available for this thesis as a whole, and hence only the basic principles are described here.

Spin or magnetic moment is an intrinsic property of nuclei in magnetic resonance imaging. The nuclei of atoms align with the main field B_0 and stop spinning randomly in every direction, when they are in a strong magnetic field. The nuclei align in the direction of B_0 in the parallel or anti-parallel, and the majority of nuclei magnetic fields cancel out each other, resulting in a net magnetisation of the imaging volume [McRobbie, 2003].

When a radio frequency (RF) pulse is applied to the imaging volume, some of the magnetically aligned nuclei revert to a temporary non-aligned high energy state. Subsequently the excess energy given by the RF pulses is released as the nuclei return to their original alignment. These two processes are called excitation and relaxation. RF receive coils detect the energy released during relaxation and the signal from each relaxation contains information used to construct the image. Voxel is a basic volume element representing image data in MRI. When a plane of voxels is excited, the acquired signals can be used to construct an image of the investigated tissue. Distinguishability of a variety of tissues is achieved based on the fact that tissue with different water proportions presents a specific relaxation curve. Multi-dimensional imaging is achievable by an implementation of gradient coils to shape the magnetic field in such a way that the field strength is different anywhere within that imaging volume.

Based on the sensitivity to the presence of water, a suspected tissue is made visible in MRI as pathology can change its water content relative to the adjacent healthy tissue, and this principle demonstrates a very good tissue contrast. MRI offers an imaging technique to provide high quality image resolution without requiring an injection of contrast agents into the body, and is capable of scanning at different orientations in the imaging volume and three dimensional image reconstructions for diagnosis without moving the subjects. Interested readers in this area are referred to the following literature for further details [McRobbie, 2003].

2.2.2 MRI Scanner Structure

The principal components of a typical MRI machine are shown in Figure 2.1 and 2.2, which primarily consist of (i) the main magnet, (ii) RF transmit and receive coils, (iii) magnetic gradient coils and (iv) a computer system.

Main Magnet

The basic unit to describe the strength of a magnetic field is the Tesla (T) and 1 Tesla represents 10,000 Gauss. In an MRI scanner, a strong and static magnetic field is provided by the main magnet. Superconductive magnets are commonly used nowadays in which winding wires are bathed in cryogenic liquids to cool down their temperature and hence reduce the resistance of their wires to practically zero, allowing a high current to circulate and hence provide a strong magnetic field [Brown, 1995, Friedman, 1989]. Magnetic field strengths of 1.5T and 3T are commonly used in clinical environments, although higher field strengths such as 7T are used mainly for research purposes [Hyder, 2000].

RF Transmit and Receive Coils

RF transmit coils are to transmit RF pulses to excite protons in the scanned area, whereas RF receive coils are to detect the MR signal during the "relaxation period" of the excited area for image

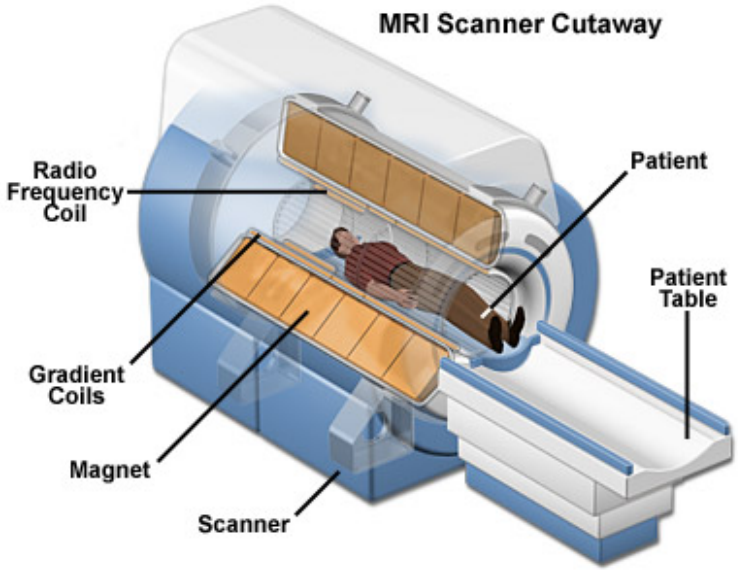


Figure 2.1: Cross section of an MRI scanner , shown its principal components

constructions. Body coils can be used to transmit or receive the MR signal, and smaller receive coils surrounding certain parts of the body, such as head coils, spine coils and neck coils, can be connected to the scanner for imaging special regions. They are designed to be placed as close as possible to the imaged anatomy to maximise the reception of the very weak MR signals and to minimise EM noise picked up from the environment.

Gradients Coils

The function of gradient coils in the scanner is to generate spatial variations of the magnetic field strength in the imaging volume to achieve spatial localisation of the MRI signal. Gradients are produced by three sets of gradient coils in Cartesian directions, in which large current pulses pass through the coils in a carefully controlled sequence to produce the required field variations; it is through this that a loud clicking sound comes from during scan. This noise together with a fairly long tunnel (bore) in a closed bore MRI systems can be a troubling experience for patients, particularly those with even mild claustrophobia and as such they are sometimes unable to tolerate a long duration of an MRI scan.

Computer system

Due to the complicated and multi-tasking nature of magnetic resonance imaging, there are many subsystems to process the commands from the host computer. Typically, the host computer is in charge of interfacing with the operators in terms of the required pulse sequence, its timing, scan orientation and position geometry factors, etc. These commands will be transferred to a microprocessor system, called the pulse programmer (PP) to control the hardware including synchronisation of RF, gradients and data acquisition. After that, the array processor will construct the images and send them to the host computer for image display and additional processing, for example windowing and archiving.

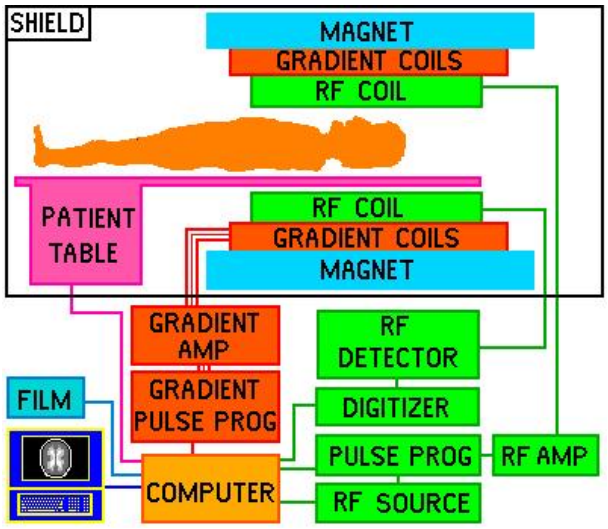


Figure 2.2: Schematic diagram of key components of a typical MRI machine.

2.2.3 Scanner Types

MRI scanners can be classified according to the configuration of the main magnet; i.e. closed bore scanner and open scanner, as shown in Figure 2.3 and 2.4. The former is able to support a higher magnetic field strength with the capability of providing better image quality, and is most commonly used in hospitals with the magnetic strength ranging from 1.5T to 3T. The long tunnel of around 150cm in a close scanner and its narrow diameter of around 60cm in the bore enforce a necessary separation from the imaging volume (near the isocentre) and the entrance of the tunnel which is the closest place a clinician can access a patient. This separation makes direct free hand interventions very different and solutions have to be found to develop manipulators for particular interventional tasks.

In contrast, open scanners are ideal for interventions because of their open magnet configuration where the imaging volume is accessible during scanning as illustrated in Figure 2.4, and these types of scanners are more suitable for patients with claustrophobia, although these advantages are antagonistic to the magnetic field strength. Special designs in open scanners are commercially available, such as a small scanner with a moveable base for use in clinics (Figure 2.4(b)) [Dotmed, 2009], and an upright type open scanner convenient for spinal scanning (Figure 2.4(c)) [Brunswick, 2009]. Modern clinical open scanners have field strengths ranging from 0.2T to 1T, meaning a sacrifice of image quality for better patient accessibility.

2.3 Challenges in MRI Environment

2.3.1 Magnetically Induced Force and Torque

MRI brings advantages in medical imaging and diagnosis but its working principle poses great challenges in designing medical devices to work in the MR environment. Conventional robot components such as steel bearings, screws and motors contain a certain amount of ferromagnetic or paramagnetic



Figure 2.3: (a) Conventional closed bore scanner (3T Siemens Trio MRI scanner) [Siemens, 2009]



(a) (b) (c)

Figure 2.4: Open bore scanners: (a) Philips Mid-Field Open MRI system Panorama, 0.6T [Hamstring, 2009]. (b) ESAOTE Hologic scanner, 0.2T permanent magnet [Dotmed, 2009]. (c) East Brunswick Open Upright MRI scanner, 0.6T [Brunswick, 2009].

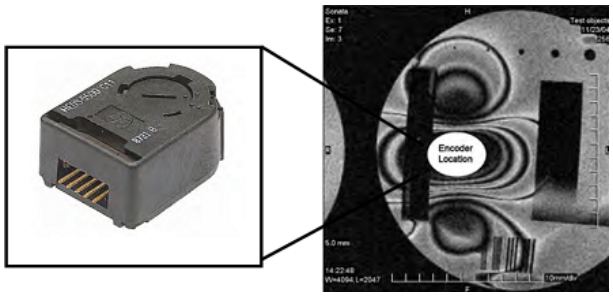


Figure 2.5: (left) Commercial optical encoder (HP HEDL-5540) (right) Image artifact caused by the magnetic metal component in the encoder.

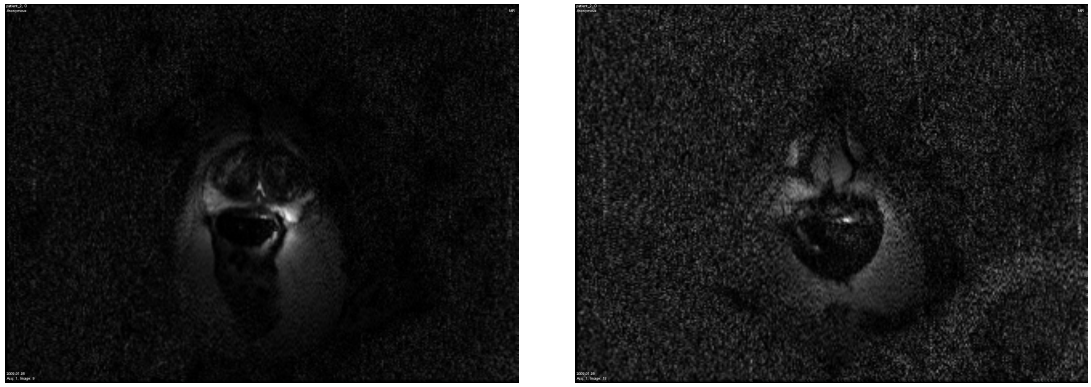
materials which induce an elevated force or torque due to the strong magnetic attraction [Schenck, 1996, Elhawary, 2006]. The attractive force can present a high risk to both patients and clinicians if adequate safety procedures are not applied [Shellock, 2002]. Accidents have even occurred where an unfixed metal object, such as a pan or paper clip has been attracted and accelerated towards the scanner bore like a missile when a patient was being scanned [GE, 2005].

2.3.2 Image Artifact and Geometric Distortion

Magnetic materials possess high susceptibility and affect the distribution of the magnetic field, causing image artifacts in a region of interest, which is a signal void in the image. For example, stainless steel with austenite crystal structure is a commonly used engineering material and it is a magnetic material as it consists of 10-15% nickel [AISI-F2119, 2004]. Even if magnetic materials are placed outside the imaging volume, it is still possible to cause warping in the image known as image geometric distortion. Conductive materials near the imaging volume can potentially provide signal voids and signal degradation of the images due to RF interference [Sled, 1998, Armenean, 2004]. Figure 2.5 shows an MR image of a commercial optical encoder (HP HEDL-5540), in which a magnetic metal component involved generated an image artifact a few times larger than the body of the encoder in the image and voided the image signal around it.

2.3.3 Degradation of Signal to Noise Ratio

Electromagnetic fields induced by electronic components interfere with the MR environment, reducing the Signal to Noise Ratio (SNR) of an image [Schenck, 1996, Shellock, 2002]. Conventional electromagnetic actuators and electronic sensing components generate substantial signal deterioration in the scanner. Figure 2.6 shows MR images of a patient prostate in transverse plane: (a) is the image taken when an electronic amplifier was not powered but placed near to the scanner bore entrance; (b) is the one taken when the amplifier was powered, showing a severe SNR reduction in the image. Research has been conducted on technologies for non-electromagnetic actuation principles in the MR environment such as application of pneumatic systems and ultrasonic motors [Muntener, 2006, Stoianovici, 2007a]. However, the power generated by ultrasonic motors is limited by their own frictional actuation principle and the voltage and current they are operated at. Additionally, their power consumption is proportional to the EM interference generated. For pneumatic actuation, system delay is the intrinsic



(a) (b)

Figure 2.6: (a) MR image of a patient prostate taken when an electronic amplifier placed near to the scanner bore entrance was not powered. (b) Image taken when the amplifier was powered.

problem. Even though the solution of using high pressures up to 8.3bars is found in literature to minimise the delay, this can be a potential danger to clinicians and patients in the case of air leakage. For position sensing, non-metal versions of optical encoders have been developed based on optical fibres, to transmit optical signal pulses to and from the scanner room. More detail will be provided in the following section reviewing the state-of-the art technology in actuation and sensing to minimise artifacts and EM interference to the scanner.

2.3.4 Magnetically Induced Thermal Effect

An eddy current is induced when a changing magnetic flux passes though a conductive material. That can occur when (i) switched gradients and RF pulses from the scanner interfere with a metal component, or (ii) a metal component is designed to rotate and move at speed in the scanner field which can impose a large changing magnetic flux on the component itself, potentially causing a thermal heating effect and damage. Thus, not only magnetic but also conductive materials, if necessary, must be considered carefully in the design of MR robots. This restriction makes it a tough task to select a suitable material for the body of the robot, considering that most of the commonly used rigid materials such as stainless steel and carbon fibre are either conductive or magnetic.

2.3.5 Workspace Limitation

The limited space in a scanner bore is also a challenge in designing an MR robot. Cylindrical MRI scanners are prevalent in medical applications due to their strong magnetic field, and consequent higher imaging resolution capability compared to open type scanners. However the cylindrical scanner, for example a 1.5T Siemens MAGNETOM Avanto scanner, has a bore diameter of just 60 cm (actual 55 cm when considering the space taken by the bore plastic cover) whilst most of the area is already occupied by the a patient body [Gassert, 2006a, Tsekos, 2008]. Figures 2.7 and 2.8 indicate the workspace of a cylindrical MRI scanner when patient is in supine position. Figure 2.9 shows a patient placed in the left decubitus position in a mock scanner which is a common posture for the transrectal biopsy, in

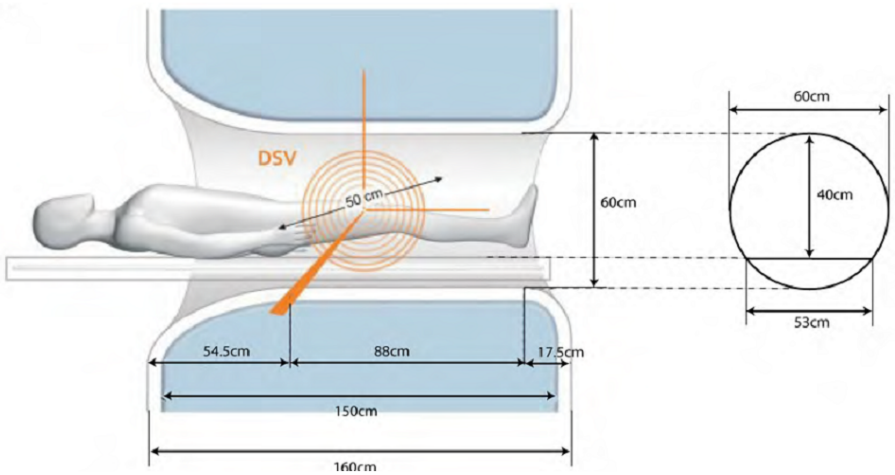


Figure 2.7: Workspace of a scanner with diameter of 60cm [Sie, 2005]

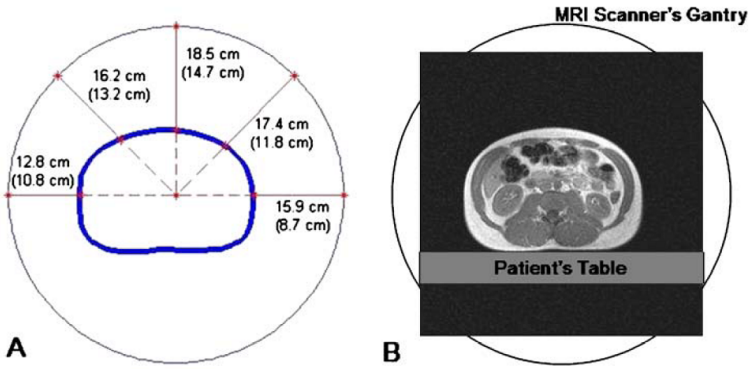


Figure 2.8: Cross sectional view of the scanner with a patient's profile, showing a very limited workspace for image guided procedures and even for the location of the device [Tsekos, 2008].

which very limited space is left for location of a biopsy device. Therefore, an MRI compatible robot is required to be compact and functional specific in order to optimise the limited working area to perform procedures.

2.4 MRI Compatible Robot

MRI robotics contribute to a wide range of research activities including interventional radiology studies, neuroscience, and elastography; in which they are utilised and coupled with MRI scanners to produce accurate and controllable procedures. It provides an essential tool in research areas including generation of precise mechanical vibration to understand the density of deep underlying tissue for tumour diagnosis in MR elastography study [McKnight, 2002a]; simulation of complex virtual environments, with a haptic motion interface coupled with functional MRI, to study human motor control in neuroscience [Gassert, 2006b]; and execution of real-time image-guided therapy in interventional radiology such as biopsy, brachytherapy and image guided focused ultrasound ablation [Krieger, 2005, Kaplan, 2002]. The following sections review the state-of-the-art technologies of actuation, position

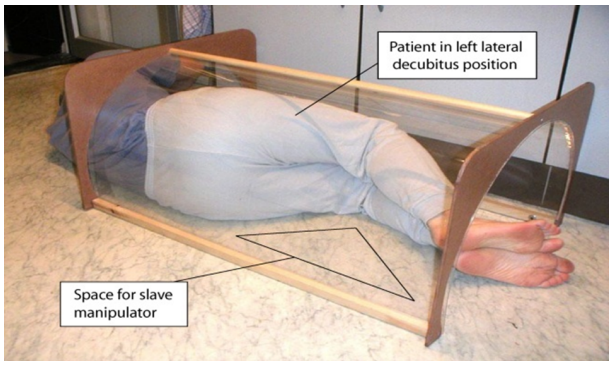


Figure 2.9: Life size mock-up of an MRI scanner with a human subject placed in the left lateral decubitus position (a common position for transrectal biopsy). The space available for the manipulator is displayed.

and force sensing in MR robotics, followed by a detailed summary of currently developed MRI robots for various percutaneous interventions.

2.4.1 Actuation Technology

Choosing a suitable actuation method in an MR robot design for particular interventions is of paramount importance. Compared with other electrical and electronic components, such as force sensors and position encoders, actuators with use of electricity drive a relatively large amount of current, meaning the potential of EM interference to the scanner is relatively higher, and therefore selection of suitable actuators is of paramount importance to guarantee the MR compatibility of the designed robot.

Ultrasonic Motor

Ultrasonic motors have been commonly used for actuation in MR compatible robots. Linear and rotational designs are available and based on piezoelectric technology. As shown in Figure 2.10, The actuators generally consist of two main parts: (i) a stator made from piezoelectric material, which generates directional and well controlled high frequency vibration when a corresponding voltage is applied; (ii) a dynamic body, which contains frictional material and which when pressed on the vibrating stator will transform the vibration into a directed movement. As ultrasonic motors do not use the electromagnetic principle for actuation, it is a good solution for actuation in MRI robotics.

Shinsei Corporation Inc. developed a few versions of the magnet free motors including the USR60 traveling-wave ultrasonic motor [Shinsei Corporation Inc., 2004], which has been proved to be MRI compatible and is widely used in MRI robotics [Chinzei, 1999, Chinzei, 2000a, Chinzei, 2000b, Gassert, 2007]. The USR60 is usable in the MR environment for actuation but it is recommended to be kept at least 0.3m-1m from the imaging volume as the use of high-frequency currents still causes a certain amount of image distortion [Muntener, 2006, Chinzei, 2000a]. Chinzei *et al.* developed a robot for general image guidance therapy in an open doughnut-shaped intraoperative MRI scanner. Ultrasonic motor USR60 was adapted to actuate the 5DOF systems and was placed above the head of the practitioners as shown in Figure 2.11 to separate the actuators, motor drives, and all necessary

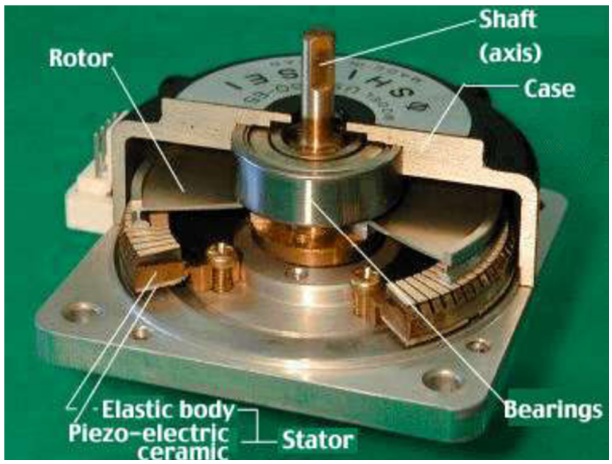


Figure 2.10: Cross sectional view of a magnetism free USB60 ultrasonic motor [Shinsei Corporation Inc., 2004]

electronics from the imaging volume by at least 1m. Two extension arms are used to transmit movement from the mechanical body above the scanner to the end effector in the imaging volume. All cables and electronics were properly shielded and grounded to the earth ground of the scanner, and wires were filtered to minimise EM interference.

Pneumatic Actuator

The pneumatic principle is an alternative actuation method, as pneumatic cylinders and motors can be made from non-ferromagnetic material and pressurised air supplies are generally available in MRI suites. Pneumatic actuators use the energy of compressed air to generate translational or rotational motions and hence they can be designed to be totally MR compatible without the necessity for the use of any electrical or electronic components. MR mechatronics with pneumatic actuation methods can be found in literature [Dresner, 2004, Bensamoun, 2006, Talwalkar, 2008], due to the good MR compatibility and relatively simple and inexpensive designs that they present, allowing a separation of the magnetic components and electronics control system from the scanner room and transmission of airflow via air pipes through the waveguide. However, the phase lag and low bandwidth of the mechanical output are the intrinsic problems of a pneumatic system as air is an easily compressible medium. A low bandwidth, generally of less than 10Hz, is reported in MR devices with the pneumatic actuation principle [Gassert, 2006b]

Generating linear movement is possible with the use of pneumatic cylinder and piston systems and they are generally classified into single action and double action pistons, depending on the number of effective directions. The generated force and speed are subject to the air pressure and the airflow applied to the cylinder barrel. To allow a defined movement or to keep the piston in a selected position, the control system has to regulate the pressure and airflow, and controllable motion is possible with the aid of more sophisticated cylinder design. DiMaio *et al.* developed an MR compatible robot for transperineal prostate biopsy and brachytherapy in a 3T closed bore MRI scanner [DiMaio, 2006]. The robot with 5DOF as illustrated in Figure 2.12 was actuated by custom designed double action



Figure 2.11: A robot for general purpose image guided inventions was develop by Chinzei and integrated with an open intraoperative scanner. Ultrasonic motor USR60, motor drives, and all necessary electronics are placed at a meter away from the imaging volume and mounted to the top of the scanner.

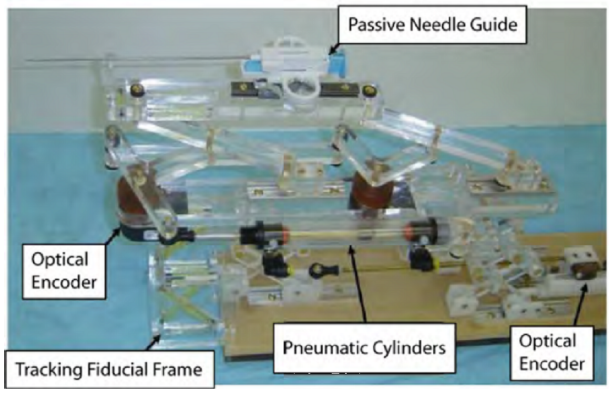


Figure 2.12: A 5DOF robot designed for transperineal prostate biopsy under MR image guidance and actuated by custom design double action pneumatic cylinders [DiMaio, 2006].

pneumatic cylinders made from glass, with piston seals made of graphite. This cylinder design has inherently low friction, and is able to provide smooth linear motion. It is also coupled with a pneumatic brake against the piston rod once the position required is achieved, which is an improvement over conventional double action cylinders where the holding force of the device depends on an applied opposing pressure and is generally not very strong due to the compressibility of the air. Piezovalves were adapted to regulate the airflow and as they are not based on the electromagnetic principle, they are usable inside the scanner room with the added benefit of reduced hose length to mininise the problem of delay present in most pneumatic systems.

Apart from cylinder and piston mechanisms, pneumatic rotary actuators are an alternative seen in literature in the area of MRI robotics. Compared with linear cylinders, pneumatic motors can achieve a higher positioning accuracy. A pneumatic stepper motor was designed by Stoianovici *et al.* for accuracy control and minimised phase lag [Stoianovici, 2007b]. Figure 2.13 and 2.14 show the design of the pneumatic stepper motor and its working principle respectively. The motor consists



(a) (b)

Figure 2.13: (a) PneuStep, an MR compatible stepper motor driven by compressed air (b) CAD drawing of the motor showing the central nut-shaped gear head connected to a screw threaded rod to convert a rotary motion to a linear motion.

of three linear actuators arranged around the circumference of the harmonic gear mechanism. The three pneumatic ports connected to the actuators are sequentially pressurised resulting in a rotary step motion (Figure 2.14). It can produce torques of several hundred Nmm with angular accuracy of 3.33^o. This motor was specially designed for a transperineal prostate intervention device called MR-Bot, which is reviewed in the next section. To convert the rotary step motion into a linear step motion, a central nut-shaped gear head is attached to the rotor and used to drive a screw-threaded rod as shown in Figure 2.13(b). A custom fibre optical quadrature encoder is embedded and allows closed loop control with each motor step of 0.055mm (linear direction) and maximum speed of 16.6 mm/s, and its control electronics are described in Figure 2.15.

Electromagnetic Coil with the Main Field

Electromagnetic coils are used as an alternative to induce actuation in the strong magnetic field of an MR scanner room by utilising the electromagnetic principle; when a tiny current passes through a coil, which is similar to the principle of conventional DC motors except with use of a much stronger main magnetic field. A maximum torque is induced on the coil when the normal vector of its plane is perpendicular to B_0 and the induced torque is directly proportional to the number of turns in the coil. In reality the number of turns adapted is optimised in a design to achieve an adequate strength of actuation. Rossman 1999 developed a device for generation of mechanical excitation for MR elastography study [Rossman, 1999]. Figure 2.16 shows the device with two breast compartments linked to individual coils where torque is induced by an applied current. Mechanical vibration is achieved by driving with an alternating current through the coil.

Electromagetic coils provide a simple and inexpensive method for actuation in the scanner. A drawback of this method is that the actuation direction is always limited to be perpendicular to the main magnetic field and additionally its actuation characteristics such as force and speed will change with the orientation of the coil and its location relative to the scanner. As such, examples of this actuation principle are as far found only in the area of MR elastography where the location of coil and orientation are relatively fixed.

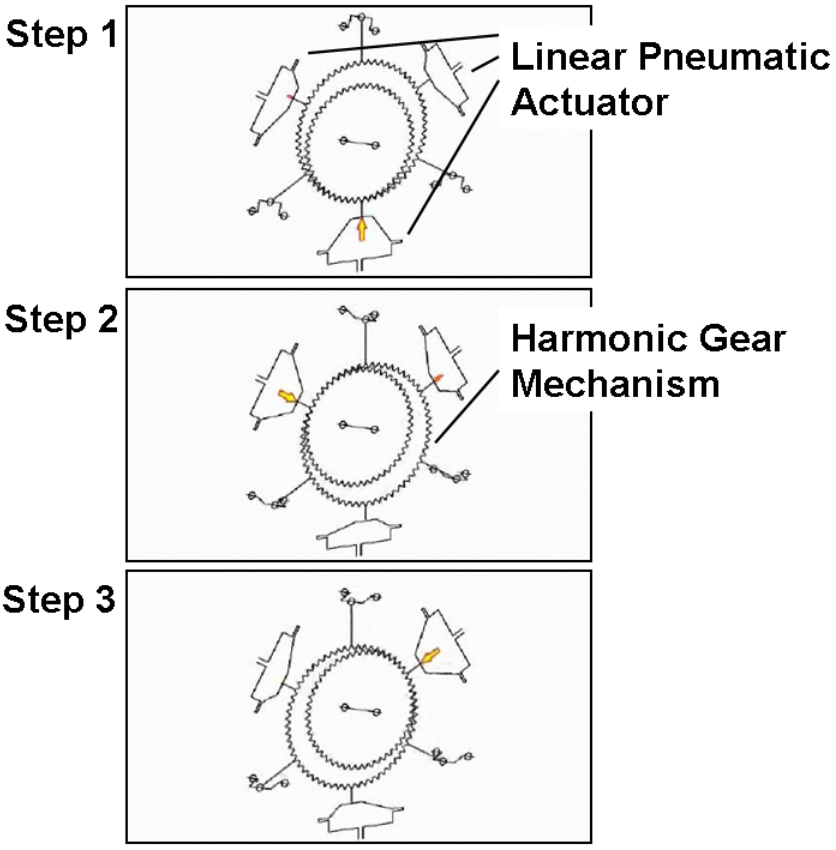


Figure 2.14: Schematic diagram of the pneumatic stepper motor, showing the sequential airflow to the three linear actuators individually.

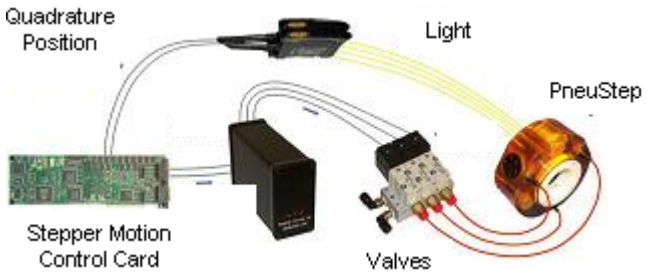
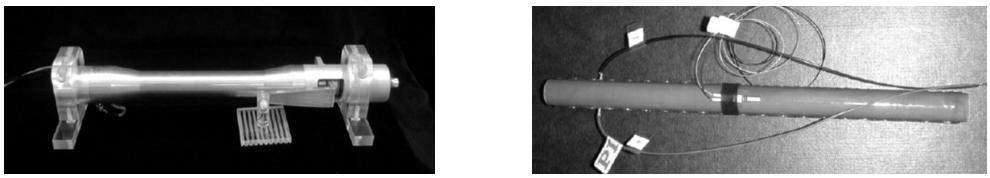


Figure 2.15: Control electronics of the pneumatic stepper motor: a custom optical encoder is embedded into the motor for position tracking, adapter to convert optical signals to electrical signals, a stepper motion control cards to generate sequential control signals, and pneumatic valves to regulate airflow to the motor.



(a) (b)

Figure 2.16: (a) Single unit of electromagnetic driver. (b) A MRE motion generator for mechanical excitation of human breast [Rossman, 1999].



(a) (b)

Figure 2.17: (a) A general purpose MRE motion generator, in which piezoelectric actuation is used with a simple level mechanism to amplify the vibration magnitude up to 1mm. (b) 250mm long piezoelectric stack from PI [PI, 2009].

Piezoelectric Stack

Another approach of generating actuation is the use of piezoelectric material for a short range of motion. Piezoelectric stack elongation is in the range of hundreds of micro meters when an electric potential is applied. This material possesses the properties for actuation with a high accuracy and fast response. Although piezoelectric ceramics can generate high forces, the small displacement amplitudes increase the complexity of the design and mechanical amplification mechanisms must be applied to achieve sufficient displacement. Uffmann *et al.* developed an actuation device indicated in Figure 2.17 for general MR elastography applications [Uffmann, 2002]. A very long piezoelectric stack with a length of 247 mm and diameter of 18.5 mm was implemented as shown in Figure 2.17(b), which generates a 200μm displacement. A lever mechanism is coupled to the stack to provide motion amplification of 1:5.

Although the small displacement produced by a piezoelectric stack makes it function-specific for a particular range of motion, it is potentially a good actuation method for force and stiffness displays on haptic medical devices, such as those which incorporate the vibrotactile principle [Verrillo, 1963, MacLean, 2000]. Also, by implementing a mechanical amplifier design and by connection of multiple piezoelectric stacks together, a range of motion up to a few millimeters can be generated and it can be suitable for generating a short range motion in medical robots such as in microsurgery or in thermal therapy for laser positioning [GlobalSpec, 2009].

Summary of Actuation Technology

In the area of MRI mechatronics, the commonly used actuation principles available in literature were reviewed and can be summarised into categories of: (i) ultrasonic motor, (ii) pneumatic actuator, (iii) electromagnetic coil, and (iv) piezoelectric actuator.

Actuation with the use of ultrasonic motors appears to be prevalent in MRI robotics. This type of actuator produces motion based on resonant vibration of the piezoelectric materials and their use has been found in many MRI mechatronic devices. Due to the use of electrical cables in the motor, it is a common strategy to keep the motor 0.3-1m from the scanner isocentre to minimise EM interference.

Pneumatic actuation allows the placement of the necessary electronics and pneumatic valves outside the scanner room and transmission of airflow to the actuator in the scanner with air pipes via a waveguide. This method is able to eliminate the MR constraints to the necessary electrical and electronic components, and has successfully demonstrated its feasibility in different MRI devices [Moser, 2003, Ganesh, 2004]. Despite the intrinsic problem of system delay and difficulty in smooth and controllable positioning, these issues have been addressed by special pneumatic actuator designs [Krieger, 2007, Stoianovici, 2007].

Actuation with an electromagnetic coil is an alternative, and it is a simple-to-use and cost-effective approach. With the use of the strong magnetic fields in the scanner, a current passing through a coil generates force perpendicular to the direction of the magnetic field. As the actuation characteristics will change according to the orientation and position of the coil, this method is found applicable in MR elastography [Rossman, 1999, Ehman, 2008, Braun, 2003].

Actuation with piezoelectric stack possesses the capability of high accuracy and fast response, although this working principle only allows a small displacement up to hundreds of micro meters. In any case piezoelectric stack incorporated with suitable mechanical amplifiers is ideal for force display and accurate positioning [GlobalSpec, 2009].

2.4.2 Position Sensing Technology

Optical Encoder

In terms of position sensing, only two different types of position encoders have been identified in MRI robotics; that is the form in which the position signal is counted by the relative optical encoders or that where the absolute position is directly shown. Optical encoders are typically reflective, consisting of light emitting diodes (LED) and a photo detector, both of which are directed towards an encoder code-disc or encoder code-strip. The LED emits light and the photo detector measures the light pulses reflected by a moving code-element which consists of alternating reflective and non-reflective surfaces. A pattern of light and dark can be recognised by the sensor, so that the position and direction of the movement can be measured incrementally relative to the initial position. With a more complex design it is possible to determine the absolute position. Figure 2.18 illustrates this operating principle [Avago, 2003].

To avoid image quality degradation due to EM interference and artifact generation due to magnetic material used, custom designed MR compatible position sensors have been developed based on the principle described above. Virtanen designed a magnetic free, absolute position encoder, in which the

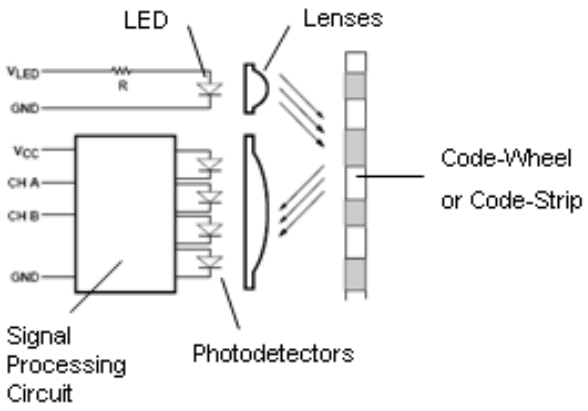


Figure 2.18: Optical position encoder [Avago, 2003].

light source and photo detector were placed in the control room but the light signals were transferred to and from the device body in/near scanner bore with a bundle of optical fibres [Virtanen, 2003]. The schematic diagram of this design is described in Figure 2.19. Light transmission through optical fibres allow the placement of all necessary electronics from the scanner room and this method has been proven highly MR compatible [Virtanen, 2003]. This approach was also found in Chapuis's design shown in Figure 2.20 [Chapuis, 2004]. Anyway, it is reported in literature that carefully selected commercial optical encoders have been used for position sensing. With the proper shielding of all electrical cable and filtering, image quality degradation and artifact generation can be minimised [DiMaio, 2006]. This is a cost-effective, simple and robust approach, so long as a compromise of image quality is within an acceptable level for a particular intervention.

Summary

Position sensing technology has been developed and offers high MRI compatibility in robot design. These include incremental and absolute position sensors with the use of optical fibres for signal transmission and with placement of electronic components outside the scanner room. Even though the technology has been implemented in MRI robots, the sophisticated design of the position sensor such as the one demonstrated in Figure 2.19 increases the robot design complexity and cost of manufacture. Unlike actuators optical encoders generally do not consume much electricity, and this property intrinsically limits the potential SNR reduction due to EM interference to a low level, and such a high degree of MR compatibility is required only if the sensors are to be placed very close to the field of view.

2.4.3 Force Sensing Technology

Optical Force Sensor

Force measurement is an important ability for a robotic device required to perform tasks with adequate force, and force sensing forms a fundamental element in haptic technology. Haptics refers to the

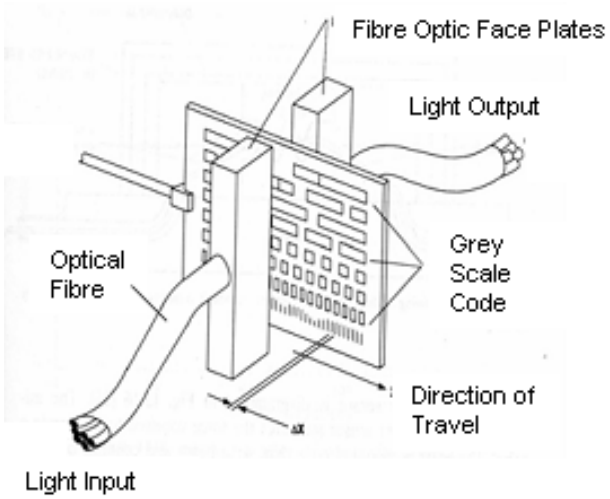


Figure 2.19: Schematic diagram of an MRI compatible absolute position encoder design: optical signals are transmitted to and from the LED and photo detector placed outside the scanner room to avoid EM interference [Virtanen, 2003].

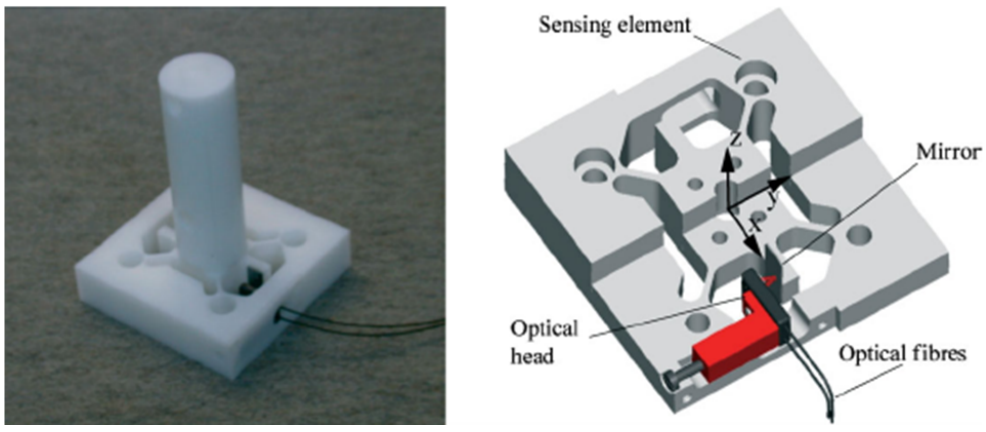


Figure 2.20: Device based on a MR compatible sensor where optical signals are transmitted to and from LED and photo detected based in control with optical fibres [Chapuis, 2004].

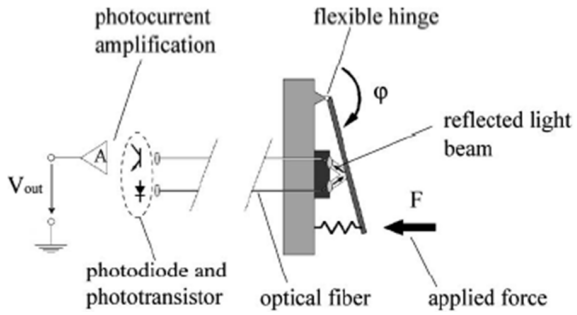


Figure 2.21: Principle of force sensing by detection of the displacement of the hinge spring with light-intensity measurement [Moser, 2003].

technology that interfaces to the user via the sense of touch by applying forces, vibrations, and/or motions to the user. This mechanical stimulation has been used to assist in the creation of virtual environments, and to enhance the remote control of devices (teleoperation). This capability has found useful applications in a variety of research areas including percutaneous and tissue removal procedures [Cobb, 2006, Howe, 1999] and neuroscience rehabilitation [Gassert, 2006b]. In the area of MRI robotics, there is a strong demand for the development of MR compatible sensing technologies for neuroscience studies, although the combination of haptic feedback to medical instruments can also benefit MR guided interventions [Gassert, 2006a, Riener, 2005].

By adding force sensors, haptic control can be implemented in a positioning robot to perform functions related to force control. In conjunction with fMRI, a haptic interface brings advantages in neuroscience and rehabilitation by improving the study of the neuromuscular response in the brain when a patient is required to perform tasks with limb motions and interact with a virtual environment using a haptic manipulator [Gassert, 2006a].

Designs of MR compatible force sensors have been seen in literature [Gassert, 2006a, Riener, 2005, Flueckiger, 2005]. An optical sensor designed to detect the displacement of a flexible hinge spring using light-intensity measurement, was proposed by Gassert as a system for force sensing. A light beam is reflected on a mirror in a flexible polymer probe and transmitted via optical fibres, out of the scanner room. This concept of force measurement allows a compact design with only two fibres per DOF required and can be applied in torque measurement as indicated in Figures 2.21 and 2.22. Gassert incorporated this design in a haptic interface in the form of a handle (Figure 2.23), to study the neuromuscular response when a patient was required to perform motion tasks with his arm.

Tada developed an optical 2DOF force sensor shown in Figure 2.24 and the principle is based on a measurement of the variation of light intensity onto photo sensors on four different quadrants. A light source is mounted on an elastic frame located at the centre of the four photo sensors. When a force is applied to the frame, the light is deflected away from the central area and so the magnitude and direction of the exerted force can then be calculated from the distribution of light intensity measured by the four sensors [Tada, 2002]. This concept was further improved upon by placement of the light emitting and receiving electronics outside the scanner room and by application of the principle of two-dimensional optical micrometry between two lenses to produce accurate and sensitive displacement measurement as indicated in Figure 2.25 [Tada, 2004]. The proposed sensor is capable of measuring

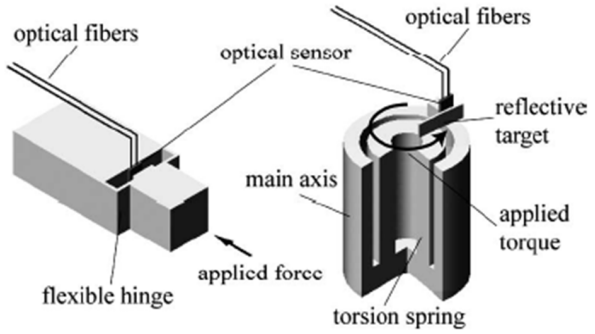
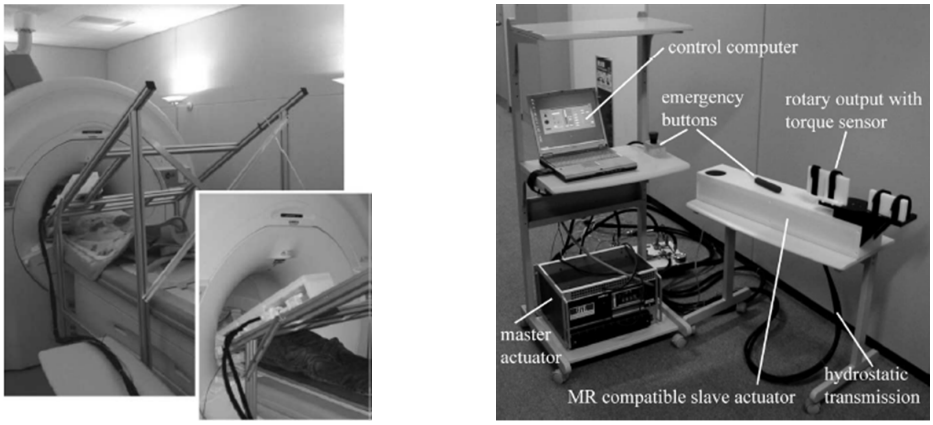


Figure 2.22: Configurations of (a) a force sensor based on a hinge spring and (b) a torque sensor based on a torsional spring [Gassert, 2006a].



(a) (b)

Figure 2.23: (a) A haptic interface mounted on a large aluminum frame, which was developed to investigate the neuromuscular response in human brains [Gassert, 2006a]. (b) The system setup.

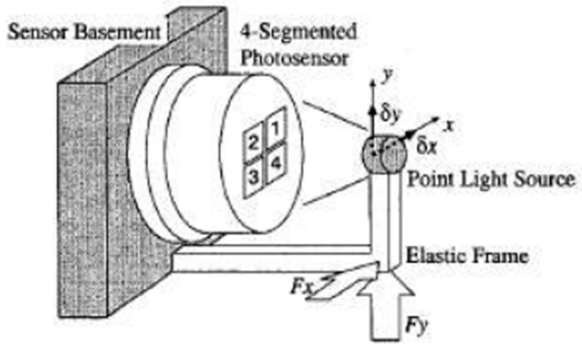


Figure 2.24: An optical 2DOF force sensor [Tada, 2002].

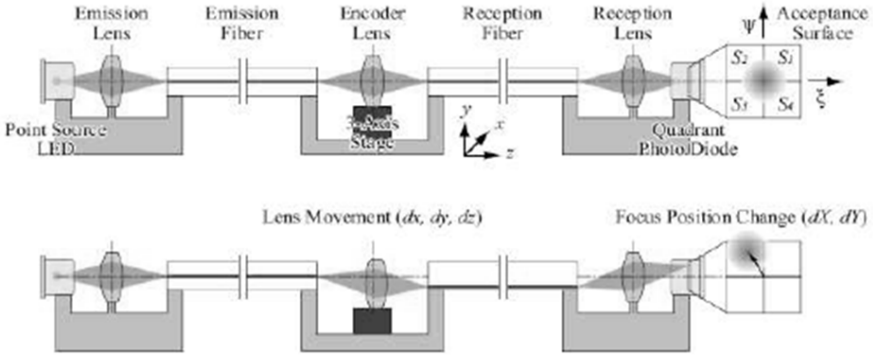


Figure 2.25: Principle of the two-dimensional optical micrometry. The 2DOF sensor consists of emitting and receiving electronics, fibre optics and lenses. Electronics are located outside of the scanner room [Tada, 2004].

forces from 0N to 6N with accuracy of 0.06N.

Summary

MR compatible force sensors allow the possibility of implementing force control algorithms in medical devices and applications are mainly found in neuroscience research where a haptic motion interface coupled with functional MRI is used to understand human neuromuscular response. Currently developed MR compatible force sensors make full use of the variation of light intensity onto photo sensors for the force measurement.

Whilst force sensing technology is evidently significant in medical robotics, applications in MR-guided interventional devices are still very rare. With force feedback in MR guided therapy, clinicians are able to retrieve partly the sense of touch during the procedure even if they are physically separated from the target tissue in the imaging volume, and it has been reported that the haptic information can enhance clinician's performance, especially when cutting and piercing tissues are involved [Gerovichev, 2002 , Marti, 2003].

2.4.4 Medical Robots for Percutaneous Interventions

MR compatible robots open up a new category of minimally invasive surgery and gives rise to many possible concepts for image-guided interventions, especially in percutaneous interventions where robots combined with high resolution MR images provide the capability of highly precise and repeatable targeting. This section provides an overview of the state-of-the-art percutaneous devices developed for use in conjunction with MR imaging, and their functionality and mechanical designs are presented.

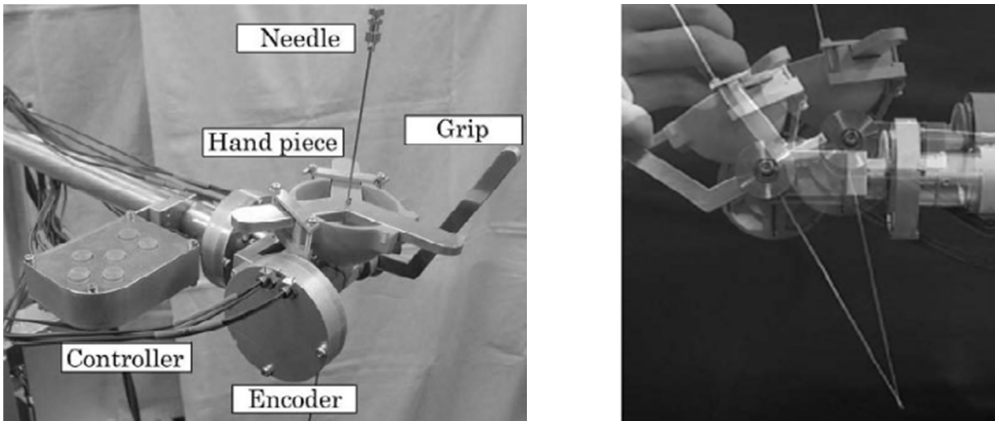
Robot for Liver Biopsy

Conventional liver biopsy with the ultrasound guidance is a different task. As the liver is in motion due to the heart beat and breathing, the clinician must manually track the liver movement during a procedure, whilst ultrasound imaging does not provide sufficient clarity to adequately indicate the target location. In addition to manually tracking the liver, the clinician must also perform the needle insertion and triggering for the biopsy. This step has to be performed quickly and accurately to minimise the pain suffered by the patient and reduce the deformation of the target tissue. This demanding procedure requires the expertise of a skilful radiologist, although there is still a possibility to make mistakes and compromise the accuracy of the needle placement [Hata, 2005].

Hata developed an MRI compatible robot to assist in the performance of liver biopsy as shown in Figure 2.26. The device is capable of tracking the liver motion from the MRI image and keep the needle aligned accordingly [Hata, 2005]. The device consists of a body structure made from aluminium, and a needle positioning unit to guide the needle orientation, which is actuated by ultrasonic motor; to provide a needle alignment. Once the alignment is confirmed by the tracking image, the needle positioning unit stops in its motion as long as the clinician is ready to insert and fire the biopsy needle. This liver tracking provided by the device, assists the clinician to automatically align the biopsy needle to the target point, shorten the time for the procedure, and have demonstrated a high and repeatable accuracy of needle placement. Motion tracking is an interdisciplinary research area, combining the technology of MRI robotics, MR tracking sequences and image processing [Hata, 2005, Hata, 2004].

Robot for General Proposal MRI Guided Therapy

With the increase of publications in the field of MR guided interventions, a growing number of universities and research institutes are investigating MR compatible systems for different procedures such as breast biopsy and prostate brachytherapy [Gassert, 2008]. A general propose 7DOF robotic system was proposed by Tsekos for multi-functional MR guided interventions. The system is equipped with ultrasonic motors USR60 for actuation and commercial optical encoders for position tracking. The system consists of a gantry with 3DOF in Cartesian coordinates for global positioning and an extension arm carrying an end effector. Figure 2.27 illustrates the whole system where the extension arm is connected to the gantry. The arm itself has another 3DOF in the 3 Euler angles for targeting and one additional linear DOF at the end effector for insertion of an interventional tool for a task such as biopsy or thermal ablation [Tsekos, 2008]. The design criteria for a general purpose interventional device means that the extra DOF are required to ensure the flexibility and sufficient maneuverability for different applications, however this causes a trade off in accuracy due to the bending of the system



(a) (b)

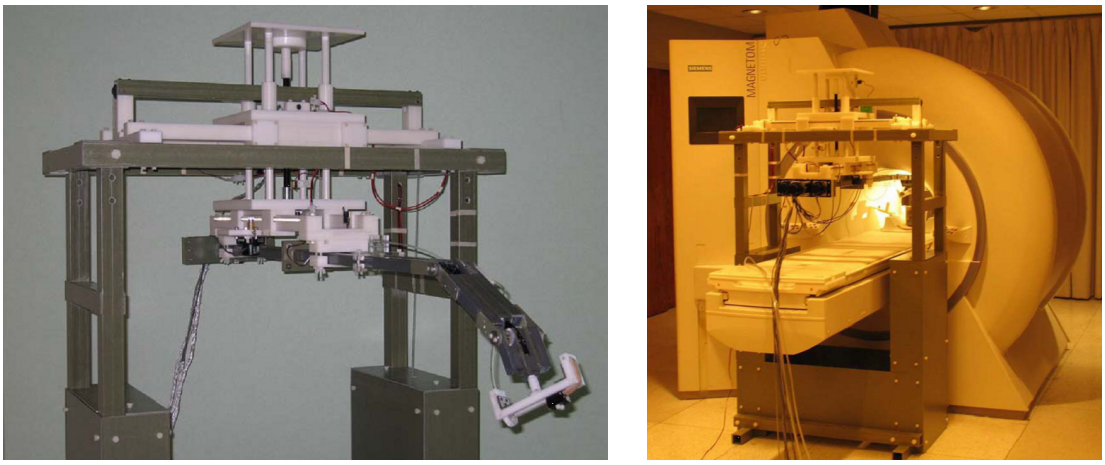
Figure 2.26: (a) MR compatible robot for liver biopsy with the ability of real-time liver tracking. (b) Needle alignment is performed according to the information from the liver tracking.

and backlash of around 2-3degrees in the 3 Euler DOFs in the extension arm.

A safety check algorithm is implemented in this system to avoid collision between the end effector and the patient or scanner bore. A robot trajectory is checked before being implemented, to ensure that the robot movement is always within the allowable maneuvering zone (scanner bore subtracted by the profile of a patient body). This system is coupled with a hardware user handle to allow the user to control the movement of the end effector and the extension arm. The kinematics of the master handle is similar to the extension arm with 3DOF in Euler angles as shown in Figure 2.28. This is the MR robot, out of a handful, for general purpose interventions that has been seen in literature and also the one with the use of a hardware user interface for control (as a master-slave system), although force feedback is still not available. In any case, controlling the orientation and position of a target movement requires the coordination of 6DOF and one can imagine the difficulty of manually controlling the robot, given that MRI anatomical images are the only visual feedback for the user to maneuver the master handle.

Robot for Transperineal Prostate Therapy

Figure 2.29 shows a 5DOF surgical robot, MR-Bot, specially designed for transperineal prostate therapy. The system is actuated with the use of a custom design pneumatic stepper motor, as reviewed in the section of actuation technology in this Chapter [Stoianovici, 2007a]. The use of pneumatic motors and optical encoders ensures its MR compatibility. A clinician controls the robot to target a suspicious tissue and observes the alignment of the biopsy needle in MR images. Besides the biopsy needle, the tool housing in the robot was designed for multiple prostate related therapies, such as brachytherapy seed placement, in which radioactive seeds are inserted in a cancerous area to destroy a malignant tissue. As it is designed for transperineal therapy, the needle must be swiftly punctured through to the prostate target via the perineum skin between the legs at the pubic symphysis. This therapy is a more painful therapy compared with transrectal prostate biopsy and only a limited region of the prostate can be targeted with this method.



(a) (b)

Figure 2.27: (a) A general proposal MRI interventional robot consists of a Cartesian gantry for gross position and an extension arm with 3DOF in Euler angles for targeting. (b) The system was placed at the front entrance of the scanner with the extension arm toward the image volume above the patient.

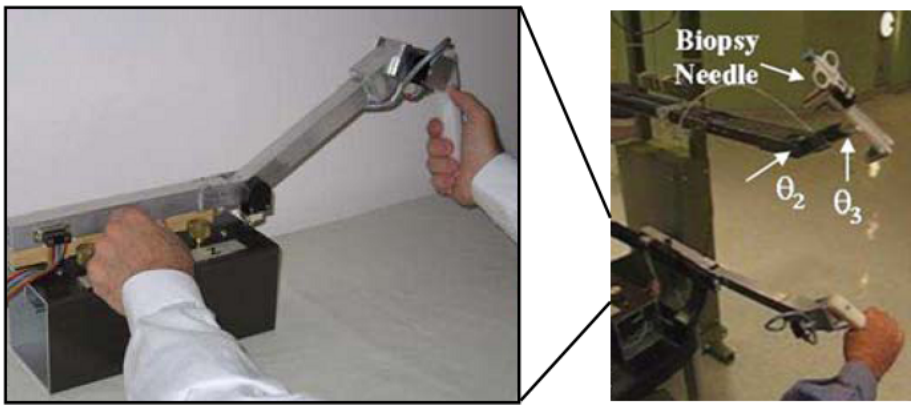
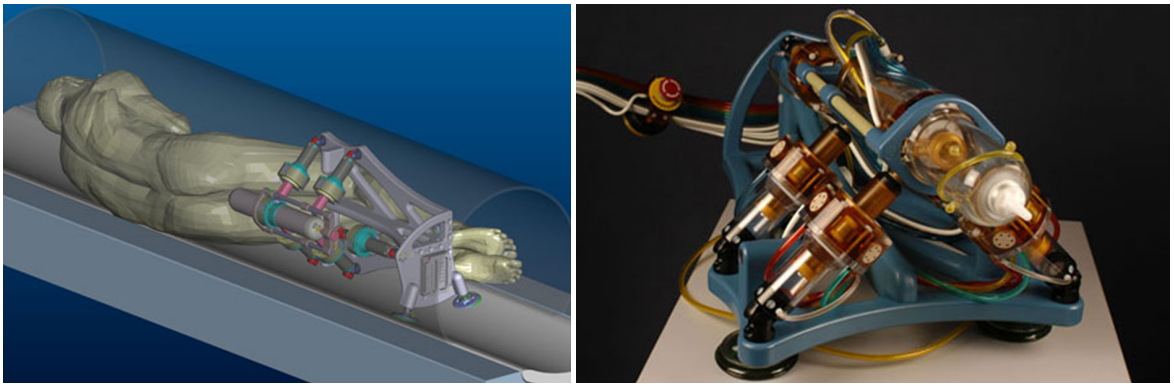


Figure 2.28: The master handle (hardware user interface) is used for control the robot in master/slave mode where the extension arm replicates the motion of the master handle. The master handle and the extension arm have the same kinematics for ease of control.



(a) (b)

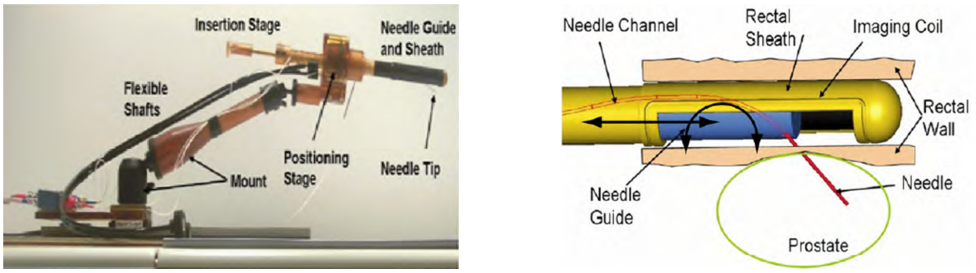
Figure 2.29: (a) CAD rendering of MR-Bot performing prostate biopsy on a patient and (b) its photo [Muntener, 2006].

Manipulator for Transperineal Prostate Therapy

A transrectal prostate biopsy manipulator was designed by Krieger *et al.* at John Hopkins University and the device is shown in Figure 2.30 [Krieger, 2007]. This device is completely manually actuated and therefore does not have the problem of EM interference with the scanner. The manipulator consists of a 3DOF positioning arm mounted on the scanner table and a needle actuation mechanism. It is fabricated mainly from non-magnetic phosphor bronze and plastic. In spite of the simple mechanism, manual actuation can avoid the problems of image degradation and the complicated control issues generated by system backlash and friction.

The positioning arm comprises of two ball joints in the arm body and an aluminium rail at the bottom which allow a range of movement for the rectal sheath. The sheath, with a diameter of 23mm was designed to be inserted into the rectum of the patient and consequently be supported by the prostatic tissue during the procedure. Within the rectal sheath is a needle guide which is allowed to rotate around its own axis and move into and out of the rectum without moving or stretching the rectum tissue therefore minimising the chance of deforming the prostate. An RF receive coil is embedded in the sheath to enhance the image quality of the prostate. Active fiducial markers, which are made from micro coils connected to the scanner imaging channel, are included in the device for position tracking, allowing an update rate of around a second in combination with a special imaging sequence. The position reading, showing the position and orientation of the needle trajectory is then used to calculate the amount of movement in each joint required to reach the target by inverse kinematics, and the clinician can adjust robot accordingly with a set of knobs in which the knob rotation is geared down and transmitted to actuate in each DOF.

Although the method of encoding and actuation make the system very simple to use, it is therapy-specific, for prostate biopsy only, and the function of the device is not quite expandable to perform other prostate related therapy.



(a) (b)

Figure 2.30: (a) A manual actuated transrectal prostate biopsy manipulator consists of two ball joints and one linear rail to allow the workspace to target the suspected tissue. (b) Inside the rectal sheath is a needle channel which allows the channel movement for needle alignment with no shear stress exerted to the prostate [Krieger, 2007].

Summary

This section presented the designs of currently developed robots which have been combined with the benefits of high resolution MR images for accurate percutaneous interventions. They are capable of accurate positioning with good MR compatibility, and most importantly, they have included some key features for interventional devices, which includes: (i) target motion compensation by online tracking, (ii) design unit separation, (iii) hardware user interface, (iv) special pneumatic actuator design for better control performance, and (v) manual actuation for design simplicity. Those approaches provide good insights in designing MRI robots in multiple aspects.

A system for liver biopsy was reviewed which is able to track the liver movement from the MR images, and control the needle insertion unit to follow the motion. This technique of motion compensation reduces the difficulty of the procedure and allows clinicians to perform accurate biopsy. A robotic system was proposed by Tsekos for general proposal MRI therapy, and the robot featured the use of two separate units for gross and fine positioning. As the two units are located at different distances from the imaging volume, they can be designed according to their own acceptable compatibility levels, and therefore have less MR restrictions on the design. This is also the first MR robot integrated with a hardware user interface for manipulation of the end effector. Despite a number of MR compatible systems being developed, only a handful have incorporated a hardware user interface, and none of them are designed with force feedback for MR guided surgery thus far. Force feedback is important for piercing, cutting of a target tissue and tissue palpation, especially in MR guided interventions where the imaged area is at the centre of the scanner and is out of the workspace where the clinician can access [McKnight, 2002b, Ophir, 1991, Brown, 2003]. Stoianovici *el at.* proposed a pneumatic actuation system for transperineal prostate therapy. This system features the use of a special motor design allowing highly controllable positioning and smooth movement with accuracy of 3.33degrees in rotational motion, which was not commonly seem in pneumatic systems. A different design approach was taken by Krieger *el at.* to develop a simple and manually actuated manipulator for transrectal prostate biopsy, with 3DOF joints connected mechanically to knobs and actuated by the clinician according to the tracking image display of the position of the needle projected relative to target point. This approach negates the MR compatibility issues aroused from electronic components,

and have successfully demonstrated its functionality and accuracy in clinical trials.

2.5 Conclusion

MRI is a conventional imaging technique for diagnosis and is commonly used in hospitals due to its capability of producing high imaging resolution, good tissue contrast and ability to produce scans of any 2D slices or 3D volume without the need for any repositioning of the patient. Combination of this imaging capability with medical robotics to provide precise and repeatable therapy image-guided therapy, is the driving force of this research. However, its method of imaging relies on the use of a strong magnetic field, switched gradients and RF fields which impose many challenges for development of medical devices suitable and safe to operate in the MR environment.

This chapter began with an introduction of the MRI principle and the scanner structure to explain the concepts required for a better understanding of the stringent environment it presents for mechatronic devices and the engineering techniques developed to alleviate those problems. The challenges can be classified into: (i) magnetically induced elevated forces and torques, (ii) image artifacts (image voids) and geometric distortion, (iii) signal to noise ratio reduction, (iv) magnetically induced thermal effect and, (v) the workspace limitation for use of devices inside the scanner bore.

To tackle the engineering challenges, technologies have been developed for actuation, position sensing and force sensing specifically for MRI robotics. Ultrasonic motors and pneumatics are dominantly adapted in MRI mechatronics due to their non-electromagnetic working principles. Ultrasonic motors make use of the tiny elongation of piezoelectric materials and the frictional design in the rotor to generate actuation with high accuracy and fast response. Pneumatic actuators are also commonly adapted due to their MR compatibility, as all necessary metal components and electronics can be placed away from the scanner room. Actuation principles with the use of electromagnetic coils and the main field, and piezoelectric stacks, were also reviewed. The fast response and accurate positioning performance of a piezoelectric stack, and the simplicity and cost-effectiveness of an electromagnetic coil are the driving force for researchers to design more sophisticated hardware for their applications in general MRI devices. In terms of sensing technology, custom design position sensors and force sensors are generally based on an optical approach, in which a light source and photo detector are kept away from the scanner room and signals are transmitted via optical fibres through a wave guide in the scanner room wall. Although MRI compatible sensing technology has been developed, commercial sensors with no magnetic or minimal magnetic parts are reported to be usable in MR robots as long as the SNR reduction in image quality is within an acceptable level for particular interventions. Adaptation of commercially available components is a simple and cost-effective approach. MR robot design is always a compromise between the image quality required and the design simplicity.

The currently developed MR robots for percutaneous interventions were also reviewed in the aspects of their mechanical design, actuation methods and functionalities. In general, the use of electronics and cables in actuators, position sensors and force sensors, if necessary, have to be shielded and grounded to the scanner ground, and signals carried on wires have to be low-pass filtered to minimise EM interference.

Chapter 3

Testing MR Compatibility of Mechatronic Components

3.1 Introduction

Before designing an MR compatible robot, the individual components to be used, including actuators, sensors and peripheral electronics, should have their MR compatibility tested to guarantee that their presence does not significantly affect the image quality for particular applications, and that they can function adequately as in standard operating conditions. This Chapter begins by presenting a few concepts related to MR safety and compatibility, followed by an introduction of susceptibility, an important criteria to determine the usability of a material in the MR environment. To further evaluate the effect a mechatronic component can cause to the scanner, individual tests were carried out to quantify the interference between a test subject and a scanner with respects to: (i) magnetically induced force and torque, (ii) signal to noise ratio reduction (iii) artifact generation, (iv) image geometric distortion, and (v) thermal effect. Based on these five criteria, a pneumatic rotary motor, linear ultrasonic motor, optical encoder, and a piezoresistive sensor were tested with the result showing their usability for MR compatible robots.

3.2 MRI Safety and Compatibility

For medical devices used inside the MRI scanner, a set of criteria have to be fulfilled in order to ensure the safety of both clinicians and patients, and their usability in the MR environment. The American Society for Testing and Materials has defined a few key terms to clarify the standard of the equipment working in an MR environment and which also cover the use of general medical robots for image guided therapy [ASTM-F2119, 2004, FDA, 2005].

1. **5 Gauss Line**: This is a border line around the MR scanner within which the static magnetic field is higher than 5 Gauss. The area outside this line is below 5 Gauss and is considered to be safe for the general public. Gauss is a unit of magnetic induction. 1 Tesla is equivalent to 10,000

Gauss.

2. **MR Environment:** This term describes the magnetic characteristic of the environment inside the 5 Gauss Line including the area inside and surrounding the scanner. This term is extended to include everywhere in the procedure room to avoid ambiguity in MR safety protocols. This magnetic characteristic is made up of three electromagnetic fields, i.e. the static magnetic field, the switched gradient fields, and the Radio Frequency (RF) fields.

3. **MR Safe:** This refers to the safety of people within the MR environment including both patients and clinicians, when the device in question is used inside the environment. This implies that devices do not become a safety hazard to the people when introduced into the MR environment; the term does not refer to general safety standards for areas outside the MR environment, because the general safety standards are supposed to be met before considering MR Safety.

4. **MR Compatible:** The term applies if the device in question fulfills the following three criteria when inside the MR environment: (i) MR safe, (ii) the device operates as intended with no performance degradation, (iii) there is no significant effect on the image quality.

It should be noted that devices are accepted as "MR safe" or "MR compatible" when they have produced evidence through a variety of tests. With this evidence, the MR environment, in which the tests took place, must be identified along with the testing procedure and results [ASTM-F2119, 2004]. Therefore, when a device is considered to be "MR safe" or "MR compatible", the MR environment must be specified.

Following this section is an introduction of an important criterion for material selection in MRI robot design, that of magnetic susceptibility. After that, five individual tests are presented to quantify the adverse effects of interference between the imager and a test subject in the MR environment, and which are then applied to quantify the MR compatibility of the actuators and sensors selected.

3.3 Susceptibility and Design Guidelines

Guidelines for designing MR compatible mechatronic devices and selection of suitable materials have been published in the area of MRI robotics [Schenck, 1996, Chinzei, 1999]. Schenck presented a detailed account of describing magnetic susceptibility as an factor in MR compatibility [Schenck, 1996]. The susceptibility of a material is a quantitative measure of its tendency to interact with an applied magnetic field, and is represented by the letter χ, a dimensionless parameter. This property is of a fundamental importance in selection of compatible materials for use in the MR environment, and this parameter is associated to the size of the artifact generation from a subject and the level of magnetic attraction caused by the main magnetic field. Susceptibility χ of most materials is associated to their magnetisation M, by the following equation:

$$M = M_0 + \chi H$$

where H is the external applied field, M_0 is the inherent magnetisation that is present in some materials even in the absence of an applied magnetic field, and the term χH represents the magnetisation in a

Material	Magnetic attraction	Influence to image quality	Susceptibility	Example
Ferromagnetic	Strong magnetic force or torque experienced	Image distorted and degraded even when the subject is located far from the imaging region	$\chi > >0.01$	Iron, steel
Paramagnetic	No	Image distorted and degraded when the subject is located close to the imaging region	$0<\chi<0.01$	Titanium, aluminium
Diamagnetic	No	Negligible even if the subject is located located near and in the imaging region	$-1<\chi<0$	Copper, zirconia

Table 3.1: Description of ferromagnetic, paramagnetic, and diamagnetic materials [Schenck, 1996]

material induced by an external field. Therefore it is important to consider the susceptibility when selecting a suitable material [Schenck, 1996]. Materials can be classified according to their susceptibility into categories of (i) ferromagnetic, (ii) paramagnetic, and (iii) diamagnetic and the definitions of these classifications are listed in Table 3.1 [Schenck, 1996]. Figure 3.1 indicates levels of susceptibility in different materials, and a susceptibility region with which a subject is regarded as MR compatible.

Although susceptibility provides a quantitative parameter to evaluate the usability of a test subject in the MR environment, it is not the only criterion. The switched gradients and the RF fields of a scanner interact with electrically conductive materials, and image artifacts can also be generated by the eddy currents induced [ASTM-F2182, 2002, Kugel, 2003]. Electrical conductivity is therefore as relevant to MR compatibility as magnetic susceptibility is [Peters, 2000]. Ideally materials chosen for mechatronic devices inside the MRI scanner should not degrade the image quality, but MR robot design is always a compromise of acceptable degradation of image quality, design complexity and cost-effectiveness.

A descriptive and practical guide to MR safety and compatibility was presented by Chinzei, and a description of selection of both active and passive components which could be introduced into the MR environment is listed [Chinzei, 1999].

1. For passive mechanical devices such as gears, cams, bearings, ball screws, and linear guides etc, a range of plastic parts are commercially available in the case that rigidity is not the main design concern. For friction reductions in movable mechanisms, plastic and ceramic bearings can be adapted and they are commercially available. Non-magnetic metals are relatively applicable, if necessary, for friction reduction provided that they are not moved or spun at fast speed which can potentially induce eddy currents.

2. For active mechanical devices such as actuators and brakes, electromagnetic devices can generate a large EM interference and are not preferable inside the scanner room, even outside the 5 Gauss

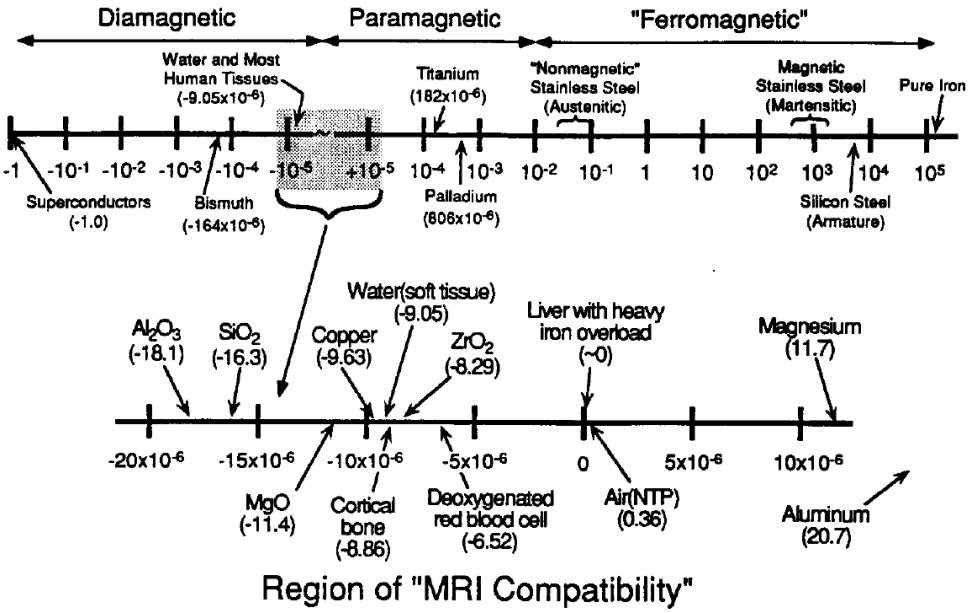


Figure 3.1: Full range of magnetic susceptibility value in susceptibility Spectrum (Top). The region of MR compatibility (bottom) [Schenck, 1996]

Line. Ultrasonic motors, hydraulic, and pneumatic actuators may be an adequate substitute for conventional EM actuators, and they can be made from non-magnetic materials.

3. For sensors, optical encoders can be custom designed, where the light source and the photo detector are placed outside the MR room; with signals transmitted to and from the scanner room through fibre optic cables. Conventional sensors generate EM noise and can potentially distort the images, as such their use in MR environment may compromise the image quality.

3.4 Testing MR Compatibility

RF pulses, static magnetic field and switched gradient fields impose a strict limitation for mechatronic components used in the MR environment. This section presents five different types of interference between the scanner and the applied electrical and mechanical component, including: (i) magnetically induced force and torque, (ii) artifact generation, (iii) signal to noise ratio degradation, (iv) image geometrical distortion, and (v) thermal effect. These five areas are the fundamental considerations required for the evaluation of MR compatibility and they are directly associated to the effect on image quality, the normal functionality of the components and most important, the safety of patients and clinicians.

3.4.1 Preliminary Screening

Engineering plastics, such as Delrin® and Ertalon®, are ideal structural materials for an MR robot if high rigidity is not a main requirement. Plastic exhibits properties of good MR compatibility,

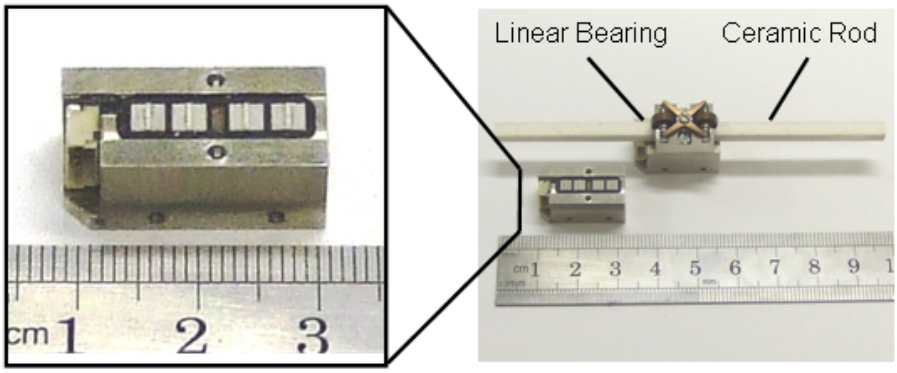


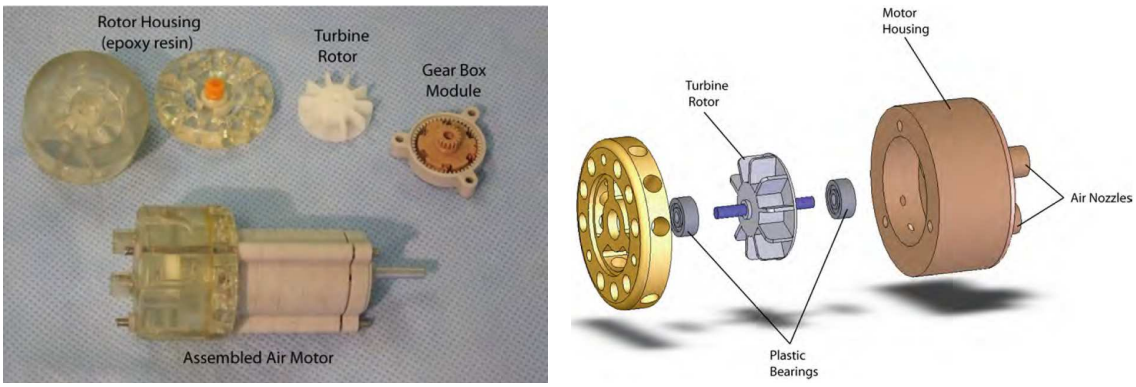
Figure 3.2: (a) Piezoleg, a type of ultrasonic motor based on the piezoelectric technology for actuation. The motor body is made from non-magnetic stainless steel, and the linear rotor is made from a ceramic material [Piezoleg, 2009].

reasonable cost, acceptable mechanical strength, and easy machining properties [Tsekos, 2007]. For MR compatible actuation and sensing technology, solutions are found in literature for commercially available components with acceptable compatibility. Alternatively it is possible to custom design the components to fulfill particular specifications.

Preliminary screening of commercially available actuators and sensors was conducted based on the criteria of (i) the use of non magnetic materials, (ii) the operating current and voltage rating, and (iii) the amount of conductive materials involved. The first criterion singles out those components with no or minimal magnetically induced force and torque, artifact generation, and geometrical distortion; the second criterion singles out those components with minimal SNR reduction; and the last one singles out those components with no or minimal thermal effect.

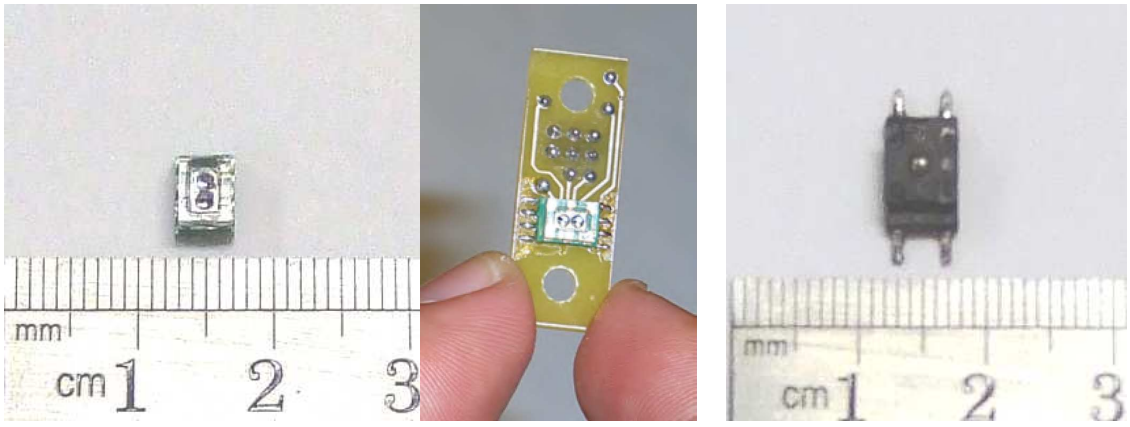
Based on the three screening criteria, an ultrasonic motor, a position sensor and a force sensor were selected from commercially available mechatronic components; and a pneumatic rotary motor, which was previously designed by Aleksander Zivanovic and Michael Lamperth in the research team, was adapted for applications with higher required power. The selected commercially available actuator is the "Piezoleg" motor (Figure 3.2), a piezoelectric ceramic motor from PiezoMotor AB Ltd, with small size, reasonable price and good accuracy [Piezoleg, 2009]. Its speed and torque are limited, with speeds of up to 17.6mm/s and linear forces of around 7.3N. MR compatible actuators with high maximum torque and fast speed, are not commercially available, and therefore the in-house pneumatic actuator design was adapted on the basis of a pneumatic motor coupled with an air turbine and a set of adjustable modular gearboxes. Its rotor and motor housing were rapid prototyped, and its speed and torque can be easily scaled up or down by changes of the gear ratio as well as the operating air pressure. Figure 3.3 indicates the parts of the pneumatic motor. A quadrature optical position encoder (Figure 3.4(a)) and a piezoresistive force sensor (Figure 3.4(b)) were selected because of their tiny sizes and minimal amount of magnetic materials involved.

As this chapter focuses on the evaluation of MR compatibility, engineering descriptions of each component will be discussed in Chapter 4. The following section presents a detailed analysis of five individual tests to assess the levels of MR compatibility of the selected components after the preliminary screening.



(a) (b)

Figure 3.3: (a) The pneumatic rotary motor consists of an air turbine and a set of modular gearboxes. The rotor and the motor housing are manufactured by rapid prototyping. (b) CAD drawing of the air turbine.



(a) (b)

Figure 3.4: (a) A quadrature optical position encoder (left), the encoder surface mounted on a custom design PCB board to form a robust unit (right) (b) piezoresistive force sensor.

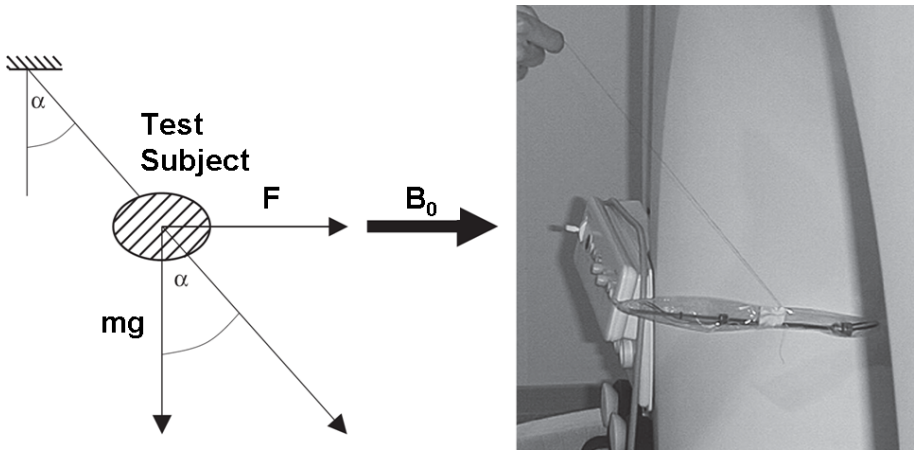


Figure 3.5: Schematic diagram of the test for assessment of the magnetically induced force experienced by the test subject. F is the induced force, mg is the gravitational force of the component, and B_0 is the static magnetic field strength [ASTM-F2052, 2004a].

3.4.2 Tests for Magnetically Induced Force and Torque

According to the test guidance of the ASTM F2052 standard, provided by the American Society for Testing and Materials, magnetically induced force can be evaluated by hanging a test subject at the entrance of the scanner with a string and then measuring the deflection angle from the vertical direction [ASTM-F2052, 2004a]. During the experiment, the deflection angle is measured by suspending the subject from a string at the magnet-bore entrance where a static spatial gradient field is created. The schematic diagram of the test is demonstrated in Figure 3.5. With the angle measured, the magnetic attraction force can be deduced from the equation $F = mg \tan \alpha$, where F is the magnetically induced force, m is the mass of the subject, g is the gravitational field ($9.81 \mathrm{s}^2/\mathrm{m}$) and α is the deflection angle measured from vertical line with a plastic protractor. An angle higher than 45degrees means that the magnetically induced force is higher than its gravitational force, and extra safe handling is required in this situation to ensure their immobility in the scanner room. The test for evaluation of magnetically induced torque is based on a similar approach. A torque can potentially be induced on a ferromagnetic component by the main field, acting to align the long axis of the subject with the field [ASTM-F2052, 2004b]. This effect can be qualified with a torsional pendulum method (Figure 3.6), in which the test subject is placed on a holding platform suspended by a torsional spring, and located at the isocentre of the scanner for uniformity of the magnetic field [ASTM-F2052, 2004b]. The deflection angle of the platform is measured relative to the fixed base, and the induced torque can be deduced from the equation $\tau = k\beta$, where β is the deflection angle, and k is the spring constant. The test is repeated a few times, with each of the principle axes of the test subject placed in the vertical, to look for the maximum magnetically induced torque.

For a movable test subject, they should be examined and assessed for the amount of magnetically induced force and torque, if any, to guarantee that their existence in the MR environment will not pose any risk to patients and clinicians due to unintended movements. For floor and ceiling mounted devices, they must be installed with a proper fixation to that can withstand the induced force and

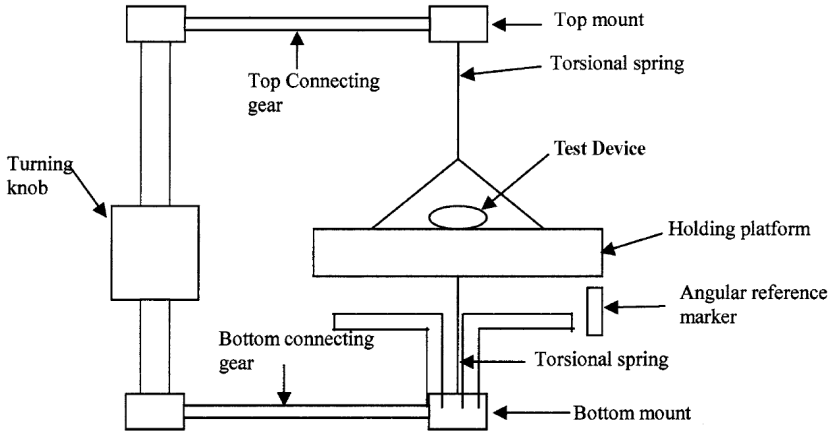


Figure 3.6: Schematic diagram of the torsional pendulum method [ASTM-F2052, 2004b]

torque. A thorough instruction of safety handling is provided in the ASTM F2052 .Test subjects, which experience an induced force or torque, have to be firmly anchored to a fixed supporting structure, and for those which do not experience any induced force and torque, they may present a certain degree of compatibility, but there are still other required tests in different aspects before being used inside the scanner room.

The test for magnetically induced force was conducted on the components chosen with the results showing no detectable forces measured for either of the two actuators or the optical position encoder. The force sensor, however, was deflected slightly to an angle of 10degrees in the static spatial gradient magnetic field because of a tiny amount of ferromagnetic materials within it, but the corresponding induced force was only around 0.07N. This test demonstrated that the magnetic attraction was minimal in the force sensor and its use in the MR environment would be acceptably safe when it was mounted firmly on a fixation. No magnetically induced torque was observed on any of the test subjects. The two actuators and the optical position encoder, do not contain any ferromagnetic material and therefore did not experience any induced torque. For the force sensor, the only ferromagnetic part is a spherical steel ball with a diameter of 0.7mm, and the corresponding attractive force was shown to be very tiny. Considering the symmetric geometry of the steel ball, the magnetically induced torque on the force sensor, if any, was negligible.

Besides the magnetically induced force and torque on fixed components, it was also noted that large electrically conductive components involving high speed motion can potentially experience dynamic magnetically induced force according to Lenz' law [Shellock, 2002, Shellock, 2003]. However, the conductive parts tested were either intended to be stationary (in position and force sensors) or to involve only slow motions (in the two actuators), as such there was no noticeable induced force or torque measured in the scanner room.

3.4.3 Tests for Signal to Noise Ratio Reduction

Electrical and electronic components emit electromagnetic noise that can be picked up by the receive coil of the scanner, causing degradation of the image quality. EM interference can generate redundant

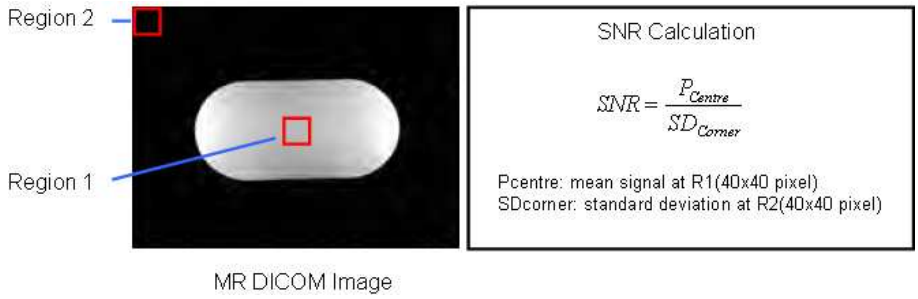


Figure 3.7: Calculation of signal to noise ratio: $SNR = \frac{P_{Centre}}{SD_{Corner}}$, where P_{Centre} is the mean signal of a 40×40 pixel region at the centre of the phantom (Region 1), and SD_{Corner} is the standard deviation of the signal at a 40×40 pixel region at a corner of the image (Region 2) [Chinzei, 2000a].

spots in the image, affecting the clarity of the image and thus undermining diagnostic evaluation. Therefore, to evaluate the MR compatibility of the components, it is important to quantify the Signal to Noise Ratio (SNR) reduction of the image quality when an individual test subject is presented to the scanner. This result is useful in evaluating the usability of each component in robot designs. The protocol for evaluation of SNR reduction that has been adapted, was proposed by Chinzei for electrical and electronic components, and the steps are listed in Table 3.2 [Chinzei, 2000a].

Reduction in SNR of up to 10% is generally considered as an acceptable level of EM interference between the equipment and the MRI machine [Chinzei, 2000a]. However, it is not a strict indicator of compatibility. An image for diagnosis in identifying an abnormal soft tissue may only tolerate the level of SNR reductions mentioned by Chinzei, however, a larger decrease in SNR is acceptable if an image is used only for the purpose of image guidance and gross positioning. The nature of the application that the image is used for, and how high the resolution is required to be for a particular application, are all factors that determine the definition of an acceptable level of SNR reduction.

SNR tests were performed individually to the selected mechatronic components used in robot design together with their connected electrical circuitries. To avoid EM interference between the circuitries and the scanner, all electronics were placed in a tightly shielded aluminium enclosure as shown in Figure 3.8, which was located 2m away from the entrance of the scanner bore. This served the purpose of placing the potential noise sources inside a Faraday cage grounded to the scanner shield and thus electromagnetically isolate them from the scanner.

All cables connected from the Faraday cage to the test components can act as antennas which pick up the RF signals from the scanner or emit EM noise from the noise sources in the Faraday cage to the scanner receive coil. To tackle this problem, all cables were shielded, and hardware low-pass filters (TUSONIX 4209-053) with 55dB attenuation at the cut-off frequency of 64MHz were installed at the wall of the shielded enclosure to each cable (Figure 3.9). The purpose is two fold; first it is to attenuate the high frequency noise close to the Larmor frequency of a 1.5T MRI scanner (64MHz) from the electronics in the Faraday cage and secondly it is to suppress the high frequency noise induced by the scanner RF pulses in the cables which may potentially damage the normal operation of the electronics. In this test, lead-acid batteries were used as a clear power source, and images were taken with TSE and True FISP image sequences with parameters listed in Table 3.3.

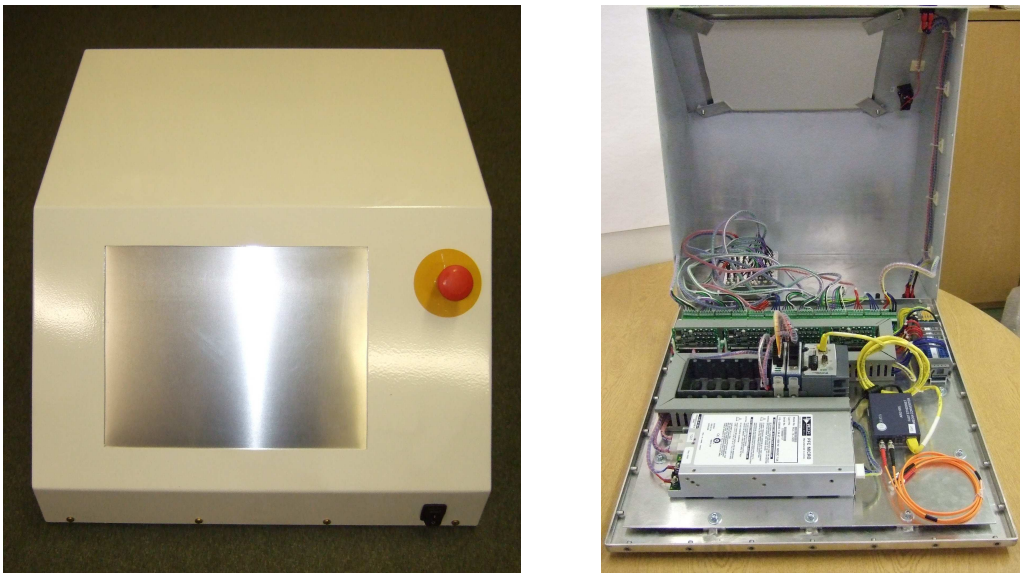
The SNR tests were carried out on all the components with the image sequences mentioned and

Step	Description
Phantom Preparation	A bottle filled with $CuSO_4$ solution is used as a phantom to provide a control image. $CuSO_4$ solution is adapted as it is an easily accessible chemical which is a paramagnetic substance, and it allows tailoring the concentration to obtain any desired T1.
Control Image	The phantom is placed at the isocentre of the scanner and scanned with spin echo and gradient echo image sequences.
Test Subject Presented	The test subject is introduced to the imaging volume alongside the phantom but with power and cable disconnected. Images are then taken with the two sequences respectively.
Powered, No actuation	The test object is powered but not actuated. Images are taken with the two sequences respectively.
Powered, actuated	The test object is then powered and actuated in its full range. Images are taken with the two sequences respectively.
SNR Calculation	SNR is calculated as followed: $$SNR = \frac{P_{Centre}}{SD_{Corner}}$$ P_{Centre}: The mean signal of a 40x40 pixel region at the centre of the phantom SD_{Corner}: The standard deviation of the signal at a 40x40 pixel region at a corner of the image. As MR signals from the phantom should theoretically presents nothing at that corner, any signals measured at that point must be contributed by EM noise, and so the standard deviation at that corner area quantifies the level of noise. A schematic diagram about SNR calculation is shown in Figure 3.6.
Comparison of SNR Variation	The SNR variation of each condition above is compared to the SNR of the control image with equation: $$Degradation = \frac{SNR_{Condition} - SNR_{Control}}{SNR_{Control}} \times 100\%$$ SNR variation is subject to different image sequence applied and so the degradation is calculated individually for both gradient echo and spin echo sequences.

Table 3.2: Procedures for calculation of signal to noise ratio Reduction

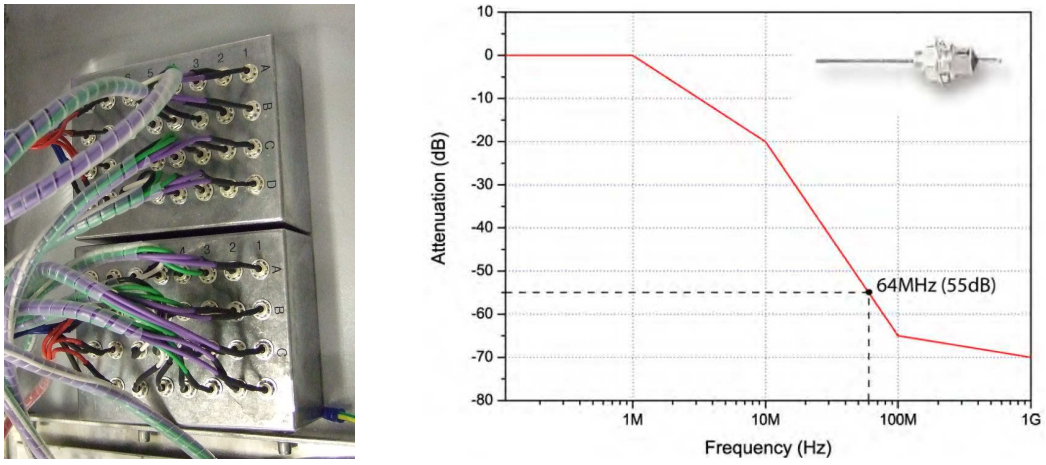
	TR (ms)	TE (ms)	FA (degree)	No. of slice	Thickness of slice (mm)	Spacing (mm)	Resolution	FOV (mm)	BW (Hz/px)
TSE	3600	120	180°	15	5	5	256 ×256	300	130
True FISP	22	10	30°	15	5	5	256 ×256	300	130

Table 3.3: Details of the image sequences



(a) (b)

Figure 3.8: (a) The aluminium enclosure acts as a Faraday cage to electrically isolate the noise source from the scanner room. (b) Its internal view.



(a) (b)

Figure 3.9: (a) A group of low-pass filters mounted at the wall of the aluminum enclosure to attenuate RF interference at the Larmor frequency of 64MHz. (b) Attenuation characteristics of the low-pass filters

		TSE			True FISP		
		Power off	Power on	Actuated	Power off	Power on	Actuated
Pneumatic motor	SNR Reduction	0.11%	N/A	0.12%	0.10%	N/A	0.10%
Piezoceramic motor	SNR Reduction	0.54%	1.5%	2.1%	1.6%	3.9%	4.2%
Force sensor	SNR Reduction	0.76%	0.91%	0.91%	2.5%	2.7%	2.62%
Encoder	SNR Reduction	0.3%	0.67%	0.72	0.2%	2.4%	2.4%

Table 3.4: SNR degradation under different test conditions

the results are shown in Table 3.4. The maximum SNR reductions in the pneumatic motor, ultrasonic motor, optical position encoder and force sensor were 0.12%, 2.1%, 0.91%, and 0.72% with the TSE sequence, and 0.10%, 4.2%, 2.7%, and 2.4% with the True FISP sequence. Even though the SNR reduction varies in different scan conditions, they are all within the acceptable level of 10% proposed by Chinzei [Chinzei, 2000a], showing good compatibility of the individual components. This experiment demonstrated the usability of individual electrical and electronic components in the MR environment, and the tests would be required to be conducted again when the assembled robot prototype was available to quantify the combined effect of the all components together.

3.4.4 Tests for Artifact Generation

Components with high magnetic susceptibility materials or electrically conductive materials involved are the potential sources of artifact generation. An image artifact is any feature which appears in an image which is not present in the orginal imaged object. Intentionally created artifacts generated by RF interference with special design resonating coils coupled with signal amplifying circuitry, can be used for active device tracking in MR interventions [Zhang, 2001]. However, unintended artifacts can void significant information in the images, and are generated in three dimensions from the component; this can happen even if the robot is placed away from the imaging volume. Artifacts appearing in MR images generally do not affect patient safety; however, can present a critical obstacle for target position identification; especially for needle insertion or other interventional procedures where exact positions are required. Artifacts can affect the image quality by voiding information, and cause a shift in the depicted position of a device in the MR image, potentially leading to diagnostic misinterpretation [Bartels, 2002].

Selection of low susceptibility materials, for example, Delrin® and Ertalon® for the structural materials in a robot design can minimise the chances of artifact generation [Schenck, 1996]. However, plastic parts may contain hydrogen protons leftover from the manufacturing procedure, thereby still causing unwanted artifacts. Therefore, it is paramount to conduct artifact tests on the selected components at an early stage of the robot design to determine if they can be used within or close to the

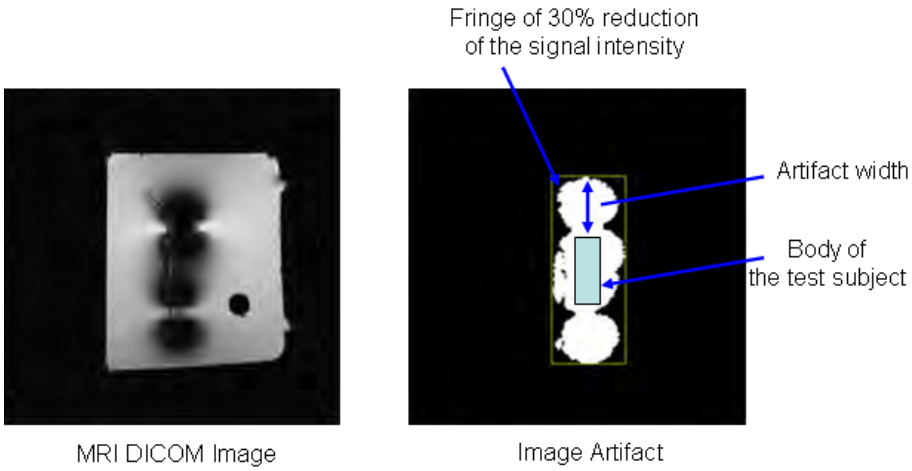


Figure 3.10: Artifact measurement suggested by the ASTM standard F2119. The artifact width is measured from the subject body to the artifact fringe where there is a 30% change of pixel intensity relative to the reference image where the subject is absent [ASTM-F2119, 2004].

imaging volume.

The ASTM standard F2119 was used to quantify the image artifacts generated by each test subject (pneumatic motor, ultrasonic motor, optical encoder, and force sensor) [ASTM-F2119, 2004]. Each of them was placed in a container of $CuSO_4$ solution with their power source disconnected. The subject was orientated in three different directions with the imaging plane aligned with the coronal plane, sagittal plane, and transverse planes in each consecutive scan. The spin echo and gradient echo image sequences were used with the same parameters shown in Table 3.3. As defined in the ASTM standard F2119, the size of an artifact (artifact width) is measured from the body of a test subject to the artifact fringe. An artifact is defined as a region in which the pixels exhibit a 30% change of intensity compared with the corresponding pixels of the reference image, where the test subject is absent, as illustrated in Figure 3.10. The results of the artifact measurements are indicated in Table 3.5, and the images showing maximum size of artifacts among different orientations and image sequences are demonstrated in Figure 3.11 for each of the test components.

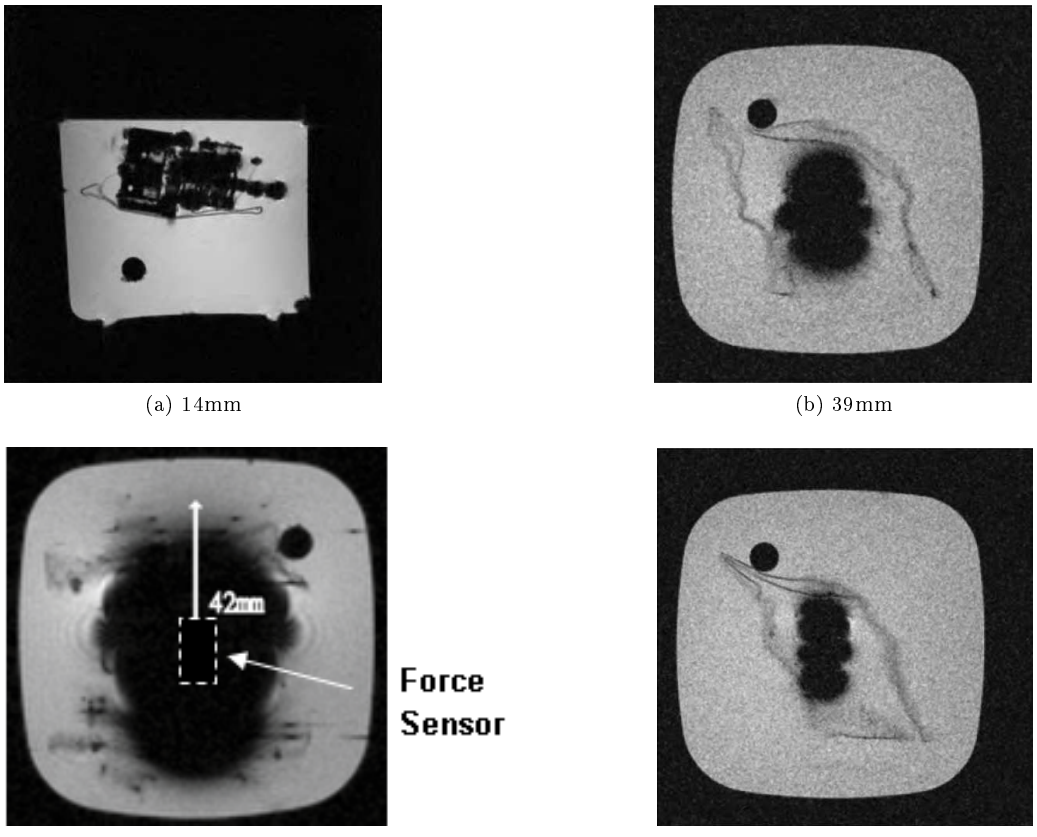
Among different orientations and image sequences, the maximum artifact size is 14mm for the pneumatic motor, 39mm for the ultrasonic motor, 42mm for the piezoresistive force sensor, and 20mm for the optical encoder. The force sensor generated the largest artifact as it consists of a 0.7mm stainless steel ball with a content of ferromagnetic material. The artifact sizes indicated the minimum and necessary separation of the component from the imaging volume to avoid producing image artifacts. One can also observe that the gradient echo image sequence (True FISP) is more sensitive to the susceptibility of materials as larger artifacts were displayed compared with the spin echo (TSE).

3.4.5 Tests for Image Geometrical Distortion

Presence of a high susceptibility material near or in the scanner can cause distortion of the main magnetic fields, and this can potentially cause geometric distortion, i.e. warping of the image, leading to misinterpretation of a target point in an intervention [Maurer Jr, 1996]. To quantify the degree

Size of artifact	Coronal plane	Sagittal plane	Transverse plane
	TSE		
Pneumatic motor	12mm	12mm	12mm
Piezoceramic motor	36mm	15mm	15mm
Force sensor	40mm	40mm	40mm
Optical encoder	17mm	16.5mm	16.5mm
	True FISP		
Pneumatic motor	14mm	14mm	14mm
Piezoceramic motor	39mm	16mm	16mm
Force sensor	42mm	42mm	42mm
Optical encoder	20mm	19mm	19mm

Table 3.5: Artifact size measured from different orientations according to the ASTM standard F2119



(a) 14mm (b) 39mm

(c) 42mm (d) 20mm

Figure 3.11: MR images showing size of image artifacts generated by: (a) pneumatic motor (14mm), (b) ultrasonic motor (39mm), (c) piezoresistive force sensor (42mm), and (d) encoder (20mm). The sizes of artifact were quantified by the ASTM F2119 standard. All the largest artifacts appeared in the True FISP image sequence.

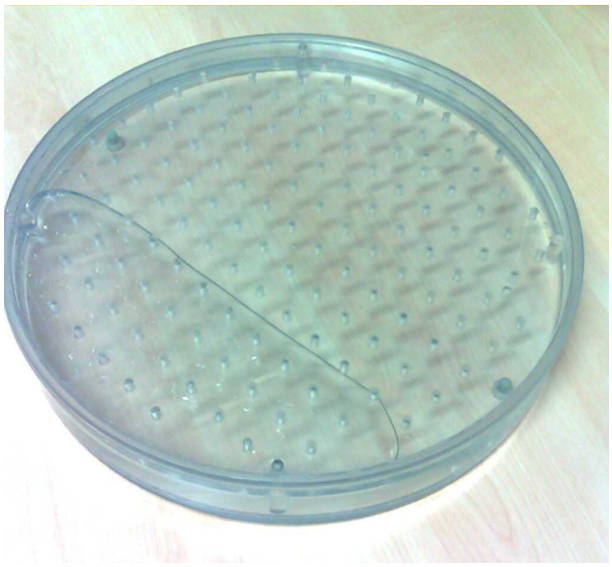


Figure 3.12: A phantom with geometric patterns and filled with $CuSO_4$ fluid was used to quantify geometry distortion, if any, induced by a test subject.

of geometrical distortion, tests were performed on the components placed along with a phantom with geometric patterns and filled with $CuSO_4$ fluid as shown in Figure 3.12. As the purpose of this test is to quantify the geometrical distortion produced by a test subject, rather than the image artifact, the components were placed alongside the phantom which itself occupied the centre of the imaging volume, such that their generated artifacts were not overlap the scanned region. The position of the test subject from the phantom was at a distance suggested by the size of its artifact generation. The images were taken whilst the test objects were powered and actuated. The same image sequences were applied as in Table 3.3. The scanned images after the introduction of the subject were subtracted from the control images, and it was found that the geometric patterns in the images remained clear and undistorted for all tested components with both spin echo and gradient echo sequences. As the images taken and the subtraction images produced before and after a test subject was introduced are very similar in the case of all test components, Figure 3.13 only demonstrates the images in the case of the piezoresistive force sensor with the TSE image sequence. It was concluded that the test components produce no noticeable geometrical distortion in the image.

3.4.6 Tests for Thermal Effect

Before a medical device is used in the MR environment, it is necessary to conduct tests to evaluate the thermal effect on the device that may be caused by interaction with the RF pulses and the switched gradient magnetic fields. The frequency of RF is in the order of tens of MHz, and is generally the more significant source of the thermal effect, when compared to the switched gradient magnetic field which is at frequencies in the order of kHz [ASTM-F2182, 2002, Dempsey, 2001]. It is a necessary precaution as electrically conductive materials in a medical device can be susceptible to induced voltages and eddy currents, which can cause sparking due to high voltage and skin burns to the patients and clinician

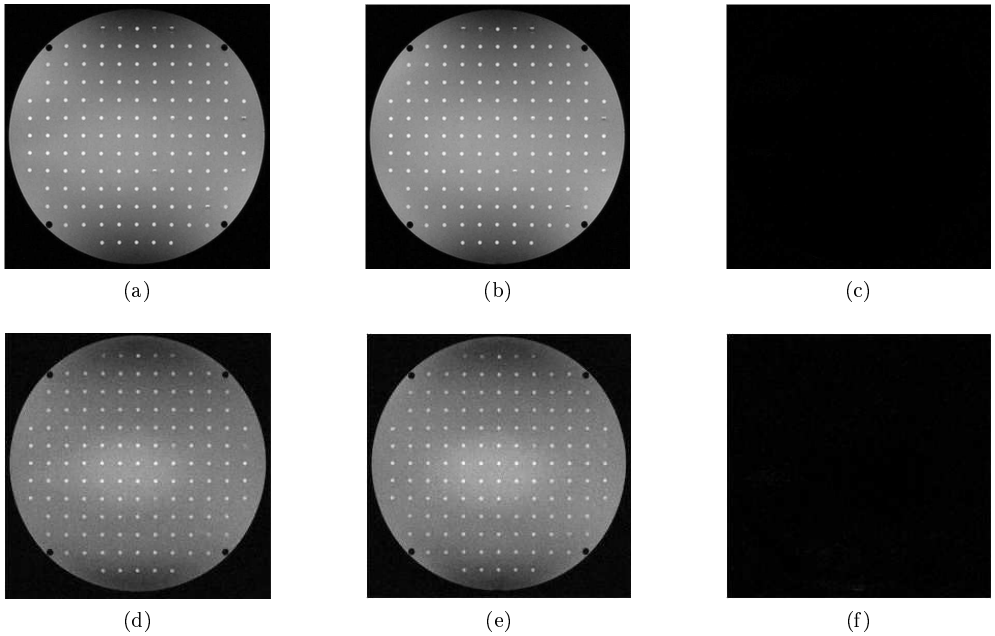


Figure 3.13: (a) TSE control image with fine geometrical patterns shown, (b) TSE image with the force sensor introduced and actuated with load applied to the force sensor, and (c) subtraction image between (a) and (b). Images (d)-(f) are the same images but with the True FISP image sequence

[Dempsey, 2001]. Analysis of RF heating is a complex issue and an ongoing research area. The effect is governed by many parameters; as far as the test subject is concerned, it is related to the electrical conductivity, the geometry, its location in the MR environment, and its loop-closing contacts etc; for the scanner concerned, it can be associated with the placement and orientation of specific MR coils, the image sequence parameters, its magnetic strength, and the scanner room design etc [Armenean, 2004, Sled, 1998].

As far as the robot design is concerned, an endorectal probe for prostate localisation in the prostate biopsy robot (refer to Chapter 5) is the component most likely to experience a thermal effect compared with other components during imaging, as the probe consists of a receive coil and an inductor-capacitor (LC) circuit tuned to resonate at the Larmor frequency. Moreover, taking into consideration the function and placement of the probe which was designed to localise the MR signal from the prostate and to be inserted into a patient's rectum, it is most necessary to evaluate the thermal effect in the probe, if any, for the safety of patients.

The thermal test were conducted using the ASTM F2182 standard which is the current standard for RF heating testing [ASTM-F2182, 2002]. The probe was set up in its approximate operational orientation and position, and was placed into a rectum phantom which comprised of plastic bags filled with $CuSO_4$ to mimic the situation in which the probe was inserted into a patient rectum and surrounded tightly by the rectal tissue. Additionally, two large phantoms (filled with $CuSO_4$) were placed close to probe and were arranged in the shape of a human torso to simulate the tissue properties of a patient body. The endorectal probe was scanned with a modified FLASH 2D sequence for 30mins and its temperature was recorded using a fiber optic thermometer. The implemented image sequence

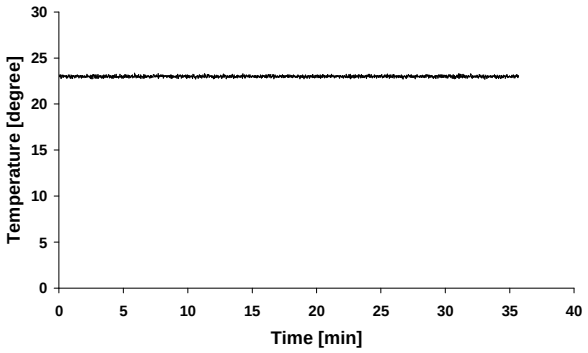


Figure 3.14: Temperature variation of the endorectal probe during a 30min scan with FLASH 2D image sequence, demonstrating no noticeable thermal effect recorded.

was specifically designed for probe tracking and has been used in the clinical trials of the prostate biopsy robot as described in Chapter 8.

The temperature versus time graph is presented in Figure 3.14 with the result showing no perceivable change of temperature observable over the 30min scan. In reality the imaging time with the use of the endorectal probe is always within 5mins during a prostate biopsy. The tests were repeated individually with the pneumatic motor, ultrasonic motor, force sensor, and optical encoder, and no noticeable thermal effect was observed.

In the research area of RF heating, computational analysis of the interaction between the test subject and RF pulses requires the information of the specific setup of an MR machine, such as which coil and pulse sequences produce which RF output, and how the specific absorption rate (SAR) is calculated, measured, and adjusted in the built-in scanner programme [Nyenhuis, 1999]. It is still an ongoing research area to investigate how electromagnetic fields, RF pulses and SAR affect each other [Ibrahim, 2001, Chen, 1998].

3.5 Conclusion

This chapter has presented the technical background of MR compatibility and magnetic susceptibility together with terminologies relating to MR safety, although some of the concepts mentioned are still being refined from time to time. Five different types of interactions between the scanner and the introduced test components; magnetically induced force and torque, SNR reduction, artifact generation , image geometrical distortion and thermal effect , have been discussed in detail, and the corresponding tests have been performed to quantify the level of MR compatibility of the selected components. The discussed tests have provided a systematic way to assess and select suitable mechatronic components for designs of MR compatible robots.

The test for magnetically induced force and torque is designed to determine the maximum amount of attractive force and torque that might be encountered by the test subject in the MR environment, and to determine if a modified use is necessary in a robot design to counteract the magnetic attraction . The SNR reduction test provides a good insight of how the EM interference from the introduced

component affects the image quality. The result gives a good engineering approximation of the image quality degradation that might be expected when several tested components are to be adapted in a robot design together. The artifact generation test presents an important role to measure the size of an artifact and evaluate the minimum and necessary separation from the imaging volume that the test subject can be placed at without affecting the image quality . The image geometrical distortion test is a further verification if the presence of the component at the distance suggested from the artifact generation test is suitable, by assessing if it will still cause a warping effect in the image. Last but not least, the thermal effect test quantifies the temperature variation of a test subject caused by the RF pulses and the switched gradient magnetic fields. This test is of paramount importance to evaluate the MR safety of a medical device particularly when it is close to or in touch with the patient body, such as in the case of the endorectal probe, as high voltages can potentially be induced and cause sparking, skin burns and even fire.

Low susceptibility materials, such as engineering plastic, Delrin® and Ertalon® , can be used for the structural components of an MRI robot, but actuators, position sensors and force sensors compatible with the MR environment are still desirable. Two types of motors based on piezoelectric and pneumatic technologies respectively were selected and had their compatibility tested in the five aspects mentioned. An ultrasonic motor, which is based on a piezoelectric principle and made from paramagnetic stainless steel, was selected, and it is suitable for fine positioning with fast response. For applications with higher power requirements, a pneumatic rotary motor was adapted. Both actuators demonstrated that their presence in the imaging volume provided an SNR reduction within the acceptable level of 10% [Chinzei, 2000a]. They also had their artifact sizes measured and found to be 39mm for the ultrasonic motor and 14mm for the pneumatic motor. These are the minimum necessary distances they have to be kept away from the imaging volume. Their performance in the five individual tests, has demonstrated their excellent compatibility in the MR environment.

In terms of sensing technology, a small surface mount optical encoder was selected for position sensing in the scanner; whilst a small piezoresistive force sensor was chosen for the use of force sensing. Only a tiny amount of magnetic material was contained in the sensors and hence their generated artifacts were within an acceptable size of 22mm for the position sensor and 42mm for the force sensor, and both demonstrated a small amount of SNR reduction of 2.4% (position sensor) and 2.7% (force sensor). Despite the current technology making it possible to custom fabricate sensors without the use of electrical based sensing principles, the availability of the two selected commercial sensors brings the benefit of cost-effectiveness, high accuracy, and excellent robustness.

The tests performed act as qualitative measures which can enable the drafting of mechatronic components for MR compatible devices. However they do not assure MR compatibility in all cases. Testing of specific robot prototype is the only way to demonstrate its MR compatibility. In any case, the proposed testing methods were used to select the actuators, position and force sensors for the robotic systems mentioned in Chapter 5 and Chapter 7, which were later demonstrated to be MR compatible.

Chapter 4

Actuation Control and Evaluation

4.1 Introduction

MR imaging provides high resolution anatomical images and is ideal for image guided interventions. However, challenges are raised to both passive and active components in the MR environment. Selection of suitable mechatronic components for MR robot designs and evaluation of their MR compatibility are two critical steps to ensure their usability, as was covered in detail in Chapter 3. Conventional motor control has generally focused on industrial related actuators; commonly of those based on the electromagnetic principle, being ferromagnetic, driven by high currents and therefore noisy to the scanner and potentially a source of eddy current generation. This chapter focuses on characterisations of control performance, and evaluation of control strategies for the two MR compatible actuators; the linear ultrasonic motor; and the pneumatic rotary motor.

The linear ultrasonic motor consists of four piezoelectric ceramic legs and actuation is achieved when they are excited by a set of sequential signals. This motor features high accuracy and fast response, but its actuation is restricted by its limited speed and force. This actuator is ideal for light duty applications and fine positioning, for example, positioning in percutaneous interventions and creation of force feedback to the clinician during the interventions. Despite its fast response, its nonlinearity and non-backdrivability impose practical challenges in applying the motor in master-slave haptic control. A control strategy making use of a neural network based speed model is proposed to improve the control performance, and experiments with a 1DOF master-slave haptic test rig has demonstrated the usability of the ultrasonic motor and its control strategy.

The pneumatic motor consists of an air turbine and a set of modular gearboxes, in which the speed and torque are adjusted by changes to the gear ratio or the operating pressure. This feature makes it very suitable for heavy duty applications and gross positioning, for example movement of a limb. The actuator has been characterised with respect to its control performance in open loop tests and closed loop tests respectively. A self-tuning PID control algorithm was implemented to the motor for use in different load situations and was proven to be robust enough to guarantee the position accuracy of 0.25degrees in the pneumatic motor control. This control strategy has been verified with a 1DOF test rig to orientate a palm and different load conditions at a particular angle, and has been demonstrated

the feasibility of the use of the pneumatic motor with the control strategy for limb positioning.

4.2 Actuation Specifications

Actuators used in the MR environment should be considered in a few different aspects for suitability. MR compatibility is the first and prerequisite, followed by its torque and speed generation, its accuracy, and its response. These four requirements are subject to the conformation of particular interventions; however, they must generally be compromised with each other. Pneumatic principles are an ideal solution for interventions requiring high torque and speed, although delays in the actuator are always an intrinsic problem due to the compressibility of air. For the application of limb positioning, the capability of generating enough power to move a heavy limb and orientate target tissue are the priority function, and the pneumatic motor is therefore assigned for the use of limb positioning. Due to the actuation principles of the ultrasonic motor based on piezoelectric technology, it features an short rise time and high position accuracy. These characteristics suit the use of the motor for implementation of force control related schemes and fine positioning in robot designs more appropriately when compared with the pneumatic system. The following section discusses the use of the MR compatibility tested pneumatic and ultrasonic motors mentioned in Chapter 3 to match up different robot design requirements.

4.3 Ultrasonic motor

4.3.1 Principle of the Ultrasonic Motor

Ultrasonic motors are a type of actuator based on piezoelectric technology and have been used in several previously developed MR compatible devices to replace conventional DC motors for actuation [Chinzei, 2000b, Larson, 2004, Hata, 2005]. Figure 4.1 shows the general structure of a ultrasonic motor, with a stator (piezoelectric ceramic) and a rotor (dynamic body). The piezoelectric ceramic generates ultrasonic vibration, when excited by a control signal, to provide movement in the rotor and hence achieve actuation with no use of coils or magnets as driving source. The model of ultrasonic motor USR60 is a commonly used motor in MR devices, however, this actuator is not entirely MR compatible with the scanner and requires a 0.3-1m separation from the imaging volume to avoid electromagnetic disturbances [Muntener, 2006].

The solutions found in literature to avoid signal to noise ratio reduction by the USR60 are that:

1. The motor is located far away from the isocentre of the scanner (for example, mounted on top of the scanner), and the robotic system requires a long mechanical transmission to link the motor and the end effector. The disadvantage in this design is that it is generally large and inconvenient for installation on a scanner [Chinzei, 2000a]. Also long mechanical transmission leads to unwanted bending and backlash in the device, and affect the positioning accuracy.

2. For particular applications, the device only needs to be placed at the entrance of the scanner to interact with a patient's limb, for example in rehabilitation research study in which the actuator is designed to be used only outside the scanner bore. In this specific application, a low-level of

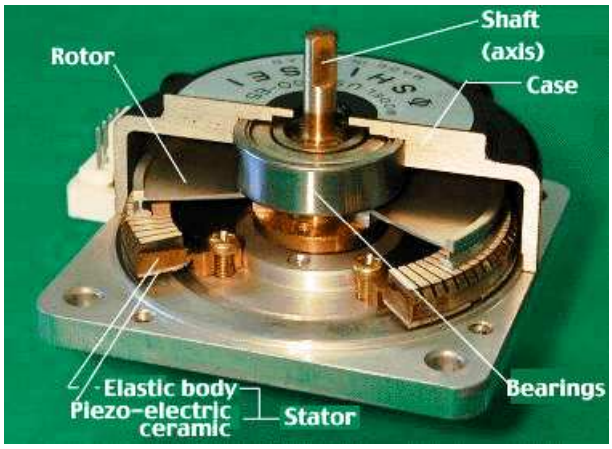


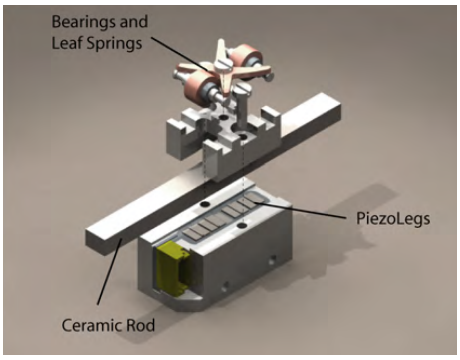
Figure 4.1: A cross section of a general structure of a ultrasonic motor. The stator (piezoelectric ceramic) generates ultrasonic vibration to push the rotor [Shinsei Corporation Inc., 2008].

MR compatibility is still acceptable, but this is generally not the case for MR guided therapy robots as the target tissue for operation is always in the imaging volume around the isocentre [Flueckiger, 2005].

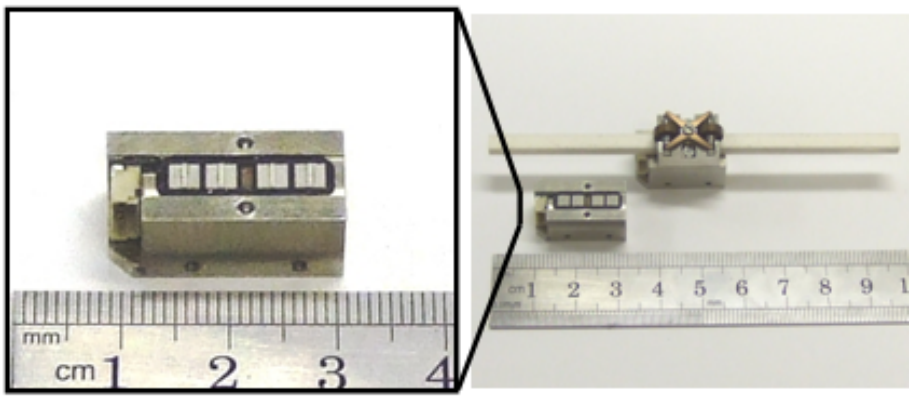
Piezoleg- A highly MR Compatible Ultrasonic Motor

Instead of using USR60, Piezoleg, a linear ultrasonic motor, was sourced. Previous experiments, described in Chapter 3, demonstrated its desirable performance in the isocentre of a scanner; with negligible SNR reduction, and an acceptably small artifact. The actuator as shown in Figure 4.2 contains four piezoelectric ceramic legs, a ceramic rod with well polished surfaces on two opposing sides, and a linear guide with a pair of brass bearings, and an adjustable brass spring to press the rod into a tight contact with the ceramic legs. The compressive force is around 100N. Each leg is basically an individual bimorph of piezoelectric ceramic materials. Different combinations of current directions and magnitudes applied to the two layers are able to produce overall motions of bending, extension and retraction of the legs at different degrees. Extension and retraction of the ceramic legs are the functions that brake and release the ceramic rod; whilst bending is the function that pushes it for motion. Therefore, the actuator can provide a linear pushing/pulling motion when the legs are excited with repeated sequential signals. A schematic drawing of the Piezoleg working principal is shown in Figure 4.3, demonstrating the movement of two groups of legs, A and B, where they are driven by the same voltage signal within each group. In Step 1, group of legs A extends, holding the ceramic rod tightly, in preparation to push the rod by bending themselves to the right, in the next step. Then, in Step 2, group A pushes the rod, whilst group B bends itself in the opposite direction (left) in preparation to push the rod in the next step. In Step 3 and Step 4, group B gives a full stroke to the ceramic rod by bending from one direction to the other (from the left end to the right end), whilst group A prepares for the next cycle by bending its body to the left. The motor can be programmed to lock the motion of the rotor by full extension of the four legs.

This mechanism can provide a maximum force of 14.6N when a pair of motors are used and



(a)



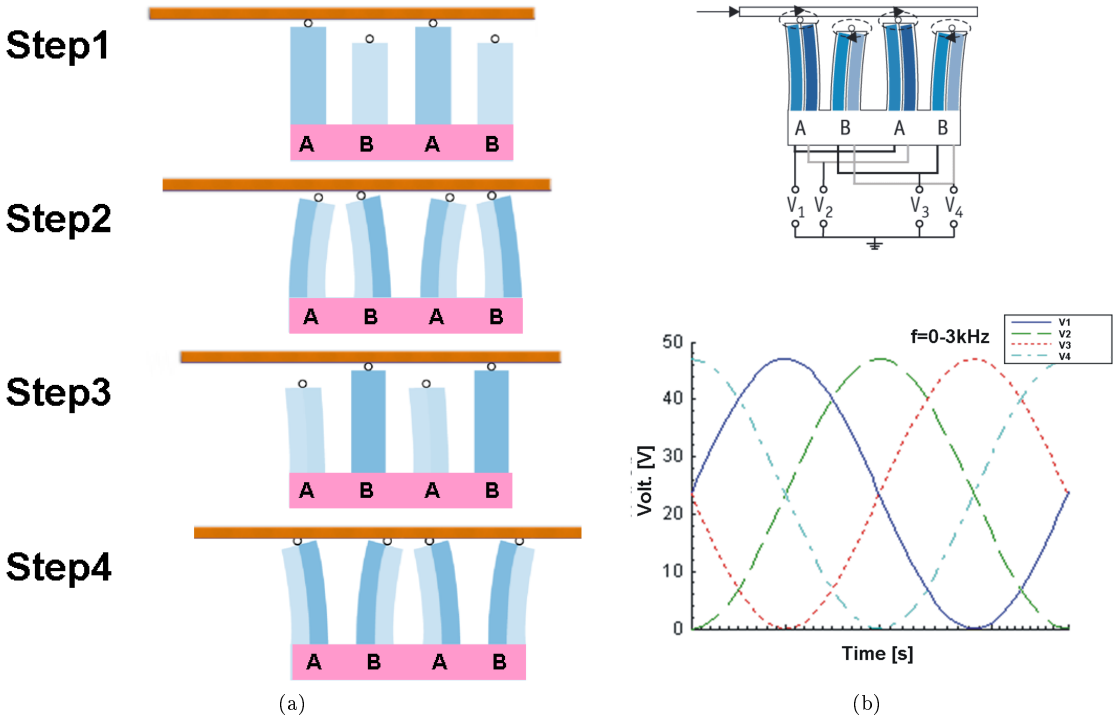
(b)

Figure 4.2: (a) CAD rending of the Piezoleg, showing its components including a well polished ceramic rod, a pair of brass bearings, a adjustable brass spring, and four piezoelectric ceramic legs. (b) Its photo.

actuated with a sinusoidal signal with a 50V magnitude. The generated force can be multiplied by linking of further actuators together. By changing the frequency, amplitude and phase difference of the waveforms to the piezoelectric ceramic legs, the speed of the actuator can be controlled from 0 to a maximum speed of 17.6mm/s.

4.3.2 Control Electronics for Motor Synchronisation

The force required for general percutaneous procedures is subject to the needle size, the properties of the tissue involved and the nature of the procedures, but it is generally around 10N or less, as suggested by the literature [DiMaio, 2003, Hing, 2007, Podder, 2006]; for example a maximum force of 8.9N was reported for the transperineal biopsy needle procedure and 5N was reported for a penetration of the prostate capsule [Podder, 2006]. In the previous section, it was discussed that the motor pair is capable of generating 14.6N which according to these references is sufficient for the required application. As such, the actuation method was designed to allow two ultrasonic motors to be linked up along the ceramic rod to multiply the generated forces as illustrated in the CAD drawing in Figure 4.4. An experiment was conducted to evaluate the feasibility of the concept with the results showing that high



(a) (b)

Figure 4.3: (a) Schematic drawings of the Piezoleg working principle [Piezoleg, 2008]. (b) Motion is achieved by exciting the four ceramic legs with repeated waveforms 1, 2, 3 and 4. The speed of the linear motion can be controlled by the amplitudes, the frequency and the phase difference of the voltage waveforms to the ceramic legs.

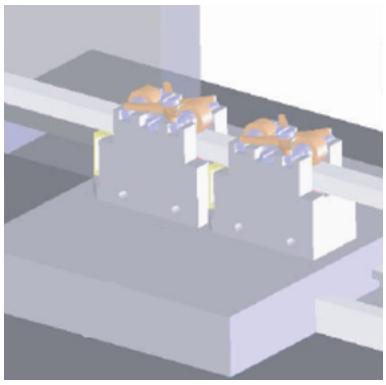


Figure 4.4: CAD drawing of a pair of Piezoleg connected together to form a stronger actuation link

frequency mechanical vibrations were produced by one motor and interfered with the operation of the second motor. The actuators did not work effectively in this situation due to mechanical destructive interferences and resulted in a loss of force and speed output. As destructive interferences are due to the phase difference of the individual signal sources driving each motor, a synchronisation circuit was set up to drive the motor group together with the same source for elimination of the phase difference in the signal, and it was observed that synchronisation of the motor group successfully doubled the actuation force and maintained the same motor speed.

A circuit based on four non-inverting amplifiers was designed for synchronisation of multiple Piezoleg motors. Four high power operational amplifiers (LM1876 National Semiconductor, bandwidth of 100 kHz) were obtained to amplify the signal from a motor drive and provide synchronised signals with an amplitude of 50V, in which the motor drive works solely as a function generator, creating four sinusoidal waves, the phase differences of which are 0, 90 180 and 270degrees. The synchronisation circuit is presented in Figure 4.5 with its circuit diagram schematic shown in Figure 4.6. The magnitude of the output signal in the circuit is adjustable by changing the gain of the amplifiers $\left(1+\frac{R2}{R1}\right)$, providing an additional method to control the speed of the motors by changing the signal magnitude, besides the frequency and the phase difference of the four sinusoidal waveforms.

4.3.3 Characteristics of the Piezoleg

Linear and Nonlinear range in Piezoleg

To characterise the motor, experiments were conducted to drive the motor with the design circuit and signal generator at its working frequency ranging between 0 to 200 kHz under varying load conditions from 0N to 8N. The results, shown in Figure 4.7(a), indicate that the speed-frequency relationship was rather linear in a frequency range up to 80kHz, but became nonlinear in a range from 80kHz to 200kHz. Figure 4.7(b) shows the speed-frequency relationship with a load of 2N applied. The data points fluctuate seriously without an obvious trend after 80kHz, and do not fit any polynomials from second order to fourth order for regressions. The fluctuation of the motor performance results from the constructive and destructive interferences where the frequencies of the ceramic leg vibration reach the natural frequencies of the motor structure in which a long ceramic rod acts as a beam absorbing

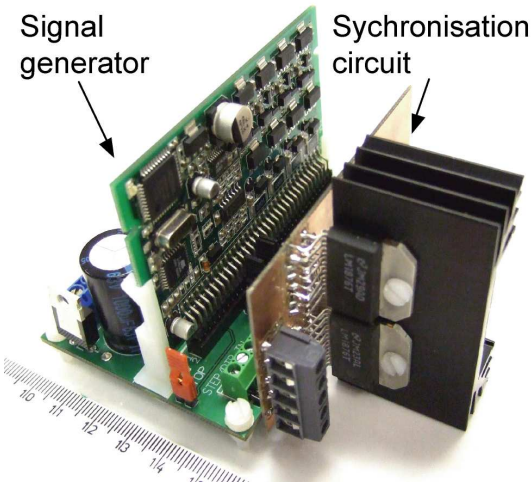


Figure 4.5: The synchronisation circuit mounted on a motor drive (four-channel signal generator).

energy from the vibration.

Neural Network based Speed Model

The Piezoleg motor possesses a linear and nonlinear range of speed characteristics due to mechanical vibrations caused by its working principle. Giving up the use of the nonlinear region will lose around one third of the speed range and is not preferable.

The Piezoleg maintains a linear speed performance in the low speed range, and one of the approaches to keep the high controllability, inclusive of the high speed range, is to model the nonlinear region. Devising an analytic model for the motor involves study of tribology between the surface of the piezoelectric ceramic materials and the ceramic rod, study of vibration and expertise of piezoelectric ceramic bimorphs. All of these require knowledge of a number of parameters regarding the characteristics of the ceramic materials, fictional coefficient and the motor structure. It is thus impractical to analytically model the motor due to its complexity. A Neural Networks based speed model was therefore proposed to empirically model the characteristics of generated force, velocity, and input voltage frequency. The motor is considered as a black box, whilst its performance can be effectively predicted provided that a sufficient amount of data sets are taken for neuron training, and suitable number of layers and neurons are adapted [Nelles, 2000]. As the velocity of the motor pair is related to the phase difference of signals to each ceramic leg ϕ, the voltage amplitude V, the driving frequency f, and the load applied to the motor F, the mathematical relationship can be presented as follows:.

$$\dot{x} = G_1(\phi, V, f, F)$$

In a speed model, it is desirable to investigate the frequency of the input signal required to cause the motor to have a desired velocity of $\dot{x}$ under a load condition F. Hence frequency f is set to be the subject of the equation, and force is known from the reading of a force sensor. Voltage amplitude V and phase ϕ of the driving signal are controllable by the motor drive, and are set to be constant for model simplicity. Therefore, we have:

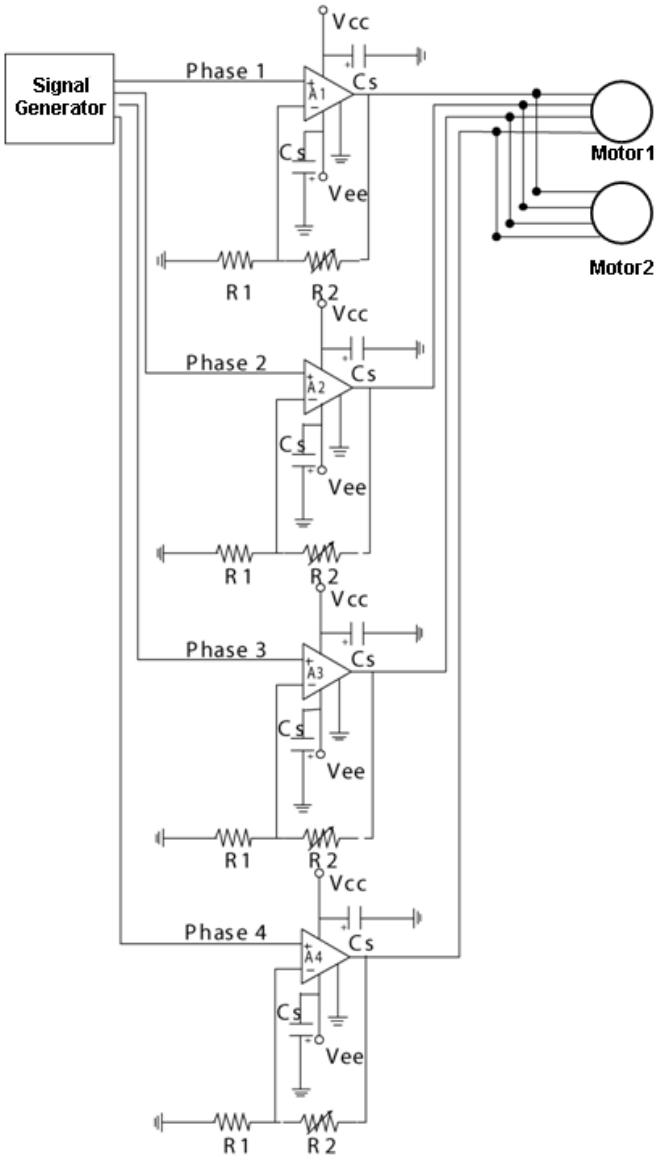
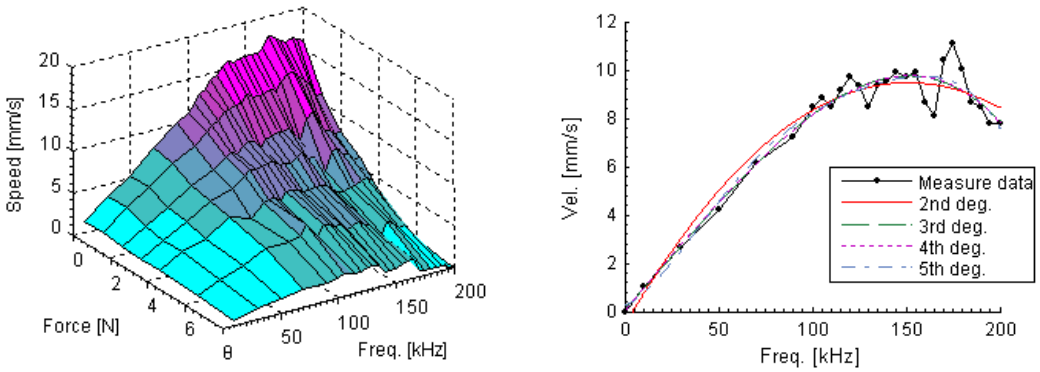


Figure 4.6: Diagram of a synchronisation circuit with magnification $\left(1 + \frac{R2}{R1}\right)$for signal supplies to a group of Piezoleg motors.



(a) (b)

Figure 4.7: (a) the speed-frequency relationship of the Piezoleg motor under different load conditions and (b) under a load of 2N, showing its nonlinear characteristics. Polynomial regressions from 2nd to 5th orders do not fit well the nonlinear range of the curve from 80kHz onward in (b)

Symbols	Definitions
$W^1{}_{j,i}$	Weight of the corresponding connection between the input of the network and the log-sigmoid layer
$W^2{}_i$	Weight of the corresponding connection between the log-sigmoid layer and the linear layer
$b^1{}_i$	The bias vector for the log-sigmoid layer
b^2	The bias vector for the linear layer
p	A vector with elemental entry velocity and load, $p = \begin{pmatrix} \dot{x} \\ F \end{pmatrix}$
$a^1{}_i$	Neuron of the corresponding position in the log-sigmoid layer
f	Neuron of the linear layer, which is also an frequency output of the neural network to drive the motor at desired velocity
F^1	$F^1(x) = \frac{1}{1+e^{-x}}$, Log-sigmoid transfer function used in a log-sigmoid layer
F^2	$F^2(x) = x$. Linear transfer function used in a linear layer

Table 4.1: List of symbols in the neural network

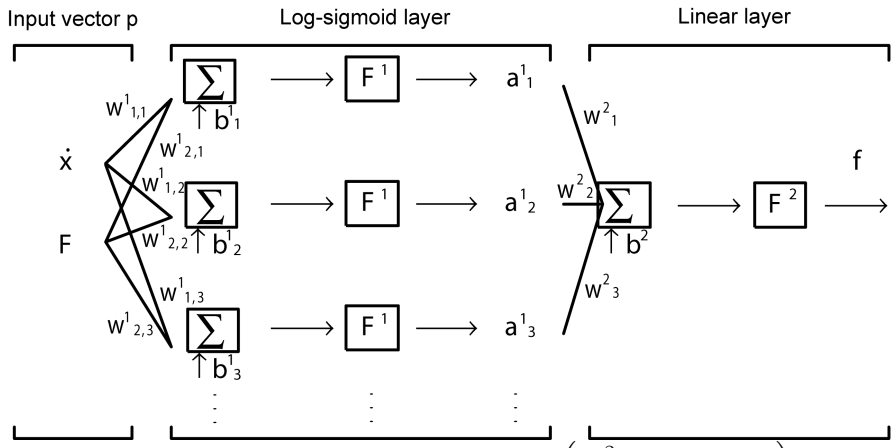


Figure 4.8: The Architecture of the Neural Network with $n = 30$ neurons in the log-sigmoid layer and a single linear neuron in the linear layer.

$$f = G_2\left(\dot{x}, F\right)$$

The architecture of the neural network is presented in Figure 4.8, and the definitions of the symbols used are shown in Table 4.1. Neurons are the basic element in neural networks and work in parallel in a layer. The neurons are linked to previous layers with weighted connections W, and F^1 and F^2 are their corresponding transfer functions. A backpropagation algorithm was used to train the neurons to achieve each value of weight W in the networks [Nelles, 2000, Kim, 1999]. The convergence rate and performance index of the backpropagation algorithm can be optimised by choosing a suitable number of neurons and layers in the networks. 30 neurons and 2 layers were adapted with a log-sigmoid function and a linear transfer function, and 1000 epochs was computed in the backpropagation algorithm.

4.3.4 Haptic Control

Haptic Technology in Master-Slave System

Haptic technology and haptic control are often referred to as master-slave systems. A master-slave system forms a method of communication, by way of such as motion and force feedback, between a user and a controlled device. 'Master' refers to a control interface to interact with the user, whilst 'slave' refers to a remote controlled device used to interact with a remote environment, away from the user. Haptics in a master-slave system, allows effective remote control of devices with real time touch sensation [Ganesh, 2004, Gerovichev, 2002]. This is an advanced form of teleoperation, with the controls to perform remote manipulation tasks dexterously, whilst creating the feeling that the user exists in the remote device in the remote environment. An example of a situation in which this would be useful is in minimally invasive surgery, in which direct access to the target tissue is not available [Howe, 1999]. Much effort has been made for the development of teleoperation, through use of haptic

Symbols	Definitions
$\dot{x}$	Velocity of the motor
ϕ	Phase difference of the four input signals to the Piezoleg motor
V	Voltage amplitude of the input signals
f	Frequency of the input signals
F	Load applied on the motor
F_H	Load applied from the human hand
F_T	Reaction force from a biopsy needle against a target tissue measured by a slave force sensor
$\dot{x}_M$	Master velocity
$\dot{x}_S$	Slave velocity
f_M	Frequency of the input signals to the master motor
f_S	Frequency of the input signals to the slave motor
x_M	Displacement of the master measured by an encoder
x_S	Displacement of the slave measured by an encoder
SP_M	Speed controller for the motor group in the master
SP_S	Speed controller for the motor group in the slave

Table 4.2: List of symbols used in the haptic control

information which a remote device has acquired, to provide the user with a real time sense of touch.

Impedance Control and Admittance Control

Impedance control and admittance control are two general control schemes for haptic devices. Impedance control is suitable for systems with light-weight and backdrivable actuators [Seraji, 1994, Hashtrudi-Zaad, 2001]. A user moves the device a certain distance and a corresponding force is mechanically displayed back to the user; the general rule is "position in, force out" in the control interface. Input current to the motor (at the master end) can be used as a control parameter to estimate the force/torque exerted to the user. For non-backdrivable systems such as the Piezoleg, admittance control is applied. When a user applies a force to the motor, force sensors are needed in both the master and slave parts to measure the force applied on the master by the user as well as the force applied on the slave by a subject. Force exerted on the user does not form an obvious relationship with the input current and voltage, as the motor is held rigid against any movement during power off [Flueckiger, 2005, Volpe, 1993]. Even though the Piezoleg is a good alternative for actuation with fast response and has proven MR compatibility, its inherent hard brake of the friction motor makes it a challenge for implementation of force control in the non-backdrivable actuator; especially in the situation of haptic control where the master system (user control panel) is required to be moved freely by the user, when the slave system (robot end-effector) is not in touch with any object or material.

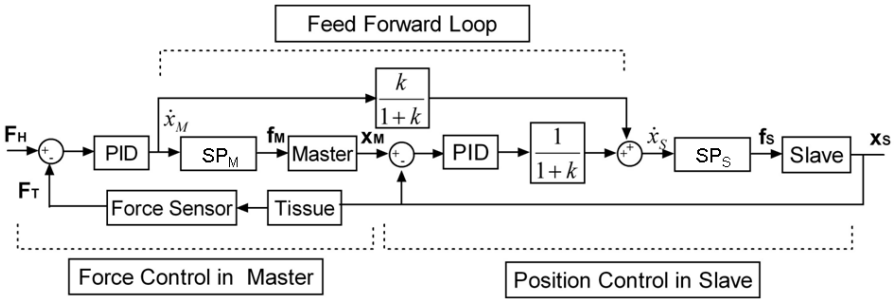


Figure 4.9: Block diagram of admittance control implemented in the master-slave master

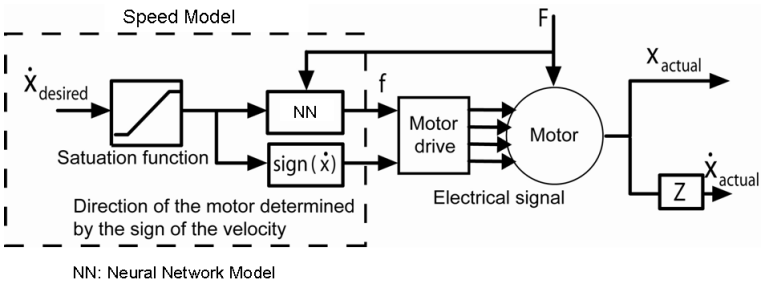


Figure 4.10: Speed model consists of a neural network model of the Piezoleg motor

Force Control in the Master

The proposed control scheme as shown in Figure 4.9 consists of (i) force control in the master and (ii) position control in the slave. Table 4.2 indicates the symbols used in the control scheme. For the force control, the force difference between F_H and F_T becomes a velocity signal to go into a speed model (SP_M) which computes an adequate frequency to drive the motors in the master for the desired velocity $\dot{x}_M$ under load F_H. The speed model consists of the neural network based model, as indicated in Figure 4.10.

Position Control in the Slave with Feed Forward

For position control in the slave, the displacement of the master x_M becomes a setpoint of the slave system, and is compared to the displacement of the slave x_S to compute the velocity value for the PID controller. After that, the speed model (SP_S) works out a suitable driving frequency f_s for the slave motors by considering the sum of a $\frac{k}{1+k}$ portion of signal fed forward from the force control and a $\frac{1}{1+k}$ portion from the position control. A feed forward loop connecting directly from the force control in the master to the position control in the slave, is beneficial for the slave to spontaneously follow the movement of the master, hence to improve the response of the slave. k is adjustable in the range from 0 to $+\infty$ to control the portion of the feed forward signal from the master. The larger the k is, the faster the slave follows the movement of the master, but the position control in the slave is compromised, meaning that tuning the k is important to balance the response following the master and the position accuracy of the slave.

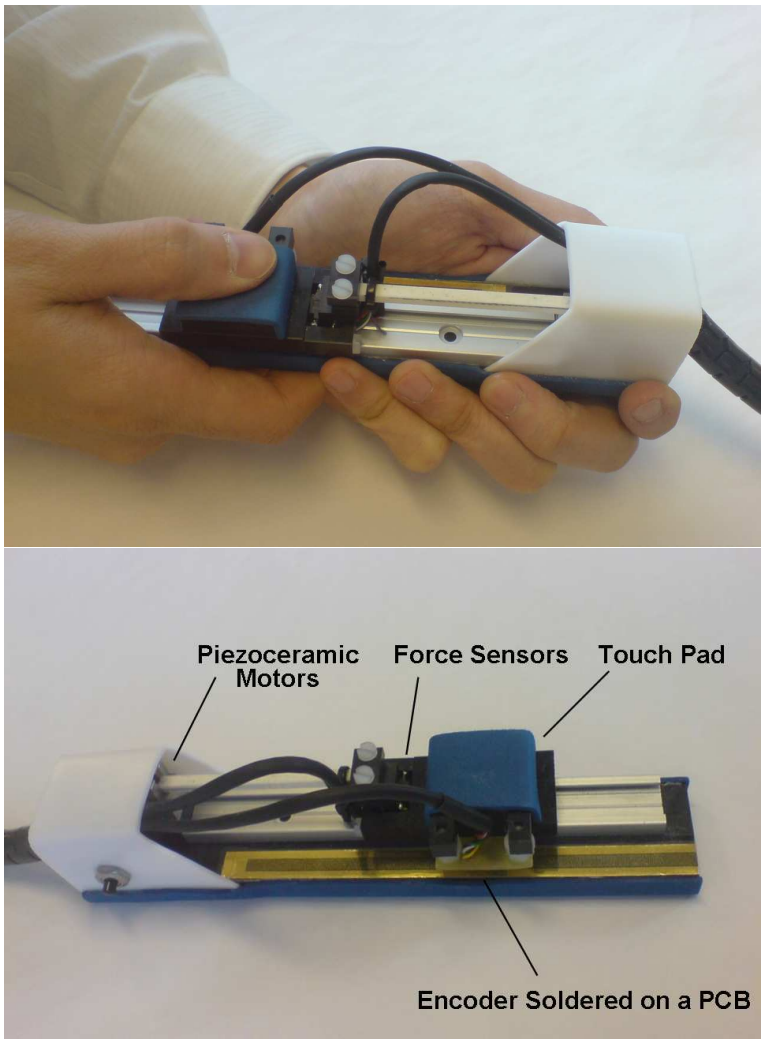


Figure 4.11: Master control interface

4.3.5 Specifications of a Master-Slave Test Unit

Functionality Specifications

A 1DOF master prototype and slave prototype were fabricated to experiment the proposed control scheme described in Section 4.3.4, and the designs are shown in Figure 4.11 and 4.12. Both prototypes consist of force sensors, optical position encoders, and motors, and their bodies were made from Delrin® and Ertalon® materials. Piezoresistive force sensors and reflective surface mount incremental optical encoders, were adapted and their specifications are referred to in Table 4.3. .

Control Tuning Specifications

The PID tuning in the master-slave test unit was based on the Zieglar-Nichols method. The PID gains were first tuned in the position control of the slave, and then in the force control of the master. The k term in the feed forward loop was tuned manually to further improve the response of the slave system.

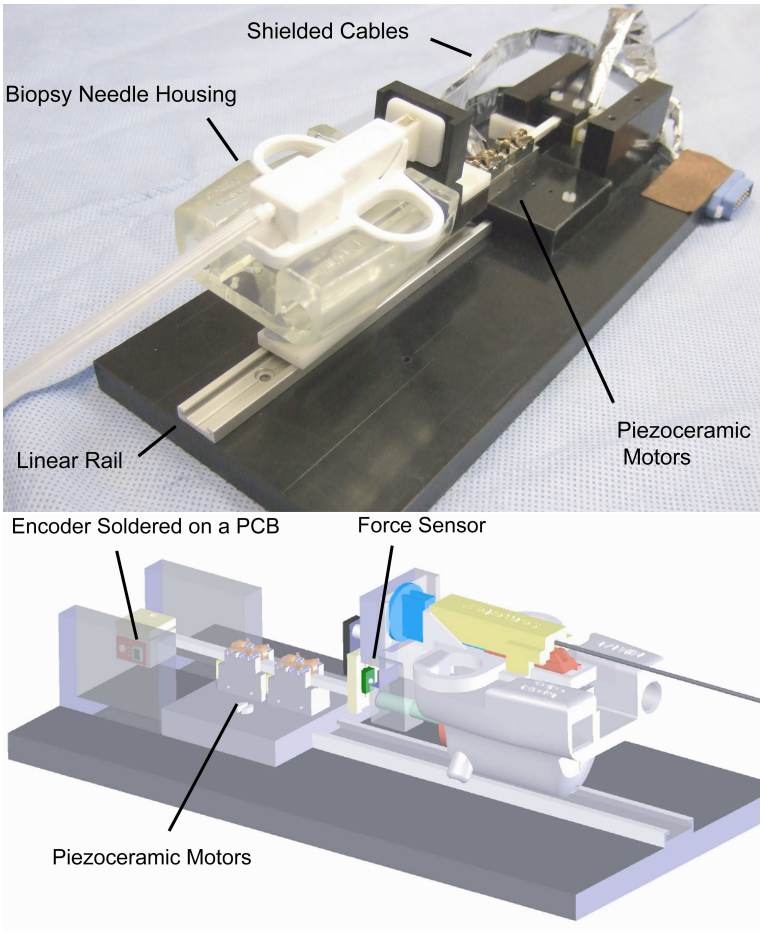


Figure 4.12: Slave prototype and its CAD drawing

	Slave-Master System
Motion Range	100 mm
Position Sensor Resolution	80 μm
Max. Holding Force	14.6 N
Max. Speed	17.6 mm/s
Sensitivity of Force Measurement	0.1N
Max. Measurable Force Range	15N

Table 4.3: Specifications of the system

	10mm/s		2mm/s	
Force [N]	2	4	10	12
Speed Error [mm/s]	0.21	0.24	0.25	0.24

Table 4.4: Speed errors of the model under different load conditions

As the choice of suitable PID gains affects the stability and response of the master-slave system, the design parameters follow the criteria below:

- The response of the master-slave system was qualified by measurement of the phase lags in (i) the force response and (ii) position response, between the master and slave. To achieve a realistic haptic response, the phase lags have to be minimised, and the control parameters should be tuned to reduce both phase lags within 50ms. The normal human response to a perceivable force of 1N is around 10Hz (100ms) [Hamed, 2009], and therefore the phase lag criterion here was set to be half of the response for good quality of haptic realisation.

- The position control in the slave should avoid overshoot, as the master-slave control was designed to be applied in a prostate biopsy system (in Chapter 5) in which the slave, as a needle firing unit, was to drive a biopsy needle to a target tissue. Also, the steady-state position error in the master-slave system should be within a count of 80μm for accuracy of positioning.

4.3.6 Discussion

Evaluation of the Neural Network based Speed Model

To verify the validity of the neural network based speed model, an open loop control test was conducted to control the motor velocity solely with input parameters $\dot{x}$ and F.

To evaluate the performance of the model in both the linear range and nonlinear range, tests were set up to control the velocity of the motor at (i) a high speed of 10mm/s under the load conditions of 2N and 4N which were within the nonlinear range, and (ii) a low speed of 2mm/s under the load condition of 10N and 12N which were within the linear range. The corresponding driving frequencies to the motor drive were computed to control the speed under different load conditions and the actual speed of the motor was then measured, the results are shown in Figure 4.13. In the condition (i), the speed model computed the corresponding frequencies (c), for the load conditions of 2N and 4N (b), to control the motor speed, at 10mm/s (a). Similar to condition (ii), the computed frequencies from the speed model are shown in (f), for the load condition of 10N and 12N (e), to keep the motor speed at 2mm/s (d). The maximum errors that occurred in each of the tests are listed in Table 4.4. The proposed neural network based speed model was verified to adequately model the motor speed under different load conditions, with maximum errors of 0.25mm/s in both the linear and nonlinear speed ranges, and thus it was shown that the model is useful in linearisation and regulation of the motor speed.

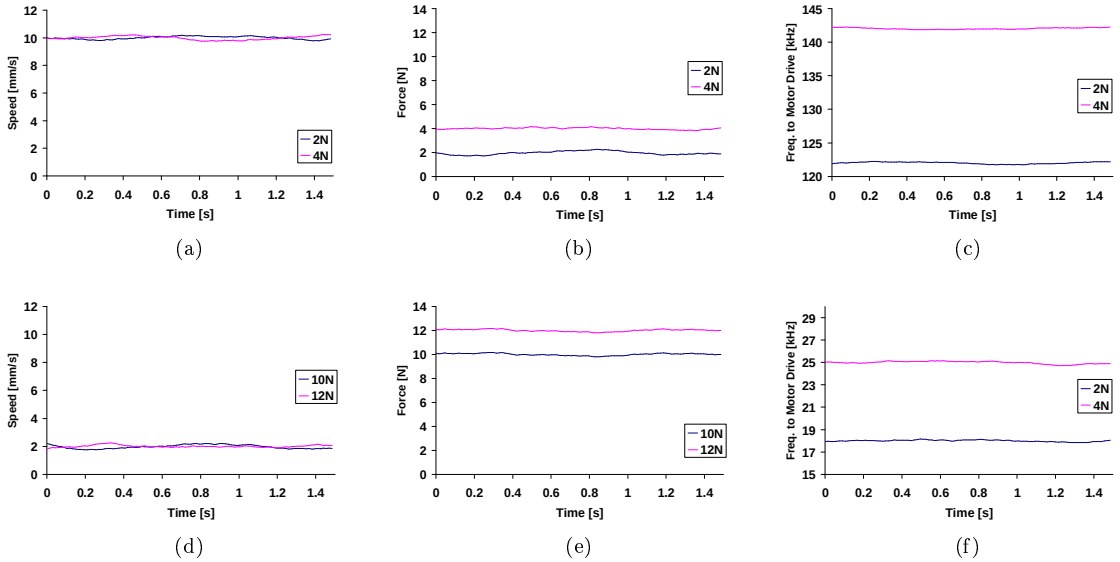
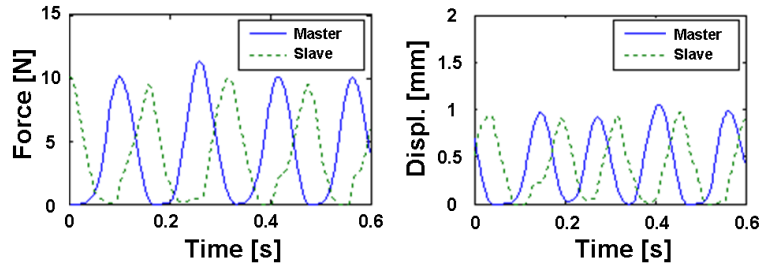
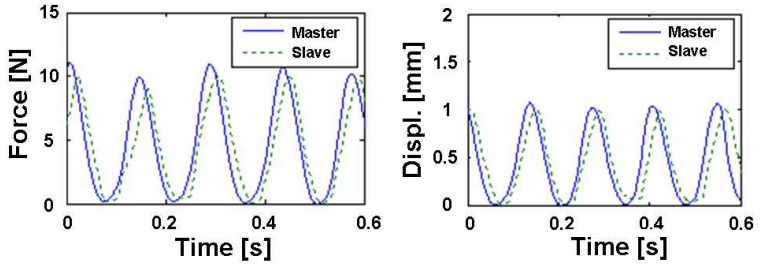


Figure 4.13: Open loop velocity control of the ultrasonic motor with the neural network model: (i) under low load conditions of 2N and 4N (b), with a controlled speed of 10mm/s (a). The computed driving frequencies are shown in (c) and is in the nonlinear speed range; (ii) under high load conditions of 10N and 12N (e), with a controlled speed of 2mm/s (d). The computed driving frequencies are shown in (f) and is in the linear speed range.



(a) No neural network speed model



(b) Neural network speed model

Figure 4.14: Force and displacement responses in the master-slave system with (a) no speed model, and (b) with the speed model

Evaluation of the proposed Haptic Control

An experiment was set up to evaluate the control scheme implemented in the master-slave test unit. The objective of this experiment was to evaluate the system performance by comparing the system phase lags with and without the use of the speed model.

The PID gains in the haptic control were selected by the Zieglar-Nichols method and the k term in the feed forward loop was tuned manually to optimise the response of the slave system. The system was tuned according to the specifications in Section 4.3.5 with (i) the selected PID gains $K_c = 30.2$, $T_i = 0.032$, $T_d = 0.0056$ at the force control in the master, (ii) $K_c = 34.3$, $T_i = 0.041$, $T_d = 0.0061$ at the position control in the slave, and (iii) $k = 0.34$ at the feed forward loop. The steady-state position error in the master-slave system was within a count of 80μm. A user was asked to use the master-slave test unit to palpate a prostate tissue phantom and the force and displacement of the master and slave were recorded. The force and displacement responses under the proposed control scheme are illustrated, with no neural network speed model in Figure 4.14(a), and with the use of the model in Figure 4.14(b); a phase lag improvement of 20ms was observed in the system position response, from 30ms (without the speed model) to 10ms (with the speed model), and an improvement of 23ms was observed in the system force response, from 35ms (without the speed model) to 12ms (with the speed model). It was concluded that the presence of the speed model compensated for the nonlinearity caused by the varying load during probing in the palpation. The speed model has demonstrated its functionality for linearising the ultrasonic motor and has hence improved the response of the master-slave system by shortening the phase lag to about 10ms.

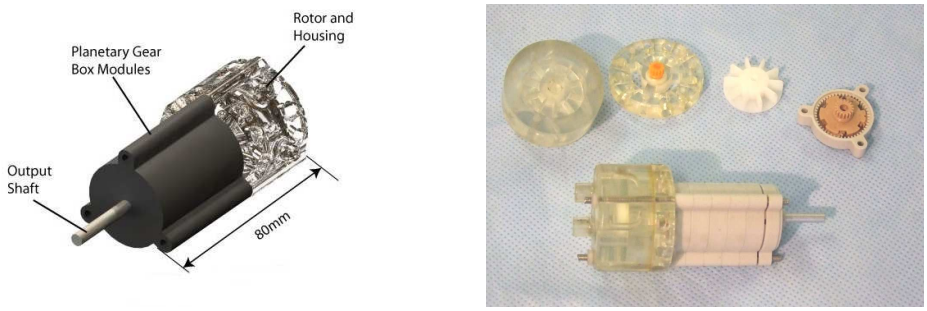
4.3.7 Summary

This section has studied the feasibility of applying haptics to an MR robot with the use of the Piezoleg, an MR compatibility proven ultrasonic motor. It started with an introduction of the motor's working principle with the use of four piezoelectric ceramic legs to generate different actuation modes of the motor, followed by the electronics required to synchronise the motor group to work in synchrony with the same driving signals. The Piezoleg motor was investigated in terms of its speed performance under different driving frequencies and load conditions, and the nonlinear characteristics of the motor were modelled by a neural network based speed model, which was verified with an open loop test showing a maximum error of 0.25mm/s. A haptic control scheme was proposed with the use of the speed model, and their functionality was demonstrated, verifying the concept of implementation of haptic control in MR robots.

4.4 Pneumatic Rotary Motor

4.4.1 Principle of the Pneumatic Motor

The MRI environment imposes huge challenges on actuators with an electromagnetic principle. The main fields, RF pulses, and switch-gradients from the scanner interfere with the normal operation of the actuator, whilst its use in the scanner room can cause image degradation due to its EM noise emission. [Chinzei, 2000b, Larson, 2004, Tsekos, 2005]. All of these reasons have driven the research



(a) (b)

Figure 4.15: (a) CAD rendering of the pneumatic air motor. (b) Photo of the air motor with its components.

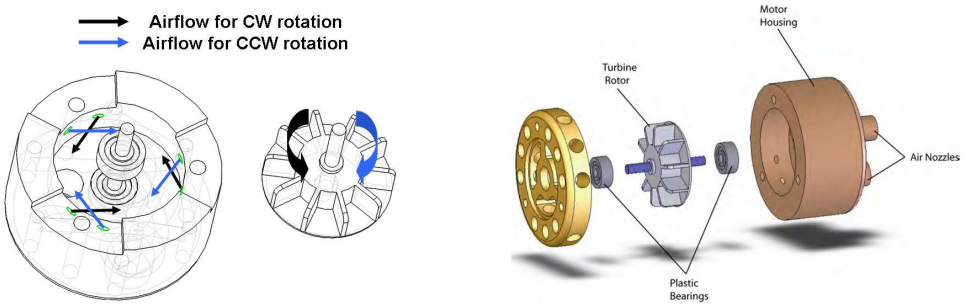
to develop the capability to accurately control a magnetism-free pneumatic actuator, especially for the purpose of generating high torque and speed for heavy duty applications, such as limb positioning.

A pneumatic air motor shown in Figure 4.15 was previously developed by the research team. Air is introduced to the motor housing through converting nozzles to speed up its velocity before hitting a turbine rotor. The compressed air drives the air turbine at around 1bar, after which a gear set is adapted to provide a high torque up to 0.3Nm and maximum speed of 24rpm. The schematic diagram is shown in Figure 4.16(a) to illustrate the working principle. Plastic ball bearings with polyacetal races, glass balls, and nylon cages are added to the air turbine shaft to reduce friction . The design of the turbine shaft assembly is demonstrated in Figure 4.16(b).

A commercially available modular gear set from Tamaya® (Planetary Gearmotor - Tamiya 72001) was modified to couple with the air rotor. The planetary gear train comprises of multiple gear modules and an aluminium output shaft. The necessary gear ratio is determined by the actual turbine speed and by the desired motor output speed. As far as the torque required to move and position a human limb was concerned, a gear ratio of 2000:1 was set, which could be easily scaled up or down by changing the number of gear modules in the gear set. The internal structure and components of the gear set is described in the CAD drawing in Figure 4.17. For the operating pressure, it was designed to operate at a low pressure of around 1-2bar to ensure the patient safety even if an air leakage was to occur near the patient.

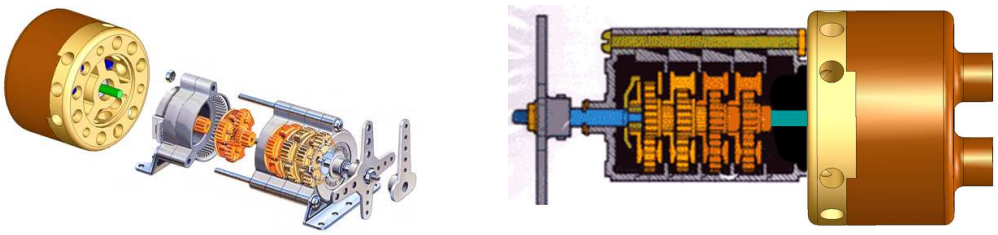
4.4.2 Control Electronics

The pneumatic motor was controlled by two solenoid valves, one for each direction. To implement open loop and closed loop, the motor was coupled with an optical quadrature position encoder , and a circular code-disc mounted on a plastic wheel. The code-disc resolution was 0.25degrees in this setup but increase in resolution can be achieved by printing a higher resolution code-disc if necessary. A block diagram of the system is presented in Figure 4.18. The electronic pulses (channel A and B) from the encoder were transmitted to the motion controller (NI CompactRio 9004), to decode the pulses into a position signal, and position control was implemented with a PID algorithm programmed in the LabView® graphical programming software, which subsequently adjusted the air supply to the



(a) (b)

Figure 4.16: (a) Schematic diagram of the working principle in the pneumatic turbine. (b) CAD drawing of the turbine shaft assembly.



(a) (b)

Figure 4.17: (a) CAD drawing of the planetary gearbox and pneumatic turbine assembly [ServoCity, 2009]. (b) Its side view [Tamiya, 2009]

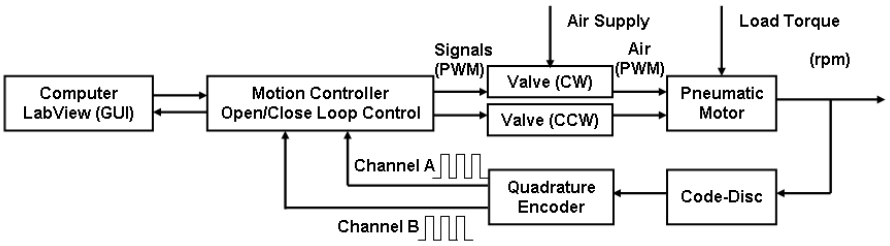


Figure 4.18: Block diagram of a simple close loop control in the pneumatic motor

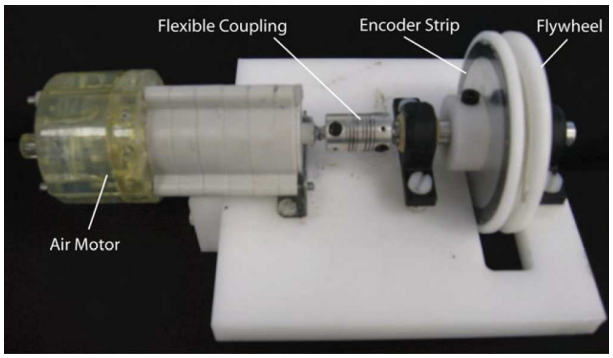


Figure 4.19: Test unit consists of a pneumatic motor with gear ratio 2000: 1, and an optical quadrature encoder with its code-disc.

air turbine by pulse-width modulating (PWM) the solenoid valves. The test unit is demonstrated in Figure 4.19. This unit formed a simple closed loop control pneumatic system and assisted to evaluate the control performance and characterise the pneumatic motor.

4.4.3 Control Performance and Characteristics

Open Loop Tests

In this section, the pneumatic motor performance was characterised with open loop tests to quantify; (i) its speed characteristics: rise time, maximum speed in step response, and speed-duty cycle relationship, and (ii) torque characteristics: maximum torque and speed-torque relationship. The motor was operated at 1.3bars in the open loop tests.

I. Speed Related Characteristics In the test of step response, the aperture of the valve controlling the airflow to the motor was set to be fully open, which was equivalent to the case of a step from 0% to 100% duty cycle in the PWM airflow, and the angular velocity was calculated from the encoder reading.

The plastic wheel attached to the motor was connected to a reel of string which allowed adjustable load to be placed on the motor. The step responses of the pneumatic motor are indicated in Figure 4.20 under the condition of no applied load and 25N (approximating the force required to move a limb). The average steady state speeds of 15.5rpm and 13.2rpm were obtained from the encoder reading with the rise time measured to be 82ms and 130ms, unloaded and loaded respectively. The rise time, which

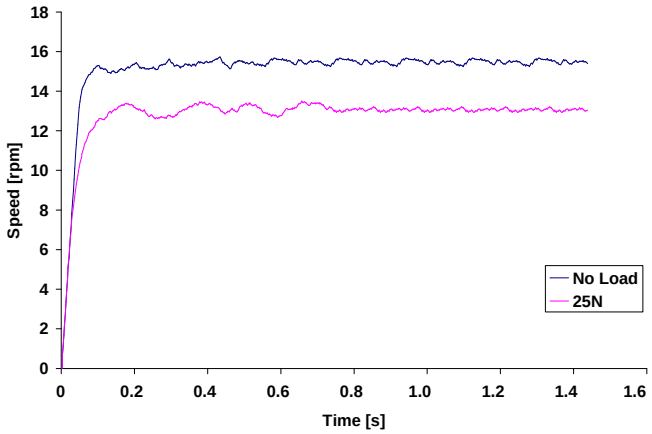


Figure 4.20: Step response of the pneumatic motor at 100% duty cycle at an operating pressure of 1.3bar

was the time taken for the angular speed to change from 10% to 90% of its steady state average speed, indicates the level of delay in the system response to a step reference signal. The rise time indicated shows an increase of 58% when a load was applied to the plastic wheel which effectively increased the inertia of the system; while steady state speed was reduced by 14.8%. This data shows that the system response and the steady state speed changes according to the load conditions in the open loop test, but the changes are within an acceptable level. The steady state speed shown in Figure 4.20 fluctuated slightly around the average speed for both conditions, and this result probably arises from the resolution of the encoders, the slight mechanical misalignment, and the vibration of the test unit during the motion rotation.

The rotational motion of the pneumatic motor is driven by the incoming airflow which is pulsewidth-modulated by the valve. Therefore, it is useful to know how the motor speed is related to the duty cycle of the airflow pulses and the pulse period. Experiments were performed on the test unit to investigate the speed-duty cycle relationship for different duty cycle periods, and the result is shown in Figure 4.21. The experiment was conducted in the condition of no applied load. It was observed that a longer duty cycle period, such as T=200ms and 300ms, had a duty cycle covering a wider range of speed, and had a quite linear speed-duty cycle relationship. However, long cycle periods in the PWM traded off in the motion smoothness of the motor, as observed during the experiment. Irregular motion is unfavorable for control, stability and positioning, especially in medical devices. In contrast, short duty cycles, such as T=30ms provided smooth motion in the motor, but a short range of linearity in the speed-duty cycle relationship also made them unfavorable for motor control. For periods of 30ms, 40ms, 50ms and 60ms, it was observed that the motor did not move if the duty cycle was lower than 10%, which was due to the friction in the gearbox and also due to the fast mechanical response time required for those duty cycles being beyond the bandwidth of the pneumatic valves. Based on these considerations, a cycle period of 150 ms was selected as a compromise between motion smoothness and linear range of motor speed.

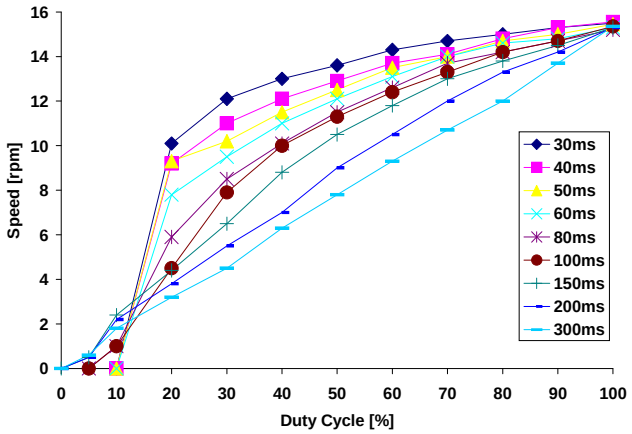


Figure 4.21: Relationship between speed and duty cycle under different periods for pulse width modulation of air supply (No load, operating pressure of 1.3bar)

II. Torque Related Characteristics To consider the maximum torque generated by the pneumatic motor, different weights were loaded to the motor to investigate how the rotary speed was affected by different load situations. The valve was fully open during the experiments and the loads were applied in each test iteration until the motor was finally stopped by the weights. The speed and torque relationship were also recorded with similar setup and the result plotted in Figure 4.22. The motor possessed a quite linear relationship between the speed and the torque, and its nonlinearities (defined as the ratio of the largest difference to the least square straight line fit to the range [Chapuis, 2004]), are 3.2%, 12.2%, 12.3%, 13.1% and 10.4% at the operation pressure of 0.8bar, 0.9bar, 1.0 bar, 1.1bar, 1.2bar and 1.3 bar respectively. The nonlinearities of the speed-torque relationship are all below about 13% at different operational pressures, and a simple closed loop control design is probably robust enough for good position control. The maximum torque of the motor is 2.2Nm at the operation pressure of 1.3bar, which is equivalent to 55N at the movement arm of 40mm, and is sufficient for most of medical applications. Also the generated force can be scaled up or down by an adjustment of the gear ratio according to the requirement.

Closed Loop Tests

I. PID Control The proposed pneumatic motor has been characterised in the open loop tests in the previous section and the speed of the motor was found to be quite linear to the torque applied. The next step is to attempt a closed loop control on the motor with practical control strategies and to characterise its closed loop position control performance. The Proportional–Integral–Derivative controller (PID controller) is a generic closed loop feedback control method and is widely used in industrial control systems. Due to its simplicity and practical usefulness, it was implemented in the pneumatic motor for position control. The general discrete equation of PID control is as follows:

$$u(t) = K_c e(t) + \frac{K_c}{T_i}\left(\sum_{i=0}^{t} e(i)\right) T_\triangle + K_c T_d \frac{(e(t) - e(t-1))}{T_\triangle}$$

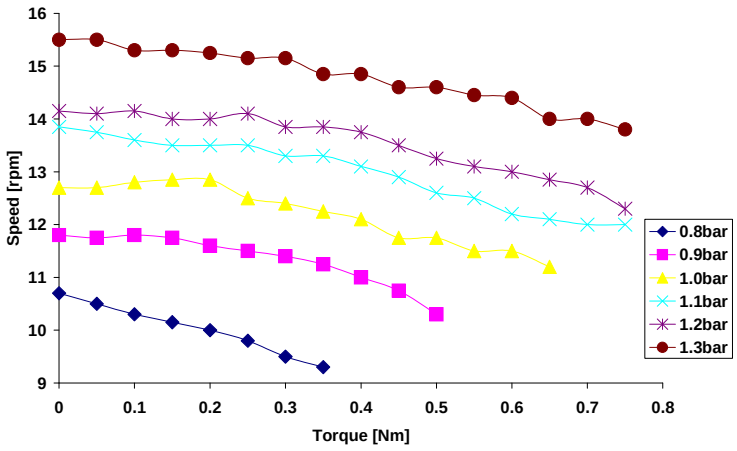


Figure 4.22: Relationship between torque and speed under different operating pressures.

Then,

$$u(t) = u(t-1) + K_c\left[e(t) - e(t-1)\right] + \frac{K_c T_d}{T_i}\left[e(t) - 2e(t-1) + e(t-2)\right]$$

where e(t) is the error between setpoint and the process variable u(t); K_c is the controller gain; T_i is the integral time; T_d is the derivative time; $T_\triangle$ is the time interval between each sample.

II. Control Tuning Specifications The choice of design parameters in PID gains plays a crucial role in the achievement of good performances and stability of the closed-loop position control system. Design parameters must ideally satisfy three principal requirements:

- The pneumatic motor should be controlled to keep the level of its overshoot minimal, and ideally to achieve its percentage overshoot (PO) within 5%, that is, 3 degrees in the range of a 60-degree rotation. In medical devices, unexpected overshoot in the end-effector trajectory can be dangerous to the patients and its surrounding hardware. In applications of needle alignment in prostate biopsy described in Chapter 5, and limb positioning described in Chapter 7, a PO within 5% is an acceptable range. However, a small PO always compromises the rise time of a system.

- The pneumatic motor should have a rise time ideally within 15s for a rotation from 0degrees to 60degrees, which would ensure that the robotic systems actuated by the motors in Chapter 5 and 7 have a short response time for positioning. This point should be considered together with the first point to optimise the system performance.

- The pneumatic motor should be able to provide a positioning accuracy within a count of 0.25degrees to ensure its precision in the biopsy needle alignment and the limb positioning. It is preferable that the PID controller is insensitive to disturbances from the surroundings, such as patient movements.

Controller	K_c	T_i	T_d
P	0.13K	N/A	N/A
PI	0.13K	0.8T	N/A
PID	0.15K	0.5T	0.12T

Table 4.5: Tuning formula under PID control

III. Auto-Tuning PID Controller Even though the three parameters in PID control, K_c, T_i and T_d are possibly calculated in analytical forms, this requires modelling of the pneumatic actuator, the system dynamics, and the performance of related components, and hence is impractical in reality. Instead, the PID can be tuned manually or with the help of software tools. The Ziegler–Nichols method is a widely used method, which can systematically provide a good estimation of the tuning parameters and fine tuning can be followed to further revise the parameter for better performance. The PID controller was implemented in the test unit with an embedded PID auto-tuning feature from the PID toolkit, in the LabView® software. Based on the Ziegler-Nichols method, and the condition of higher damping ratio was selected in the programme to minimise overshoot. The tuning formulae are listed Table 4.5 in which K and T are the ultimate gain and the oscillation period at this gain.

IV. Step Response under Different Load Conditions A second test unit as shown in Figure 4.23 was implemented to: (i) evaluate the step response of the pneumatic motor under different load conditions with the PID controller and (ii) verify the concept of using the purposed motor for limb positioning where the load condition varies according to the compliance of the test limb at particular orientations and gestures. The design of this test unit was based on that of the previous test unit, with the same motor and encoder, but the plastic wheel was connected to a limb platform with a plastic linkage. The limb platform (adapted for hand motion), base board, plastic wheel and the plastic linkage, form a four bar linkage system, so that the inclination of the palm platform is known by tracking the angular movement of the wheel and solving the kinematics. The platform was designed to move a palm, by flexing of the wrist, from 0 to 90degrees.

Step response tests were repeated with a tuned PID closed loop controller. A setpoint of 60degrees was defined and motion was initiated when the limb platform was horizontal. The system response was recorded under the conditions of: (i) no load applied; (ii) a palm placed on the limb platform, as a load varying to its compliance at different orientations and (iii) with 25N load applied to the plastic wheel; as shown in Figure 4.24. The rise time changed from 8.3s, 11.2s to 13.9s under different load conditions, meaning that the load had altered the system characteristics and that new PID parameters may be necessary for different load conditions. In the test in which a palm was placed on the platform, the convergence and the stability of the system was not much affected by the varying load conditions, showing the feasibility of the use of the proposed pneumatic motor and controller for positioning. Although it took a few seconds more for the system to achieve the set point, it is still quite acceptable as a device for positioning..

The step response tests were also conducted to observe the system performance with the PID value tuned in each load condition, with the results shown in Figure 4.25 and Figure 4.26. It is observable that the response of the motor can be largely improved with auto-tuned PID parameters in each load

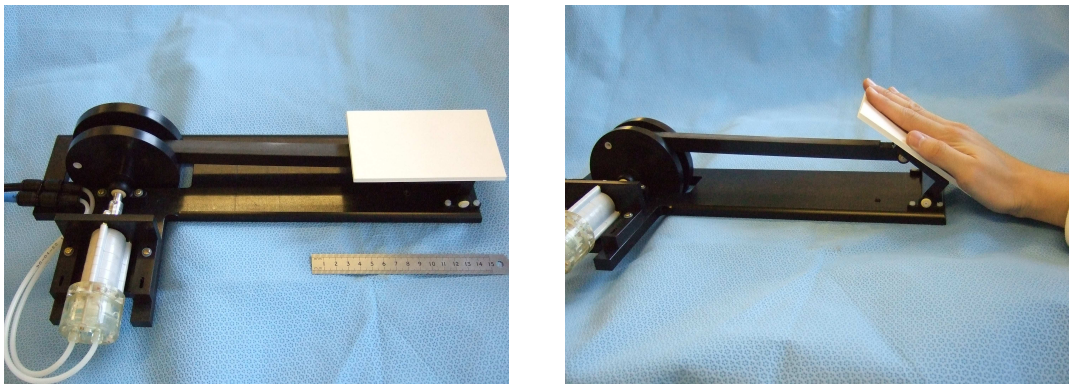


Figure 4.23: Test unit II consists of a pneumatic motor, optical position encoder, and plastic wheel and limb platform. The platform, base board, wheel plastic and the plastic linkage forms a four bar linkage system.

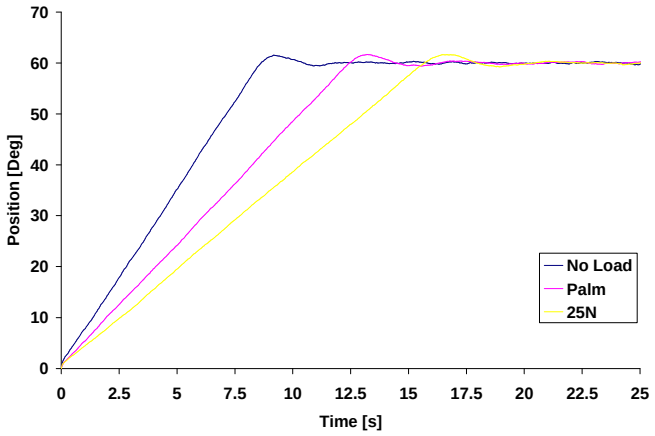


Figure 4.24: Step response of the closed loop PID control in the pneumatic system under the condition of no load, a palm and load of 25N at the operation pressure of 1.3bar. The PID parameters were kept unchanged in each condition.

condition, and that a PID controller coupled with the pneumatic motor is good enough for positioning under a large range of load conditions from 0N to 50N, if a matched PID parameter is provided. The set of PID parameters deduced in this experiment provided a reference for the manual or auto PID tuning of the pneumatic motor controller in which the motor was adapted in two types of MR robots, as mentioned in Chapter 5 and 7.

4.4.4 Summary

A pneumatic motor with its MR compatibility tested in Chapter 3 has been presented with its working principle, supporting electronics and control strategy. The actuator was characterised with a series of open loop and closed loop tests, in terms of its speed, torque, rise time performance, and an auto-tuning PID controller was proposed for the control system. The motor coupled with a 2000:1 gear ratio has been demonstrated to generate a speed of 15.5rpm and a sufficient torque of 2.2Nm (55N at the

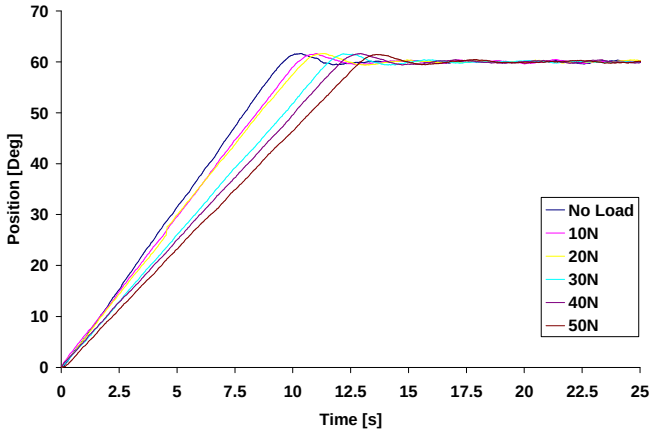


Figure 4.25: Step response of the closed loop PID control in the load conditions of 0N, 10N, 20N, 30N, 40N and 50N (1.3bar). The PID parameters were auto-tuned in each condition.

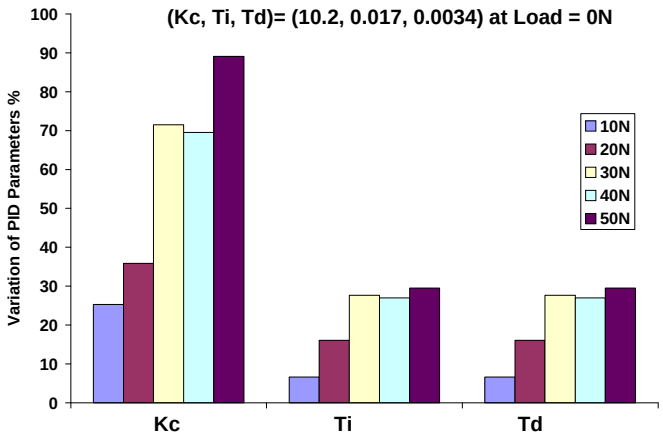


Figure 4.26: Variation of PID parameters under the load conditions of 0N, 10N, 20N, 30N, 40N and 50N. The parameters were tuned by Ziegler–Nichols method based on the function of Auto-tuning PID in LabView®.

moment arm of 40mm) with the achieved positional accuracy of 0.25degrees. Finally, the positioning capability of the pneumatic motor under a variety of load conditions, and its functionality to position a limb to a specific angle, have been verified in the presented test unit. The control information and design experience acquired provide a foundation to implement this actuator for a complex and sophisticated robot design, which will be discussed in Chapter 5 and Chapter 7.

4.5 Conclusion

This chapter covers the evaluation and implementation of two proposed actuators based on piezoelectric and pneumatic principles which have had their MRI compatibility evaluated in Chapter 3. Performance tests and characterisations have been conducted using two separate test rigs; one for realisation of sensing and haptic control in needle therapy, and the other for positioning purposes.

Due to the spatial constraints of a closed bore MR scanner, a robotic system incorporating a force-position control located within the bore, is useful to assist clinicians accessing the imaged tissue inside the MR scanner during the intervention. Therefore, the first focus of this chapter is an investigation of the feasibility of implementing Piezoleg, an MR compatibly proven actuator with fast response, to reconstruct the sense of touch in the MR environment. A master-slave prototype together with its electrical circuitries for motor synchronisation was presented. A neural network based controller was developed for speed control based on the driving frequency to the motor and the applied load, and was subsequently used to linearise the ultrasonic motors in a proposed haptic control scheme. Its functionality was demonstrated to improve the response of the haptic control.

The second focus is to control an MRI compatible actuator developed based on the principle of a pneumatically driven turbine motor coupled with a modular gear set. The feasibility of the motor concept has been proven and its performance has been evaluated with respect to the open loop and closed loop control. To evaluate the concept of using pneumatic principles for limb positioning in MR robot, a test unit for orientating a palm at angles from 0 to 90degrees, has been developed with an auto-tuning PID control algorithm implemented. The test unit realised the concept successfully to position a range of load conditions from 0N to 50N at a particular orientation, demonstrating its robustness for good positioning.

Chapter 5

System for MR Guided Prostate Biopsy

5.1 Introduction

Currently Transrectal Ultrasound (TRUS) imaging is the main technique to guide prostate biopsies. The problems with this technique are its low tissue contrast and poor image resolution, which often lead to samples being taken not in the area of the suspected target tissue but in the surrounding tissues of the prostate capsule; leading to reduced accuracy in lesion detection. As such, many biopsy samples are often required in order that one is successfully taken from the suspected area [Carroll, 2008]. In comparison to TRUS, MRI demonstrates good soft tissue contrast, sensitivity and specificity, and hence presents a potential channel to provide better guidance during biopsy.

This chapter begins with the design guidelines and specifications of the MR robot for transrectal prostate biopsy, including the use of MR compatible materials and components to avoid EM interference, the robot workspace and kinematics required to perform the biopsy, and the design of the control strategy and image display. Based on those specifications, a prostate biopsy robot design is presented, and the issues of its kinematics, registration, workspace analysis in the scanner bore, and real-time needle tracking with the use of fiducial markers are investigated. Following this is a detailed discussion of the engineering design of a pneumatic actuated Cartesian positioning robot and of an ultrasonic motor actuated haptic needle firing unit, as two main parts of the prostate robot. At the end of the chapter the system electronics used in the scanner room and the methods for scanner, robot, and control PC communication are studied.

5.2 Design Specifications and Guidelines

The following are the objectives and specifications of the prostate biopsy robot which were set with our radiologist Prof. Nandita deSouza at the Royal Marsden Hospital, Surrey, UK. They are based on the clinical considerations in transrectal prostate biopsy, and the robot is intended to be designed with its work flow similar to existing interventions with the ultrasound guidance. The objectives and

specifications are shown as follows:

5.2.1 General Objectives

The system is designed to perform prostate biopsy under image guidance in a 1.5T closed bore MRI scanner, the procedure of transrectal prostate biopsy is chosen because of its benefit of requiring no anaesthetic injections for the patient and its direct adaptation from the conventional TRUS biopsy. In any case, the complexity in this procedure, in that an endorectal probe is inserted into a patient rectum and pivoted by the rectal sphincter, means that a robot kinematics related to the sphincter position for biopsy, has to be taken into consideration, and is more complicated than its alternative as transperineal biopsy (in which the robot is not connected to the patient body and the biopsy needle is inserted through the perineal wall).

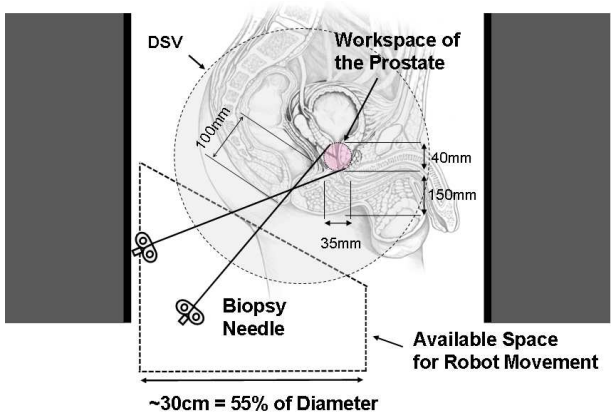
It was requested by our radiologist that the biopsy should be performed manually such that the radiologist could take control at anytime during the procedure. The robot design should be such that the user can control the scanner host computer and the robot itself in the scanner room near to the patient, which allows the user to monitor closely the patient as well as the robot movement. As the system is designed to be non-autonomous, its main functionality is (i) to track the real-time position of the biopsy needle relative to the target point, (ii) to resolve robot kinematics to provide calculated sets of joint movement in the robot to align the needle to the target point at three dimensional space, and (iii) to provide a graphical user control interface and a hardware needle insertion interface, such that the robot can perform needle alignment and insertion, following the command from the radiologist. The control interface should be easy to use, intuitive, and have caused no unfavourable interference within the MR environment. It is anticipated that the procedure time could be within 30-40mins, similar to its ultrasound counterpart.

5.2.2 Acceptable Level of MR Compatibility

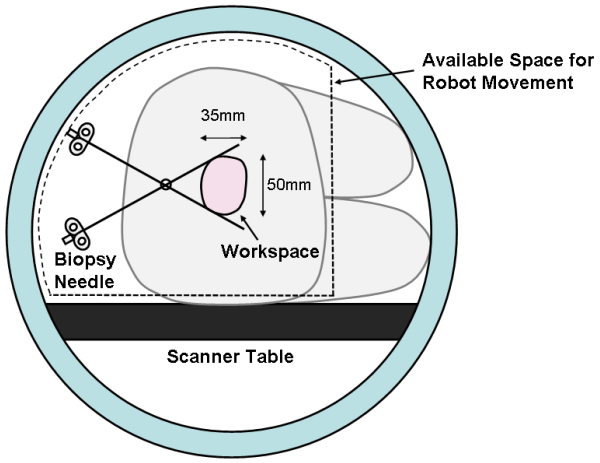
The robotic system has to be designed to be MR compatible at a level that its presence will not affect the image quality for the biopsy procedure including real-time tracking. The acceptable level of SNR reduction is set to be below 10%, as with different MR robots seen in literature and image artifacts should not be generated in the imaging volume. This implies the use of non-magnetic materials for the structural components and non-electromagnetic actuation, position sensing, and force sensing. As cables and electronics are potential sources of EM noise as well as thermal induction, they are required to be shielded, connected to the ground of the scanner and prevented from direct contact with both patients and operators for their safety.

5.2.3 Required Workspace

The prostate is a small sized gland in the male reproductive system, with the average dimensions of 50mm in the lateral direction of a man, 35mm in the anterior-posterior direction, and 40mm in the foot-head direction. This gland is located 150mm from the perineal wall and 100mm from the rectal sphincter. If the prostate gland is approximated in shape by an ellipse with the dimension specified above, the range of motion required by the robot is illustrated in Figure 5.1, where the patient is



(a)



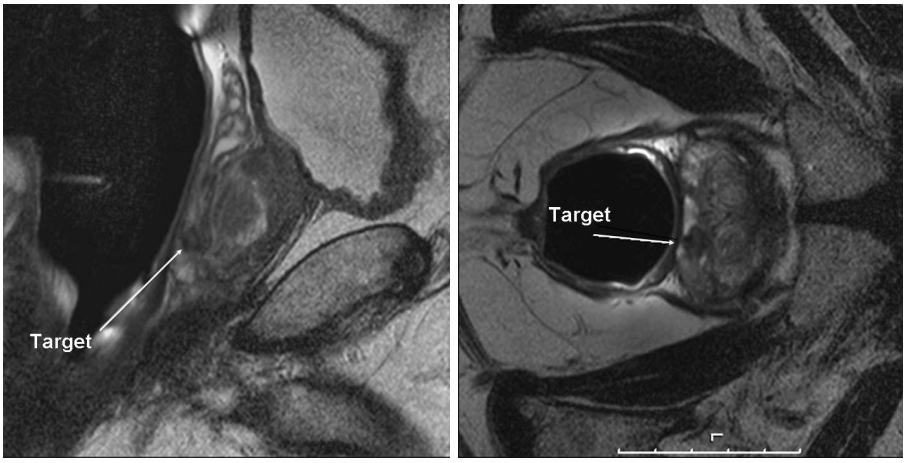
(b)

Figure 5.1: Schematic diagrams of (a) posterior-anterior view and (b) foot-head view, showing the required workspace covering the prostate.

in left lateral decubitus position, a common gesture for transrectal prostate biopsy. In the robot specification, the workspace of the robot should allow targeting of any point in the prostate, especially the adenocarcinomas area, which is located mostly close to the periphery of the capsule. Figure 5.2 shows the MR image of the adenocarcinomas area in the prostate, in the posterior-anterior view and the head-foot view.

5.2.4 Spatial Availability for Robot Movement

The patient is positioned in the left lateral decubitus position during the prostate procedure which is a common gesture for transrectal biopsy. The patient body is placed right in the middle of the scanner as shown in Figure 5.1, for two reasons: (i) it is important to have the prostate, rectum and anus within the imaging volume and as close as possible to the isocentre, to acquire a good image quality of the prostate and related geometry for needle tracking; (ii) putting the patient body at the centre of the scanner axis allows a large robot working area approximated by a trapezoid with the height of 30cm



(a) (b)

Figure 5.2: MR images of (a) posterior-anterior view and (b) foot-head view, showing the adenocarcinomas area in the periphery of the capsule.

in posterior-anterior direction (Figure 5.1(a)), which is about 55% of the diameter of the semi-circle in the cross sectional view of a scanner bore (Figure 5.1(b)).

5.2.5 Robot kinematics

The device is designed to be fixed to the scanner table with an adjustable mount that allows for different patient body sizes and flexibility in positioning of the patient. The patient is positioned on the scanner's couch in the lateral decubitus position. For a transrectal procedure, an endorectal probe is required as the end effector which is inserted into the rectum and contains the needle. Once inserted into the rectum, the probe must be moved to a suitable position and orientation for an alignment of the biopsy needle to the target area. In this application, the device should have at least 4DOF of actuated motion, as indicated Figure 5.3: (i) a translation for the movement of the endorectal probe front and back; (ii) pitch and yaw about the rectal sphincter to align the needle to the target; (iii) and another translation for the needle insertion; the 4 DOF are the basic kinematics for the needle alignment. Additionally the robot should have enough flexibility to allow the end effector to be placed close enough to the patient's rectal sphincter, which requires an adjustable support for different size of patients.

5.2.6 Robot Control and Tracking

Assistive Robot Strategy

Autonomous robotic systems are widely used in industry to reduce manufacture cost and time, achieve standardised quality of product, and hence boost up productivity. However, this is not comparable to the situation in medical robotics where each patient is individual and the practices are patient oriented. A dialogue with our radiologist reveals that clinicians prefer to be involved in the procedure and have robots designed for an assistive role to help perform simple but repetitive tasks. Therefore, a

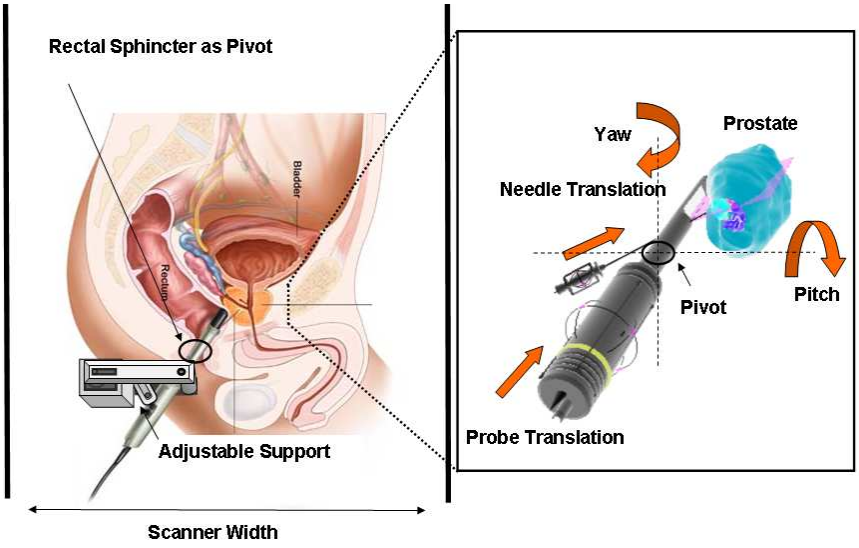


Figure 5.3: Robot kinematics for transrectal prostate biopsy: at least 4 actuated DOF for the needle alignment and insertion, and a support frame to place the end effector close to the patient anus. [Blue, 2009, Harald H. Quick, 2005].

"clinician-in-the-loop" approach is taken when designing the control strategy, in which the user controls the movement of the robot and inserts and fires the biopsy needle manually with the corresponding interface; whilst the robot works as a slave manipulator to follow the command of the user to align the biopsy needle in three dimensional space, and provide stable holding of the needle. In addition to this, the control interface provides instructions of robot movements to the user for the needle alignment to a user defined target, and provides simulation of the robot trajectory whilst avoiding collision with the scanner bore boundary. These goals are achievable by derivation of the robot kinematics.

Real-time Image Display

As the robot is designed to be assistive to the user, a real-time image display of the prostate target lesion and the relative needle position are necessary for the user to control and monitor the needle alignment. It was requested by our radiologist that a display of the real-time MR images be made available inside the scanner room, so as to allow monitoring of the patient and the procedure closely, and implementation of an immediate stop if necessary.

Spatial tracking

The spatial tracking of the robot and needle localisation are both achieved by the optical position encoders embedded in robot joints and MRI fiducial markers embedded in an endorectal probe. The fiducial markers appear as a bright spot in MR images, and are attached to the head of the endorectal probe for position tracking. When the markers are within the linear region of the magnetic field in the DSV, they are able to provide fine position measurements. Therefore, position control of the robot relies on the optical encoder reading, when the end effector is in a region far from the isocentre of the scanner, and on the fiducial markers when it is close to the centre.

5.3 Design Overview

Figure 5.4 presents the design of the biopsy robot and the overview setup of the whole system including the control interface. The robot design consists of: (i) a Cartesian positioning robot actuated by the custom design pneumatic motor, (ii) an extension arm, (iii) a haptic needle firing unit coupled with gimbals, which is connected to the extension arm, and (iv) an endorectal probe attached to the unit. The needle firing unit is actuated by the Piezoleg motor, and attached to the gimbals which allow the unit to be set in pitch and yaw direction.

During the biopsy procedure, an endorectal probe is inserted into the patient's rectum, and his rectal sphincter works approximately as a pivot, supporting the probe. The cooperative movement of the three axes of the Cartesian robot allows the rotation of the probe in pitch and yaw, as well as, translational movement of the probe towards and away from the rectum. Pitch, yaw, translation of the endorectal probe and needle insertion are the minimum necessary motion for transrectal prostate biopsy, and they are similar to the required probe movement in TRUS prostate biopsy.

Attached to the gimbals is the needle firing unit which comprises of 2DOF: one is a linear needle insertion axis; another is a needle firing trigger. The former is in charge of the insertion and retraction of the biopsy needle when a needle alignment in terms of the pitch, yaw, and translation of the probe is confirmed ; the latter is to fire the biopsy needle to obtain a prostate sample in which only a forward movement is required and can be achieved with the use of a pneumatic cylinder. In terms of the specifications of each axis, a thorough discussion is presented in the next Section of Robot Kinematics Analysis.

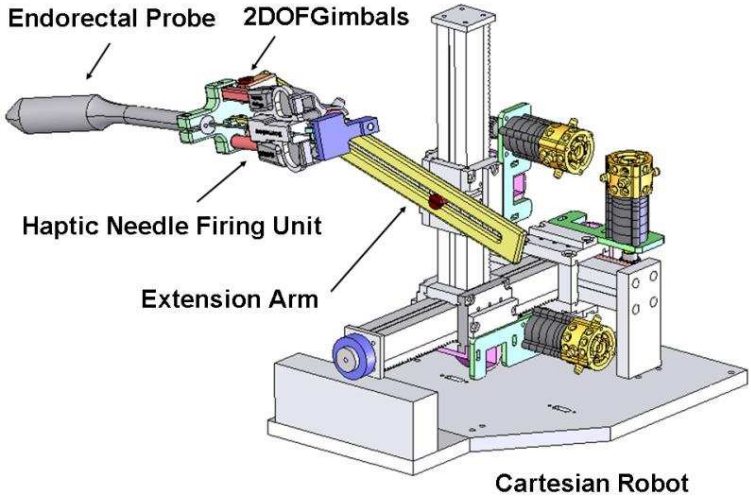
5.4 Robot Kinematic Analysis

5.4.1 Forward Kinematics

Forward and inverse kinematic problems are fundamental to the study of robotics. For relatively simple robots, with few degrees of freedom, both of these kinematic problems can usually be solved directly and without much difficulty. However, for more sophisticated robots, it is useful to apply a more general and systematic approach that can be applied to most kinematic configurations and obtain the forward kinematic equations of any multi-link robot; to determine both position and orientation of the end effector relative to the robot base.

The objective of forward kinematics is to determine the end effector position and orientation as a function of the joint variables and link lengths [Lewis, 1993]. In the case of the prostate biopsy robot, the position of the needle notch is calculated with the given movement of each joint in the Cartesian robot and in the gimbals, which are either encoded by the position encoders or the fiducial markers. Denavit Hartenberg (D-H) coordinate transformation, is the most common technique to construct the forward kinematic equations of a manipulator and hence is adapted in analysis of the robot kinematics [Lewis, 1993].

The kinematic diagram of the prostate biopsy robot is illustrated in Figure 5.5. Frame 0 is the base frame of the robot; and frame N is the frame of the end effector corresponding to the centre of the needle notch near to the tip of the needle, to which a biopsy specimen will be stored after the



(a)



(b)

Figure 5.4: (a) CAD drawing of the robot design consisting of a Cartesian positioning robot, an extension arm, a gimbals mechanism and a haptic needle firing unit with an endorectal probe attached. (b) The setup of the biopsy robot with its control interface.

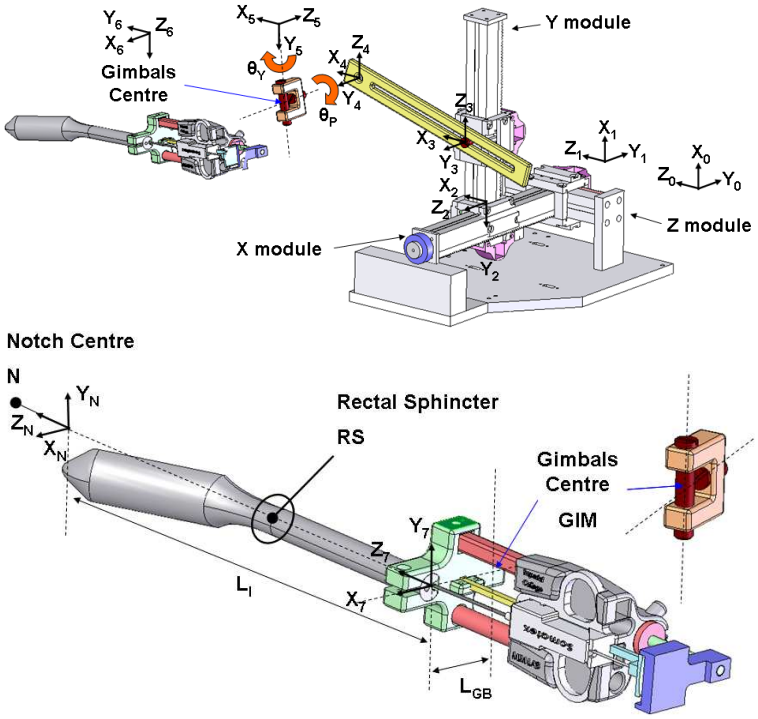


Figure 5.5: Kinematic diagram of the prostate robot design.

needle is triggered. A list of symbol notations used in the kinematic calculation is listed in Table 5.1. The DH transformation matrices defining the geometric relation between each connected frames from frame 0 to frame N are indicated in Table 5.2.

Multiplication of all the DH transformation matrices from frame 0 to frame N can result in a transformation matrix representing the coordinate of the end effector (needle notch centre) with respect to the robot base frame 0 and the matrix is listed in Table 5.3 (Equation (5.1)).

In the transformation matrix T_0^N, variables governing the movement of the robot are the joint variables of translation in X, Y and Z modules of the Cartesian robot D_X, D_Y, D_Z, the pitch angle θ_P and the yaw angle θ_Y of the gimbals. In reality, the two angles are not freely rotated during the procedure, and they are governed by the position of the rectal sphincter and the centre of the gimbals, as shown in Figure 5.6.

The centre of the gimbals relative to the frame 0 is ${}^0r_{GIM} = \begin{bmatrix} D_Y + L_Y + D_E cos\theta_E \\ -D_X - L_X - L_{TH} - L_{EG} \\ D_Z + L_Z + D_E sin\theta_E \end{bmatrix}$ from the kinematics diagram in Figure 5.5, and the position of the rectal sphincter ${}^0r_{RS} = \begin{bmatrix} b_1 \\ b_2 \\ b_3 \end{bmatrix}$ is measurable from MR images of the patient body. Therefore, the pitch angle θ_P and the yaw angle θ_Y can simply calculated by dot product of the vector from the gimbals centre to the rectal sphincter $\left({}^0r_{RS} - {}^0r_{GIM}\right)$ to its projection vector in X_0Y_0 and Z_0X_0 planes, and θ_P and θ_Y can be in terms of D_X, D_Y and D_Z.

	Description	Range/Value
	MRI Scanner	
Frame S	Frame of the scanner	
	Cartesian Robot	
Frame 0	Frame in the Z module of the robot	
Frame 1	Frame in the X module of the robot	
Frame 2	Frame in the Y module of the robot	
Lz	Link in Z module	49.8 mm
Lx	Link in X module	52.7 mm
L_Y	Link in Y module	52.8 mm
Dz	Movable Range in Z module	0-80 mm
Dx	Movable Range in X module	0-180 mm
Dy	Movable Range in Y module	0-180 mm
	Extension Arm	
Frame 3	Frame of the extension arm	
L_{TH}	Thickness of the arm in Y_3 direction	13 mm
D_E	Extension length	0-220 mm
θ_E	Angle inclination of the extension arm from the vertical axis	0-150 ^{o}
	Gimbals	
Frame 4	Frame in the first joint in the pitch direction	
Frame 5	Frame in the first joint in the yawn direction	
θ_P	Gimbals pitch angle	-90-90^o
θ_Y	Gimbals yawn angle	0-90 ^{o}
L_{EG}	Link from the extension arm to the gimbals	52.4 mm
GIM	Centre position of the gimbals. Its coordinate is $^0r_{GIM}$ in frame 0	
	Haptic Needle Firing Unit	
Frame 6	Frame of the haptic needle firing unit (gimbals centre (GIM))	
Frame 7	Frame of needle insertion	
Frame N	Frame of needle trigger	
L_{GB}	Perpendicular distance from the centre of the gimbals to the biopsy needle	44.1mm
α	Angle formed by the needle axis and the line joining centre of the rectal sphincter RS and the centre of the gimbals GIM (Refer to Figure 5.6(b)).	
D_I	Needle insertion depth	0-45 mm
L_I	Distance from point 7 to point N	105.9mm
D_F	Length of Needle trigger	0 or 22 mm
N	Notch centre position	
RS	Centre position of the rectal sphincter. Its coordinate is $^0r_{RS}$ in frame 0	
$^0r_{T\arg et}$	The target point coordinate in frame 0	

Table 5.1: Definition of symbols in the kinematics calculation

DH Transformation Matrices	Descriptions
$T_0^1 = \begin{bmatrix} 1 & 0 & 0 & 0 \\ 0 & 1 & 0 & 0 \\ 0 & 0 & 1 & D_Z + L_Z \\ 0 & 0 & 0 & 1 \end{bmatrix}$	**Z, X and Y module** D_Z , D_X , and D_Y are the joint variable of translation in Z, X, Y modules of the Cartesian robot.
$T_1^2 = \begin{bmatrix} 0 & -1 & 0 & 0 \\ 0 & 0 & -1 & -D_X - L_X \\ 1 & 0 & 0 & 0 \\ 0 & 0 & 0 & 1 \end{bmatrix}$	Lz, Lx, Ly are the length of the links in each the Z, X, Y modules. They are also equal to the distance between point 0 and 1, point 1 and 2, and point 2 and 3 respectively when $D_Z = D_X = D_Y = 0$.
$T_2^3 = \begin{bmatrix} 1 & 0 & 0 & 0 \\ 0 & 0 & -1 & -D_Y - L_Y \\ 0 & 1 & 0 & 0 \\ 0 & 0 & 0 & 1 \end{bmatrix}$	
$T_3^4 = \begin{bmatrix} 1 & 0 & 0 & D_E \sin\theta_E \\ 0 & 1 & 0 & L_{TH} \\ 0 & 0 & 1 & D_E \cos\theta_E \\ 0 & 0 & 0 & 1 \end{bmatrix}$	**Extension Arm** L_{Th} , D_E , θ_E are the thickness of the arm in y_3 direction, its extension length, and its angle inclination from the vertical axis z_3.
$T_4^5 = \begin{bmatrix} \cos\theta_P & -\sin\theta_P & 0 & 0 \\ 0 & 0 & 1 & L_{EG} \\ -\sin\theta_P & \cos\theta_P & 0 & 0 \\ 0 & 0 & 0 & 1 \end{bmatrix}$	**Gimbals- Pitch Angle and Yaw Angle** The pitch angle θ_P and the Yaw Angle θ_Y can be encoded from the two coordinates of the centre position of the gimbals GIM and the centre position of the rectal sphincter RS. (Refer to Figure 5.6, equation 3 and 4)
$T_5^6 = \begin{bmatrix} \sin\theta_Y & \cos\theta_Y & 0 & 0 \\ 0 & 0 & 1 & 0 \\ \cos\theta_Y & -\sin\theta_Y & 0 & 0 \\ 0 & 0 & 0 & 1 \end{bmatrix}$	
$T_6^7 = \begin{bmatrix} 1 & 0 & 0 & L_{GB} \\ 0 & 0 & 1 & 0 \\ 0 & -1 & 0 & 0 \\ 0 & 0 & 0 & 1 \end{bmatrix}$	**Needle Insertion Unit** L_{GB} is the perpendicular distance from the centre of the gimbals GIM to the biopsy needle at point 7.
$T_7^N = \begin{bmatrix} 1 & 0 & 0 & 0 \\ 0 & 1 & 0 & 0 \\ 0 & 0 & 1 & D_F + D_I + L_I \\ 0 & 0 & 0 & 1 \end{bmatrix}$	**Needle Insertion and Triggering Axis** D_I is the needle insertion depth; and L_I corresponds to the distance from 7 to N. As biopsy is either at the stage of "ready to fire" or "fired", D_F has only possible values, i.e. D_F = 22mm or 0mm. Point N is the notch centre of the

Table 5.2: DH transformation matrices for each connected link in the prostate robot

$$T_0^N = \begin{bmatrix} a_1 & a_2 & a_3 & a_4 \\ a_5 & 0 & a_6 & a_7 \\ a_8 & a_9 & a_{10} & a_{11} \\ 0 & 0 & 0 & 1 \end{bmatrix}$$

where

$a_1 = \text{-sin}(\theta_{\text{P}}) \cdot \sin(\theta_{\text{Y}})$,

$a_2 = \text{-cos}(\theta_{\text{P}})$,

$a_3 = \text{-sin}(\theta_{\text{P}}) \cdot cos(\theta_{\text{Y}})$,

$a_4 = -\sin(\theta_P) \cdot \cos(\theta_Y) \cdot (D_F + D_I + L_I)$

$-\sin(\theta_P) \cdot \sin(\theta_Y) \cdot L_{GB} + D_E . \cos(\theta_E) + D_Y + L_Y$

$a_5 = \text{-cos}(\theta_{\text{Y}})$,

$a_6 = sin(\theta_{\text{Y}})$,

$a_7 = \sin(\theta_Y) \cdot (D_F + D_I + L_I) - \cos(\theta_Y) \cdot L_{GB}$

$-(L_{EG} + L_{TH} + D_X + L_X)$,

$a_8 = \text{-cos}(\theta_{\text{P}}).\sin(\theta_{\text{Y}})$,

$a_9 = sin(\theta_{\text{P}})$,

$a_{10} = \cos(\theta_{\text{P}}).\cos(\theta_{\text{Y}})$,

$a_{11} = \cos(\theta_P).\cos(\theta_Y).(D_F + D_I + L_I)$

$+\cos(\theta_p).\sin(\theta_Y).L_{GB} + D_E . \cos(\theta_E) + D_Z + L_Z$

(5.1)

Table 5.3: DH transformation matrices from frame 0 to frame N:

From Figure 5.6(a) (by dot product), we have

$$cos\theta_P = \frac{\left({}^0r_{RS} - {}^0r_{GIM}\right).{}^0r_{YZ}}{|{}^0r_{RS} - {}^0r_{GIM}|.|{}^0r_{YZ}|}$$

, where ${}^0r_{RS} - {}^0r_{GIM} = \begin{bmatrix} b_1 - (D_Y + L_Y + D_E cos\theta_E) \\ b_2 + (D_X + L_X + L_{TH} + L_{EG}) \\ b_3 - (D_Z + L_Z + D_E sin\theta_E) \end{bmatrix}$ and ${}^0r_{YZ}$ is the projection vector of ${}^0r_{RS} - {}^0r_{GIM}$ in Y_0Z_0 plane in frame 0, i.e. ${}^0r_{YZ} = \begin{bmatrix} 0 \\ b_2 + (D_X + L_X + L_{TH} + L_{EG}) \\ b_3 - (D_Z + L_Z + D_E sin\theta_E) \end{bmatrix}$.

From Figure 5.6(b) (by dot product), we have

$$cos\left(\alpha - \theta_Y\right) = \frac{\left({}^0r_{RS} - {}^0r_{GIM}\right).{}^0r_{XZ}}{|{}^0r_{RS} - {}^0r_{GIM}|\,|{}^0r_{XZ}|}$$

,where ${}^0r_{XZ}$ is the projection vector of ${}^0r_{RS} - {}^0r_{GIM}$ in X_0Z_0 plane in frame 0, i.e. ${}^0r_{XZ} = \begin{bmatrix} b_1 - (D_Y + L_Y + D_E cos\theta_E) \\ 0 \\ b_3 - (D_Z + L_Z + D_E sin\theta_E) \end{bmatrix}$ and $\alpha = sin^{-1}\left(\frac{L_{GB}}{|{}^0r_{RS} - {}^0r_{GIM}|}\right)$.

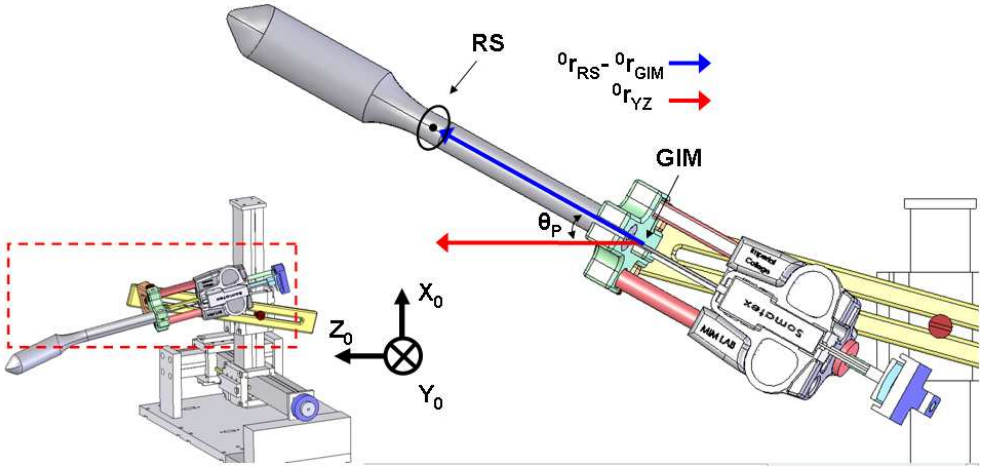
5.4.2 Robot-Scanner Registration

Point-to-point Registration

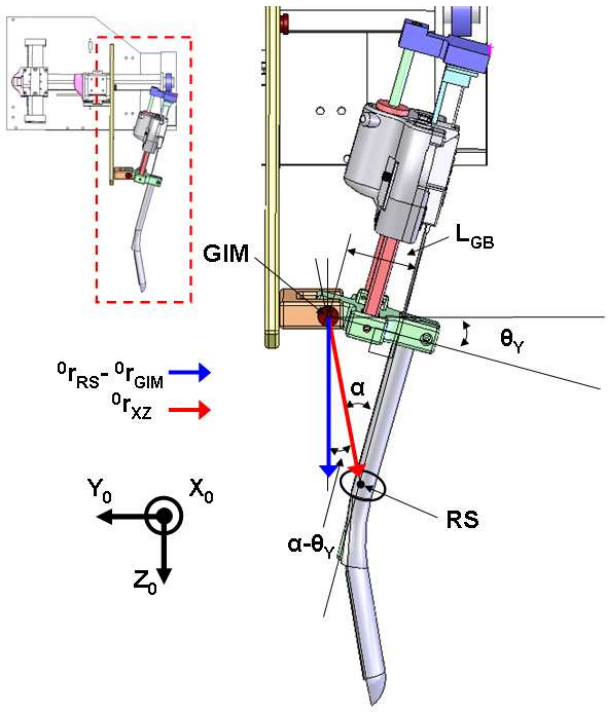
Registration is a mapping operation to transform the coordinate system of one object from one space into another space, which is an important technique in image-guided interventions to relate the scanner base frame into the robot base frame. In the case of the prostate biopsy robot, the coordinates of the suspected target and the centre of the rectal sphincter are obtained from the MRI images, and transformed from the scanner frame S into the robot base frame 0, where the frame S corresponds to the data point and coordinate system used in the scanner measured from the isocentre; The rectal sphincter and target position are then represented in the robot base frame 0 and are used for calculation of forward and inverse kinematics. The equation governing the transformation from the scanner frame to the robot base frame can be expressed as:

$${}^0r = T_0^S.{}^Sr \tag{5.2}$$

where T_0^S is a 4×4 transformation matrix from scanner base to robot base; ${}^Sr$ is the point concerned in the scanner frame, and ${}^0r$ is the corresponding coordinate in robot base frame 0. To compute the transformation matrix T_0^S, a minimum number of 3 points, which are not collinear, are required to be measured in both frames. Algorithms are found in literature for the point-to-point registration, and toolboxes for registration are available in research software, such as Matlab® [Birkfellner, 2001, Friston, 1995]. The scanner-robot registration was performed with the use of Matlab® and LabView® based on the registration method of least-squares fitting of two 3-D point sets by Arun and Horn [Arun KS, 1987, Horn, 1987]. As shown in Figure 5.7, three passive fiducial markers were embedded in the



(a)



(b)

Figure 5.6: (a) Side view and (b) top view of the gimbals, showing the geometric relationship between the pitch angle θ_P, the yaw Angle θ_Y of the gimbals, the centre of the gimbals, and the position of the rectal sphincter.

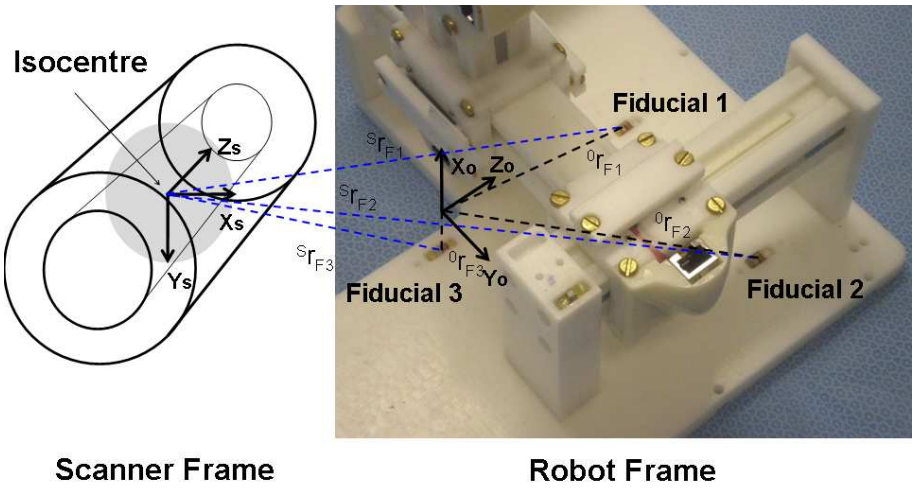


Figure 5.7: Three passive fiducial markers were embedded in the robot base for registration. The process for registration involves localisation of the markers in scanner coordinates and maps the points to the robot coordinates which were pre-obtained with the use of Microscribe®, a digital measurement device with a maximum error of 0.05mm.

robot base and were localised with a modified 2D FLASH sequence in the scanner frame, and their coordinates in the robot frame were measured with Microscribe®, a digital measurement device with a maximum error of 0.05mm.

Passive Fiducial Marker

A passive marker is a source of MR signals, commonly made from a piece of material which can appear bright in the image, and localisation is achieved with an image processing technique and does not necessitate the use of any additional hardware or post-processing steps. Contrast agents and susceptibility artifacts produced by materials are commonly used in passive markers to generate a spot in the image that appears brighter than the background.

In the case of the robot-scanner registration, three passive fiducial markers were placed within the robot base and their MR signals were more intense when compared with the plastic robot which appeared as a dark area, as no signal is generated from plastic materials (Figure 5.8), therefore it would not be a problem to obtain good contrast to visualise the markers. For the fiducial marker design, Spenco® was chosen as the signal generating material, due to its MR properties being similar to water but with a solid/gel texture and so more easily adapted. The Spenco® was placed in a micro coil connected with a capacitor, which acted as an inductor-capacitor (LC) circuit and was tuned to resonate at 63.6MHz. The micro coil made from 0.46mm enamelled wire with a hand-wound 6 turns was equivalent to an inductance of 55nH, and was soldered to a small piece of stripboard with a non-magnetic capacitor of 110pF connected, as illustrated in Figure 5.9. As Spenco® dries out within a few hours and it is important to maintain the moisture of the signal generating material, the Spenco® was sealed by resin glue in the coil once it was fine tuned with the network analyser.

This work of fiducial marker design was completed at the Radiological Science Unit, Charing Cross Hospital, London, U.K. The fiducial marker and a modified FLASH 2D image sequence particularly

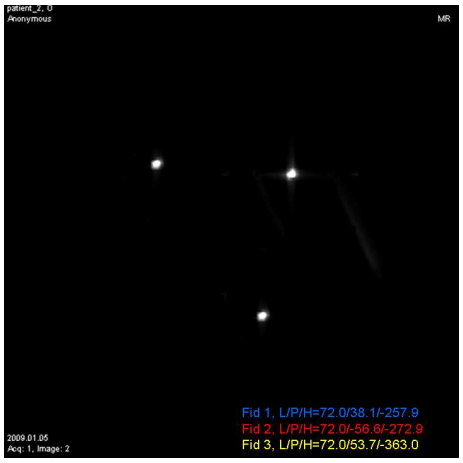


Figure 5.8: MR image of the three fiducial markers localised for registration. A modified 2D sequence was adapted to process the coordinates with accuracy of 0.2mm [Rea, 2008].

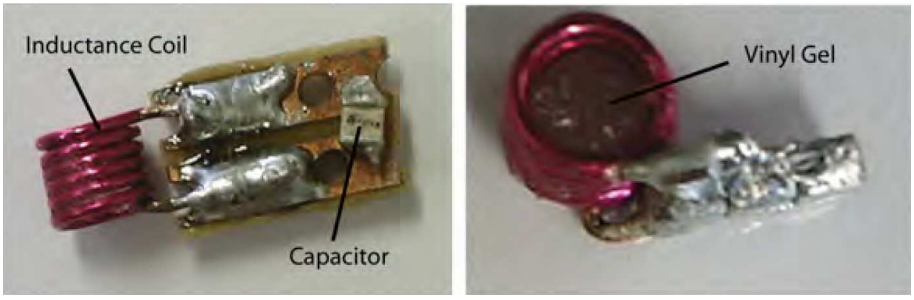


Figure 5.9: A 3mm×3mm fiducial micro-coil marker with Spenco® embedded as a signal generating material. The LC circuit was tuned to resonate at 63.6MHz.

designed for fiducial tracking and localisation were developed by that research group. A detailed description of the developed tracking method is beyond the scope of this thesis, and readers who are interested are recommended to refer to a published paper by Marc Rea, the physicist on the team [Rea, 2008].

5.4.3 Inverse Kinematics

Forward kinematic problems of determining the position and orientation of the end effector relative to the base, as a function of given link values, were considered in the previous section. Here inverse kinematic problems of the prostate biopsy robot are considered, to determine a particular set of link values that will produce a known and desired end effector configuration. As these types of problems, in common with other inverse kinematic problems, generally involve solving of nonlinear multi-variable equations, they contain the questions of existence, uniqueness, and the methods used to solve the equations. However, the inverse kinematic problem involved in the prostate robot is relatively simple, as the target point and the centre of the rectal sphincter govern the orientation and position of the biopsy needle, therefore the solution must be unique, and is either in the range of the robot joint, or out of the range (meaning that it is geometrically unachievable in reality and repositioning of the robot is required).

The inverse kinematics of the prostate robot is handled with the use of Matlab®, in which the target point ${}^{S}r_{Target}$ in the scanner frame is localised manually by our radiologist, and its corresponding coordinate of ${}^{0}r_{Target}$ in the robot base is solved, given that T_0^S in Equation (5.2) is known after the scanner-robot registration. Therefore, we have:

$$ {}^{0}r_{Target} = T_0^S . {}^{S}r_{Target} \tag{5.3} $$

${}^{0}r_{Target}$ can be calculated from Equation (5.3) and after that, the joint movement D_X, D_Y and D_Z can be calculated from Equation (5.1).

5.4.4 Workspace Analysis

The workspace of a robot is the space which the end effector can access when considering all possible motions that the joints can execute. This space is governed by the robot kinematic design, and is obtained by solving the forward kinematics of the robot for every single possible joint value. In the case of the prostate biopsy robot, an important constraint was added to the workspace analysis, that is, the movement space available to the robot. As shown in Figure 5.1, the space available is the area of the scanner bore minus the space taken up by the patient, and is approximately the volume shown as dotted lines in the figure. In the workspace analysis, the robot movement should be considered and if it is outside the volume boundary, the corresponding workspace overlies the scanner bore, and hence is not achievable in reality.

The robot workspace varies depending on how the patient is positioned, where the centre of the rectal sphincter is (as the entrance point of the endorectal probe), and where the robot is placed correspondingly. Clinical data from a patient for prostate biopsy was used in our workspace analysis to describe the space occupied by a patient in the scanner, so that a CAD model can be developed

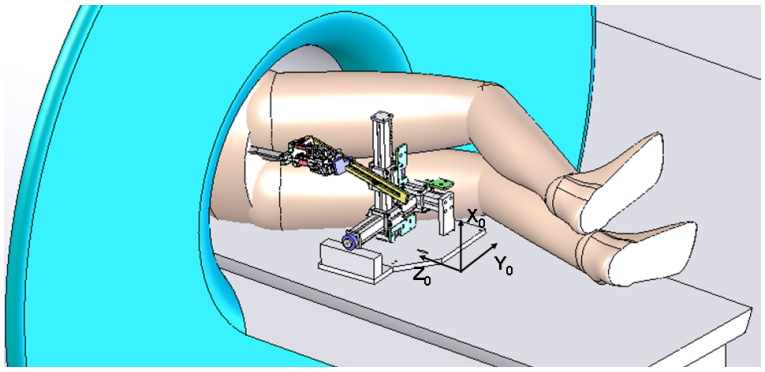
representing the actual location of the robot and the patient as shown in Figure 5.10(a). Workspace analysis was implemented in Matlab®, in which the centre of the rectal sphincter was located at a normal distance of 120mm from the gimbals. Figure 5.10(b) and (c) presents the biopsy needle sampling workspace, where the size of the patient prostate (38mm×42mm×53mm) was obtain from the MR image, and was 102 mm away from the sphincter centre in Z_0 direction of the robot, 39 mm in Y_0 direction, and its height was 112mm from the isocentre (Data were measured from MR images of the patient). For the given kinematic design of the robot, the whole area of the prostate is covered by the workspace, showing the capability of the robot to cover all the potential prostate area for biopsy in the current configuration. For reason of clarity, only the contour of the needle notch and the contour of the needle firing unit are illustrated in the diagram.

The workspace analysis presented here acts as a measure which can enable a quick visualisation of the workspace that the prostate robot can achieve on a particular position of the patient and on a particular robot setup. However, it does not assure the end effector capable of reaching the target in all cases. Testing the workspace with a specific patient and robot setup before a biopsy is the only way to absolutely demonstrate if the target point is accessible by the robot. In any case, workspace analyses were performed in the biopsy patients in the clinical trials to realise the workspace of the robot, and most of their biopsy targets were within the accessible area.

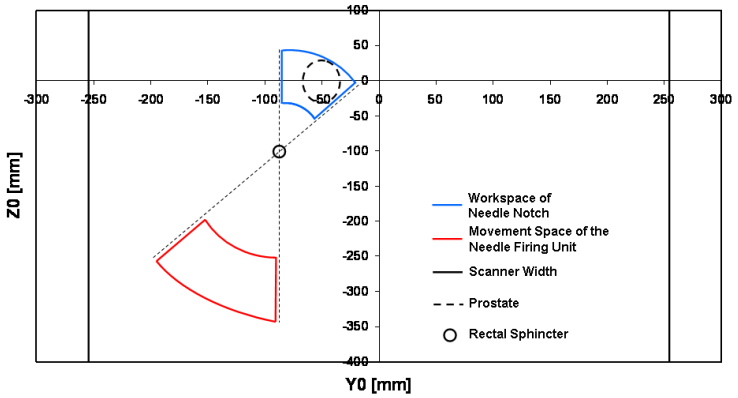
The workspace analysis has also indicated two practical considerations of about how the patient position affects the workspace during clinical trials.

1. A patient with a relatively large prostate (e.g prostate infection and inflammation) in which the biopsy target is at the far anterior side ($+Y_0$ direction) may cause difficulty in the biopsy procedure, as the rear end of the biopsy needle is placed very posteriorly ($-Y_0$ direction)) and may potentially collide with the scanner bore (Figure 5.11). In this case, the patient needs to be positioned in such a way that his body is placed away from the scanner's central axis, towards his anterior side ($+Y_0$ direction) to allow more movement space to be available for the robot. However this approach can be inhibited if the patient has a relatively large thigh, which would limit the degree of possible movement to the anterior side ($+Y_0$ direction) before his knee collides with the scanner bore.

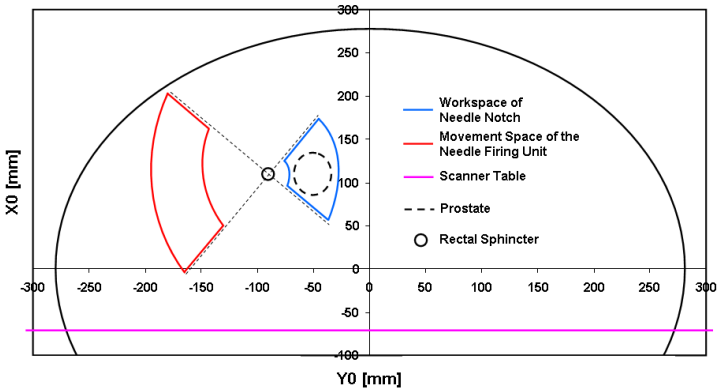
2. A patient with a small hip has his rectal sphincter at a lower position relative to the scanner table when he is in lateral decubitus position, and the rear end of the biopsy needle may collide with the scanner table if a higher region is targeted (Figure 5.12). In this situation, the patient should be setup on the scanner table with his hip lifted up by a cushion, so that his rectal sphincter is high enough to prevent the collision between the scanner table and the rear end of the biopsy needle. An alternative solution is to remove the spinal coil and have the patient body supported by a body cushion. The spinal coil is normally embedded into the slot of 40mm depth that is built into the scanner table (e.g a Siemens 1.5T MAGNETOM Avanto scanner), and it is removable if necessary to provide extra space for robot movement.



(a)



(b)



(c)

Figure 5.10: (a) CAD model of the prostate biopsy robot placed according to the position of the patient. Workspace analysis of the prostate robot in (b) Y_0Z_0 and (c) X_0Z_0 plane (robot frame 0). The contour of the needle notch workspace is presented in blue, showing the space covering the whole prostate.

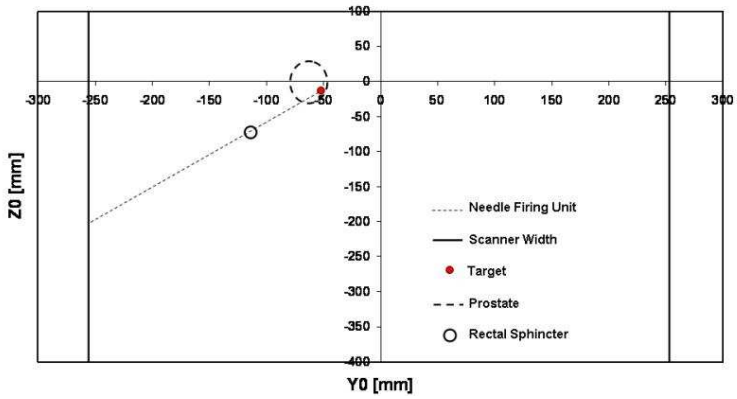


Figure 5.11: Potential workspace constraint of the prostate robot: patient with the biopsy target at the far anterior side ($+Y_0$ direction).

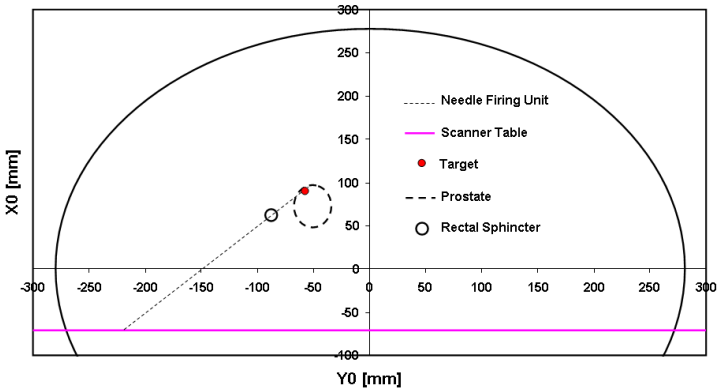
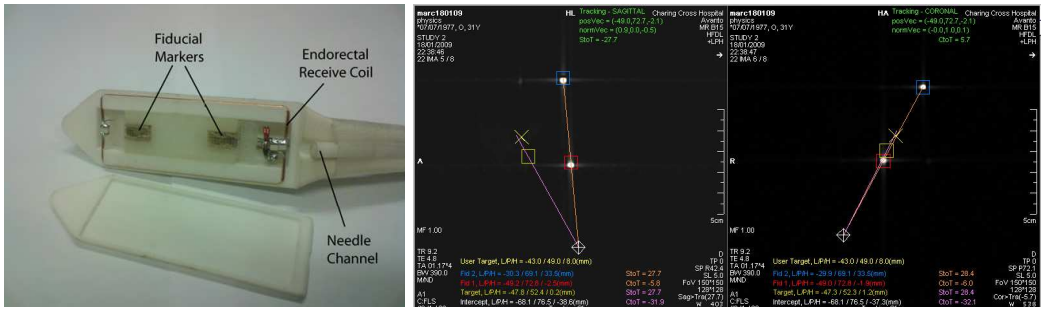


Figure 5.12: Potential workspace constraint of the prostate robot: patient with a small hip and therefore with his rectal sphincter at a lower position.



(a) (b)

Figure 5.13: (a) Endorectal probe with a receive coil and two fiducial markers embedded. (b) Fiducial markers appear as bright points in the MR image for localisation of the position of the biopsy needle notch (yellow box).

5.4.5 Real-Time Tracking

To monitor the orientation of the needle, two passive fiducial markers were embedded in the terminal part of the endorectal probe as illustrated in Figure 5.13, and the positions of the markers formed a fixed geometric relationship to the position of the biopsy needle notch where prostate tissue will be sampled. Therefore, tracking of the two fiducial markers can provide localisation of the needle notch for needle alignment. The endorectal probe was designed in Solidworks®, a CAD software and fabricated with rapid prototyping, and an endorectal receive coil was embedded to enhance prostate image quality. This receive coil and the fiducial marker designs were completed at the Radiological Science Unit, Charing Cross Hospital Unit, London, U.K.

5.5 Engineering Design

5.5.1 Cartesian Robot

The strong static magnetic field in the scanner leads to a large attractive force on ferromagnetic materials and the switched gradients and RF fields induces eddy currents on conductive materials. In consequence, development of an MRI compatible mechatronic system equates to a large amount of work in hardware design. Standardisation of key MR compatible components can save time and simplify the robot design. Therefore, a 1DOF robotic module was designed in which an MRI compatible position encoder and a pneumatic motor as described in Chapter 3, were embedded for implementation of the closed-loop position control. The dimensions of the module can be varied and the modules themselves can be connected together to form a multi DOF MR robot for positioning in different applications. A Cartesian MRI compatible robot is formulated by the combination of three of the modules (Figure 5.14(a) and (b)), and is coupled to a haptic needle firing unit linked by gimbals and an extension arm as illustration in Figure 5.14(c). Figure 5.15 shows the side view and top view of the prostate robot mounted onto a scanner table.

To ensure the MR compatibility of the system, Delrin® and Ertalon® materials were selected for the body and components were joined with nylon screws. The performance of the selected optical

encoders, pneumatic air motors, and their control were mentioned in terms of their MR compatibility in Chapter 3, and their specifications and control in Chapter 4. The MRI compatibility issue of newly developed devices can be roughly estimated in the preliminary design process with the standardised components, even though the MR compatibility of each medical robotic system is still required to be quantified before being used.

5.5.2 Haptic Needle Firing Unit

Needle Firing Unit

Imaged guided interventions in a conventional closed bore scanner impose a necessary separation distance between the tissue of interest and the workspace accessible by a clinician. This spatial restriction limits tactile information during the procedure. Force feedback is important in percutaneous therapy, and therefore a haptic needle firing unit and a force feedback control interface were designed to retrieve touch sense information during prostate biopsies, with the intention that the clinician performs the insertion with a hardware control interface to reconstruct the sense of touch. Both parts were built with the MR compatible force sensors, encoders and ultrasonic motors mentioned in Chapter 3, of which the performance characteristics and the control strategies were discussed in detail in Chapter 4.

The needle firing unit was developed to be integrated with the Cartesian robot, and a CAD drawing of the haptic unit is shown in Figure 5.16, which comprises of: (i) a biopsy needle housing design, (ii) a pair of force sensors for measurement of insertion and retraction of the needle, (iii) a linear encoder for position tracking, (iv) ultrasonic motors for actuation, and (v) a plastic linear rail guide. The needle mount was manufactured by rapid prototyping according to the shape and the size of the needle and the rest of structural components are made from Delrin® and Ertalon® connected with Nylon screws.

Hardware Control Interface

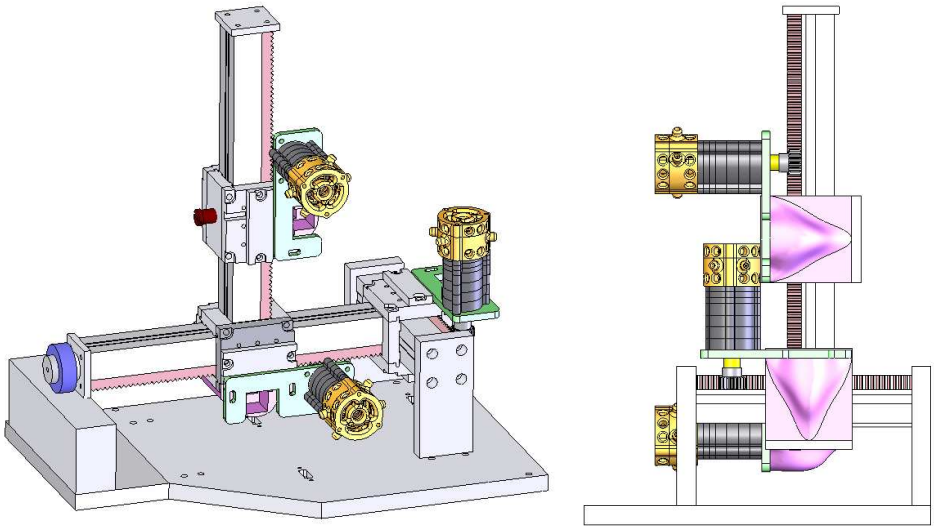
The haptic control interface was designed to be MRI compatible to allow clinicians to operate the biopsy robot from within the scanner room, providing them with the best accessibility to the patient. During needle puncturing, the user controls the insertion depth by adjusting the control pad of the interface, and it correspondingly, reproduces in real time, the amount of force measured by the force sensors during needle movement, giving a sense of piercing tissue, as it would be felt if performed by free hand.

The specification and control strategy of the haptic needle firing unit and the hardware control interface has been presented in Section 4.3 in Chapter 4, and part of the haptic unit design has been published in a journal paper [Tse, 2009].

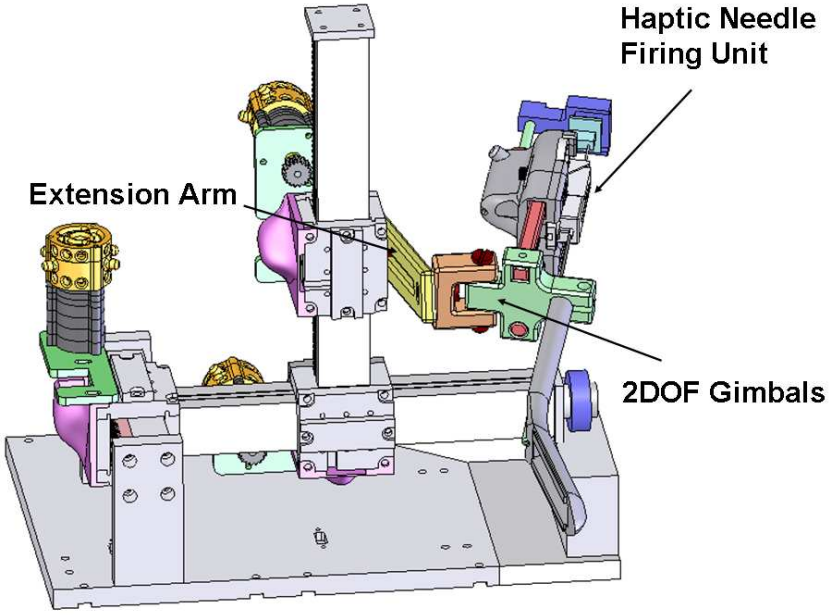
5.6 System Electronics

5.6.1 Faraday Cage

The biopsy robot together with its control system, was designed to usable in the scanner room, and thus all supporting electronics were placed in a shielded Faraday enclosure to electromagnetically isolate

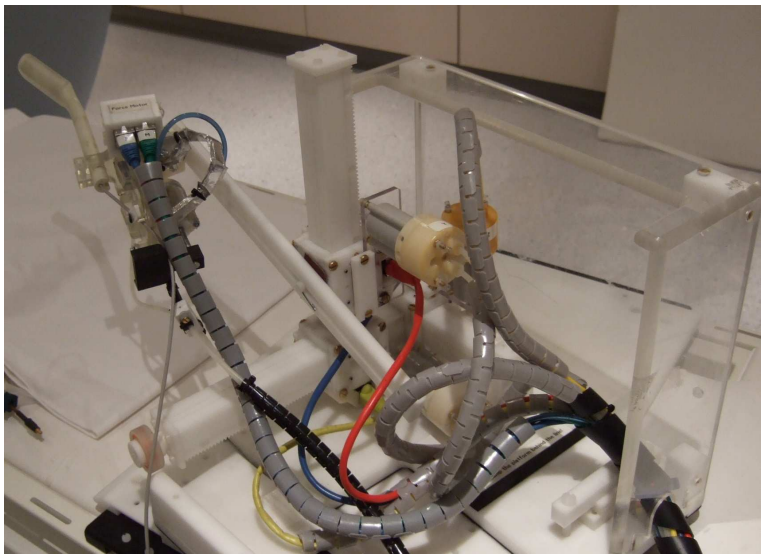


(a) (b)

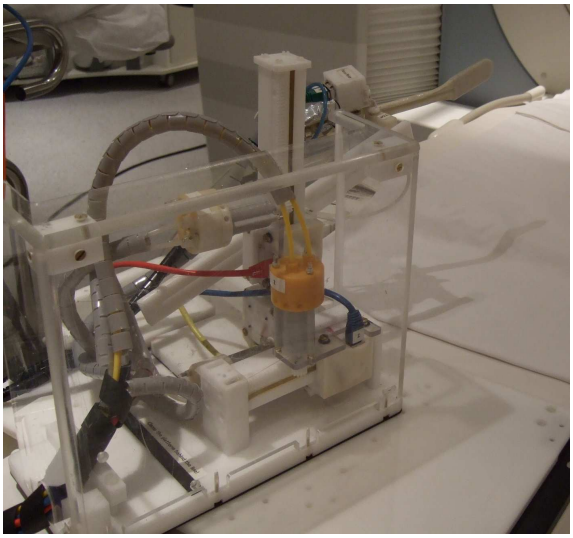


(c)

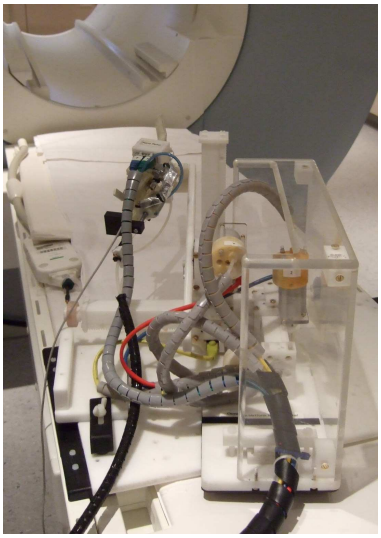
Figure 5.14: (a) A Cartesian robot formulated by interconnecting three modules. Each module is incorperated with a rack and pinion mechanism, a pneumatic air motor and an optical encoder. (b) Its side view. (c) The robot integrated with a haptic needle firing mechanism for transrectal prostate biopsy which is linked with the use of gimbals and an extension arm.



(a)

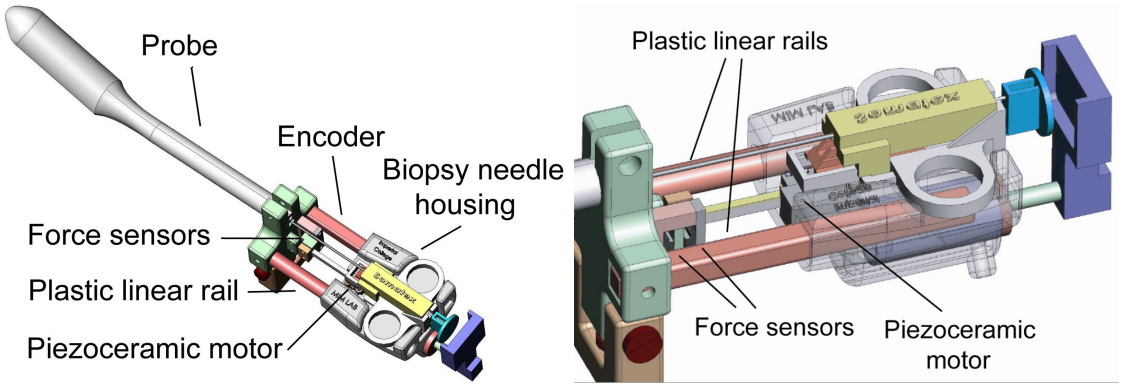


(b)



(c)

Figure 5.15: The side view (a) and (b), and the top view (c) of the prostate biopsy robot mounted onto the scanner table.



(a) (b)

Figure 5.16: (a) CAD model of the haptic unit carrying a biopsy needle coupled with an endorectal probe. (b) Its zoom view: a pair of force sensors embedded for force measurement in two directions for push and pull. The biopsy needle mounted on the needle housing is moved by the ultrasonic motor along the plastic linear rails.

the EM noise source from the scanner. The Faraday cage, which comprises of a shielded aluminium enclosure, is placed 2m from the scanner bore entrance and connected to the ground of the scanner room. All electrical cables linking to the biopsy robot and the hardware control interface from the aluminium enclosure are filtered and shielded. Inside the enclosure is: (i) an FPGA processor (NI CompactRIO 9004) with haptic control and robot position control implemented, (ii) pneumatic motor and ultrasonic motor drives, (iii) signal filtering and amplification circuits for the force sensors , (iv) AC/DC medical standard power supply, (v) touch screen PC to display real-time MR tracking images and graphical user interface for the prostate robot, and (vi) an ethernet-optical signal converter for the touch screen PC to communicate with and receive images from the host computer in the control room. Figure 5.17 illustrates the electronics within the enclosure and Figure 5.18(a) shows its setup in the scanner room.

5.6.2 Touch Screen Control PC

A PC (Intel Pentium M, 400MHz, 1GB RAM, Windows XP) interface integrated to a 15inch touch screen for graphical display and user input was embedded in the Faraday cage. The PC executes programmes and stores data in a flash disk drive, as preliminary experiments reported that the use of a PC with a conventional magnetic principle based hard disk drive, which stores digitally encoded data on rapidly rotating platters with magnetic surfaces, can potentially interfere with the main field resulting in the loss of stored data. The PC incorporates two Ethernet plugs, one for communication to the FPGA processor and the other for image transmission and remote control of the host computer. The large aluminium enclosure contains an aperture within which the touch screen was mounted as shown in Figure 5.18 and which was covered by conductive transparent sheets connected to the ground of the enclosure to avoid RF leakage from the electronics. The power supply of the PC was placed in an individual shielded enclosure to avoid EM noise emission. The PC was installed with an application executable file which was programmed based on LabView® and Matlab® to provide a graphical user

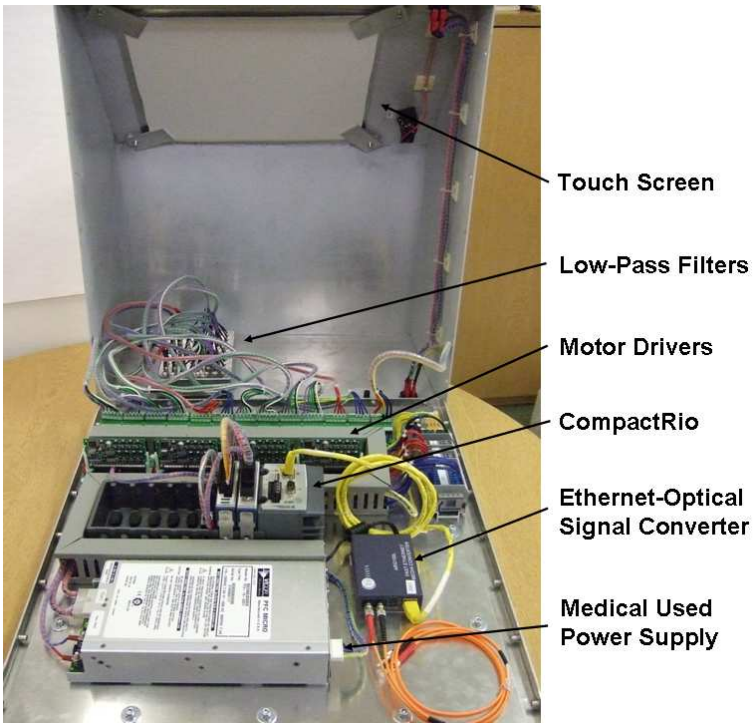
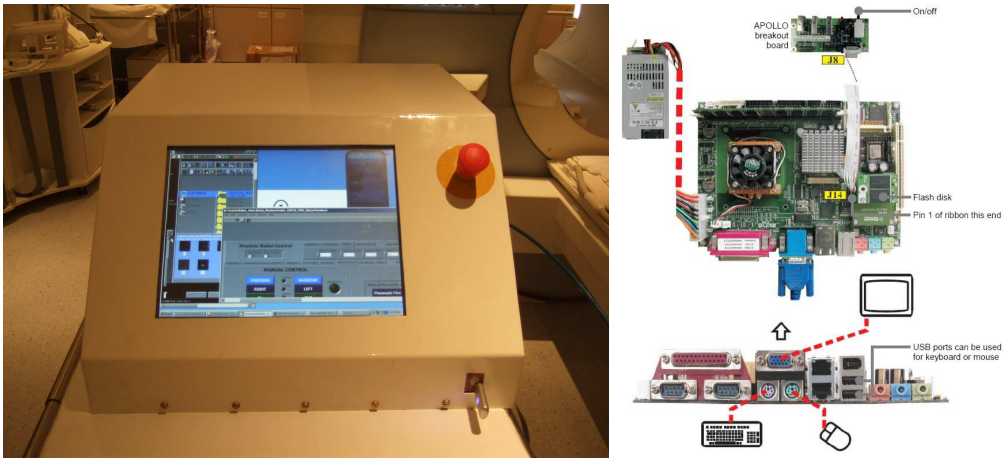


Figure 5.17: Electronics components used within the aluminium enclosure.

interface for the robot control, an image tracking display, and to solve the kinematics of the robot.

5.7 Scanner, Robot and Control PC Communications

The prostate biopsy robot was connected to the control hardware in the Faraday cage via standard shielded Ethernet cables for motor and encoder signal transmission, and pneumatic pipes for airflow supply (Figure 5.19(a)). Every signal cable was properly shielded and low-pass filters with cut-off frequencies of 64MHz were implemented to suppress RF noise picked up from the scanner (Figure 5.19(b)). The control PC in the Faraday cage was connected to a host computer in the control room to allow our radiologist to control the scanner during the procedure, and to allow image transfer. Preliminary experiments showed that the scanner is very sensitive to electrical cables passing from the control room to the scanner room, as the cables act as antennas for stray RF outside the scanner room and the EM noise is then picked up by the RF receive coils in the scanner. Therefore, the connection between the control PC and the scanner host computer was achieved using a TCP/IP protocol over a fiber optic cable (TF - STST62DOR10, ST Duplex Multimode) and an optical converter (ARG100LM/ST2, Techaya), as shown in Figure 5.19(c).



(a) (b)

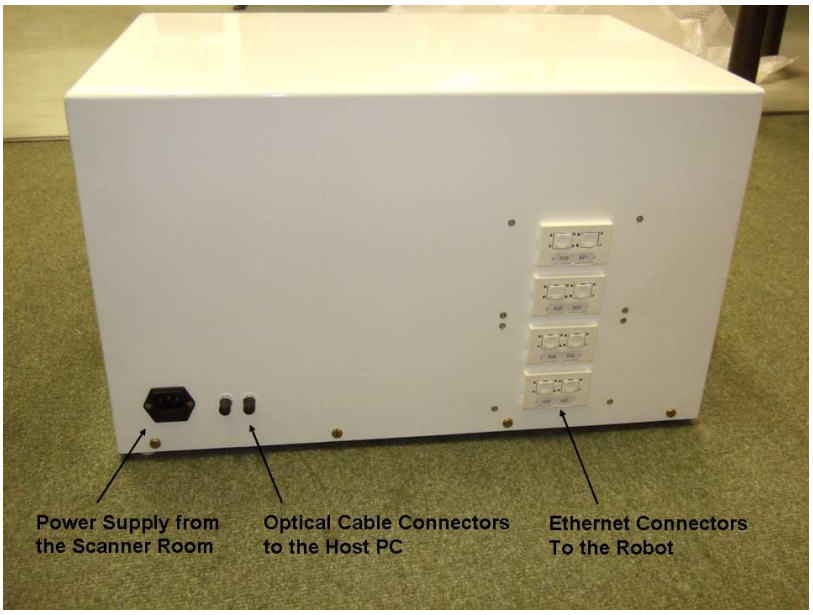
Figure 5.18: (a) 15inch touch screen for graphic user interface in the aluminum enclosure for the image tracking display and robot control interface, and (b) the flash disk PC embedded.

5.8 Conclusion

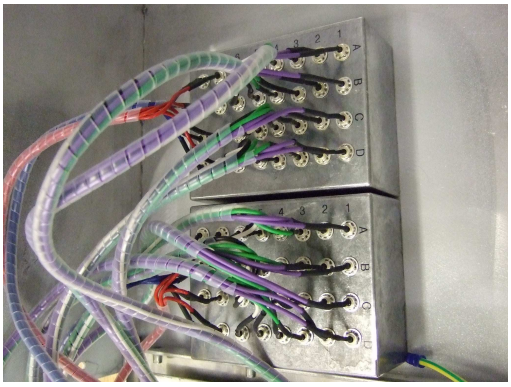
To make use of the benefits of the high image resolution from MRI for image guidance, a transrectal prostate biopsy robot has been developed. The design guidelines and specifications were first introduced in the chapter in the aspects of the required level of MR compatibility, the required robot kinematics, the robot workspace, the spatial availability for movement, and the robot control. Following this was a thorough kinematic analysis based on the Denavit Hartenberg coordinate transformation of the proposed robot, which includes the issue of forward and inverse kinematics, the robot-scanner registration, workspace analysis, precautions for patients with extreme sizes and image tracking.

After that, the mechanical design of the proposed prostate biopsy robot was presented with the use of proven MR compatible actuators and sensors as evaluated in Chapter 3, although a test must be conducted to evaluate its compatibility as a whole system. The biopsy system consists of a Cartesian positioning robot based on a modular design, with a pneumatic motor and position encoder embedded on each axis, and a haptic needle firing unit for reconstruction of the sense of touch during the needle procedure. The needle firing unit is connected to the Cartesian robot using gimbals and an extension arm, allowing the biopsy needle to be placed in the rectum, and to have the necessary DOF for movements. The needle can be inserted, fired and retracted in a short time once its alignment has been confirmed. The needle firing unit incorporates haptic force feedback, and allows reconstruction of the sense of touch to the user manipulating the needle insertion with a hardware control interface. This unit has proven the concept of applying haptics in MR-guided interventions. The haptic unit developed here has been used to insert a biopsy needle, but other functionalities are possible depending on the needs of surgical interventions [Starkie, 2001, Jakopec, 2001, Rossi, 2005].

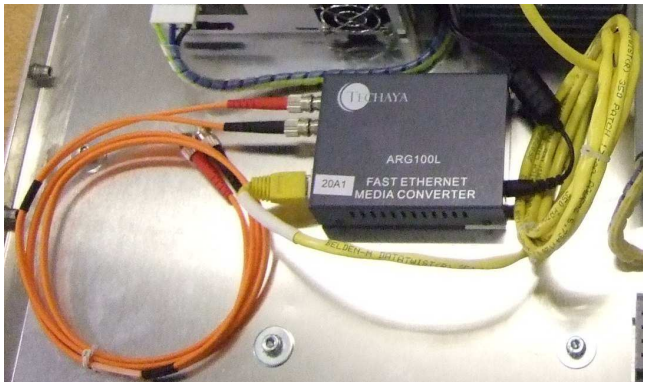
Electronics supporting the biopsy robot have been discussed, along with the use of shielding, earthing, filtering and application of a Faraday cage for electromagnetic insulation from the scanner fields. A touch screen control PC with a flash disk drive was adapted for image display and graphic



(a)



(b)



(c)

Figure 5.19: Standard shielded Ethernet cables connecting the robot to its supporting electronics in the control enclosure (Faraday cage) and the signals pass though a group of low-pass filter with cut-off frequency of 64MHz to suppress the RF interference. (a) Back view of the control enclosure showing the electrical and optical cables connectors. (b) Low-pass filter group. (c) Ethernet optical signal converter connecting the control PC in the enclosure to the host PC in the control room.

user interface. The system communication between the scanner, robot and control PC has also be investigated with the use of optical fibre and shielded Ethernet cables.

Chapter 6

Evaluation and Clinical Experience of the Prostate System

6.1 Introduction

The kinematic analysis, and the mechanical and electrical design of the prostate biopsy robot have been reported in Chapter 5. The workspace analysis demonstrated that the robot is capable of driving the end effector to target any point within a prostate, although it is also subject to the size of the patient. In this chapter, the MR compatibility of the whole system, including the control enclosure, is presented in terms of the SNR reduction it leads to when the whole system is introduced into the scanner room. Two approaches for users to control the robot and align the biopsy needle towards the suspected tumour target, i.e. auto and manual needle alignment, are presented. Subsequently, clinical trials on three recruited patients, undertaken at the Royal Marsden Hospital in Surrey are reported, where the system was implemented for MR guided transrectal prostate biopsy to demonstrate its functionality. The results reported that the needle alignment accuracy of the robot was 9.7mm on average with around 40mins taken for the procedure, and the patients did not report any discomfort, which fulfills the previous system specifications. The trial procedures, results and an evaluation of the robot design are discussed in detail.

6.2 MR Compatibility of the System

MRI compatibility tests were performed with the prostate biopsy robot placed in the imaging volume and connected to the control enclosure located 2m away from the scanner entrance; the setup to be applied during clinical trials. The purpose of this test was to quantify the SNR reduction caused by the introduction of the whole system. It was necessary to carry out this further SNR reduction test due to the additional introduction of the electrical devices within the control enclosure, although all the core components of the robot were already tested for compatibility, as reported in Chapter 3. The test was conducted in a 1.5T Siemens MAGNETOM Avanto scanner with the same settings of imaging sequences described in Table 3.3 and the same procedure described in Table 3.2 in Chapter 3. The

	TSE			True FISP		
	Power off	Power on	Actuated	Power off	Power on	Actuated
SNR Reduction	0.11%	5.2%	9.6%	0.10%	5.1%	8.1%

Table 6.1: SNR degradation under different test conditions

robot was placed next to a phantom filled with $CuSO_4$ solution which generated MR signals during scans. The image sequences used to test the robot were both TSE and True FISP. TSE stands for Turbo Spin Echo, and is a variation of spin echo image sequence, and has a rather short scan time [McRobbie, 2003]. True FISP stands for True Fast Imaging with Steady-state Precession, which is a gradient echo image sequence with balanced rewinding gradients [McRobbie, 2003].

As the force sensor was the only ferromagnetic material used in the robot and its maximum generated artifact was qualified to be 42mm, the artifact test was not required to be repeated. As long as the artifact of the force sensor does not overlie the region of interest, it will not produce a noticeable distortion within the image. With respect to the SNR reduction test, the SNR of an image with the whole system introduced along side the phantom was compared to that of the image without the system, to quantify the interference. The definition of SNR used is the ratio between the mean signal in the 40×40 pixel region in the centre of the phantom on the image, and the standard deviation of the signal in the 40x40 pixel region at the top left corner of the image (as explained in Chapter 3).

To test the variation of the SNR produced by the whole system, it was tested under various conditions: no power, powered with no actuation, and fully actuated. The test results are listed in Table 6.1, in which the SNR of the images with the system were compared to that of with the phantom alone, and the reduction in SNR was calculated as a percentage. The results indicated that the maximum SNR reduction due to the introduction of the system is 9.6% in TSE and 8.1% in True FISP, and the amount of image degradation does not affect the biopsy procedure.

6.3 User Control

Needle alignment in the prostate biopsy is achieved by cooperative joint movements of the robot calculated from the inverse kinematics. The joint movements are separated into two schemes: (i) auto needle alignment for gross positioning and (ii) manual needle alignment for fine positioning to correct the target error between the predefined target point and the biopsy projection position. With the use of kinematics only for the joint movement calculation, the first approach can only bring the needle notch near to the target, due to imperfect localisation of the rectal sphincter location and its deformation during the endorectal probe movement. However, the approach is good enough for gross positioning, and the procedure will be followed by manual needle alignment (the second scheme) with the use of real-time image display plus kinematics to correct the target error.

6.3.1 Auto Needle Alignment

Trajectory planning in the prostate robot is a specification of the desired, time-dependent paths of the needle notch in the workspace of the robot and is related to optimisation of patient's comfort and safety. The robot movement must not be hazardous to the patient, and actions such as stretching and rubbing of the patient rectum wall by the endorectal probe are invasive and avoidable. Also, it is preferable that the trajectory produces only minimal tissue deformation during the robot movement.

The rectal wall is a sensitive soft tissue and it is easy to cause bleeding by rubbing and stretching; this commonly happens to patients undergoing ultrasound guided prostate biopsy. Furthermore, applying shear stress to the rectum wall can deform the prostate, meaning that the target point is shifted to the deformed location and resulting in the reduced accuracy of the biopsy. To minimise rubbing of the rectum wall and deformation of the prostate during the endorectal probe movement, each axis in the robot is actuated sequentially following the scheme below:

1. The probe is inserted manually, set in an orientation such that it does not stress any particular direction of the rectum, and then attached to the prostate device. This can minimise the friction exerted on the tissue when the robot moves the probe in and out.

2. The Z module of the robot, which governs a large amount of inward/outward movement of the probe in the rectum as illustrated in Figure 6.1, is first actuated to D_Z, where $\begin{bmatrix} D_X & D_Y & D_Z \end{bmatrix}$ is the joint movement in the each Cartesian axis computed by inverse kinematics such that the needle notch is targeting the target point of ${}^{S}r_{Target}$.

3. The Y module of the robot, which governs a large amount of the pitch direction movement of the probe, is actuated to D_Y after the Z axis. Then lastly, the X axis, which largely governs the yaw direction movement, is actuated to D_X. It is because the probe is designed with a large rectangular endorectal coil embedded which forms a large surface area facing the anterior direction, that rubbing of the rectum surface and compression can be minimised when the X axis is kept to be actuated last. A schematic diagram illustrating the sequence of the actuation axes is shown in Figure 6.1.

4. A scan is taken to confirm that the needle projection is aligned closely to the target. If the target point is shifted significantly due to tissue deformation, steps (1) to (3) are repeated with the newly selected target point until the needle is well aligned. This procedure may take a few iterations, and the deformation is subject to the stiffness, size and geometry of the prostate and the rectum, as well as the location of the suspected target relative to the prostate. If the needle alignment is close enough to the defined target point, the manual needle alignment is then applied by the user to bring the needle alignment further closer to the target.

6.3.2 Manual Needle Alignment

There are two assumptions in the kinematics calculation: (i) the pivot point is approximately the centre of the patient's rectal sphincter. Yet it is supported by the rectal sphincter which is actually a ring of muscle in a shape of a tube, (ii) the pivot is approximately a fixed point. When the robot is actuated, the pivot point of the endorectal probe changes due to deformation of the rectal sphincter

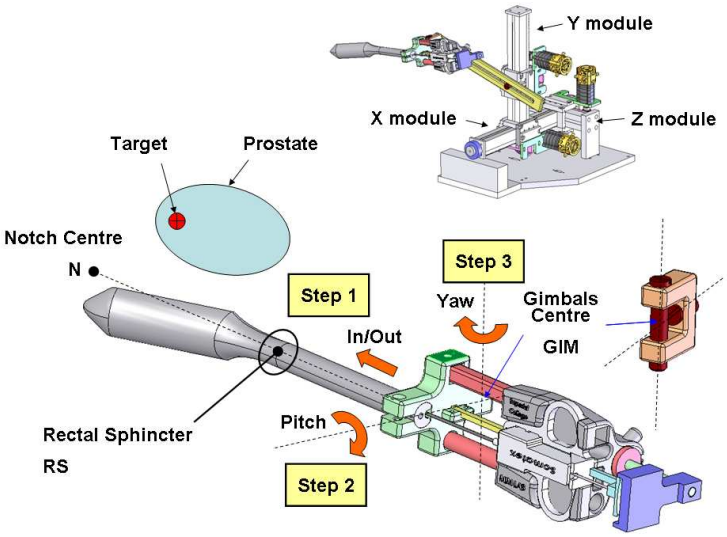


Figure 6.1: The movement sequence of the prostate biopsy: in/out direction (Z module), pitch direction (Y module), and yaw direction (X module) to minimise friction exerted to the rectum wall and to reduce prostate deformation caused by the endorectal probe.

in reality. Although these are the necessary two assumptions to be made in order to work out the forward and inverse kinematics of the robot, these are also the source of errors in the needle targeting. Manual control is an additional and essential step to correct the error, and to bring the needle into a good alignment with the target point, after gross positioning is achieved by auto targeting according to the joint movements derived from the inverse kinematic calculation.

Manual control is basically required to move the end effector a small incremental distance along the pitch and yaw direction, where the probe movement is tracked by fiducial markers. To allow the user to perform the in-plane movement of the biopsy needle, three situations are considered.

1. Angular movement in the yaw direction:
   The biopsy needle is able to move at an incremental angle in the yaw direction of the robot gimbals. The needle performs angular movement about the rectal sphincter and is aligned manually by the user who sets which side in the yaw direction and how far the needle should move. As the current position of the needle notch is known from encoders and forward kinematics, the new target point is defined as ϕ_Y degree away from the current position (refer to Figure 6.2(a)), and with inverse kinematics, the joint movements are determined for the new target position. The new target point ${}^0r_{Target}$is calculated as follows:

$$ {}^0r_{Target} = \begin{bmatrix} x_0 \\ d_{YZ}tan\phi_Y + y_0 \\ z_0 \end{bmatrix} $$

   where x_0, y_0 and z_0 are the current needle notch position, and the sign of the movement ϕ_Y is subject to the movement direction. d_{YZ} is the projection distance of a vector from the rectal sphincter centre to the needle notch $\left({}^0r_N - {}^0r_{RS}\right)$ in the YZ plane in frame 0.

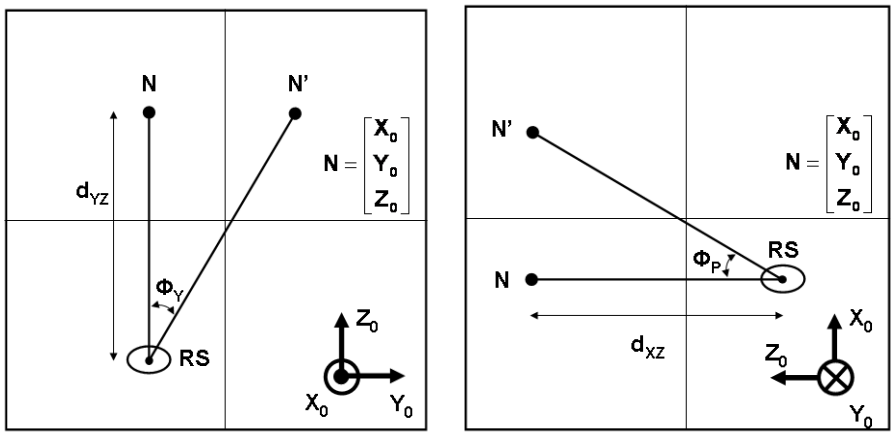


Figure 6.2: Schematic diagram of an angular movement of the needle projection in (a) yaw direction and (b) pitch direction

2. Angular movement in the pitch direction:
   The definition of this movement is similar to the previous one but is operated in pitch direction in terms of angular motion (refer to Figure 6.2(b)). The new target ${}^0r_{Target}$is calculated as follows:

$$ {}^0r_{Target} = \begin{bmatrix} d_{XZ}tan\phi_P + x_0 \\ y_0 \\ z_0 \end{bmatrix} $$

   where the sign of the movement ϕ_P is subject to the movement direction and is the d_{XZ} projection distance of a vector from the rectal sphincter centre to the needle notch $\left({}^0r_N - {}^0r_{RS}\right)$ in the XZ plane in frame 0.

3. Linear movement in the direction of depth:
   Forward and backward movement of the endorectal probe is necessary for needle alignment to the target tissue, and this movement is equivalent to one that in which the clinician pushes the probe further into or out of the rectum for better alignment in an ultrasound guided prostate biopsy procedure. The translational movement of the endorectal probe is defined as a movement h along the principle axis of the probe represented by an unit vector directing from the rectal sphincter centre to the needle notch $\frac{{}^0r_N - {}^0r_{RS}}{|{}^0r_N - {}^0r_{RS}|}$. The new target point is calculated as follows:

$$ {}^0r_{Target} = \frac{{}^0r_N - {}^0r_{RS}}{|{}^0r_N - {}^0r_{RS}|}h + {}^0r_N $$

   where the sign of the movement h is subject to the movement direction, and ${}^0r_N$ is the current needle notch position.

6.3.3 Control Setting

The pneumatic motors in the Cartesian robot were operated at 1.3bar and PID control was implemented and tuned for each axis as described in Section 4.4 in Chapter 4. When the position commands on each robot joint are computed by the inverse kinematics in auto needle alignment, they are set to be the reference points in three individual PID control loops controlling each axis of the Cartesian robot; whereas the reference point in manual needle alignment is user specified. The haptic needle firing unit and its control interface were implemented with the control strategy proposed in Section 4.3 in Chapter 4.

6.4 Functional Hazard Assessment and Safety Measures

Medical devices should be designed with redundant safety features, particularly devices designed for interventional procedures, as failure of the equipment be potentially dangerous to both patients and clinicians. Functional hazard assessment was conducted on the prostate biopsy system to provide a list of system failure conditions, and to highlight its critical safety features. They can be summarised into the conditions of structural failure, control failure, electrical failure, and MR environment induced hazards, which were all taken into consideration when the robot was designed.

1. Structural failure of the prostate robot and the endorectal probe:
   Standard safety tests for MRI devices were conducted on the biopsy system to evaluate the safety of the system and were all documented at the Royal Marsden Hospital, Surrey (Ref. no: RMH/MRI/PB1-4). The system, in particular the endorectal probe, was filed and sanded to remove any sharp edges, and therefore presented no sharp corners or other features that might in themselves cause damage to the patient. The mechanical design of the robot mainly consists of a Cartesian robot, a haptic needle firing unit, and a endorectal probe. They are all sufficiently strong, so that if used with reasonable care there is little chance of structural failure. Any conductor which potentially has a voltage applied to it was insulated in such a manner that it could not be touched by either the patients or the clinicians. Safety checks are conducted every time before the use of the system to ensure that it functions properly and shows no signs of damage. The system is stored safely in hospital after use.

2. Control failure of the robot movement and the needle insertion:
   In terms of the robot movement, needle alignment is achieved by three pneumatic motors with a maximum speed of 5mm/s, and the slow movements are monitored by a programme as well as by clinicians who can override the robot movement command anytime with the control interface. An emergency stop button is mounted on the control console to halt any robot movement if necessary. In terms of the needle insertion, the procedure is designed in a way that the insertion can only be performed if (i) the mechanical lock holding the needle is opened by the clinician, and (ii) the insertion command is confirmed by the clinician in the control interface. Insertion depth is monitored by an encoder embedded in the needle firing unit which ensures the accurate needle placement without overshoot, whilst another mechanical lock is available to limit the insertion depth to 45mm, and to avoid overshooting of the needle.

3. Electrical failure of the power supply and the control console:
   Electrical components in the control console are powered by a clinical-standard power supply connected to the main power of the scanner room. The power supply is placed in a non-conductive case in the console, and has an individual earth cable to the main power. The main power is electrically isolated from the rest of the electronics. The control console was examined and passed the electrical safety test by a registered electrician.

4. MR environment induced hazards:
   In terms of MR safety, Chapter 3 has covered in detail the potential interferences between the robot components and the scanner, as well as the potential hazards, including the aspects of (i) magnetically induced force and torque, (ii) signal to noise ratio reduction, (iii) artifact generation, (iv) image geometric distortion, and (v) thermal effect.

6.5 Clinical Trial with Patients

A series of clinical trials were preformed on three patients to verify the functionality of the prostate biopsy robot. Written informed consents were given by the patients to have the biopsies performed, and recorded for research proposes. An ethical approval was granted for the clinical trials and the procedures were carried out using a 1.5T Siemens MAGNETOM Avanto scanner at the Royal Marsden Hospital in Surrey, U. K. Patients with high Prostate Specific Antigen (PSA) value were recruited, some of whom had undertaken TRUS guided biopsy before.

6.5.1 Trial Procedure

The complete procedure involved insertion of the endorectal probe into the patient's rectum, applying the robot to align the biopsy needle to the suspected target point with real-time MR image guidance, and then firing the biopsy needle and obtaining the tissue sample. Conventional TRUS guided biopsy, requires taking several samples from the prostate under general anaesthetic to decrease the likelihood of false-negative. The idea of an MR guided prostate biopsy is to reduce the number of biopsies to just one or at most a handful with the robotic assistance, and to make the biopsy procedure less invasive and painful for the patients. The clinical procedures are as follows:

1. Preoperative scans:
   High resolution images of the prostate were taken from the patient in the supine position with a Medrad 1.5T prostate endorectal balloon coil [Medrad, 2009]. The balloon coil was inserted in the rectum and then inflated, which made the rectum wall clearly visible in the image as a circle next to the prostate. The acquired MR image which shows clearly the location of a suspected target, are shown in Figure 6.3. The MR image shows a suspicious prostate lesion which was localised by our radiologist in the acquired high resolution images. It appeared at the prostate peripheral zone which is a common area to have prostate cancerous tissue. After the brief location of the lesion was identified, the endorectal coil was retrieved and the high resolution MR images were used as a reference for MR guided or TRUS guided biopsy.

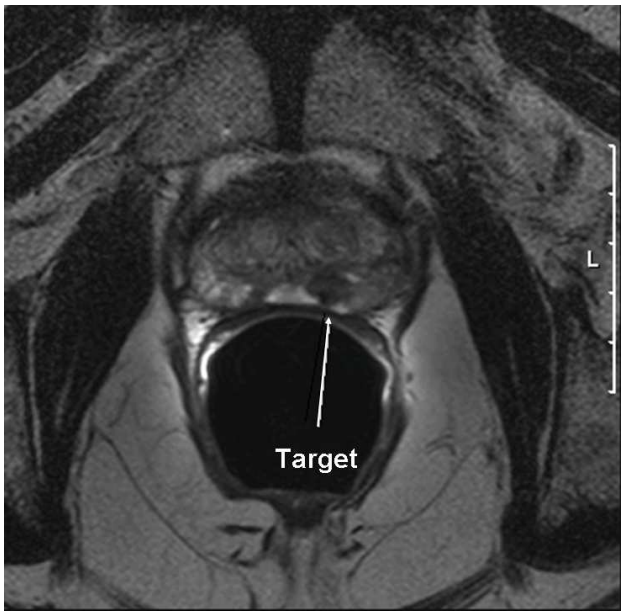


Figure 6.3: The acquired prostate image shows clear the suspected cancerous target.

2. Robot setup:
   The robot and its control hardware were designed to be as "plug-and-play" as possible. The robot was set up onto a base plate with two flexible mounts and the base plate had four flaps to plug into the special fixture of the scanner table for immobilisation. The setup overview is shown in Figure 6.4.

3. Patient setup:
   After the setup of the robot, the patient was introduced into the scanner room and placed onto the scanner bed in the left lateral decubitus position. The custom design endorectal probe, which was sterilised and covered with a condom, was inserted by our radiologist into the rectum of the patient, and the needle firing unit was then attached to the gimbals of the Cartesian robot. The robot was placed close to the patient to maximise the available space for movement, and the patient together with the robot were then moved into the scanner bore. The patient setup with the robot is illustrated in Figure 6.5. With the use of a condom to cover the endorectal probe, only the needle channel is required to be sterilised for each biopsy, and the channel can be made disposable if necessary for future clinical applications.

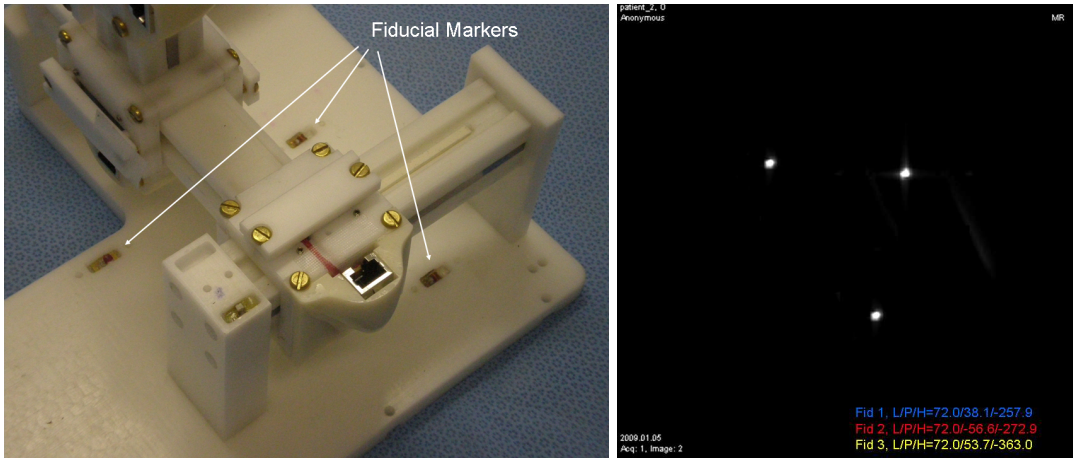
4. Robot registration:
   Three passive fiducial markers embedded into the robot base were used for robot-scanner registration, in which coordinate values of the markers were obtained, and this procedure would normally take only a few seconds, given that the fiducial markers at the robot base were always at a fixed height of 72mm below the isocentre of the scanner. The coordinates of the markers were then imported to the kinematic programme in Matlab® to calculate the robot-scanner coordinate transformation matrix T_0^S. Figure 6.6 illustrates the MR image taken for the registration where the fiducial markers appeared as bright spots.



Figure 6.4: Robot and integrated hardware panel setup



Figure 6.5: Endorectal probe inserted in a patient rectum.



(a) (b)

Figure 6.6: (a) Fiducial markers embedded in the robot base for registration. (b) MR image taken for robot-scanner registration where fiducial markers appears as bright spots for localisation.

5. Localisation of the prostate lesion target and the rectal sphincter:
   As mentioned in Chapter 5, the rectal sphincter is one of the input parameters for kinematic calculation, and it works as a pivot for the endorectal probe. A set of 20 transverse slices with thicknesses of 5mm were taken, and the rectal sphincter was displayed in the slices as a clear circular profile and was localised manually. For localisation of the biopsy target, the same technique was used for target lesion selection. To achieve greater accuracy of the spatial coordinates, a set of 30 slices with thicknesses of 3mm in both transverse and sagittal planes were taken for verification. Obtaining coordinates from different orientations can enhance the accuracy of localisation, as the lesion coordinates obtained in a scan plane are only exact in the two dimensions along the plane but not the dimension perpendicular to the plane. Combining the measured coordinates from two perpendicular scan planes can provide more accurate coordinates of the lesion than those coordinates measured only from one scan plane. The coordinates of the prostate lesion target and the rectal sphincter were then imported to the kinematic programme.

6. Fiducial tracking setup:
   Two scan planes are required to be set up manually to contain the two fiducial markers embedded in the head of the probe before the tracking protocol starts. One is a sagittal plane and the other is a fiducial plane, shown in Figure 6.7, and they are defined based on the requirement that both planes contain the two fiducial markers and that they are perpendicular to each other, meaning that the intersection axis of the two planes concurrently pass though the two markers. Once the tracking algorithm has started, the 3D fiducial positions were extracted from the current scan planes and used to locate the new scan planes where the fiducial markers appear at the centre of the image. A graphical outline showing the needle projection, position of the needle notch and the suspected lesion was overlaid on the images and displayed on the host computer in the control room. The tracking algorithm can always keep the scan planes aligned automatically with the markers and track the needle movement by the robot at up to 5mm/s. The robot speed

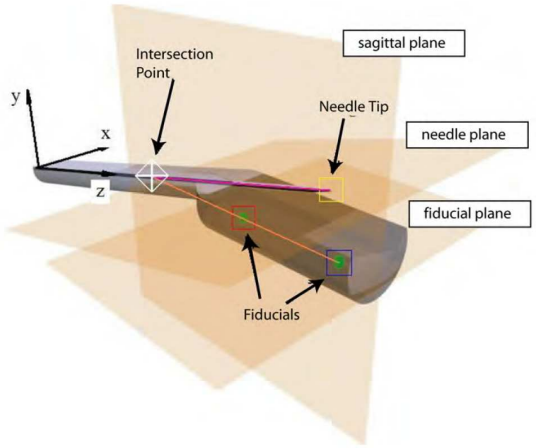


Figure 6.7: Sagittal plane, fiducial plane and needle plane in the endorectal probe

was controlled to avoid losing the tracking of the fiducial markers.

7. Needle alignment and firing:
   Needle alignment with the lesion was achieved: (i) firstly by the auto needle alignment approach for gross positioning and then by (ii) the manual approach to correct the error. At first, the coordinates of the lesion and the rectal sphincter were imported, and checked to determine if the target was achievable in terms of the workspace of the needle notch and the spatial availability for robot movement inside the scanner bore. If found to be feasible, the robot joint movements calculated using inverse kinematics were confirmed by the radiologist before being implemented. Movements were then implemented , with the sequence of: (i) in/out direction, (ii) pitch direction and (iii) yaw direction to minimise the stress applied to the rectum wall and to minimise the prostate tissue deformation. Real-time tracking images were displayed on the touch screen control PC where the needle notch projection was overlaid on the MRI images, showing the relative distance and direction from the needle notch to the target point. The tracking algorithm always kept the scan planes aligned with the two fiducial markers, and was updated every 2.4 seconds. The update rate can be speeded up, if necessary, by reducing the image resolution or increasing the slice thickness. After the auto needle alignment, the needle notch was brought close enough to the target point, for the clinician to manually correct the discrepancy between the current notch projection and the target point. With manual needle alignment, the user controls the robot to move the needle at increment distances in sagittal and needle planes respectively, to align the needle. The position correction was conducted until the needle notch position indicated by the tracking algorithm approximately coincides with the desired lesion position. The tracking steps are illustrated in Figure 6.8. After that, a quick scan was taken to provide final confirmation that the position of the needle notch would be coincident with the lesion position after firing. The needle was then introduced, fired to the sample and retracted in a short time within 5s.

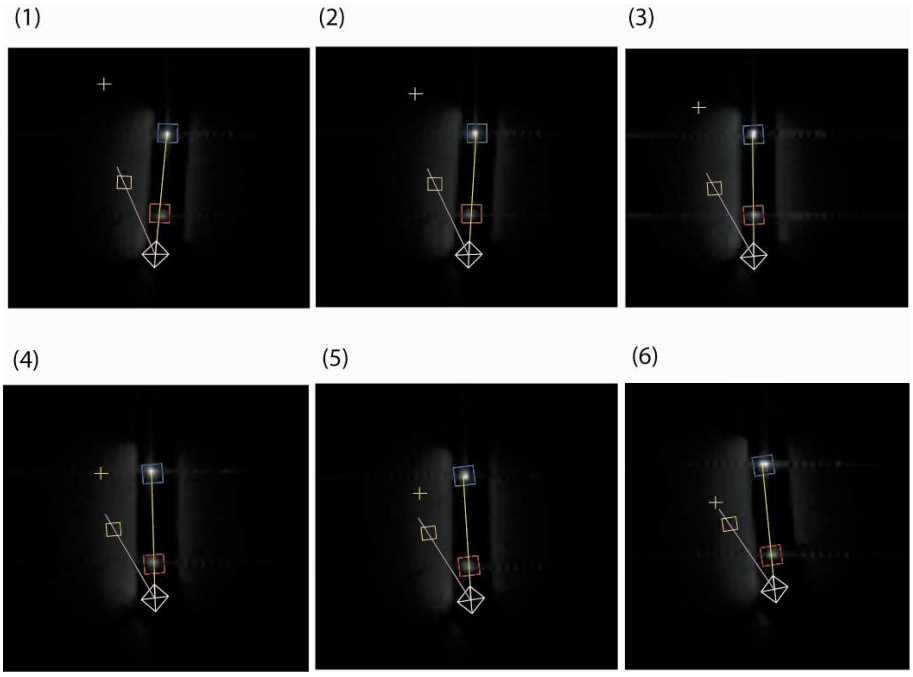


Figure 6.8: MR Tracking images showing the needle aligned step by step towards the target point. The tracking sequence kept the two fiducial always at the centre of the Field of View.

6.5.2 Results and Discussion

Phantom trials were first conducted to evaluate the functionality of the biopsy system. After that, three patients were administered the complete procedure by our radiologist Prof. Nandita deSouza, with technical support provided by the research team. An ethical approval was granted for clinical trials on the three patients.

Phantom Trials in MRI Scanner

In order to evaluate the functionality of the robotic system as well as the fiducial tracking algorithm for imaged guided biopsy, phantom trials were carried out inside an 1.5T Siemens Avanto scanner at Charing Cross Hospital, London, UK, which is the same type of scanner used for the following clinical trials. A gelatine prostate model, a latex formed rectum, and a latex formed rectal sphincter were mounted on a plastic frame. A 2mm thick layer of vinyl plastisol gel material was put on the prostate model to represent the capsule of the prostate. At the phantom prostate gland, a plasticine formed phantom tumour was embedded in the peripheral zone in which 99% of tumours are located [Blue, 2009]. A biopsy was taken on the prostate phantom, with the clinical procedure mentioned in Section 6.5.1, and was repeated 15 times with the gelatine prostate model replaced each time with a new one. Bottles filled with $CuSO_4$ were placed in the shape of a human torso to simulate the MR signals generated from a patient body during scans. Gross needle alignment was first performed by the robot joint movements calculated from the inverse kinematics, and the target error was then manually corrected by the user, as fine needle alignment with the visual feedback provided by the fiducial

tracking algorithm. Once the alignment of the needle was confirmed, the needle was inserted, and then an extra scan was taken before its retraction. The biopsy target error was measured in the MR image from the needle notch to the desired target (centre of the phantom tumour). The total time taken to run though a phantom trial was 24.6mins on average, with the mean target error being 2.2±0.3mm. Although there were several sources of error caused by the backlash of the system, registration error, tissue deformation and needle bending during the insertion, the needle notch placements were shown to be within a good accuracy with the time taken for the procedure being slightly shorter than that of the ultrasound guided equivalent (30-40mins). However it was noted that the latex formed rectum and rectal sphincter used in the experiment were of a uniform elasticity and were symmetric. In reality these tissue regions have their own non-uniform elasticity and also vary according to the anatomy of different patients, and the rectal sphincter in reality is not a clearly defined point in the MR image. The result of all of this is that (i) the actual deformation of the rectum and the rectal sphincter, and (ii) the approximation made of the rectal sphincter position as a fixed pivot point of the endorectal probe, may cause an increase in the target error during the clinical trials, causing the procedure in reality to potentially take a longer time for needle alignment.

Procedure Time taken in the Clinical Trials

The whole procedure took 41mins on average and it is anticipated that the procedure could be speeded up, through the experience of further clinical trials. The time taken for each task within the procedure is shown in Table 6.2. The most time consuming of the tasks, is the setup of the patient on the scanner table, which involves the steps of: insertion of the endorectal probe into the patient's rectum, ensuring the patient is comfortably placed in the left lateral decubitus position, and mounting of the robot as close to the patient as possible; this task took around 22mins on average. The second longest task was the localisation of the prostate lesion target and the rectal sphincter, taking around 12mins, a large part of what was taken for acquisitions of images of the anatomies in transverse and sagittal planes. Despite the time taken, this task was of significant importance, as precision of the lesion localisation greatly affects the accuracy of the biopsy result, and is the primary motivation of this research into the use of MRI guidance rather than the ultrasound counterpart. In addition, the kinematic calculations also require the coordinates of the target and the rectal sphincter to determine the joint movements. Setup of the fiducial tracking took about 2mins to adjust the tracking sequence parameters and to align the tracking image planes to include the two fiducial markers. Needle alignment and firing took 4mins in total: 0.5mins for gross positioning using the auto alignment, 3mins to correct the error by manual alignment, and a couple of seconds for a quick scan to verify the needle alignment, and another few seconds for the needle to be inserted, triggering, and retracted. The robot registration took the shortest time, around 1min, as it required only a single scan with the image tracking sequence in the horizontal plane at a defined height for acquisitions of the fiducial coordinates in the scanner frame. A problem was encountered with patient 1, when it was found that the target position was out of the workspace achievable by the biopsy robot as the patient was positioned too posteriorly in the scanner bore, and the robot movement availability was insufficient to achieve the target. The patient setup was redone in that case to provide more available space to the robot.

Step	Task	P1	P2	P3	
Preparation					
1	Preoperative scans				
2	Robot setup				
Biopsy procedures with the patient		Time (min)			Average time (min)
3	Patient setup	18.2/10	18	19	21.7
4	Robot registration	1/1	1	1	1.3
5	Localisation of prostate lesion target and rectal sphincter	9/9	9	9	12
6	Fiducial tracking setup	2	2	2	2.0
7	Needle alignment and firing	4	3.5	3.5	3.7
Total Time		54.2	33.5	34.5	40.7

/ : Patient setup was redone as the robot movement availability was not sufficient to achieve the target in the first patient setup.
P: Patient

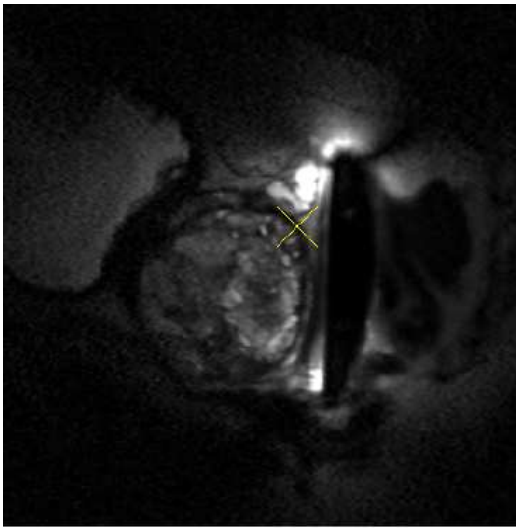
Table 6.2: Summary of the procedure time in each task

Fiducial Marker Tracking in the Clinical Trials

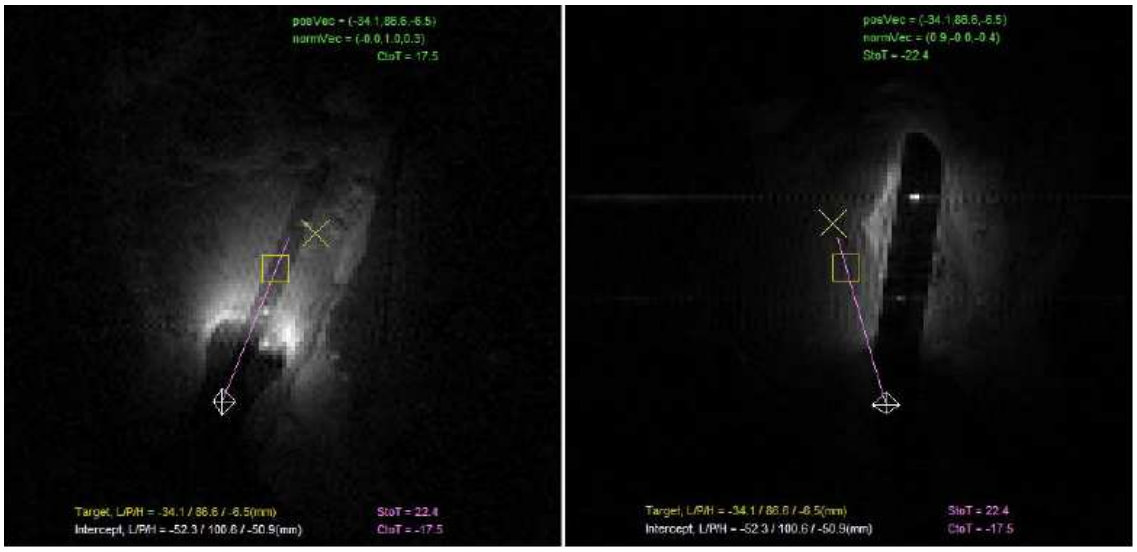
The coordinates of the two fiducial markers embedded in the endorectal probe were obtained with an image processing algorithm embedded in the tracking sequence, to calculate the needle notch position which was then overlaid on the tracking image, shown as the yellow box in the Figure 6.8. The target position is presented as a yellow crosshair, and the user was instructed to align the yellow square with the yellow cross hair. Spatial alignments in image guidance interventions are normally difficult to be performed free hand due to the high-DOF movement cooperation required, but our radiologist reported that manual needle alignment was easily done, especially with the assistance of the robot to hold the biopsy needle steadily. Figure 6.8 also shows a series of tracking images taken as the endorectal probe was aligned step by step toward the target point, and Figure 6.9 shows the MR images of the needle alignment before it was inserted. They were taken from one of the patients during the trial.

System Accuracy and Sources of Error in the Clinical Trials

The initial distances and final distances from the needle notch projection to the target during the procedure on three patients are listed in Table 6.3, where the distance is measured from the MR image. The needle notch projection, shown as the centre of the yellow box in the Figure 6.9, is the expected needle notch position after the needle insertion, and is calculated from the probe-needle geometry and the positions of the two fiducial markers. The needle notch projection error is defined as the distance between the desired target position (yellow crosshair in Figure 6.9) and the needle notch projection (centre of the yellow box). It is difficult to quantify the actual needle placement error during the procedure, as the biopsy needle was retracted from the patient's body as soon as the sample was obtained, in order to minimise the time the needle stayed in the patient body. Keeping a needle in the patient body is a potential danger to the organ tissue surrounding it. Taking into consideration the patient's safety, it was not preferable to interrupt the procedure for an extra scan to measure the actual needle placement error after the needle insertion. This is in contrast with the situation of phantom



(a)



(b)

Figure 6.9: (a) MR image of the prostate showing the target tissue. (b) Images taken in two perpendicular planes showing the needle alignment before a biopsy sample was taken.

	Initial distance from needle notch projection to the target	Rectal sphincter movement	Final distance from needle notch projection to the target
Patient 1	62mm	16mm	11.8mm
Patient 2	49mm	6mm	9.2mm
Patient 3	48mm	5mm	8.1mm

Table 6.3: Details of biopsy procedures on three patients. Needle notch projection refers to the expected position of the needle notch after it is inserted to the prostate, and it is shown as the centre of the yellow box in Figure 6.9.

trials, in which extra scans were allowed and the needle was kept in the phantom after the insertion. The actual needle placement error in the clinical trials was not measured, and was approximated from the needle notch projection error.

The procedure was first performed with auto needle alignment, which relies solely on the kinematic calculation to determine robot joint movement and align the needle close to the target point. This approach could only, on average, bring the needle notch projection to around 1-1.5cm of the target point due to the mobility and flexibility of the rectal sphincter, and movement of the patient body. A case was reported in the first patient that a maximum movement of 16mm occurred in the rectal sphincter position during the whole procedure. The first column in Table 6.3 indicates the initial distance from the needle notch projection to the target point measured from the MRI images, and the third column was the best alignment of the needle notch projection to the target that the robot achieved which were 11.8mm, 9.2mm and 8.1mm from the initial distance of 62mm, 49mm and 48mm. Those final distances were agreed upon by our radiologist to be close enough for biopsy and were confirmed from the MR tracking images. The average error of the needle notch projection was 9.7mm, which is larger than the average error of 2.3mm in the phantom trials (measured from the actual needle notch to the target in MR images). The error discrepancy can be accounted for the physical difference between the rectal tissue of the patients and the phantom used. It was found that the level of tissue deformation or movement of the rectal sphincter greatly affected the accuracy of the needle alignment. During the procedure, the endorectal probe was surrounded tightly by the rectal wall, and stress and friction were exerted on the rectal sphincter when the probe was moved, causing the deformation and movement of the sphincter. As the movement of the robot joint was calculated with inverse kinematics assuming a fixed rectal sphincter position, it entails that a high degree of sphincter deformation can cause a relatively large error in the needle alignment, as which occurred in patient 1 (16mm sphincter movement). During the procedure, the rectal sphincter acted as a flexible tube covering the endorectal probe, and was deformed easily when the probe was moved inside, which makes it difficult to predict the actual probe movement and to align the probe exactly to the target point. Also, it was observed that a higher accuracy was achieved with a shorter initial distance as in patient 2 and 3, which can be explained by the fact that a short initial distance results in less required probe movement, to bring the needle notch projection to the target point, and hence less tissue deformation of the rectal sphincter. However, the initial distance is not the only explanation, as the results were affected by the mechanical properties of the rectal tissue and its geometry.

Other sources of error in the procedure can be attributed to the following: (i) The mechanical

backlash of the robot. Compliance and unwanted bending in the plastic components of the robot were potential sources of inconsistency in the kinematic calculation of the needle notch coordinate. (ii) Robot-scanner registration error. An average registration error of 2mm was computed from the 3 fiducial markers used for the registration (approximately 0.67mm per each marker [Kozak, 2002]); however this error is likely to be reduced by an increase of the number of fiducial markers used for registration. (iii) Joint position control. The control accuracy is around 0.5mm in each pneumatically actuated joint of the Cartesian robot. Although pneumatic devices always complicate the issue of accuracy control, actuation in an MRI compatible robot has to be a compromise between its compatibility, speed/torque required for specific tasks, and its accuracy.

It was reported from the patients that holding decubitus posture inside the scanner bore for around 40mins was tiring and more pillow supports were needed to support their back so that the body could lean on the scanner bore. Among the three clinical cases, it was reported in patient 1 and patient 2 that the rear end of the needle firing unit was only a few centimeters away from collision with the scanner bore. Long upper legs in these two patients did not allow them to be positioned in the centre line of the scanner to leave sufficient space for the robot movement (in which the patient body was over the centre line and placed in their posterior side), and the robot had to be placed at a more posterior position to fit the body. Therefore, it will be part of the future work to reduce the size of the robot to give more flexibility of the system for a variety of patient body sizes. Also, an additional robot joint will be required to pivot the endorectal probe firmly, rather than solely relying on the support of the rectal sphincter. Despite the movement of the rectal sphincter affecting the accuracy of the system, the auto and manual needle alignment approaches were able to orientate the needle close enough for biopsy, the fiducial tracking algorithm provided a high precision to confirm the needle notch position, and the procedure time of around 40mins was comparable with the ultrasound guided counterpart.

6.6 Conclusion

Chapter 6 has reported a series of functional verification tests of the prostate biopsy robot. The MR compatibility of the whole system including the control unit placed inside the scanner room, was quantified showing the SNR reduction to be within an acceptable level. The auto and manual needle alignment schemes have been introduced for gross and fine positioning. The clinical procedures were described, and phantom trials were undertaken to verify the accuracy and the functionality of the biopsy system before clinical trials were undertaken with patients.

Three clinical trials have been reported to demonstrate the functionality of the robot for MR guided biopsy. The needle was first automatically aligned according to the robot joint movement calculated by the inverse kinematics, then corrected by the manual alignment with the use of real-time tracking images with a 2.2s update rate. Despite the target alignment error, mainly due to the mobility and tissue deformation of the rectal sphincter, the prostate biopsy robot has demonstrated its capability in performing MR guided biopsy with needle alignment accuracy of 9.7mm on average, and with comparable procedure time of around 40mins to the ultrasound guided biopsy alternative.

Chapter 7

System for Magic Angle Study in Man and its Evaluation

7.1 Introduction

Tendons and cartilages appear dim in conventional MR images due to their highly ordered and dense structure. Large increases in T2 relaxation time with the use of the "magic angle effect" can make the tissue more clearly visible and provide clinically useful information for diagnosis of certain tendinous disease [Marshall, 2002]. This effect is achievable by positioning and orienting tendons and cartilages at 55degrees relative to the main field, coined the magic angle; an image contrast in the tissue can be enhanced, although placing a target tissue at a specific angle inside the confined space in the scanner bore is always time-consuming and iterative. In this chapter, two mechatronic systems for lower and upper extremity positioning are presented to facilitate magic angle effect related study and tendinous diagnosis, and the required kinematics for limb positioning are studied, with the design criteria that the system can generate: (i) a trajectory for limb movement without patient's discomfort; (ii) placement of the target tissue at the desired orientation; and (iii) minimised distance between the target tissue and the isocentre of the scanner to guarantee that good image quality is obtained. A 3DOF positioning system for lower limbs and a 1DOF positioning system for upper limbs have been developed. They are actuated with pneumatic air motors, to assure their MR compatibility and high actuation power for moving patient's limbs. The positioning accuracy of 1degree in the lower limb positioning system and 0.5degrees in the upper limb positioning system is demonstrated.

The cubic segment trajectory method for controlling joint movement was implemented and evaluated in the lower limb system, and SNR reduction tests were performed individually to quantify the overall EM interferences caused by the two systems. Flexibility studies for applications of both systems in tendon imaging exploiting the magic angle effect were performed in a group of volunteers with their Achilles tendons, patellar tendons, quadriceps tendons, elbow tendons and vincula brevia tendons in forefinger studied, and the preliminary results are presented. Parts of the system designs and experimental results have been published in a journal paper [Tse, 2008].

7.2 Design Objectives and Guidelines

The aim of the mechatronic system is to position a target tendon in a musculoskeletal structure, at the magic angle relative to the main field of an MRI scanner, by controlling the movement of the patient's limb. The design specifications of the system in terms of kinematics and MR compatibility, were identified as follows:

Kinematics specifications

- Due to the spatial constraints of the scanner, the system has to be small, compact and must cooperate well with the patient's limbs in an MR scanner bore of 60cm diameter. The height of the system is limited, as a tall system would restrict the movement area of a limb in the bore, especially in the case of positioning lower extremity with the patient at lateral position in which the knee is likely to collide to the inner wall of the scanner at a premature angle. A schematic diagram is shown in Figure 7.3(b).
- The tissue of interest is placed nearest to the centre of the Diameter Spherical Volume (DSV) for good image quality, which is the volume of the best field homogeneity.
- The system should be able to offer patients a trajectory for the limb motion with his/her comfort guaranteed.

MR Compatibility and MR Safe specifications

- Components used should all be non-ferromagnetic to ensure minimal sizes of artifacts generated and no force or torque induced by magnetic attraction [Chinzei, 1999].
- The Signal to Noise Ratio (SNR) reduction caused by electronics, if any, has to be quantified to guarantee that the presence of the system does not sufficiently affect the image quality for diagnosis.
- The system is usable inside the bore of a conventional cylindrical MR scanner with a strength of 1.5Tesla, independent of the model and make.

7.3 Kinematics for Limb Positioning

Due to the difference of the length of the upper and lower extremities, different approaches are taken for positioning and orientation to maximise the space available for movement in the bore.

For lower extremity positioning, the patient's body and upper and lower leg form a 3-joint structure (Figure 7.1(a)), and the patient in the lateral position can maximise the range of movement in the horizontal plane of the scanner, which is approximately the diameter of the scanner bore. Considering the patient's hip as a fixed point, the upper and lower leg can be placed at a wide range of orientations and positions by simply controlling the the position of the ankle. Therefore a mechatronic system with at least 2 DOF in the X, and Z direction of the scanner and a rotary DOF about the Y direction as shown in Figure 7.1(a), is required to define orientation and positioning of any tissue along the lower

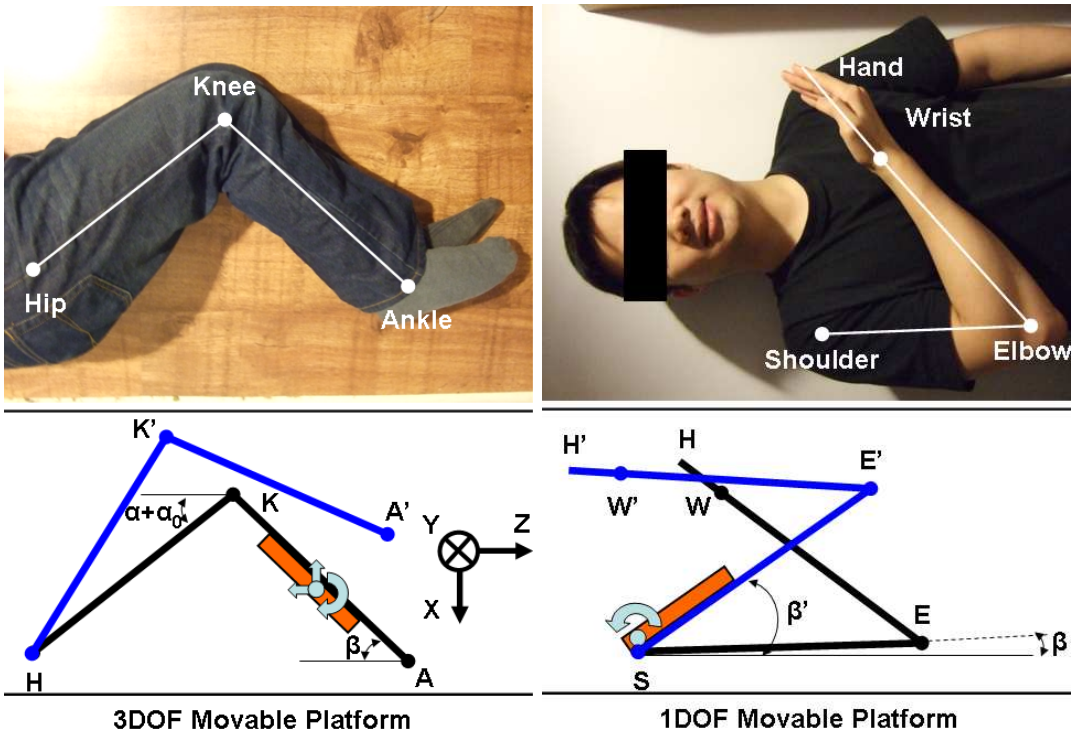


Figure 7.1: Schematic diagram showing the required DOF for: (a) low extremity positioning and (b) upper extremity positioning.

extremity; a further DOF in the scanner table, if available, can assist to keep the imaged tissue within the imaging volume, and optimise the distance from the scanned tissue to the isocentre.

For upper extremity positioning, the patient is placed in a supine position on the scanner table with their bent arms moved along the coronal plane about the shoulder as shown in Figure 7.1(b). This gesture is chosen, because the range of arm motion in the coronal plane using this gesture is maximised. This is basically a natural gesture and only 1DOF is required in the kinematics of a positioning system, to rotate the arm about the shoulder, in addition to the extra DOF in the scanner table movement, to keep the target tissue within the DSV and nearest to the isocentre. As shown in Figure 7.9(c), the upper extremity system is a four bar linkage mechanism, and its required kinematics for the limb motion are relatively simply compared with the kinematics of the lower extremity system; as such it will not be discussed in this Chapter.

The following kinematic studies will focus on positioning of tendons in the ankle and knee at the magic angle with the use of the lower extremity system. Investigating the inverse kinematics of the corresponding limb structure coupled with the mechatronic system allows us to:

- Find out the kinematic relationship between the 2DOF in the X, and Z direction, and the rotational DOF about the Y direction of the positioning system, to allow the target tissue, upper leg and lower leg following a trajectory that reaches the user defined position without causing a patient's discomfort.

- Decide the necessary movements of the patient's ankle in the X and Z directions to position the target tissue at a place where the magic angle is achieved and the distance from the isocentre is minimised.
- Calculate the minimum distance of the target tissue from the isocentre at a particular orientation of the tendon.
- Estimate the necessary movement of the scanner table to further reduce the minimum distance if a better image quality is required.
- Assist the implementation of a control scheme on the air motors if the kinematic relationships are known.

7.3.1 Kinematics of a Lower Extremity Structure

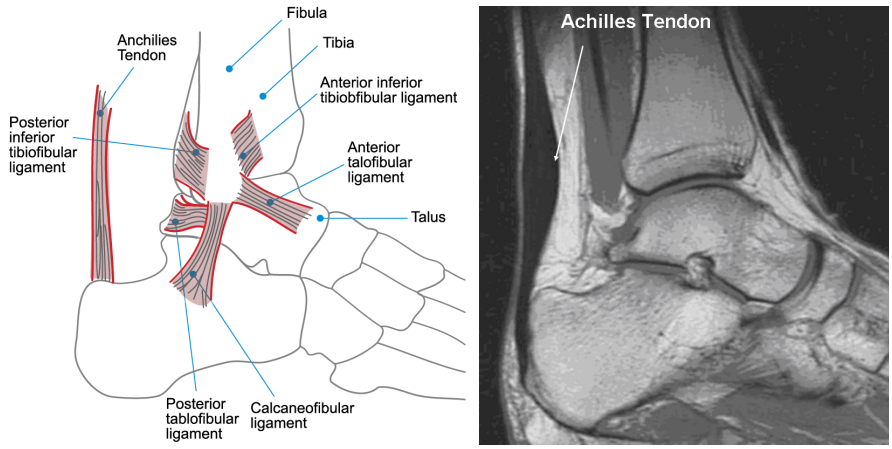
A system, which consists of: (i) 2DOF to provide movements along the XZ plane (horizontal plane) of a scanner at any point in the DSV and (ii) a rotational DOF for rotating a target at least 90degrees in clockwise and anticlockwise directions relative to the main field, was considered and its kinematics studied. The system is attached to the low leg near to the ankle (shown in Figure 7.1(a)), and the 2 translational axes and the rotational axis are actuated together to place the target tissue at the magic angle in which the target tendons can be the one attached to the upper leg or low leg. An additional DOF is made available by controlling the movement of the scanner table inward or outward with relation to the scanner, to further minimise the distance between the target tissue and the isocentre of the scanner. As tendons are connections between muscles and bones, and are largely concentrated in the ankle and the knee, the following kinematic analysis presents the approach to orientate the tendons attached, at the magic angle with the imaged anatomy closest to the isocentre. Table 7.1 indicates the nomenclature used for the different parameters and variables involved in the analysis.

Tendons in the Ankle

The ankle is a hinge joint connecting the distal ends of the tibia and the proximal end of the talus bone in the foot. As shown in Figure 7.2, the ankle joint is bound by the Achilles tendon and three lateral ligaments: the anterior talofibular ligament, the posterior talofibular ligament, and the calcaneofibular ligament. The Achilles tendon is the thickest tendon in the body with a length of about 15 cm in adults. It is a tendinous extension from three synergistic muscles, the gastrocnemius, the soleus, and the plantaris, in the lower leg, and is quite parallel to the tibia [Kettelkamp, 1969]. Due to overuse of the affected limb or strain injury, partial or complete rupture commonly occurs in the Achilles tendon in clinical cases and its complications are Achilles tendinitis (inflammation of the tendon) [Oatridge, 2001]. The following kinematics focuses on orientation of the ankle tendon, particularly the Achilles tendon, at different angles relative to the main field and always with the aim to have the ankle positioned closest to the isocentre of the scanner. In any case, the same kinematic analysis is still applicable to the ankle ligaments, with an offset angle considered from the tibia.

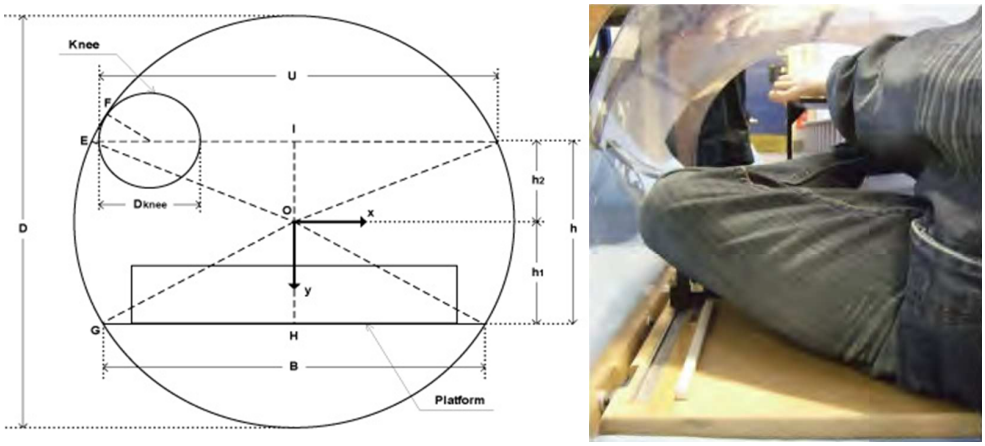
Parameters used in a transverse view in Figure 7.3(a)	
h	Vertical distance from the centre of the knee joint to the scanner table
h_1	Vertical distance from the scanner table to the isocentre
h_2	Vertical distance from the centre of the knee joint to the isocentre
D	Diameter of the scanner bore
B	Width of the scanner table
U	Maximum horizontal distance available for the cnemis to be position while oriented
D_{knee}	Diameter of the knee
Parameters used in coronal view in Figure 7.3(b)	
W_{DSV}	Width of the Diameter Spherical Volume at the sagittal plane at the height of the centre of the knee
D_{hip}	Diameter of the hip
L_t	Length of the thigh
L_c	Length of the cnemis
P	Centre of rotational axis of the device
L_2	Length from centre of rotational axis (P) to ankle
α_0	Angle of the femur relative to the main field of a scanner at initial patient position
$(\alpha + \alpha_0)$	Angle of femur relative to main field
β	Angle of the tibia relative to the main field of a scanner
$Ziso$	Distance from the centre of the hip joint to the isocentre
$Dist$	Distance from the ankle to the isocentre
$[Z_k \quad X_k]$	Z and X coordinates of the centre of the knee
$[Z_a \quad X_a]$	Z and X coordinates of the centre of the Angle

Table 7.1: List of symbol definitions

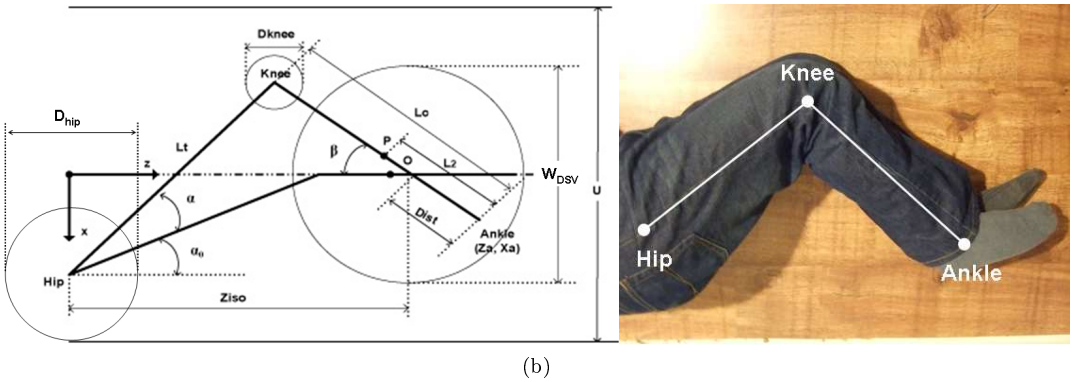


(a) (b)

Figure 7.2: (a) Anatomy of musculoskeletal structure in the ankle joint [HuAnat, 2009] and (b) its MR image.



(a)



(b)

Figure 7.3: (a) Geometric view of the knee in a transverse view of the scanner bore, and (b) geometric view of a patient's leg in the scanner coronal view.

Consider triangle IOE in Figure 7.3(a), we have

$$\left(\frac{U}{2}\right)^2 = \left(\frac{D}{2}\right)^2 - h_2^2$$

where $h_2 = h - h_1 = h - \sqrt{\left(\frac{D}{2}\right)^2 + \left(\frac{B}{2}\right)^2}$ from triangle OGH. Therefore, we have

$$U = 2\sqrt{\left(\frac{D}{2}\right)^2 - \left(h - \sqrt{\left(\frac{D}{2}\right)^2 + \left(\frac{B}{2}\right)^2}\right)^2} \tag{7.1}$$

The coordinate of point A, centre of the ankle in Figure 7.3(b), is

$$\begin{bmatrix} Z_a & X_a \end{bmatrix} = \begin{bmatrix} (L_t cos(\alpha + \alpha_0) + L_c cos\beta) & (L_t sin(\alpha_0) - L_t sin(\alpha + \alpha_0) + L_c sin\beta) \end{bmatrix} \tag{7.2}$$

Equation (7.2) is a key equation that relates α, β, Z_a and X_a together. In the case of positioning an ankle tendon with a specific orientation β, the equation suggest that the movement in the Z and X axes in the positioning robot is a function of α, and β can be any arbitrary value, as long as the positions of the knee and the ankle are within the scanner bore and are geometrical sensible. Therefore, the next step is to find an α such that the distance of the ankle position to the isocentre can be minimised to assure good image quality. The distance from the ankle to the isocentre in the plane of Figure 7.3(b) is,

$$Dist = \sqrt{X_a^2 + (Ziso - Z_a)^2 + h_2^2)}$$

$$Dist = \sqrt{[L_t sin(\alpha_0) - L_t sin(\alpha + \alpha_0) + L_c sin\beta]^2 + [Ziso - (L_t cos(\alpha + \alpha_0) + L_c cos\beta)]^2 + h_2^2} \tag{7.3}$$

Distance $Dist$ determines how far away the ankle is from the isocentre, and its minimum possible value for a specific desired orientation β, correlates with the best possible image quality. Minimisation of $Dist$ follows the constraints below:

- **Constraint (I):** Knee must not hit scanner wall:

$$|X_k| + \frac{D_{knee}}{2} \leq \frac{U}{2}$$

where $X_k = L_t sin\alpha_0 - L_t sin(\alpha + \alpha_0)$. To find out the corresponding for minimum distance $Dist$, $\frac{\partial Dist}{\partial \alpha} = 0$ is set and thus:

$$\alpha|_{\frac{\partial Dist}{\partial \alpha}=0} = tan^{-1}\left(\frac{L_t sin\alpha_0 + L_c sin\beta}{Ziso - L_c cos\beta}\right) - \alpha_0 \tag{7.4}$$

where $\alpha|_{\frac{\partial Dist}{\partial \alpha}=0}$ is an angle of the femur orientation relative to the main field such that the minimum distance between the tendon and the isocentre is achieved. This is the function of the

desired orientation of the tendon β. Now, the constraint is applied considering the Equation (7.4) for two cases:

Case 1: The knee does not hit the wall at $\frac{\partial Dist}{\partial \alpha} = 0$

$$|X_k| + \frac{D_{knee}}{2} \leq \frac{U}{2} \Leftrightarrow \left| L_t sin\alpha_0 - L_t sin\left(\alpha_{\frac{\partial Dist}{\partial \alpha}=0} + \alpha_0\right)\right| + \frac{D_{knee}}{2} < \frac{U}{2}$$

where U is calculated from Equation (7.1). Then,

$$\alpha_{mindist} = \alpha|_{\frac{\partial Dist}{\partial \alpha}=0} = tan^{-1}\left(\frac{L_t sin\alpha_0 + L_c sin\beta}{Ziso - L_c cos\beta}\right) - \alpha_0 \tag{7.5}$$

Case 2: The knee hits the wall before $\frac{\partial Dist}{\partial \alpha} = 0$

$$\left| L_t sin\alpha_0 - L_t sin\left(\alpha_{\frac{\partial Dist}{\partial \alpha}=0} + \alpha_0\right)\right| + \frac{D_{knee}}{2} > \frac{U}{2}$$

where U is calculated from Equation (7.1). Then the knee is set to be in touch with the wall to give the maximum range of β for the ankle movement (Refer to Figure 7.4). Then,

$$\alpha_{mindist} = sin^{-1}\left(\frac{U - \left(\frac{D_{knee}+D_{hip}}{2}\right)}{L_t}\right) \tag{7.6}$$

- **Constraint (II):** Motion of Z Axis (ΔZ) must be within joint range:

$$-340 \leq \Delta Z = L_t cos\left(\alpha + \alpha_0\right) + (L_c - L_2)cos\beta - L_t cos\alpha_0 - (L_c - L_2) \leq 0 \tag{7.7}$$

- **Constrain (III):** Motion of X Axis (ΔX) must be within joint range:

$$-100 \leq \Delta X = L_t sin\alpha_0 - L_t sin\left(\alpha + \alpha_0\right) + \left(L_t - L_2\right) sin\beta \leq 100 \tag{7.8}$$

The kinematic equations derived for ankle tendon positioning are summarised in Table 7.2.

Tendons in Knee

The human knee is a complex and compound joint where the femur and the tibia are linked together by the patellar tendon, the patella (kneecap), the quadriceps tendon, and a few small ligaments, as illustrated in Figure 7.5. The patellar tendon connects the bottom of the patella to the tibial tubercle on the front of the tibia. The opposite side of the patella is connected to the quadriceps tendon which is linked to the large muscle on the front of the thigh; the quadriceps muscle. The quadriceps tendon, the patella and the patellar tendon are under tension when the quadriceps muscle contracts and the tibia is pulled to move the knee from a bent position to a straight position. Conversely, the knee moves from a straight position to a position of flexion when the muscle relaxes [Ahmad, 1998]. Patellar and quadriceps tendon ruptures are commonly found in patients with sport related injuries, in which the

1). The position of the ankle for a desired orientation of the Achilles tendon β: Equation (7.2)

$$[Z_a \quad X_a] = [\ (L_t \cos(\alpha+\alpha_0) + L_c \cos\beta) \quad (L_t \sin\alpha_0 - L_t \sin(\alpha+\alpha_0) + L_c \sin\beta)]$$

2). The minimum distance from the ankle tendon to the isocentre: Equation (7.3)

$$Dist = \sqrt{\begin{matrix}(L_t \sin\alpha_0 - L_t \sin(\alpha+\alpha_0) + L_c \sin\beta)^2 \\ + [\mathrm{Ziso} - (L_t \cos(\alpha+\alpha_0) + L_c \cos\beta)]^2 + {h_2}^2\end{matrix}}$$

3). The minimum distance can be further reduced if a moving table is allowed by

$$\Delta z_{table} = \mathrm{Ziso} - (L_t \cos(\alpha+\alpha_0) + L_c \cos\beta)$$

4) Constraint (I): Knee must not hit scanner wall: Equation (7.5) & (7.6)

$$\alpha_{\min dist} = \begin{bmatrix} \tan^{-1}\left(\dfrac{L_t \sin\alpha_0 + L_c \sin\beta}{Ziso - L_c \cos\beta}\right) - \alpha_0 & for & \left|X_k\,|_{\frac{\partial Dist}{\partial\alpha}=0}\right| + \dfrac{D_{knee}}{2} < \dfrac{U}{2} \\ \sin^{-1}\left(\dfrac{2U - D_{knee} - D_{hip}}{2L_t}\right) & for & \left|X_k\,|_{\frac{\partial Dist}{\partial\alpha}=0}\right| + \dfrac{D_{knee}}{2} > \dfrac{U}{2} \end{bmatrix},$$

where $X_k = L_t \sin\alpha_0 - L_t \sin(\alpha\,|_{\frac{\partial Dist}{\partial\alpha}=0} + \alpha_0)$,

$$\alpha\,|_{\frac{\partial Dist}{\partial\alpha}=0} = \tan^{-1}\left(\frac{L_t \sin\alpha_0 + L_c \sin\beta}{Ziso - L_c \cos\beta}\right) - \alpha_0$$

$$, U = 2\sqrt{\left(\frac{D}{2}\right)^2 - \left(h - \sqrt{\left(\frac{D}{2}\right)^2 + \left(\frac{B}{2}\right)^2}\right)^2} \text{ and } h_2 = h - \sqrt{\left(\frac{D}{2}\right)^2 - \left(\frac{B}{2}\right)^2}$$

Constrain (II): Motion of Z Axis (ΔZ) must be within joint range: Equation (7.7)

$$-340 \le \Delta Z = L_t \cos(\alpha+\alpha_0) + (L_c - L_2)\cos\beta - L_t \cos\alpha_0 - (L_c - L_2) \le 0$$

Constrain (III): Motion of X Axis (ΔX) must be within joint range: Equation (7.8)

$$-100 \le \Delta X = L_t \sin\alpha_0 - L_t \sin(\alpha+\alpha_0) + (L_t - L_2)\sin\beta \le 100$$

Table 7.2: Kinematics equations for positioning Achilles tendons

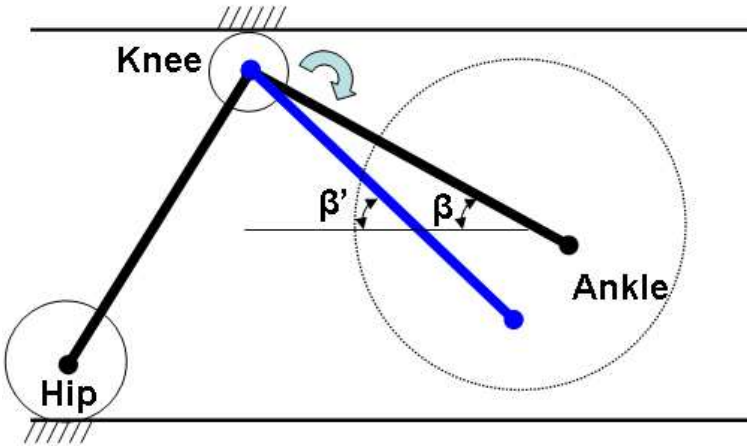


Figure 7.4: Constraint I: The knee collides with the scanner wall before the angle of the femur is optimised. In this case, orientating the ankle tendon to a larger β can be achieved only by rotating the tibia about the knee which is kept in touch with the wall.

knee is likely to buckle when the patients tries to stand up due to the patella losing its support from the tibia or femur [Marder, 1991]. In this situation, the body weight can no longer be supported by the knee in a standing position. As the patellar tendon and the quadriceps tendon are attached to the tibia and the femur respectively, the approaches taken in their orientation are different and their optimised position inside the imaging volume are also slightly different. The following kinematic analysis focuses only on these tendons, but can also be adapted to the ligament in the knee with slight modifications.

I. Patellar Tendon The coordinate of the knee in Figure 7.3(b) can be expressed as

$$\begin{bmatrix} Z_k & X_k \end{bmatrix} = \begin{bmatrix} L_t cos\left(\alpha + \alpha_0\right) & L_t sin\left(\alpha_0\right) - L_t sin\left(\alpha + \alpha_0\right) \end{bmatrix} \tag{7.9}$$

The distance from the knee to the isocentre in the plane of Figure 7.2(b) is,

$$Dist = \sqrt{X_k^2 + (Ziso - Z_k)^2 + h_2^2}$$

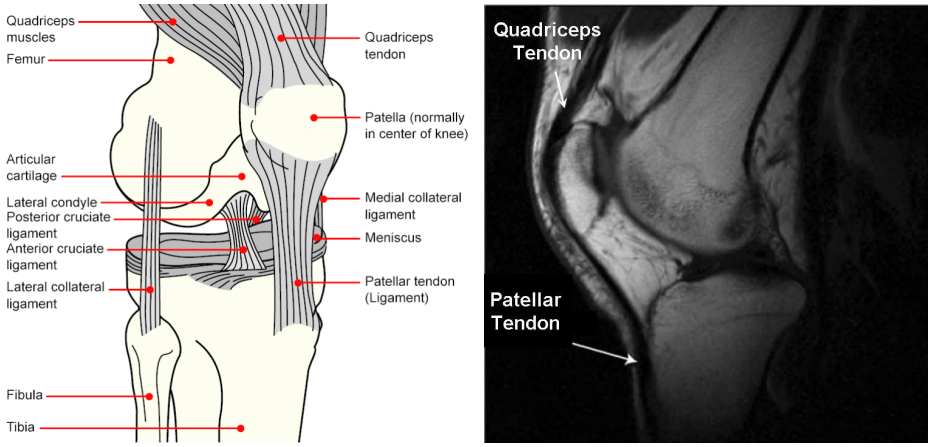
$$Dist = \sqrt{\left[L_t sin\alpha_0 - L_t sin\left(\alpha + \alpha_0\right)\right]^2 + \left[Ziso - L_t cos\left(\alpha + \alpha_0\right)\right]^2 + h_2^2} \tag{7.10}$$

Minimisation of $Dist$ follows the constraints similar to the one in the case of the kinematics in angle positioning but the first constraint is slightly different as shown in the following:

- **Constraint (I):** Ankle must not hit the scanner wall:
  To find out the corresponding α for minimal distance $Dist$, Set $\frac{\partial Dist}{\partial \alpha} = 0$ and then

$$\alpha|_{\frac{\partial Dist}{\partial \alpha}=0} = tan^{-1}\left(\frac{L_t sin\alpha_0}{Ziso}\right) - \alpha_0 \tag{7.11}$$

  where $\alpha|_{\frac{\partial Dist}{\partial \alpha}=0}$ is the angle of the femur orientation relative to the main field such that the minimum distance between the patellar tendon and the isocentre is achieved. Now, the constraint is



(a) (b)

Figure 7.5: (a) Anatomy of musculoskeletal structure in the knee and (b) its MR image in a lateral view.

applied considering Equation (7.11) for two cases:

Case 1: The ankle does not hit the wall at $\alpha = \alpha|_{\frac{\partial Dist}{\partial \alpha}=0}$ (Refer to Figure 7.3(b))

$$\left| X_a|_{\alpha|_{\frac{\partial Dist}{\partial \alpha}=0}} \right| \leq \frac{U}{2}$$

where U is calculated from Equation (7.1), and
where $X_a|_{\alpha|_{\frac{\partial Dist}{\partial \alpha}=0}} = L_t sin\,(\alpha_0) - L_t sin\left(\alpha|_{\frac{\partial Dist}{\partial \alpha}=0} + \alpha_0\right) + L_c sin\beta$ is from Equation (7.2). Then

$$\alpha_{mindist} = \alpha|_{\frac{\partial Dist}{\partial \alpha}=0} = tan^{-1}\left(\frac{L_t sin\alpha_0}{Ziso}\right) - \alpha_0 \tag{7.12}$$

Case 2: The ankle hits the wall before $\alpha = \alpha|_{\frac{\partial Dist}{\partial \alpha}=0}$

$$\left| X_a|_{\alpha|_{\frac{\partial Dist}{\partial \alpha}=0}} \right| > \frac{U}{2}$$

where U is calculated from Equation (7.1).Then the ankle is set to be in touch with the wall, and sliding along it to vary the orientation of the patellar tendon attached to the tibia β, which gives the maximum range of β for the knee movement, as illustrated in Figure 7.6. Considering the triangle FKA in Figure 7.6 (by sine law),

$$\frac{KA}{sin\,(\alpha + \alpha_0)} = \frac{KH + HF}{sin\beta} \Rightarrow \frac{L_c}{sin\,(\alpha + \alpha_0)} = \frac{L_t + \frac{\frac{Dhip}{2}}{sin(\alpha + \alpha_0)}}{sin\beta}$$

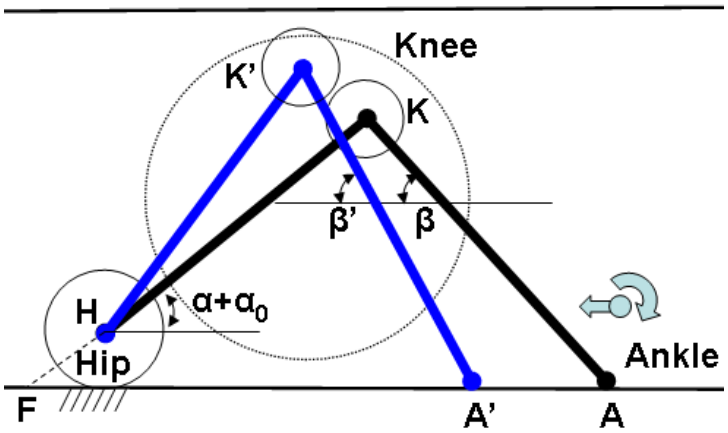


Figure 7.6: The ankle collides with the scanner wall before the angle of the femur α is optimised in constraint I. In this case, the ankle is kept in touch with the wall and slides along to orientate the tibia and to achieve a larger β.

Then,

$$\alpha_{mindist} = \alpha = sin^{-1}\left[\frac{sin\beta}{L_t}\left(L_c - \frac{D_{hip}}{2sin\beta}\right)\right] - \alpha_0 \tag{7.13}$$

- **Constraint (II) and (III):** Motion of Z axis and X axis must be within joint range, and these constraints are same as the one in ankle tendon positioning.

The kinematic equations derived for patellar tendon positioning are summarised in Table 7.3.

II. Quadriceps Tendon For the tendons of the upper part of the knee, the angle of the femur relative to the main field $(\alpha + \alpha_0)$, is of interest; whereas the angle of the tibia β is arbitrary. Therefore, the cnemis is set to be always parallel to the main field, i.e , $\beta = 0$ to maximize the spatial area available for knee movement. A schematic diagram to illustrate this case is given in Figure 7.7. The coordinates of the ankle become:

$$\begin{bmatrix} Z_a & X_a \end{bmatrix} = \begin{bmatrix} (L_t cos\,(\alpha + \alpha_0) + L_c) & (L_t sin\,(\alpha_0) - L_t sin\,(\alpha + \alpha_0)) \end{bmatrix} \tag{7.14}$$

from Equation (7.2). The distance *Dist* from the knee to the isocentre in the horizontal plane shown in Figure 7.2(b) is exactly the same as that used in Equation (7.10), but the only way for the distance to be minimised is by movement of the scanner table, as $(\alpha + \alpha_0)$ is no longer an arbitrary parameter in this case. The constraints applied to the position of the robot are the same as constraints (II) and (III), in relation to the robot movement in the previous section, but constraint (I) is that the knee must not hit the scanner wall, i.e. $|X_k| + \frac{D_{knee}}{2} < \frac{U}{2}$. The summary of the kinematic equations in this case is presented in Table 7.4.

1). The position of the ankle for a desired orientation of the patellar tendon β: Equation (7.2)

$$\begin{bmatrix} Z_a & X_a \end{bmatrix} = \begin{bmatrix} (L_t \cos(\alpha+\alpha_0) + L_c \cos\beta) & (L_t \sin\alpha_0 - L_t \sin(\alpha+\alpha_0) + L_c \sin\beta) \end{bmatrix}$$

2). The minimum distance from the patellar tendon to the isocentre: Equation (7.10)

$$Dist = \sqrt{\left[L_t \sin\alpha_0 - L_t \sin(\alpha+\alpha_0) \right]^2 + \left[\text{Ziso} - L_t \cos(\alpha+\alpha_0) \right]^2 + h_2^{\,2}}$$

3). The minimum distance can be further reduced if a moving table is allowed by

$$\Delta z_{table} = \text{Ziso} - L_t \cos(\alpha+\alpha_0)$$

4). Constraint (I): Ankle must not hit scanner wall: Equation (7.12) & (7.13)

$$\alpha_{\min dist} = \begin{bmatrix} \tan^{-1}\left(\dfrac{L_t \sin\alpha_0}{Ziso}\right) - \alpha_0 & for & \left| X_a \mid_{\alpha|_{\frac{\partial Dist}{\partial\alpha}=0}} \right| \le \dfrac{U}{2} \\ \sin^{-1}\left[\dfrac{\sin\beta}{L_t}\left(L_c - \dfrac{D_{hip}}{2\sin\beta}\right)\right] - \alpha_0 & for & \left| X_a \mid_{\alpha|_{\frac{\partial Dist}{\partial\alpha}=0}} \right| > \dfrac{U}{2} \end{bmatrix}$$

where $X_a \mid_{\alpha|_{\frac{\partial Dist}{\partial\alpha}=0}} = L_t \sin\alpha_0 - L_t \sin(\alpha \mid_{\frac{\partial Dist}{\partial\alpha}=0} + \alpha) + L_c \sin\beta$,

$$\alpha \mid_{\frac{\partial Dist}{\partial\alpha}=0} = \tan^{-1}\left(\frac{L_t \sin\alpha_0}{Ziso}\right) - \alpha_0$$

$$,U = 2\sqrt{\left(\frac{D}{2}\right)^2 - \left(h - \sqrt{\left(\frac{D}{2}\right)^2 + \left(\frac{B}{2}\right)^2}\right)^2}$$, and $h_2 = h - \sqrt{\left(\frac{D}{2}\right)^2 - \left(\frac{B}{2}\right)^2}$

Constraint (II) and Constraint (III) are the same as in Table 7.2

Table 7.3: Kinematics equations for positioning patellar tendons

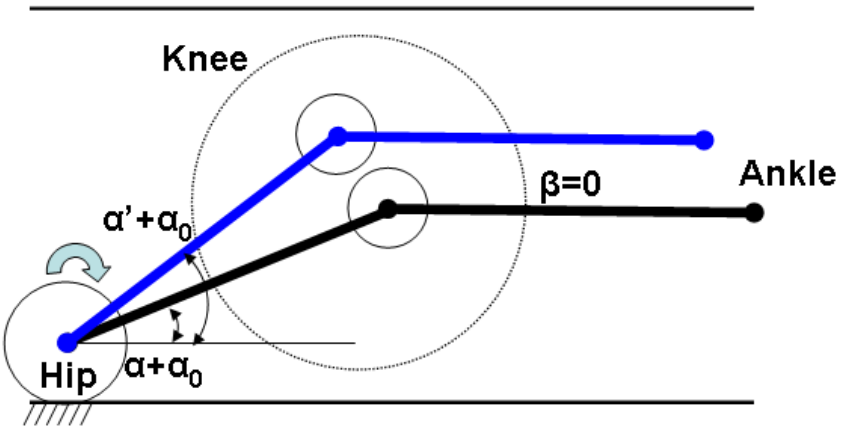


Figure 7.7: The femur is kept parallel to the main field to avoid any collision of the ankle to the scanner wall at a small angle of femur α and to provide maximum space for the knee movement.

1). The position of the ankle for a desired orientation of the quadriceps tendon $(\alpha+\alpha_0)$:

Equation (7.14)

$$[Z_a \quad X_a] = [\ L_t\cos(\alpha+\alpha_0)+L_c \quad L_t\sin\alpha_0 - L_t\sin(\alpha+\alpha_0)]$$

2). The minimum distance from the quadriceps tendon to the isocentre: Equation (7.10)

$$Dist = \sqrt{\left[\ L_t\sin\alpha_0 - L_t\sin(\alpha+\alpha_0)\right]^2 + \left[\ \mathrm{Ziso} - L_t\cos(\alpha+\alpha_0)\ \right]^2 + h_2{}^2}$$

3). The minimum distance can be further reduced if moving the table is allowed by:

$$\Delta z_{table} = \mathrm{Ziso} - L_t\cos(\alpha+\alpha_0)$$

4). Constraint (I): Knee must not hit scanner wall: $|X_k| + \frac{D_{knee}}{2} \le \frac{U}{2}$

where $X_k = L_t\sin\alpha_0 - L_t\sin(\alpha+\alpha_0)$ (Equation (7.9)),

$$U = 2\sqrt{\left(\frac{D}{2}\right)^2 - \left(h - \sqrt{\left(\frac{D}{2}\right)^2 + \left(\frac{B}{2}\right)^2}\right)^2} \quad \text{and} \quad h_2 = h - \sqrt{\left(\frac{D}{2}\right)^2 - \left(\frac{B}{2}\right)^2}$$

Constraint (II) and Constraint (III) are same as in Table 7.2 and Table 7.3

Table 7.4: Kinematics equations for positioning quadriceps tendons

Device	Error (Microscribe®)	Max. Error (Fiducial)
• Upper limb system	0.4deg	0.5deg
• Lower limb system		
-Rotation axis	0.6deg	1.0deg
-X direction	0.4mm	1.1mm
-Z direction	0.9mm	2.8mm

Table 7.5: Accuracies of the two systems as measured on the bench in the laboratory using conventional metrology equipment and in the MRI scanner using fiducial markers

7.4 Mechanical Design

Kinematic study provides an insight of how a robotic system should be designed to fulfill the specifications. Both of the magic angle positioning systems for upper and lower limb were developed with the kinematic guidelines, made from engineering plastics Delrin® and Ertalon®, and actuated with the pneumatic air motors mentioned in Chapter 3. Optical quadrature encoders were adapted in both of the systems for position tracking.

For the lower extremity system, it comprises of a 3DOF movement platform as shown in Figure 7.8, which consists of a linear axis in the X direction of the scanner and a rotational axis about the Y direction at the centre of the platform. The platform is mounted on a wooden baseboard and movable in the Z direction. Z and X axes are actuated by a rack-and-pinion mechanism on two aluminium slider rails and the rotational axis is coupled with a worm gear set to minimise backlash. Each axis is actuated by an individual pneumatic air motor as shown in Figure 7.8(b). During scanning, the patient is placed on the scanner table in the lateral position, with his scanned leg strapped to a limb fixture with a surface coil wrapped around the target tissue; the other leg is placed on a limb support, allowing enough space for the bottom leg to move without physical collision between them. The limb is moved by the platform and follows a computed trajectory to ensure that the target tendon is placed at its magic angle and as close to the isocentre as possible.

The upper extremity system is a 1DOF positioning platform, and is placed on the patient with his arm strapped on the rotary platform as shown in Figure 7.9, and actuated by a rack-and-pinion mechanism with a range of movement of 70degrees. The movable platform is designed with adjustable arm holders for different size of arms, and is usable for both arms by changing the pivot point of rotation, as illustrated in Figure 7.9(a).

The accuracy of both systems were quantified in a lab environment by comparing the position encoder reading with a mechanical tracking arm (Microscribe®) which has a measurement error of less than 0.23mm, and the measurement was repeated in the MRI scanner with the use of fiducial markers mentioned in Chapter 5 which has a measurement error of less than 0.2mm. The measurement results of 30 sample points in each actuated axis are listed in Table 7.5: the 3DOF system has a maximum error of 1.0degree, 1.1mm and 2.8mm in the rotational, X and Z axes respectively; whilst the 1DOF system has maximum error of 0.5degree in the rotational axis.

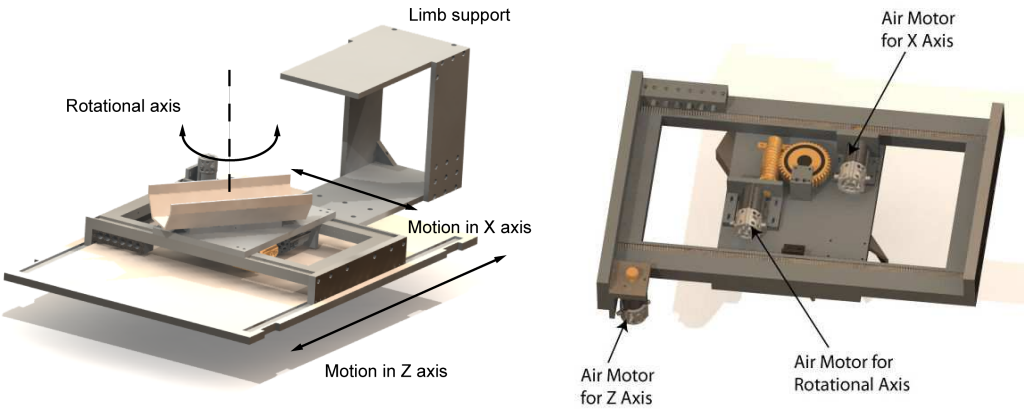


Figure 7.8: (a) CAD rendering of the low limb system. (b) The underside view of the platform. (c) Photo of the system. (d) The system is mounted on a scanner table and the patient is placed with left position and has his leg strapped on the limb fixture of the system.

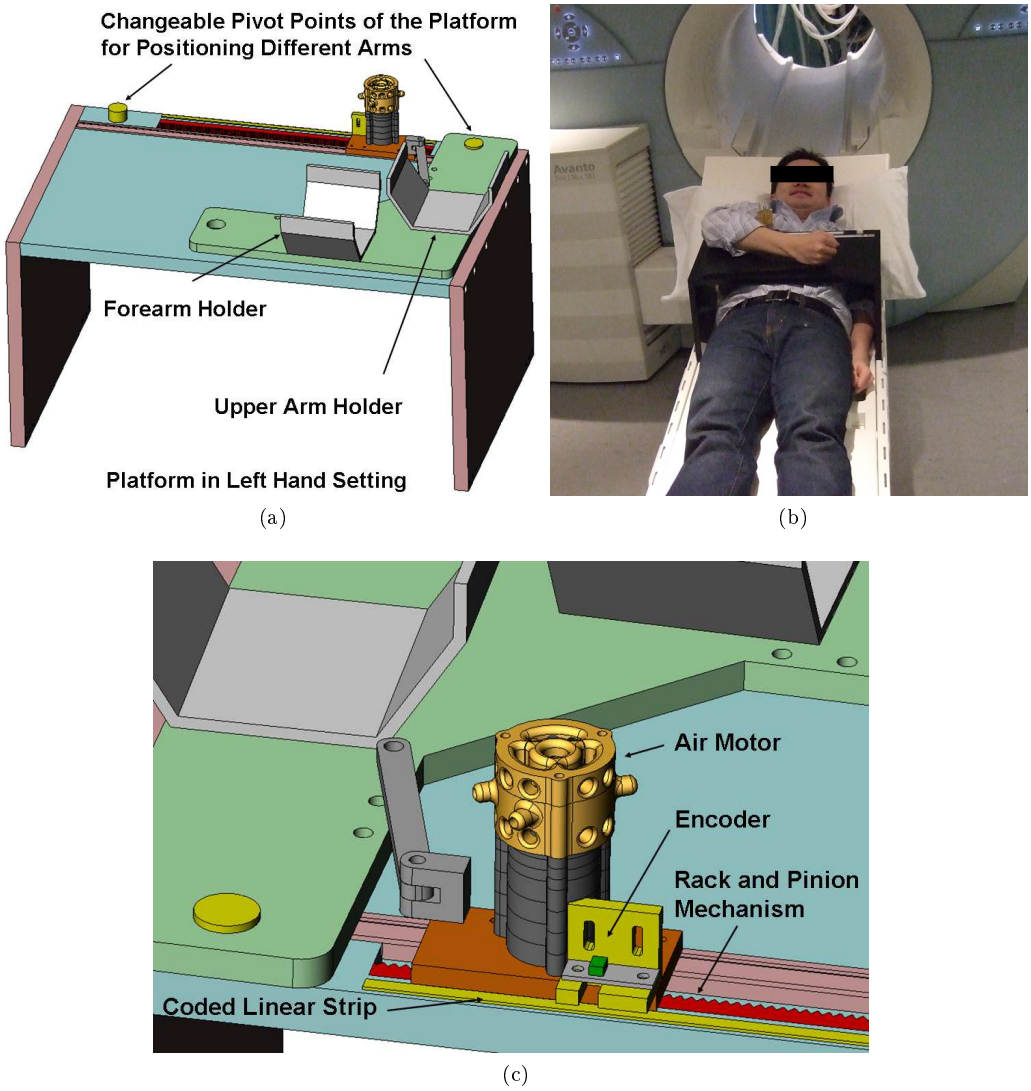


Figure 7.9: (a) CAD rendering of the upper limb system (setup for left hand positioning). (b) Photo of the system mounted on a scanner table with the patient placed in supine position and his arm strapped on the arm holder of the system (setup for right hand positioning). (c) A four bar linkage mechanism connecting the linear motion in the rack and pinion mechanism to the rotational movement in the arm holders about the pivot point.

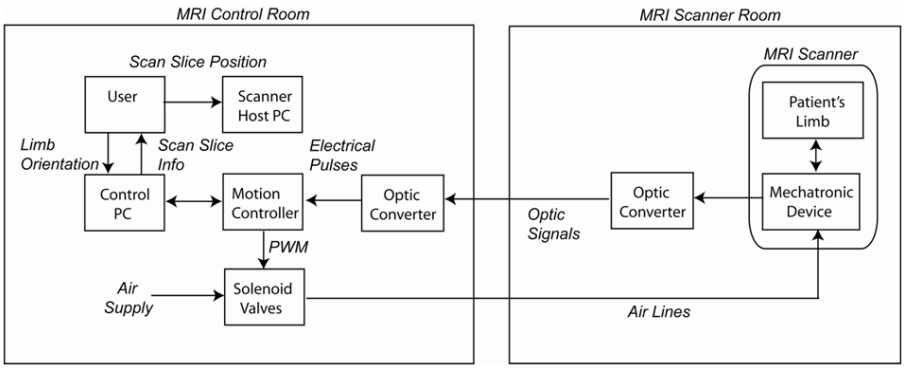


Figure 7.10: Block diagram of the control scheme in the both limb positioning system.

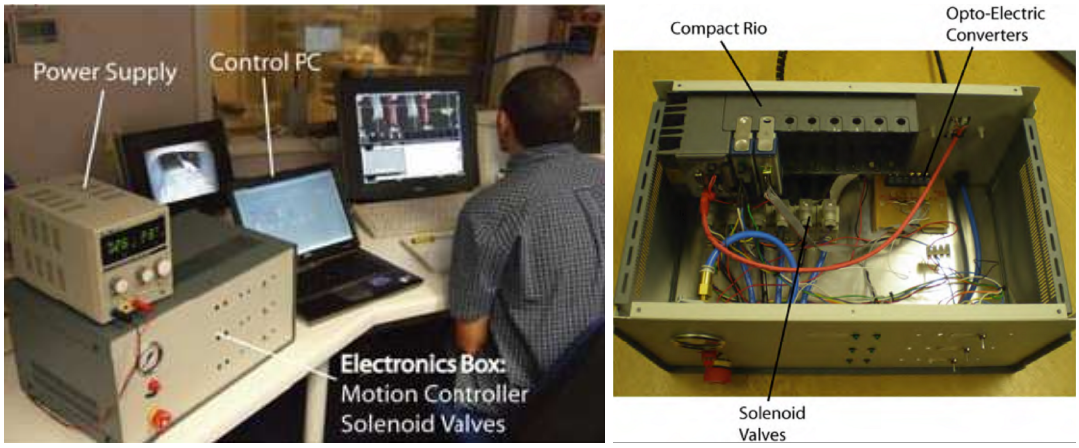
7.5 Control Hardware and Electronics

Cables from the encoders are connected to a shielded aluminium box to convert digital electrical pulses to optical signals and then transmit them through the waveguide to the auxiliary equipment in the control room. The shielded box, as shown in Figure 7.12, which is 2m away from the entrance of the scanner bore, acts as a Faraday cage to block any electromagnetic interference between the electronics inside the box and the scanner. The auxiliary equipment includes: (i) a circuit which converts the optical signals back into electrical pulses, (ii) an FPGA processor (NI CompactRIO 9004) which is in charge of movement control, (iii) six solenoid valves controlling the three pneumatic motors (two for each motor, one for each direction) and (iv) a control PC linked to the FPGA processor controlling the movement of the system with a graphical user interface developed in LabView®. A block diagram of the system communication is presented in Figure 7.10 and the auxiliary equipment setup is illustrated in Figure 7.11. A diagram of the optic converter circuits is shown in Figure 7.12(b) and (c).

Position tracking is ensured by PID position control in each individual axis, which adjusts the airflow to the air turbine by pulse-width modulating the solenoid valves. The PID parameters were auto tuned with the approach mentioned in Chapter 4 with a limb mounted on the system as a load condition. The synchronisation of each axis is achieved by the trajectory control discussed in Section 7.6. Control algorithms of the system including the trajectory control and PID control are implemented in the FPGA processor.

7.6 Movement Trajectory in Lower Limb Positioning

As discussed in the kinematic specifications in Section 7.3, the joint movement of the robot needs to follow a geometric path from a start to an end position to avoid causing discomfort to the patient, and in deriving this path the length of the upper and lower legs must be taken into consideration, such that the hip of the patient can be kept stationary. To maintain synchronisation of each actuated axis for the trajectory, a time function was adapted for generating N position points in the trajectory.



(a) (b)

Figure 7.11: (a) Auxiliary equipment in the control room. (b) Hardware devices inside the electronics box: FPGA processor (NI CompartRIO 9004), solenoid valves and circuitry to converts optical pulses from the position encoders into electrical pulses. Optical pulses are transmitted via optic fibres through the wave guide to the control room.

Let us take Equation (7.2) for Achilles tendon positioning as an example,

$$\begin{bmatrix} Z_a(t) \\ X_a(t) \\ \beta(t) \end{bmatrix} = \begin{bmatrix} L_t cos(\alpha_{mindist} + \alpha_0) + L_c cos\beta \\ L_t sin\alpha_0 - L_t sin(\alpha_{mindist} + \alpha_0) + L_c sin\beta \\ f\left(t = \frac{i}{N}T\right) \end{bmatrix}$$

, where β is the orientation angle of the Achilles tendon, and $(\alpha_{mindist} + \alpha_0)$ is a specific angle of femur such that the distance from the scanned tendon to the isocentre is minimised, $f(t)$ presents a time function, T is the period of the trajectory and i is the i^{th} point out of N. A cubic polynomial function as the time function $f(t)$ was adapted, which can ensure the smoothness of the movement by specifying its velocity at the start and end points, and is based on a Cubic Segment Method (CS). The robot joint movement can be defined to be accelerated smoothly along each axis from its starting position, such as β_0 in the rotational axis to angular velocity Ω, and furthermore decelerate from Ω to zero velocity at β_f, and we have

$$\begin{bmatrix} \beta(t=0) \\ \dot{\beta}(t=0) \\ \beta(t=T) \\ \dot{\beta}(t=T) \end{bmatrix} = \begin{bmatrix} \beta_0 \\ 0 \\ \beta_f \\ 0 \end{bmatrix}$$

, where slopes at $t = 0$ and $t = T$ are set to be zero to ensure the smoothness of the movement. A simple polynomial function of time to satisfy the four constraints with a minimum number of terms is a cubic polynomial, which is identified by four parameters as shown in Equation (7.15).

$$f(t) = a + bt + ct^2 + dt^3 \tag{7.15}$$

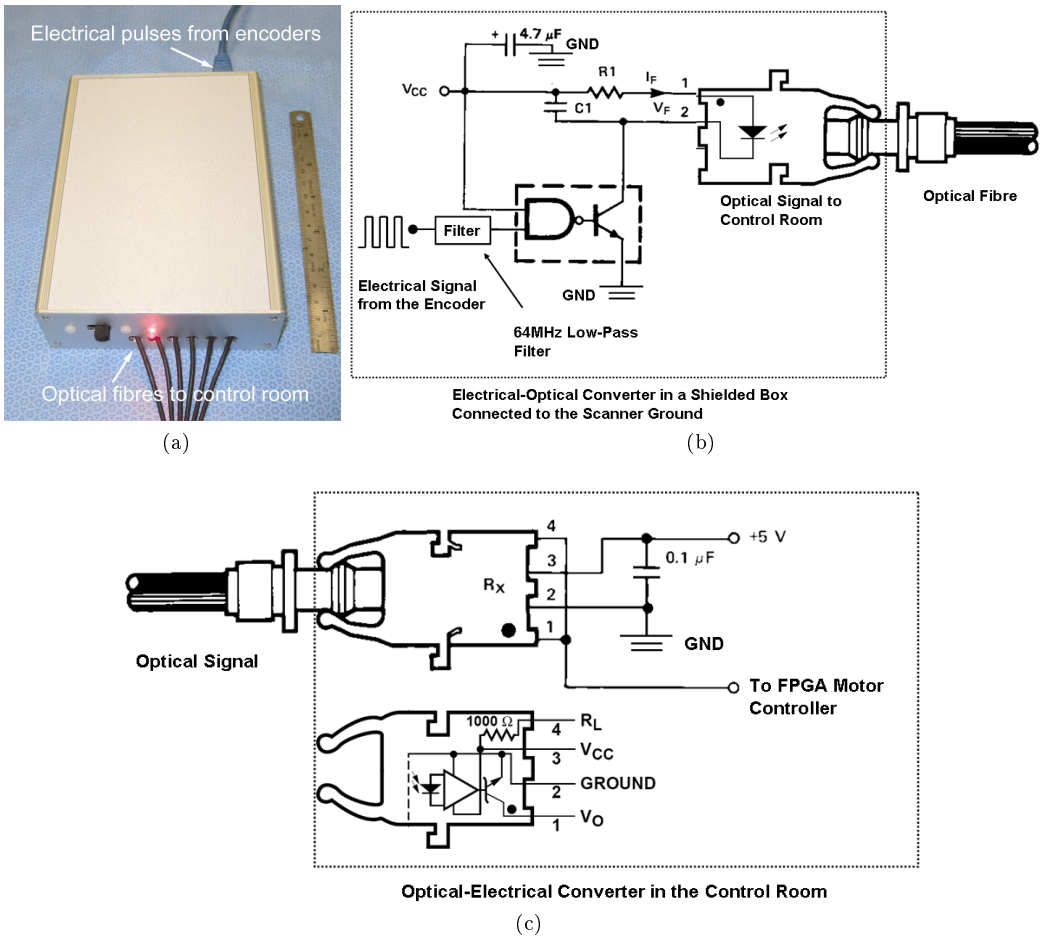


Figure 7.12: A custom design electrical-optical converter capable of dealing with six channels (two for each encoder), (b) its circuit diagram in one channel. The device converts electrical pulses from the encoders to optical pulses and transmits the signals to the receiver in the control room via optical fibres. (c) The circuit diagram of the optical-electrical converter (receiver) in one channel.

where a, b, c and d follow the relations as follows [Wolovich, 1987]:
For a smooth trajectory,. Then we have

$$a = \beta_0$$

$$b = \dot{\beta}_0 = 0$$

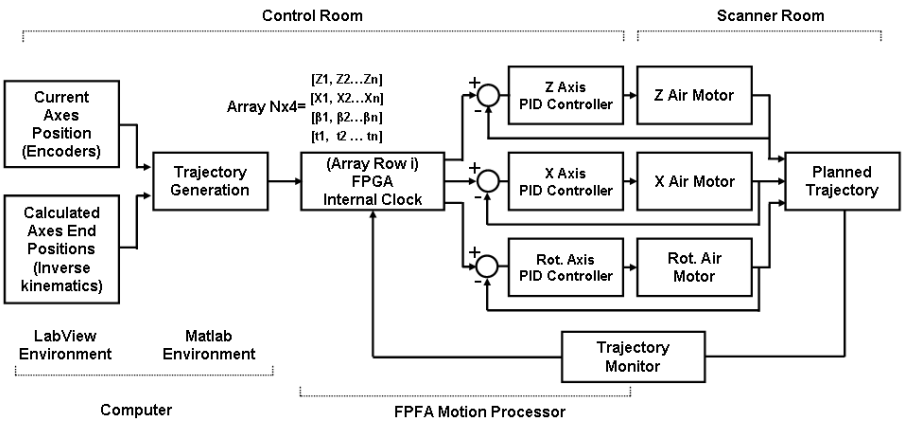
$$c = \frac{3(\beta_f - \beta_0) - (2\dot{\beta}_0 + \dot{\beta}_f)T}{T^2} = \frac{3(\beta_f - \beta_0)}{T^2}$$

$$d = \frac{2(\beta_f - \beta_0) + (\dot{\beta}_0 + \dot{\beta}_f)T}{T^3} = \frac{2(\beta_f - \beta_0)}{T^3}$$

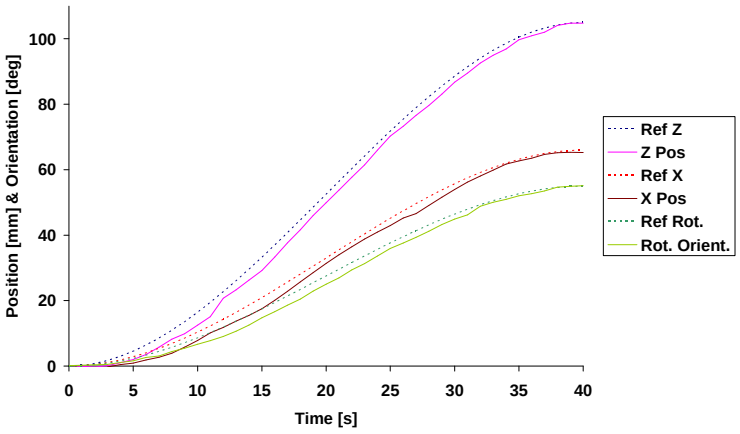
Figure 7.13(a) illustrates a diagram of the trajectory control. With this method, $\beta(t = \frac{i}{N}T)$ for different points in the trajectory can be calculated, and as can the corresponding $\begin{bmatrix} Z_a(t = \frac{i}{N}T) \\ X_a(t = \frac{i}{N}T) \\ \beta(t = \frac{i}{N}T) \end{bmatrix}$.
The trajectory algorithm was implemented in Matlab®, and the positions of the N points pertaining to the path were passed into LabView® and stored in a $N \times 4$ array including the 3 rows of position values for each axis and a row of the corresponding time. The position points were then sent to the PID control of each of the three axes in the robot as the setpoint, and from these a trajectory of movement was generated. Figure 7.13(b) shows the time history of the three axes moving in a planned trajectory.

7.7 Signal to Noise Degradation Test

Five different tests were discussed in Chapter 3 to quantify the MR compatibility of a device to be used in the MR environment, in terms of SNR reduction, image artifact generation, image geometrical distortion, magnetically induced force and torque, and thermal effect. As the pneumatic motor and the encoder are the only active components in the magic angle systems and their compatibility have been demonstrated in Chapter 3, only the SNR reduction test was required to be performed again to quantify the image degradation when the system as a whole is presented and actuated in the scanner. A cylindrical phantom filled with a $CuSO_4$ doped solution was placed at the isocentre of the scanner, and images with a turbo spin echo (TSE) sequence and a True FISP sequence were taken, both with use of the spine coil. The image sequences adapted are listed in Table 7.6, and the experiments were conducted in a 1.5T Siemens MAGNETOM Avanto scanner. The SNR reduction of the image was computed using the method discussed in Table 3.2 in Chapter 3. The test was repeated: (i) when the system was introduced and unpowered inside the scanner with the phantom, (ii) with the system's active components powered but not actuated and (iii) with the system actuated. Results of these experiments are shown in Table 7.7. The maximum reduction in SNR was found to be always under 4%, which verifies the MR compatibility of the upper limb and lower limb devices with no significant SNR reduction.



(a)



(b)

Figure 7.13: (a) Block diagram of the trajectory control in the low extremity positioning system. Cubic Segment method is adapted to ensure the joint movement smoothness and synchronisation of each actuated axis. (b) Measured position for all three axes following a defined trajectory.

	TR (ms)	TE (ms)	FA (degree)	No. of slice	Thickness of slice (mm)	Spacing (mm)	Resolution	FOV (mm)	BW (Hz/px)
TSE	3600	120	180°	15	5	5	256 ×256	300	130
True FISP	22	10	30°	15	5	5	256 ×256	300	130

Table 7.6: Details of the image sequences

		TSE			True FISP		
		Power off	Power on	Actuated	Power off	Power on	Actuated
3DOF system	SNR Reduction	1.7%	3.2	3.5%	2.3%	3.5	3.9%
1DOF system		1.4%	1.6	1.31%	1.3%	2.64	1.76%

Table 7.7: SNR reductions in image sequences of TSE and True FISP

7.8 Functional Hazard Assessment and Safety Measures

To evaluate the potential hazards, functional hazard assessment was conducted in the upper and lower limb positioning systems as listed below, and the corresponding safety features in the system designs were highlighted.

1. Structural failure of the devices:
   The two positioning devices were filed with all sharp edges removed. Being designed to support and position human limbs, the devices have sufficiently strong mechanical structures which are unlikely to fail when used in reasonable care.

2. Control failure of the limb positioning trajectory:
   The two devices were designed to facilitate the magic angle effect by positioning and orientating the scanned tendinous tissue at the magic angle. The movement trajectory is monitored by the clinician who can override the robot movement command if necessary. An emergency stop button is available to immediately stop the movements in case of failure. In addition, the pneumatic motors were designed to slip and decouple with the gears involved in joint movements when they encountered any strong resistive force. This safety feature intends to avoid damaging patient limbs when the control fails.

3. Electrical failure of the devices and the control electronics:
   The two limb positioning devices are actuated by pneumatic motors, and optical position encoders are the only electronics embedded. These are powered by a 5V battery source. All conductors in the devices were insulated in such a manner that they could not be touched by either the patients or the clinicians. The positioning devices are electrically safe, containing no exposed conductive parts, and the low voltages and currents mean they are very unlikely to cause sparking or burning. The electronics box containing all of the control electronics, is placed in the control room, and powered by a standard 24V power supply. The two devices and the electronics box were tested and passed the electrical safety test by a registered electrician.

4. MR environment induced hazards:
   Detailed analysis has been performed in Chapter 3, in the aspects of MR safety and potential inferences between the robot components and the scanner.

7.9 Preliminary Trials

7.9.1 Procedure

Preliminary clinical trials were performed on a group of volunteers with a variety of body sizes to demonstrate the functionality of the designed system in orientating target tissue at desired angles. Five types of tendons: the Achilles tendon, the patellar tendon, the quadriceps tendon, the elbow tendon and the vincula brevia tendon in forefinger, were selected to be the imaged targets, as our radiologist suggested that tendon ruptures and inflammation commonly occur in those tendons. MR images were taken in a 1.5 T Siemens MAGNETOM Avanto scanner, with a turbo spin echo sequence (TSE) used to image the tendons (Table 7.8). The tendons were then oriented from γ_0 (the initial angle relative to the main field) to angles of 20, 30, 40, 45, 47, 49, 50, 51, 53, 55, 57, 59 and 61degrees with respect to the main field of the scanner and γ_f (the angle that the patients' knees or ankles collided to the scanner wall), with an image taken each time.

The desirable image format is that the plane of the image is always the same relative to the target tissue, for every angular orientation of the tissue. This means that images are initially sagittal, when the tendon is approximately parallel to the main field, and then become nearer to transverse after movements of the tendon are made and its angle relative to the main field increases. As the surface coil sensitivity is potentially affected by its magnetisation and its location with respect to the scanner isocentre, the signal intensity at the tendon received by the coil was also affected. To consider only the image contrast variation, that was caused by the magic angle effect, the signal of the tendon was normalized with the signal of a proximal structure in the tissue of which the intensity was only subject to magnetisation; for example, bone marrow, which consists of a large percentage of lipids (Refer to Figure 7.14). Magic angle effects are insignificant in bone marrow, and thus, its change in signal intensity is dominantly due to the change of its relative position to the isocentre. The experimental setups of the two systems in the MRI scanner are illustrated in Figure 7.15. Figure 7.15(a) shows the 3DOF lower limb system placed on the scanner table with the patient left leg strapped tightly to the rotational platform with a Velcro strap. The patient was in left lateral position and a flexible surface coil was attached around his ankle for better image signal from scans of his Achilles tendon. Figure 7.15(b) shows the patient in right lateral position with a similar system configuration, but with the surface coil strapped around his knee for scans of his patellar tendon and the quadriceps tendon. Figure 7.15(c) shows the setup of the 1DOF upper limb system on the table with the patient in supine position. His forearm and upper arm were stabilised firmly on the rotational platform with an angle formed between the elbow tendon attached to the forearm and the main field, and a similar posture was used for imaging the vincula brevia tendon in the forefinger, in which the hand was kept open and stabilised with a plane fixture. The flexible surface coil was used during scans, although it is not shown in Figure 7.15(c) for clarity reason.

7.9.2 Results and Discussion

The experimental results obtained from imaging the Achilles tendon are illustrated in Figure 7.16, showing the normalised signal of the tendon plotted against at its orientation, in four volunteers. The experiments started at an initial orientation of the tendon γ_0, at which the platform was at its start



Figure 7.14: Average signals in the region of interest RIO1 at the tendon is normalized with that at a proximal structure RIO2 which is only subject to magnetisation (such as bone marrow).

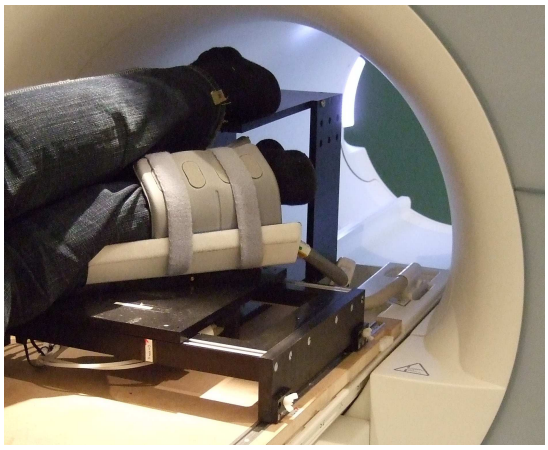
	TR (ms)	TE (ms)	FA (deg)	No. of slice	Thickness of slice (mm)	Spacing (mm)	Resolution	FOV (mm)	BW (Hz/px)	Scan Time (s)
TSE	1800	83	180°	9	5	1	256×256	300	130	1m33s

Table 7.8: Details of the TSE image sequence

position, parallel to the main field, and ended at the angle γ_f, at which the patients' knees had collided with the scanner wall. For the four patients, the end angle γ_f, was always larger than 65degrees. The end angles in the four cases were 69, 68, 65 and 72degrees, and were subject to the size of the patients' legs. It is reported that even for the largest patient (height 182cm) of the four, it was possible to have his ankle tendon placed at 65degrees with the use of the limb positioning system, before his knee collided with the scanner wall; although the ankle images were slightly affected by artifacts due to the close distance of the surface coil to the body coil of the scanner.

As shown in Figure 7.16, it is demonstrated in the trial results that almost a two-fold increase in signal intensity was observable at around 40-45degrees on average, after which the signal largely increases and peaks at 55degrees with a 12-24 times signal intensity increase. The MR images of the Achilles tendons at the magic angle and at the initial orientation γ_0 in Figure 7.17, illustrate the significant increase in signal intensity achieved by exploitation of the magic angle effect; the tendon is clearly visible in Figure 7.17(b), compared with the apparent void in the same region of the ankle at the initial orientation in Figure 7.17(a). At greater than the magic angle of 55degrees, the signal intensity then reduces in value swiftly, as the scaling factor of the dipolar interaction between protons, which is proportional to $3cos^2\theta - 1$, is minimal at the magic angle of 55degrees. The results obtained are consistent with the magic angle theory discussed in Section 1.2.2 in Chapter 1.

The experiments were repeated to examine the magnitude of the magic angle effect with the patellar tendon and quadriceps tendon, using the lower limb system; the elbow tendon and vincula brevia tendon in forefinger were also imaged with the use of the upper limb system. Figures 7.20-7.24,



(a)



(b)



(c)

Figure 7.15: The 3DOF lower limb system with patients set up for scans of: (a) the Achilles tendons, (b) the patellar tendons and quadriceps tendons. (c) The 1DOF upper limb system for scans of elbow tendons and vincula brevia tendons in forefinger.

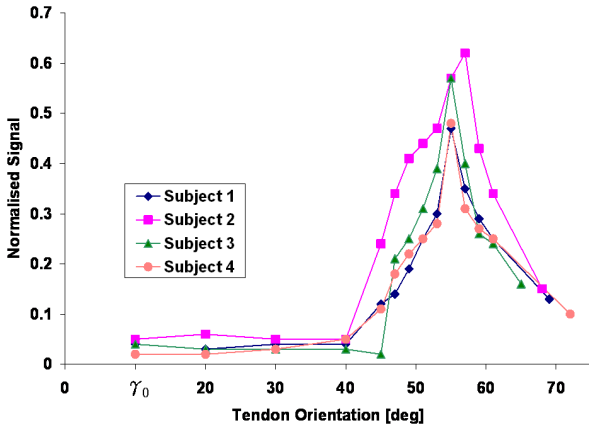


Figure 7.16: Signal intensity at the Achilles tendons from four volunteers normalised to bone marror. Increase in the signal is observed from around 40degrees, peaks at around 55degrees, and then decreases rapidly. Subjects had their knee in touch with the scanner wall at different angles when the experiments ended, but all were at greater than 65degrees. The final angle γ_f is subject to the size of patients.



(a) (b)

Figure 7.17: (a) and (b) respectively show the 0degrees and 55degrees images of a slice through the Achilles tendon of a volunteer acquired using the 3DOF system.

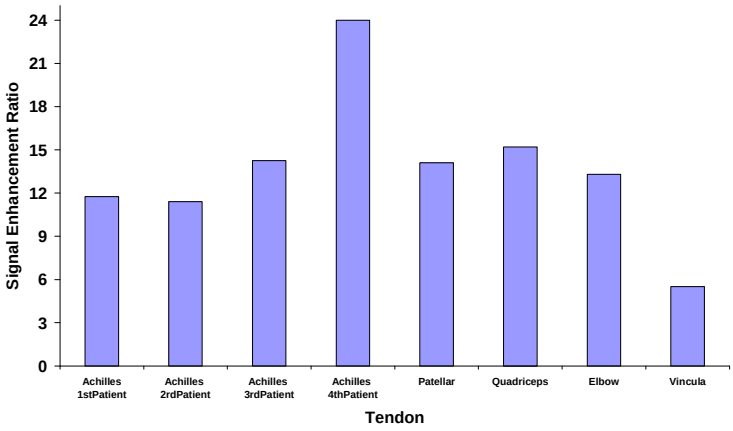


Figure 7.18: Signal enhancement ratios of different tendons at the magic angle. Comparison between the signal intensity at magic angle and that at their initial orientation γ_0.

illustrate the results of the experiments with an obvious increase of tendon signal intensity at the magic angle; their signal enhancement ratios are plotted in Figure 7.18. The ratio is a comparison between the signal intensity at the magic angle and that at the initial orientation γ_0, and it was found to have a maximum value of 24 times in the case of the scans of the Achilles tendon of the fourth patient, and a minimum of value 5.5 times in the case of the scans of the vincula brevia tendon. This ratio varies significantly in different tendons and even in different patients, subject to the tissue structures and properties of a particular tendon. The magic angle effect in the vincula brevia tendon is visualised in Figure 7.24, in which the tendon orientations varied incrementally from 0degrees to 59degrees are depicted and the tendon is seen to become gradually more visible as the magic angle is approached (Figure 7.23).

Examination time taken to perform the entire procedure for each subject, is another factor required to evaluate the effectiveness of the two systems to be applied in clinical environments for diagnostic purposes. Figure 7.25 shows the hardware setup time and the time for acquisition of the entire set of images for different angles. For the Achilles tendon scans, the time taken for the whole procedure on the first volunteer was 78mins and remained around 45mins for the third and fourth; these were the longest procedure times. The next longest times taken were for the patellar and quadriceps tendon scans, which were around 42-43mins. Although a large time was reported for the first subject, the successive scans were drastically reduced due to the development of an optimised method of performing the procedure, found through experience. For the elbow tendon and vincula brevia tendon scans, the times taken for both the hardware setup and the image acquisition were shorter using the 1DOF system (around 35-36mins in total), due to the simpler design of the system, and the existence of no redundant joints and components leading to a shorter learning curve. In each of the trials, no significant discomfort was reported during the motion of the systems, but more cushion support was suggested to help the subject maintain their position in the scanner.

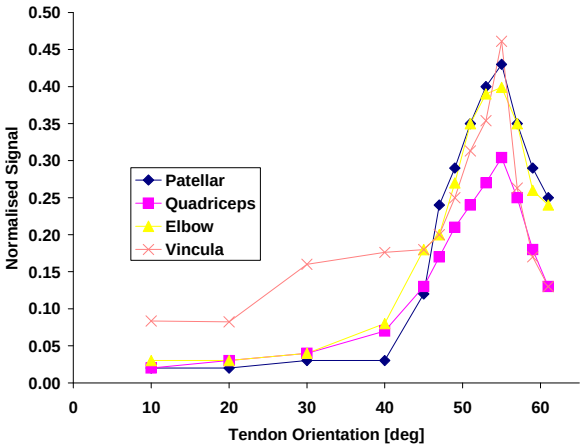
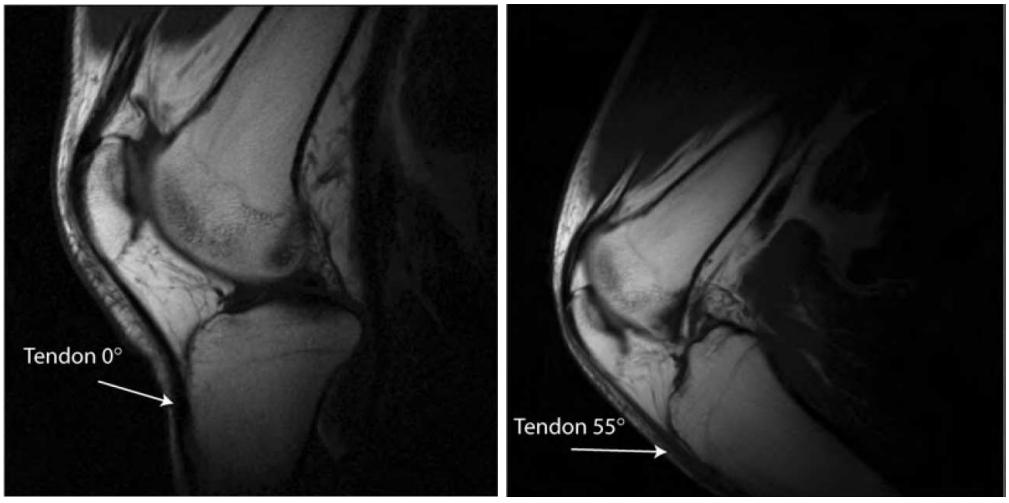
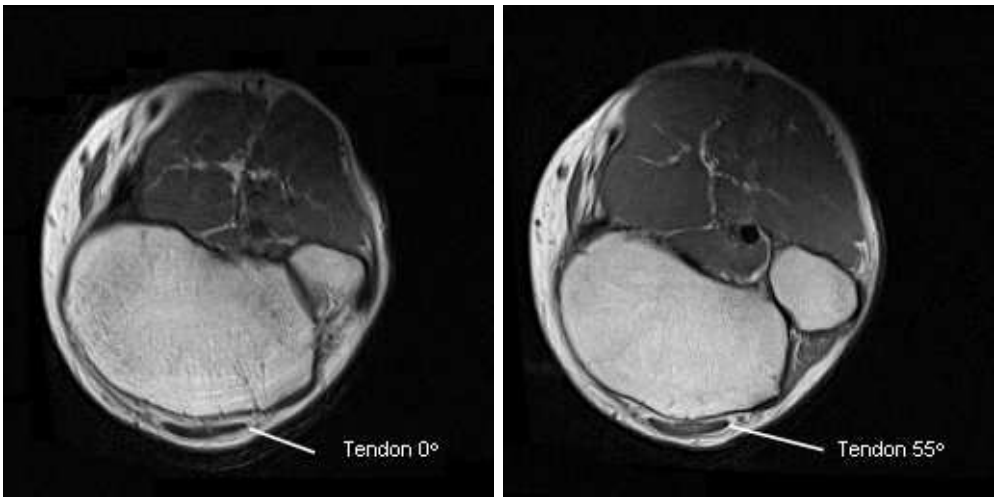


Figure 7.19: Normalised signal intensity at the patellar tendon, quadriceps tendon, elbow tendon and vincula brevia tendon in forefinger plotted against their orientation to the main field.



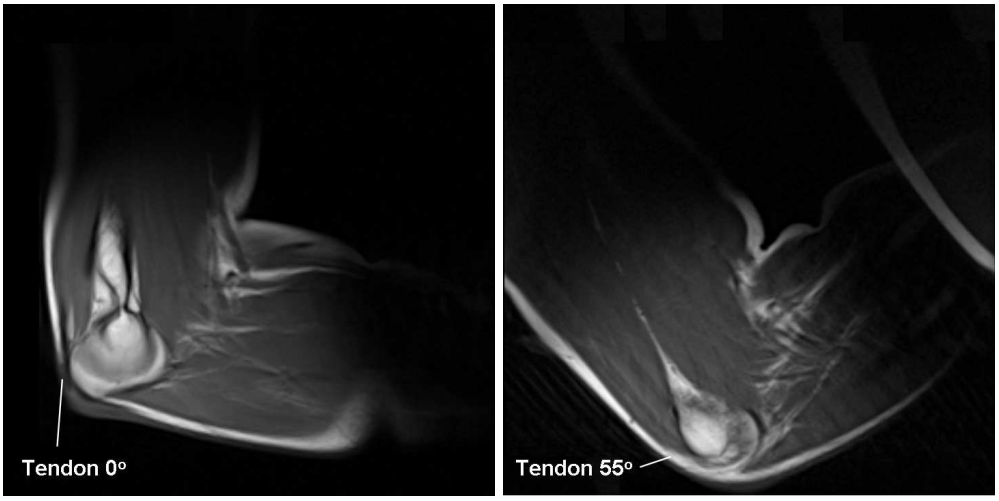
(a) (b)

Figure 7.20: (a) and (b) respectively show the 0degrees and 55degrees images of a slice through the patellar tendon of a volunteer, acquired using the 3DOF system.



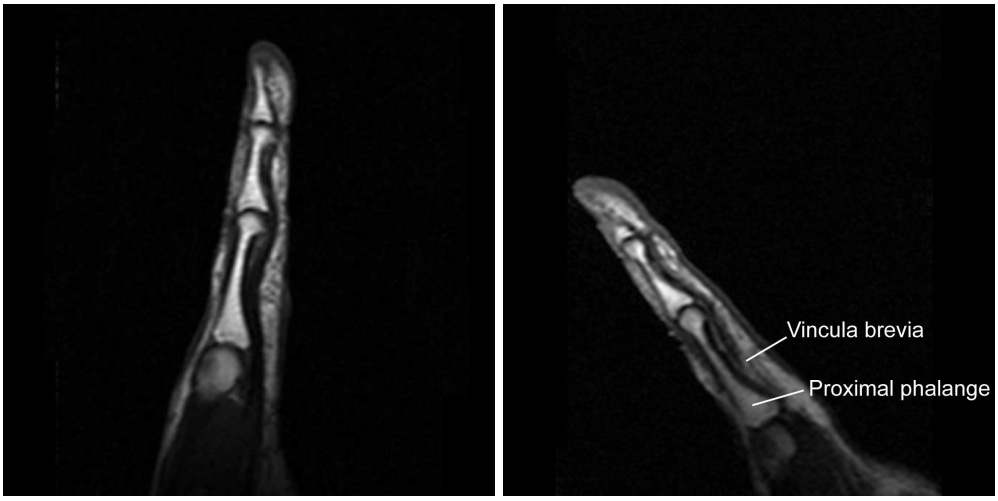
(a) (b)

Figure 7.21: (a) and (b) respectively show the 0degrees and 55degrees images of a slice through the quadriceps tendon of a volunteer, acquired using the 3DOF system.



(a) (b)

Figure 7.22: (a) and (b) respectively show the 0degrees and 55degrees images of a slice through the elbow tendon of a volunteer, acquired using the 1DOF system.



(a) (b)

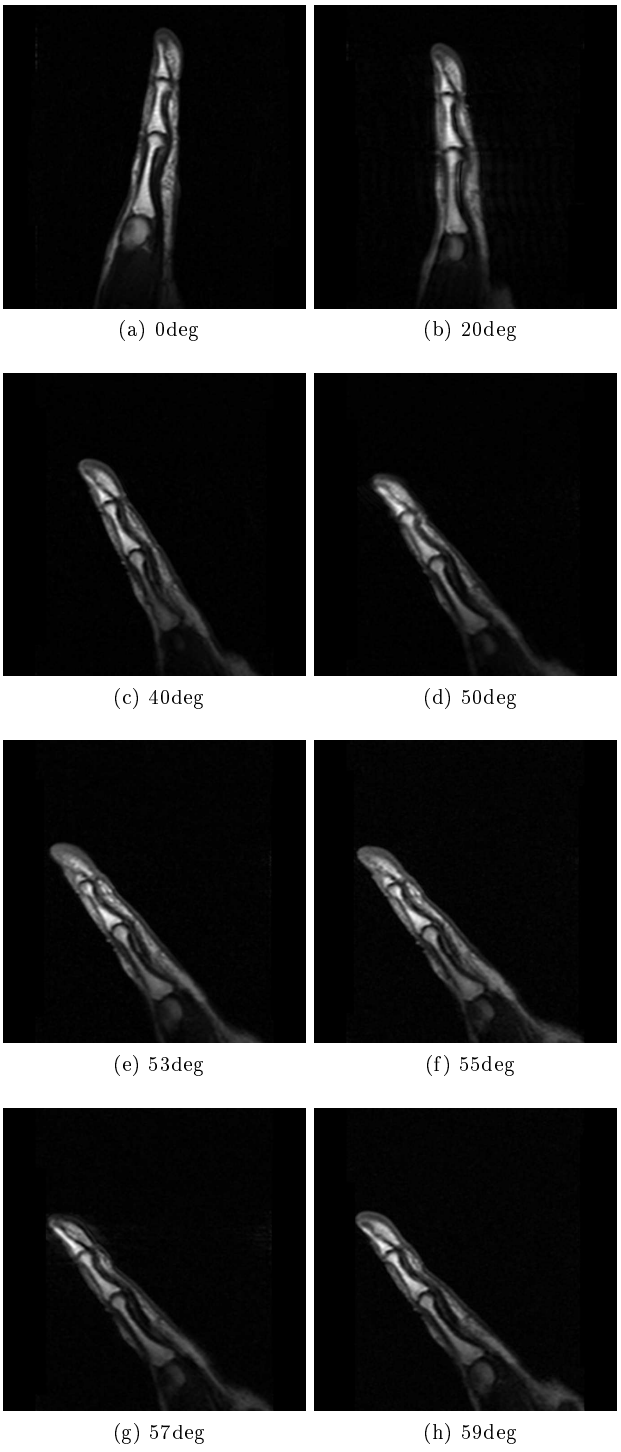
Figure 7.23: (a) and (b) respectively show the 0degrees and 55degrees images of a slice through the vincula brevia tendon in forefinger of a volunteer, acquired using the 1DOF system.

7.10 Conclusion

Two mechatronic systems for upper and lower extremity positioning have been presented in this chapter as a diagnostic tool for tendinous diagnosis and magic angle related research. The kinematics of a 3DOF lower limb system was first studied to relate each axis in the system design. Kinematic relationships of each DOF and the required joint movements were derived to optimise the distance from the target tissue to the scanner isocentre at different orientations, although the kinematics of the 1DOF upper limb system was not discussed due to its simplicity.

The development of the two mechatronic systems based on the design specifications and guidelines was presented: (i) a 1DOF device to facilitate magic angle effect diagnostic procedures in the upper extremities including the hand, forearm and elbow, in which a patient has his elbow strapped in a rotary platform; and (ii) a 3DOF device for lower extremity procedures including the knee, the ankle, and the foot, in which a patient's ankle is strapped in a movable platform and the three axes work together to position the target. Surface coils can be added to enhance the image quality of the scanned tissue. Both systems are coupled with highly geared down pneumatic motors, and optical encoders, and their performance and MR compatibility have been evaluated in Chapter 3 and 4.

Both systems have had their overall SNR reduction quantified, and a wide range of tendons, including the Achilles tendon, patellar tendon, quadriceps tendon, elbow tendon, and vincula brevia tendon in forefinger were studied in the preliminary trials from a group of volunteers, to demonstrate the functionality of the two systems in assisting tendinous related diagnosis with exploitation of the magic angle effect. The selected tendons are the type of commonly injured tendons suggested by clinical professionals and radiologists. The functionalities of the systems have been verified in imaging tendons on a group of volunteers with different lengths of upper and lower limbs. The results showed a 4-24 times increase in signal intensity of the different tendons at 55degrees, as anticipated in theory.



(a) 0deg (b) 20deg

(c) 40deg (d) 50deg

(e) 53deg (f) 55deg

(g) 57deg (h) 59deg

Figure 7.24: MR images of an vincula brevia tendon taken from 0degrees to 59degrees

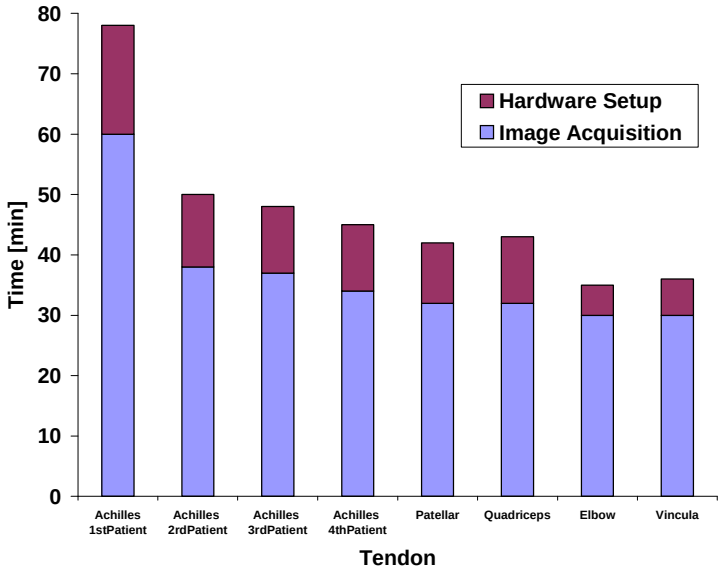


Figure 7.25: Time taken for hardware setup and image acquisition for different tendinous imaging studies

The two mechatronic systems have demonstrated their excellent performance in positioning limbs inside the scanner, and their ease of control and capability of reducing diagnostic time by quick and accurate orientation of target tissue to the magic angle. The systems are designed as scanner independent, which means that they are suitable for scanners of different makes and models and with no problems of interfacing and system connection. Even though only two general limb positioning systems were presented here, more specific designs can be developed with a similar methodology, and tailor designed medical devices equate to a reduction of design complexity, redundant movement joints and functionality, allowing more robust and simpler systems with less training time for clinicians to adapt to the technology.

Chapter 8

Conclusions and Future Work

8.1 Introduction

This chapter provides a concise summary of the research presented in this thesis, followed by a discussion of the conclusions that can be drawn and future work foreseen. Reflecting on the scope of the research objectives as stated in Section 1.3 in Chapter 1, the conclusions are divided into the following four main topics, which comprise:

- The investigation of a systematic approach to evaluate the MR compatibility of actuators, force sensors and position sensors usable in the MR environment. Those components which can operate whilst suffering from no mutual interference are the fundamental elements for general MR robots.
- The investigation of control strategies for use with the adapted actuators being implemented for interventions with different specifications, an actuator for fine positioning and fast response suitable for haptics and force control in an MR robot, and a different actuator for high force and speed suitable for general positioning.
- The development of a robotic system to perform transrectal prostate biopsy under real-time image guidance. The system is incorporated with a 1.5T scanner to display tracking images to the users, for achieving needle alignment to the suspected target tissue.
- The development of robotic systems to facilitate tendinous related diagnosis and studies with the exploitation of the magic angle effect in a 1.5T scanner. The two systems, one for upper limb, and the other for lower limb application, are capable of positioning tendons at the magic angle, whilst optimising the spatial constraints imposed by the scanner bore.

Finally, suggestions for future work in all four areas are given, and a list of publications based on this research follows.

8.2 Chapter Summary

Chapter 1 started by describing the research motivation and objective of the integration of medical robotics with the MR imaging modality for image guided diagnosis and therapy, which is driven by the

benefits of MRI, in that high resolution preoperative scans of target tissue and intraoperative real-time images are available without the exposure of patients to ironising radiation. The design and development of MRI compatible robots is the way to achieve the objective, but this produces the major problem that many conventional mechatronic components in actuation and sensing cannot perform acceptably in the MR environment and interfere with the RF signal from the scanner. Thus, development of a systematic approach to evaluate the MR compatibility of active mechatronic components, and investigation of control strategies in MR compatible actuators are the first two objectives. This approach and the technology developed were adapted to develop two medical robots; one to perform transrectal prostate biopsy with MR guidance, and the other to position tendinous tissue inside the scanner bore to make use of the magic angle effect for better diagnostic images. They are the second and third objectives of this research work.

Chapter 2 commenced by providing a brief background knowledge of MR imaging techniques, to assist the reader in understanding the approaches used in the research for the development of an MR robot. This information included a brief synopsis of the MRI working principle, the elementary components of the scanner including the main magnet, the gradient, the RF transmit and receive coil, and the computer system. Due to its imaging principle, the MR environment imposes stringent constraints on MR robot designs in terms of the electromagnetic interferences that can be caused and the limited free space in the bore which restricts the access of the clinician. The spatial restriction inhibits the ability of the clinician in performing free hand interventions in the imaging volume, as well as the tactile information available during the procedure. After the technical descriptions of MRI, there was an overview of the state of the art of the mechatronics solutions for use in MR robotics, which are classified into: MR compatible actuators based on the principles of ultrasonic motor, electromagnetic coil, pneumatic and piezoelectric principles; position sensors based on optical principles with fibre optic cables for communication to and from the scanner room; and force sensors also based on optical principles and with the same signal transmission method. At the end of this chapter, a review focused on the current development of MR percutaneous robots was presented; those robot required the characteristics of accurate positioning and needle manipulation, and their review provided an insight into the design of a robotic system with different specifications and the clinical needs that must be taken into consideration.

Chapter 3 focused on the descriptions of a systematic approach to evaluate the usability and compatibility of active mechatronics components in the MR environment. It commenced by introducing the concepts of MR compatibility and MR safety, and continued with an explanation of magnetic susceptibility as an important material property relating to artifact generation. A series of tests were then presented to evaluate the components in terms of their magnetically induced force/ torque, SNR reduction, artifact generation, geometrical distortion and thermal effect caused in the MR environment.

Chapter 4 related to the control issue of using MR compatible actuators for positioning and force control related functions. Due to the challenges imposed by the MR environment, compatible actuators must be based on non-magnetic actuation principles. A proposed alternative was to use a special type of ultrasonic motor, the Piezoleg, which is highly compatible compared with other ultrasonic motors, and is possible to be adapted for use in/near to the isocentre of the scanner. Its working principle and custom design control circuit were presented. Its fast response makes its ideal for implementation

to force control related applications; whereas its non-backdrivable and nonlinear characteristics raise practical difficulties that must be overcome. As such, a neural network based speed controller was proposed to linearise the performance of the actuator, and a haptic control scheme was implemented and evaluated, demonstrating the feasibility of use of this motor for haptic applications in an MR robot. Despite the excellent MR compatibility and fast response of the Piezoleg, its actuation principle limited the force and speed output, and therefore a pneumatic rotary motor was proposed for applications where higher generated force and speed were required, ideally for positioning heavy loads. The actuator was characterised in open and closed loop control tests, and a PID control scheme was implemented in the motor, which controls its speed by pulse-width modulating the airflow. The PID controller was designed to have its parameters automatically tuned for different load conditions, and its control performance was demonstrated in a test unit to position a variety of load conditions, from 0N to 50N, with accuracy of up to 0.25degrees.

Chapter 5 and 6 narrated the development of a robotic system for transrectal prostate biopsy under MR guidance as well as the evaluation of its functionality in three cases of clinical trials. The research motivation was driven by the limitations of the conventional transrectal ultrasound biopsy, i.e. poor image quality for guidance and high rate of false negative diagnoses. Therefore a prostate biopsy system was developed, which comprised of an endorectal probe, a haptic needle firing unit, and a Cartesian robot to move the probe within the rectum for needle alignment to the suspected target tissue. The needle firing unit consists of two actuated DOF to insert, fire and retract the biopsy needle in a quick time, when the needle alignment is confirmed. The Cartesian robot and the needle firing unit are actuated by the pneumatic motors and ultrasound motors respectively. The needle movement is tracked by both optical encoders embedded in each axis of the robot and fiducial markers embedded in the head of the endorectal probe. A detailed kinematics study and a workspace analysis of the system were also presented, together with a description of its supporting electronics. The user controls the robot movement inside the scanner room by means of a touch screen console, linked to a PC, embedded in a shielded enclosure. The needle alignment approach was firstly performed by the robot joints moving to the required position according to the calculation from the inverse kinematics after the input of the target position by the user. This constituted a gross positioning step which was then followed by manual control for fine alignment. The whole system was evaluated in terms of its MR compatibility and targeting accuracy, followed by full clinical trials on three patients to examine its functionality.

Chapter 7 focused on the development of two robotic systems to facilitate tendinous related diagnosis with exploitation of the magic angle phenomena, and their preliminary trials. Two systems, one with 3DOF for positioning tendons in the lower limbs, and the other with 1DOF for positioning tendons in the upper limbs, were actuated by the pneumatic motors with tracking achieved using the optical encoders. The components adapted had been evaluated in terms of their MR compatibility and control performance in Chapter 3 and 4. The two systems are capable of positioning tendons in the ankle, knee, elbow and hand. Kinematics studies were presented to allow orientation of the target tendon at a specific angle, and to have the tendon positioned closest to the isocentre for good image quality, and to avoid collision between the patient body and the scanner bore. The MR compatibility of both of the systems were demonstrated in a 1.5T scanner with no significant SNR reduction. An

accuracy of 1degree and 0.5degrees were achieved in the lower and upper limb systems respectively, showing the capability of the robot designs for repeatable and robust positioning. The functionality of both systems were further verified with preliminary trials on four volunteers with their Achilles tendons, patellar tendons, quadriceps tendons, elbow tendons, and vincula brevia tendons in forefinger positioned and imaged. The target tissues were imaged at different orientations to observe the incremental increase in signal intensity brought about by the magic angle effect, and an increase of 4 to 24 times was reported in accordance with the theory. The time taken for the whole procedure including hardware setup and image acquisition, was reported to be within 35 to 45mins, showing the ability and the clinical value of the devices to assist in magic angle related diagnosis.

8.3 Conclusions

8.3.1 MR Compatibility Evaluation

MR Compatibility of an mechatronic component depends on a large number of the factors, inherent to the component itself as well as to the scanner. A systematic approach was adapted based on five individual tests to evaluate the usability of a component in the MR environment. The conclusions that can be drawn with respect to the effectiveness of the approach are:

- A series of tests to evaluate the usability of mechatronic components were presented, which include: (i) to determine the magnetically induced force and torque on the components by the main magnetic field, if any magnetic material is involved; (ii) to quantify the signal to noise ratio reduction due to the electromagnetic noise emitted from electrical and electronic components involved; (iii) to evaluate the level of artifact generation (seen as an void in an MR image) and (iv) to evaluate geometrical distortion (seen as image warping), caused by materials with high susceptibility; and (v) to determine any thermal effect induced by switched gradients on conductive materials which potentially form a closed loop for induction of eddy currents. Based on the presented methods, an ultrasonic motor, a pneumatic motor, and a position and force sensor were thoroughly evaluated in terms of their MR compatibility.

- Selection and evaluation of mechatronic components usable in the MR environment without generating mutual interferences, are much more difficult than the selection and evaluation of passive components, which can be found in plastic or non-magnetic and non-conductive materials. In any case, active components such as actuators, position sensors and force sensors are the fundamental elements in any general robot systems. Commercially available components generally contain magnetic and electrical parts, affecting the image quality at a certain level. Although it is possible to custom design all robot components with compatible materials and with nonmagnetic principles, careful screening and systematic evaluations of commercially available components can also assist robot design to achieve a specific good level of MR compatibility. A good MR robot design should be a balance of system simplicity, cost effectiveness, and an acceptable level of resultant image quality.

- The impact which a mechatronic component causes to the scanner is subject to a large number of factors both inherent to the component itself such as its electrical conductivity, shielding,

magnetic susceptibility, geometry, and to the scanner such as field strength, image sequence, and the scanner calibration. Performing a rigorous analysis of each of these factors for different components would be impossible within the time constraints of a PhD research. The five tests presented act as measures to enable preliminary evaluation of the usability of a component, and provide a very brief estimation of the MR compatibility of an assembled robot design with those components. However, the only way to conclusively demonstrate the MR compatibility is by testing of the operating robot prototype on a specific scanner. In any case, the proposed test methods were applied to the selected components for the robot designs, which were later demonstrated to be MR compatible at an acceptable level for their particular interventions intended.

8.3.2 Control Strategies of MR Compatible Actuators

A special type of ultrasonic motor, the Piezoleg, and a pneumatic rotary motor, were adapted for applications with different requirements. The conclusions that can be drawn with regard to their individual control strategies are:

- Due to the higher level of MR compatibility compared with other ultrasonic motors, the Piezoleg was applied to generate actuation in percutaneous interventions because of its greater usability in/near the isocentre, and was also applied to reconstruct force feedback at the master control interface during prostate biopsies, because of its fast control response. Due to its nonlinear characteristics, a neural network based speed controller was developed to learn the characteristics and to linearise its performance. Due to its non-backdrivable characteristics, a haptic control scheme based on explicit force control was implemented in a master-slave test unit to demonstrate the feasibility of implementing haptics in an MR percutaneous robot.

- Despite its excellent MR compatibility, the force and speed which a Piezoleg motor can generate are limited, and commercial compatible actuators with the characteristics required for positioning a heavy load were not available. Therefore, a pneumatic motor based on the rotation of a turbine rotor driven by a pulse-width modulated airflow, was adapted, and the high speed of the rotor was geared down by a set of modular gearboxes. The motors have a simple design, very cheap manufacturing cost, and are possible to reproduce by the rapid prototyping technique in a short period of time. Open loop and closed loop control tests were performed to characterise the motor, and its maximum speed and torque were 15.5rpm and 2.2Nm, with an accuracy of 0.25degrees. This torque was equivalent to generating 55N at the mount arm of 40mm, sufficient for most of the medical applications. An optimised duty period of 150ms was selected as a compromise between the linearity of the motor speed and the motion smoothness for good position control. Despite its desirable speed and torque output, the motor performance varies subject to the load conditions. A PID auto tuning control scheme was implemented to the motor, for selection of optimal control parameters under varying load conditions, and a significant improvement of motor performance was demonstrated.

8.3.3 Prostate Biopsy System

The MR compatible biopsy system was designed to perform transrectal prostate biopsy under real-time image guidance. The conclusions that can be drawn with regard to the feasibility of the proposed biopsy system are:

- An MR compatible robot prototype was developed with compatible components verified in Chapter 3, and the compatibility of the system as a whole was verified as well, to demonstrate its usability in MR interventions with no noticeable interference to the image quality. The robot consists of a Cartesian positioning robot made by connection of 1DOF modules, and a haptic firing unit incorporating a force sensor to provide force feedback to the user during the procedure. Needle alignment was achieved by first moving the robot joint to a desired position calculated from the inverse kinematics. As this step required the position of the rectal sphincter centre and assuming it as a fixed position, the automatic approach for needle alignment was used only for gross positioning. Manual needle alignment then followed for fine positioning, with the use of the real-time tracking images as a visual feedback to the user for navigation. The tracking was achieved with a modified FLASH 2D sequence, to detect the 3D coordinates of two fiducial markers embedded in the endorectal probe. The robot prototype and the proposed alignment approaches led to three successful clinical trials, with the procedure time around 40mins, which achieved our system specifications.

8.3.4 Magic Angle Positioning Devices

The presented upper limb and lower limb positioning systems, are two practical mechatronics systems to facilitate magic angle related study, and have a large clinical application in tendinous diagnosis. The conclusions that can be drawn with respect to their designs and preliminary trials are:

- Both limb positioning systems were designed to be used in 1.5T closed bore scanners which are commonly applied in hospitals. The devices were actuated by pneumatic motors because of the high force required for movement of a limb and also the availability of air supplies in most MRI suites. Kinematics for limb positioning were studied to orientate a target tendon to a specific angle, placing it as close as possible to the isocentre to assure good image quality, whilst taking into consideration the spatial constraint imposed by the confined scanner bore. By placing the supporting electronics in the control room and transmitting a PWM airflow and optical position signals via a waveguide, the system demonstrated excellent MR compatibility. To demonstrate the functionality of the systems to enhance image quality in tendinous tissues, preliminary trials were carried out on four volunteers to have their Achilles tendons, patellar tendons, quadriceps, elbow tendons and vincula brevia tendons in forefinger imaged at different angles. Results were reported to show a 4 to 24 times increase in the signal intensity of the tendons with the exploitation of the magic angle effect, and the time taken for the whole of any of the procedures was around 35-45mins. This result shows the feasibility of applying these systems into clinical environments in the future.

8.4 Future Work

8.4.1 Adaptation in 3Tesla Scanners

A systematic approach was presented to evaluate the mechatronic components and further work on this subject could include the following topic:

- With the use of higher magnetic fields, 3T scanner can provide better image quality over their 1.5T counterparts, and they have started to be adapted in hospital environments, although 1.5T scanners are still prominent in clinical diagnosis. Adaptation of the MR robot to a 3T scanner would be the future trend, meaning that the used mechatronics components as well as the whole system must be evaluated once more in the 3T environment before the compatibility claims can be made at the new field strength. Low-pass filters adapted in the 1.5T environment are favorable in the 3T environment for RF elimination with their greater noise attenuation at the new Larmor frequency of 128MHz. Endorectal coils and fiducial markers are required to be tuned at the new resonance frequency, and the scanner tracking sequence also needs to be adapted to a 3T scanner.

8.4.2 Investigations into Position and Force Control Strategies

With respect to the accuracy of the pneumatic motor and the further applications of the ultrasonic motor, the following points should be considered for future work:

- The ultrasonic motor together with a pair of piezoresistive force sensors were embedded in the needle firing unit to generate force feedback to the user in the master control handle during needle insertion, which compensates for the loss of tactile information due to the separate between the imaging volume and the workspace which the clinician can access. Besides the tactile realisation, by combining the force and position information, a force profile can be generated when the needle is introduced to the prostate. A future application is to use the profile as an indicator of when the needle is piercing the prostate capsule, and to investigate the correlation of different force profiles acquired during the procedure and the pathological results from the biopsy sample, as it is reported in literature that malignant tissue is at least several times harder than the healthy tissue surrounding it. Analysis of the tissue mechanics with the use of the force information may be useful to extract additional pathological information [Taylor, 2005, Souchon, 2003].

- With the current PID controller implemented in the pneumatic motor, accuracy of 0.25degrees was achieved in the test unit, and accuracies of 1degree and 0.5degrees were achieved in the lower limb and upper limb positioning systems. The PID controller is considered adequate for current interventions in prostate biopsy and limb positioning, but an increase in accuracy of the motor would be beneficial for the actuator to be adapted to other interventions. A more complex control algorithm could reduce the error in the motor, and compensate for the backlash and unwanted bending of the plastic components, making it suitable in an application that requires high torques as well as high accuracy. In terms of the mechanical design, the motor bandwidth could be improved by using piezovalves, to control the airflow to the motor, as piezovalves are controlled by non-magnetic principles and hose length for air transmission can be largely reduced by placing the piezovalves close to the scanner bore.

8.4.3 Improved Prostate Biopsy System

The prototype of the prostate biopsy system in its current design, constitutes a first step towards the clinical application of the MR transrectal prostate biopsy in a conventional closed bore scanner. Based on what were achieved up to this point, proposed steps for future development are as follows:

- The system accuracy and maneuverability can be improved by introducing a fixed mechanical pivot in the movement of the endorectal probe, to replace the use of the rectal sphincter as part of the system kinematics. As it was reported the movement and deformation of the rectal sphincter affected the maneuverability of the probe in the rectum and was a main source of error in the kinematic calculation. A mechanical pivot placed right outside the sphincter would provide a stable pivot position in the system kinematics, and negate the effect of sphincter deformation from the calculation. Besides this, a future design modification of the biopsy system would be to include a rotational DOF in the endorectal probe to allow a larger workspace for biopsy and to provide a higher degree of flexibility for targeting, meaning more than one way to position the robot joints for the end effector to achieve the same target. A more compact robot design with the added DOF should be favorable for a wide range of patients of different body sizes.

- In the current fiducial tracking algorithm, the fastest update time is 2.4s and the maximum movement speed must be below 5mm/s with the use of the modified FLASH 2D sequence. The fiducial positions can be lost if the robot speed is beyond this limit. Reducing the slice thickness allows the robot to move faster, but will compromises the accuracy of the tracking. An alternative could be to implement the tracking with a faster pulse sequence, such as TRUE FISP, which would considerably reduce the update time without compromising the accuracy. With an increase in the update rate, another interesting option in future work would be to use the 3D fiducial coordinates from the tracking algorithm to servo the movement of each robot joint when the fiducial markers are close enough to the isocentre. Combining the fiducial tracking and position encoders in the closed loop position control could increase the system accuracy by providing a time to time calibration of the encoder reading (to compensate for the accumulative error inherent in incremental encoders). This method could also compensate for any deflection of the structure and backlash in the system, which can be important for MR robots, as they are generally made from a large amount of plastic parts.

- Based on the knowledge developed in this research, it is possible to adapt the current robot with simple engineering modifications to other transrectal modalities, such as brachytherapy in which a radioactive seed is inserted to the target lesion within the prostate. In addition, the modular stage of the robot design with a pneumatic actuator and encoder embedded forms a basic robot actuation unit, and makes it possible to use as a basic building block to develop other MR compatible robots to perform biopsies or other similar interventions on other organs.

8.4.4 Improved Magic Angle Positioning Devices

To implement the systems into clinical environments for further validation of their clinical value, proposed continuative steps with regards to the clinical considerations are as follows:

- Literature has indicated how the magic angle theory can enhance diagnostic results in the study of tendon, nerve and muscle [Fullerton, 1985, Marshall, 2002]; proposed devices have achieved the objective of providing accurate positioning inside the scanner. Ease of use, high repeatability and being time and cost effective are of importance for clinical justification of the system functionality. The system must be made to be intuitive and robust, and the procedure should be performed in a significantly short amount of time, as the MR suite is already a very scarce and costly resource shared for clinical and research proposes. The system should be designed to be as "plug-and-play" as possible and require no presence of technical staff to supervise and monitor it during a procedure. Also the training time required to learn the system should be reduced to a period affordable by the already busy clinicians, meaning a system with relatively simple design and shorter learning curve is preferable.

- Another future work would be to collaborate with interested orthopedic specialists and clinicians in muscular-skeletal research, and a more function specific device can be designed for particular study targets. A design based on the positioning of particular regions of tendons can mean a reduced number of components and joints, and a simplified system design is beneficial to shorten its setup time and learning curve, and also make it more cost effective and feasible for use inside the MRI suite.

8.5 Publication Output

Parts of this research work have been accepted and published in journal papers, and two patents have been filed relating to the robot designs. The details are as follows:

1. Journal Papers

   - Tse, Z. T. H., Elhawary, H., Zivanovic, A., Rea, M., Paley, M., Bydder, G., Davies, B. L., Young I., Lamperth, M. U. ,
     A 3 Degree Of Freedom MR Compatible Mechatronic System for Magic Angle Related Diagnosis in vivo. Mechatronics, ASME/IEEE Transactions on Mechatronics, vol. 13, pp. 316-324, 2008.
   - Tse, Z. T. H., Elhawary, H., Rea, M., Young, I, Davies, B. L., Lamperth, M. U. ,
     A Haptic Unit designed for Magnetic-Resonance-Guided Biopsy. Proceedings of the IMECHE Part H Journal of Engineering in Medicine, vol. 223, pp. 159-172, 2009.
   - Tse, Z. T. H., Janssen, H., Hamed, A., Ristic, M., Young, I., Lamperth, M. U.,
     Magnetic Resonance Elastography Hardware Design: A Survey. Proceedings of the IMECHE Part H Journal of Engineering in Medicine, vol. 223, pp. 497-514, 2009.
   - Tse, Z. T. H., Elhawary, H., Zivanovic, A., Rea M., Paley, M., Bydder, G., Davies B. L., Young I., Lamperth, M. U. ,
     System to Facilitate Magic Angle Experiments in Man. Journal of Magnetic Resonance Imaging. (Submitted)

2. Patents

   - 2008 Patent Office: "MRI Compatible Pneumatic Actuator";
     Application No.: PCT/GB2007/004362; Pub. No: WO/2008/059253
   - 2008 Patent Office: "MRI Compatible Manipulators";
     Application No.: PCT/GB2007/004376; Pub. No: WO/2008/059263

Bibliography

- [ACS, 2005] ACS, "American cancer society, prostate cancer,"
  World Wide Web: http://www.cancer.org/docroot/CRI/content/CRI5fCancer, 2005.
- [AISI, 2008] AISI, "Stainless steel - SS 2346,"
  World Wide Web: http://efunda.com/materials/alloys/stainless_steels, 2008
- [Armenean, 2004] C. Armenean, "RF-induced temperature elevation along metallic wires in clinical magnetic resonance imaging: Influence of diameter and length," Magnetic resonance in medicine, vol. 52, pp. 1200-1206, 2004.
- [ASTM-F2052, 2004a] ASTM-F2052, "Standard Test Method for Measurement of Magnetically Induced Displacement Force on Medical Devices in the Magnetic Resonance Environment, Designation F2052-02. ASTM: American Society for Testing and Materials," 2004a.
- [ASTM-F2052, 2004b] ASTM-F2052, "Standard Test Method for Measurement of Magnetically Induced Torque on Medical Devices in the Magnetic Resonance Environment, Designation F2052-02. ASTM: American Society for Testing and Materials," 2004b.
- [ASTM-F2119, 2004] ASTM-F2110, "Standard Test Method for Evaluation of MR Image Artifacts from Passive Implants, Designation F2110-01. ASTM: American Society for Testing and Materials," 2001.
- [ASTM-F2182, 2002] ASTM-F2182, "Standard Test Method for Measurement of Radio Frequency Induced Heating Near Passive Implants During Magnetic Resonance Imaging, Designation F2182-02a. ASTM: American Society for Testing and Materials," 2002.
- [Avago, 2003] Avago, "Optical incremental position encoder, Avago Technologies," 2003.
- [Ballinger, 1996] J. R. Ballinger, "Magic Angle Effects ",
  World Wide Web: www.mritutor.org/mritutor/magica.htm, 1996.
- [Bartels, 2002] L. W. Bartels, "Improved lumen visualization in metallic vascular implants by reducing RF artifacts," Magnetic resonance in medicine, vol. 47, pp. 171-180, 2002.
- [Bensamoun, 2006] S. F. Bensamoun, S. I. Ringleb, L. Littrell, Q. Chen, M. Brennan, R. L. Ehman, and K. N. An, "Determination of thigh muscle stiffness using magnetic resonance elastography," Journal of magnetic resonance imaging, vol. 23, pp. 242-247, 2006.

- [Bishop, 2000] J. Bishop, "Two-dimensional MR elastography with linear inversion reconstruction: methodology and noise analysis," Physics in Medicine and Biology, vol. 45, pp. 2081-2091, 2000.
- [Blue, 2009] Blue, "General Information About Prostate Cancer," in Blue of California, 2009. World Wide Web: https://www.blueshieldca.com/hw/articles/
- [Braun, 2003] J. Braun, K. Braun, and I. Sack, "Electromagnetic actuator for generating variably oriented shear waves in MR elastography," Magnetic Resonance in Medicine, vol. 50, pp. 220-222, 2003.
- [Brown, 1995] M. Brown and R. Semelka, MRI. Basic Principles and Applications: Wiley-Liss, Inc., 1995.
- [Brown, 2003] D. Brown, "New Imaging Technology Deciphers Tumors," Distinction, The university of Texas
  World Wide Web: http://distinctions.uthouston.edu/archive/2003/oct/tumor.html, 2003
- [Brunswick, 2009] Brunswick, "Open upright scanner, East Brunswick Open Upright MRI," 2009.
- [Bykhovski, 1996] A. D. A. Bykhovski, "Piezoresistive effect in wurtzite n-type GaN," Applied physics letters, vol. 68, pp. 818-819, 1996.
- [Carroll, 2009] P. Carroll and K. Shinohara, "Transrectal Ultrasound Guided Prostate Biopsy." World Wide Web: http://urology.ucsf.edu/patientGuides/pdf/uroOnc/Prostate_Biopsy.pdf, 2009
- [Chappell, 2004] K. E. Chappell, M. D. Robson, A. Stonebridge-Foster, A. Glover, J. M. Allsop, A. D. Williams, A. H. Herlihy, J. Moss, P. Gishen, and G. M. Bydder, "Magic Angle Effects in MR Neurography," AJNR Am J Neuroradiol, vol. 25, pp. 431-440, 2004.
- [Chapuis, 2004] D. Chapuis, R. Gassed, L. Sache, E. Burdet, and H. Bleuler, “Design of a Simple MRI/fMRI Compatible Force/Torque Sensor”, Proceedings of the IEEE/RSJ International Conference on Intelligent Robots and Systems, Sendai, Japan, 2004
- [Chen, 1998] J. Chen, "Numerical simulation of SAR and B-field inhomogeneityof shielded RF coils loaded with the human head," IEEE Transactions on Biomedical Engineering, vol. 45, pp. 650-659, 1998.
- [Chinzei, 1999] K. Chinzei, R. Kikinis, and F. Jolesz, "MR Compatibility of Mechatronic Devices: Design Criteria," presented at Proceedings of the 2nd International Conference on Medical Image Computing and Computer-assisted Interventions, Cambridge, UK., 1999.
- [Chinzei, 2000a] K. Chinzei, N. Hata, F. A. Jolesz, and R. Kikinis, "MR compatible surgical assist robot: System integration and preliminary feasibility study," presented at Proceedings of the 3rd International Conference on Medical Image Computing and Computer-Assisted Intervention, Pittsburgh, Pennsylvania, USA., 2000a.

- [Chinzei, 2000b] K. Chinzei, N. Hata, F. A. Jolesz, and R. Kikinis, "Surgical assist robot for the active navigation in the intraoperative MRI: Hardware design issues," presented at Proceedings of the IEEE International Conference of Intelligent Robots and Systems, Maui, HI, USA, 2000b.
- [Cobb, 2006] J. Cobb, J. Henckel, P. Gomes, S. Harris, M. Jakopec, F. Rodriguez, A. Barrett, and B. Davies, "Hands-on robotic unicompartmental knee replacement: a prospective, randomised controlled study of the acrobot system," Journal of Bone and Joint Surgery, vol. 88, pp. 188-197, 2006.
- [D'Amico, 2000] A. V. D'Amico, C. M. Tempany, R. Cormack, N. Hata, M. Jinzaki, K. Tuncali, M. Weinstein, and J. P. Richie, "Transperineal magnetic resonance image guided prostate biopsy," Journal of Urology, vol. 164, pp. 385-387, 2000.
- [DiMaio, 2003] S. P. DiMaio and S. E. Salcudean, "Needle insertion modeling and simulation," IEEE Transactions on Robotics and Automation, vol. 19, pp. 864-875, 2003.
- [Dotmed, 2009] Dotmed, "Hologic E-Scan Extremity MRI Scanner, ESAOTE," 2009.
- [Doyley, 2003] M. M. Doyley, J. B. Weaver, E. W. Van Houten, F. E. Kennedy, and K. D. Paulsen, "Thresholds for detecting and characterizing focal lesions using steady-state MR elastography," Medical physics, vol. 30, pp. 495-504, 2003.
- [Dresner, 2004] M. A. Dresner, J. L. Fidler, and R. L. Ehman, "MR elastography of in vivo human liver " presented at Proceedings of the 12th Meeting of the International Society for Magnetic Resonance in Medicine, Berkeley, California, 2004.
- [Dempsey, 2001] M. F. Dempsey, "Investigation of the factors responsible for burns during MRI," Journal of Magnetic Resonance Imaging, vol. 13, pp. 627-631, 2001.
- [Ehman, 2008] R. L. Ehman, "Plenary Lecture: Overview of MRE, Driver Technology, and Applications for Abdominal Imaging," presented at Proceedings of the 16th Annual Meeting of International Society of Magnetic Resonance Medicine, Toronto, Canada, 2008.
- [Elhawary, 2006] H. Elhawary, A. Zivanovic, B. Davies, and M. Lamperth, "A review of magnetic resonance imaging compatible manipulators in surgery," Proceedings of the Institution of Mechanical Engineers, Part H: Journal of Engineering in Medicine, vol. 220, pp. 413-424, 2006.
- [Erickson, 1993] S. J. Erickson, R. W. Prost, and M. E. Timins, "The "magic angle" effect: background physics and clinical relevance," Radiology, vol. 188, pp. 23-25, 1993.
- [FDA, 2005] FDA, "A Primer on Medical Device Interactions with Magnetic Resonance Imaging Systems," Food and Drug Administration, 2005.
- [Flueckiger, 2005] M. Flueckiger, M. Bullo, D. Chapuis, R. A. Gassert, and Y. A. Perriard, "fMRI compatible haptic interface actuated with traveling wave ultrasonic motor," presented at Proceedings of the IEEE Fortieth Industry Applications Annual Meeting, Hong Kong, China, 2005.

- [Friedman, 1989] B. R. Friedman, G. Chaves-Munoz, C. R. B. Meritt, J. P. Jones, and A. P. Salmon, Principles of MRI: McGraw Hill, Inc., 1989.
- [Ganesh, 2004] G. Ganesh, R. Gassert, E. Burdet, and H. Bleuler, "Dynamics and control of an MRI compatible master-slave system with hydrostatic transmission," presented at Proceedings of the IEEE International Conference on Robotics and Automation, Orleans, Los Angeles, USA, 2004.
- [Gassert, 2006a] R. Gassert, "MRI/fMRI-Compatible Robotic System With Force Feedback for Interaction With Human Motion," IEEE/ASME Transactions on Mechatronics, vol. 11, pp. 216-224, 2006.
- [Gassert, 2006b] R. Gassert, A. Yamamoto, D. Chapuis, L. Dovat, H. Bleuler, and E. Burdet, "Actuation methods for applications in MR environments," Concepts in Magnetic Resonance Part B: Magnetic Resonance Engineering, vol. 29, pp. 191-209, 2006.
- [Gassert, 2007] R. Gassert, E. Burdet, and K. Chinzei, "Opportunities and Challenges in MR-Compatible Robotics," IEEE Engineering in Medicine and Biology Magazine, vol. 27, pp. 15-22, 2007.
- [GE, 2005] GE, "GE Medical Systems, MR Safety and Compatibility: Test Guidelines for Signa SP, Version 1," 2005.
- [Gerovichev, 2002] O. Gerovichev, P. Marayong, and A. M. Okamura, "The Effect of Visual and Haptic Feedback on Manual and Teleoperated Needle Insertion " Proceedings of the 5th International Conference on Medical Image Computing and Computer-Assisted Intervention, Part I, pp. 147-154, 2002
- [GlobalSpec, 2009] GlobalSpec, "Amplified Piezoelectric Actuators (APA)," World Wide Web: http://www.directindustry.com/prod/cedrat-technologies, 2009.
- [Hall-Craggs, 2000] M. A. Hall-Craggs, "Interventional MRI of the breast: minimally invasive therapy," European Radiology, vol. 10, pp. 59-62, 2000.
- [Hamed, 2009] A. M. Hamed, Z. T. H. Tse, I. Young, B. L. Davies, M. Lamperth, “Applying Tactile Sensing with Piezoelectric Materials for MIS and MR-Guided Interventions,” Proceedings of the IMECHE Part H Journal of Engineering in Medicine, vol. 223(1), pp. 99-110, 2009.
- [Hashtrudi-Zaad, 2001] K. Hashtrudi-Zaad, "Analysis of Control Architectures for Teleoperation Systems with Impedance/Admittance Master and Slave Manipulators," The International journal of robotics research, vol. 20, pp. 419-445, 2001.
- [Hata, 2001] N. Hata, M. Jinzaki, D. Kacher, R. Cormak, D. Gering, A. Nabavi, S. G. Silverman, A. V. D'Amico, R. Kikinis, F. A. Jolesz, and C. M. Tempany, "MR imaging-guided prostate biopsy with surgical navigation software: device validation and feasibility," Radiology, vol. 220, pp. 263-268, 2001.

- [Hata, 2004] N. Hata, F. Ohara, R. Hashimoto, M. Hashizume, and T. Dohi, "Needle guiding robot with five-bar linkage for MR-guided thermotherapy of liver tumor," Lecture Notes in Computer Science vol. 3217, pp. 161-168, 2004.
- [Hata, 2005] N. Hata, R. Hashimoto, J. Tokuda, and S. A. Morikawa, "Needle guiding robot for MR-guided microwave thermotherapy of liver tumor using motorized remote-center-of-motion constraint," presented at Proceedings of the IEEE International Conference on Robotics and Automation, Barcelona, Spain, 2005.
- [Hayes, 1996] C. W. Hayes and J. A. Parellada, "The magic angle effect in musculoskeletal MR imaging," Topics in Magnetic Resonance Imaging, vol. 8, pp. 51-56, 1996.
- [Hing, 2007] J. T. Hing, A. D. Brooks, and J. P. Desai, "A biplanar fluoroscopic approach for the measurement, modeling, and simulation of needle and soft-tissue interaction," Medical Image Analysis, vol. 11, pp. 62-78, 2007.
- [Howe, 1999] R. D. Howe and Y. Matsuoka, "Robotics for surgery," Annual Review of biomedical Engineering, vol. 1, pp. 211-240, 1999.
- [Hyder, 2000] F. Hyder, R. P. Kennan, I. Kida, G. F. Mason, K. L. Behar, and D. Rothman, "Dependence of Oxygen Delivery on Blood Flow in Rat Brain: A 7 Tesla Nuclear Magnetic Resonance Study," Journal of Cerebral Blood Flow and Metabolism, vol. 20, pp. 485-498, 2000.
- [Hynynen, 1993] K. Hynynen, A. Darkazanli, E. Unger, and J. F. Schenck, "MRI-guided noninvasive ultrasound surgery," Medical Physics, vol. 20, pp. 107-115, 1993.
- [Ibrahim, 2001] T. S. Ibrahim, "Analysis of B1 field profiles and SAR values for multi-strut transverse electromagnetic RF coils in high field MRI applications," Physics in Medicine and Biology, vol. 46, pp. 2545, 2001.
- [Kaplan, 2002] I. Kaplan, N. E. Oldenburg, P. Meskell, M. Blake, P. Church, and E. J. Holupka, "Real time MRI-ultrasound image guided stereotactic prostate biopsy," Magnetic Resonance Imaging, vol. 20, pp. 295-299, 2002.
- [Kim, 1999] B. Kim and P. Roschke, "Linearization of magnetorheological behaviour using a neuralnetwork," presented at Proceedings of the American Control Conference, USA, 1999.
- [Kozak, 2002] J. Kozak, M. Nesper, M. Fischer, T. Lutze, A. Gegelmann, S. Hassfeld, and T. Wetter, "Semiautomated registration using new markers for assessing the accuracy of a navigation system," Computer Aided Surgery, vol. 7, pp. 11-24, 2002.
- [Krieger, 2005] A. Krieger, R. C. Susil, C. Menard, J. A. Coleman, G. Fichtinger, E. Atalar, and L. L. Whitcomb, "Design of a novel MRI compatible manipulator for image guided prostate interventions," IEEE Transactions on Biomedical Engineering, vol. 52, pp. 306-313, 2005.
- [Krieger, 2007] A. Krieger, C. Csoma, I. I. Iordachita, P. Guion, A. K. Singh, G. Fichtinger, and L. L. Whitcomb, "Design and preliminary accuracy studies of an MRI-guided transrectal

prostate intervention system " presented at Proceedings of the 10th International Conference on Medical Image Computing and Computer-Assisted Intervention, Brisbane, Australia, 2007.

- [Larson, 2004] B. T. Larson, A. G. Erdman, N. V. Tsekos, E. Yacoub, P. V. Tsekos, and I. G. Koutlas, "Design of an MRI-Compatible Robotic Stereotactic Device for Minimally Invasive Interventions in the Breast," Journal of Biomechanical Engineering - Transactions of the ASME, vol. 126, pp. 458-465, 2004.

- [Lewa, 2000] C. J. Lewa, M. Roth, L. Nicol, J. M. Franconi, and J. D. de Certaines, "A new fast and unsynchronized method for MRI of viscoelastic properties of soft tissues," Journal of Magnetic Resonance Imaging, vol. 12, pp. 784 - 789, 2000.

- [Line, 2005] Line, "Prostate line.com,"
World Wide Web: http://www.porstateline.com, 2005.

- [MacLean, 2000] K. E. MacLean, "Designing with haptic feedback," presented at Proceedings of the IEEE International Conference on Robotics and Automation, San Francisco, California, USA, 2000.

- [Marshall, 2002] H. Marshall, C. Howarth, D. J. Larkman, A. H. Herlihy, A. Oatridge, and G. M. Bydder, "Contrast-enhanced magic-angle MR imaging of the Achilles tendon," American Journal of Roentgenology, vol. 179, pp. 187-192, 2002.

- [Marti, 2003] G. Marti, P. Rouiller, S. Grange, and C. Baur, "Biopsy navigator: a smart haptic interface for interventional radiological gestures," International Congress Series, vol. 1256, pp. 788-793, 2003.

- [Maurer Jr, 1996] C. R. Maurer Jr, "Technical Note. Effect of Geometrical Distortion Correction in MR on Image Registration Accuracy," Journal of Computer Assisted Tomography, vol. 20, pp. 666-679, 1996.

- [McKnight, 2002b] A. L. McKnight, J. L. Kugel, P. J. Rossman, A. Manduca, L. C. Hartmann, and R. L. Ehman, "MR elastography of breast cancer: preliminary results," American Journal of Roentgenology, vol. 178, pp. 1411-1417, 2002.

- [McRobbie, 2003] D. McRobbie, E. A. Moore, M. J. Graves, and M. R. Prince, “MRI: From Picture to Proton”, First ed. Cambridge: Cambridge University Press, 2003.

- [Minne, 1995] S. C. Minne, "Parallel atomic force microscopy using cantilevers with integrated piezoresistive sensors and integrated piezoelectric actuators," Applied Physics Letters, vol. 67, pp. 3918-3920, 1995.

- [Moser, 2003] R. Moser, R. Gassert, E. Burdet, L. Sache, H. R. Woodtli, J. Erno, W. Maeder, and H. Bleuler, "An MR compatible Robot Technology," presented at Proceedings of the IEEE International Conference on Robotics and Automation, Taipei, Taiwan, 2003.

- [Muntener, 2006] M. Muntener, A. Patriciu, D. Petrisor, D. Mazilu, H. Bagga, L. Kavoussi, K. Cleary, and D. Stoianovici, "Magnetic resonance imaging compatible robotic system for fully automated brachytherapy seed placement," Urology, vol. 68, pp. 1313-1317, 2006.

- [Nelles, 2001] O. Nelles, "Nonlinear system identification: from classical approaches to neural networks and fuzzy models," Springer, 2001.

- [NHS, 2009] NHS, "What Is The Prostate Gland?," Department of urology, Addenbrook's hospital, NHS, UK
  World Wide Web: http://www.camurology.org.uk/davinci_robot/overview.php, 2009

- [Norberg, 1997] M. Norberg, L. Egevad, L. Holmberg, P. Sparen, B. J. Norlen, and C. C. Busch, "The sextant protocol for ultrasound-guided core biopsies of the prostate underestimates the presence of cancer," Urology, vol. 50, pp. 562-566, 1997.

- [Nyenhuis, 1999] J. A. Nyenhuis, "Heating near implanted medical devices by the MRI RF-magnetic field," IEEE Transactions on Magnetics, vol. 35, pp. 4133-4135, 1999.

- [Ophir, 1991] J. Ophir, I. Cespedes, H. Ponnekanti, Y. Yazdi, and X. Li, "Elastography: A quantitative method for imaging the elasticity of biological tissues," Ultrasonic Imaging, vol. 13, pp. 111-134, 1991.

- [Rea, 2008] M. Rea, D. McRobbie, H. Elhawary, Z. T. H. Tse, M. Lamperth, and I. Young, "System for 3-D Real-Time Tracking of MRI-Compatible Devices by Image Processing," IEEE/ASME Transactions on Mechatronics, vol. 13, pp. 379-382, 2008.

- [Petersch, 2004] B. Petersch, J. Bogner, A. Fransson, T. Lorang, and R. Peter, "Effects of geometric distortion in 0.2T MRI on radiotherapy treatment planning of prostate cancer," Radiotherapy and Oncology, vol. 71, pp. 55-64, 2004.

- [PI, 2009] Physik Instrumente, "Displacement of Piezo Actuators",
  World Wide Web:www.physikinstrumente.com/en/products, 2009.

- [Piezoleg, 2008] Piezoleg, "PiezoLegs PiezoMotor AB, Sweden,"
  World Wide Web:http://www.piezomotor.se, 2008.

- [Podder, 2006] T. Podder, D. Clark, J. Sherman, D. Fuller, E. Messing, D. Rubens, J. Strang, R. Brasacchio, L. Liao, W. S. Ng, and Y. Yu, "In vivo motion and force measurement of surgical needle intervention during prostate brachytherapy," IEEE Engineering and Medicine in Biology Magazine, vol. 33, pp. 2915-2922, 2006.

- [Riener, 2005] R. Riener, T. Villgrattner, R. Kleiser, T. Nef, and S. Kollias, "fMRI-Compatible Electromagnetic Haptic Interface," presented at Proceedings of the IEEE International Conference on Engineering in Medicine and Biology Society, Shanghai, China, 2005.

- [Rossman, 1999] P. J. Rossman, R. Muthupillai, and R. L. Ehman, "Driver Device for MR Elastography," U. S. Patent, USA., 1999.

- [Schenck, 1996] J. F. Schenck, "The role of magnetic susceptibility in magnetic resonance imaging: MRI magnetic compatibility of the first and second kinds," Medical Physics, vol. 23, pp. 815-850, 1996.
- [Seraji, 1994] H. Seraji, "Adaptive admittance control: an approach to explicit force control in compliant motion," presented at Proceedings of the IEEE International Conference on Robotics and Automation, San Diego, California, USA, 1994.
- [ServoCity, 2009] ServoCity, "Tamiya Gearboxes,"
  World Wide Web: http://www.servocity.com, 2009.
- [Shellock, 2002] F. G. Shellock, "Magnetic resonance safety update 2002: Implants and devices," Journal of Magnetic Resonance Imaging, vol. 16, pp. 485-496, 2002.
- [Shellock, 2003] F. G. Shellock, "Biomedical Implants and Devices: Assessment of Magnetic Field Interactions With a 3.0-Tesla MR System," Journal of Magnetic Resonance Imaging, vol. 16, pp. 721-732, 2003.
- [Shinsei Corporation Inc., 2008] Shinsei Corporation Inc., "Ultrasonic Motors.", 2008
- [Siemens] Siemens, "Siemens Magnetom Avanto, Siemens Medical Systems," 2005.
- [Sled, 1998] J. G. Sled, "Standing-wave and RF penetration artifacts caused by ellipticgeometry: an electrodynamic analysis of MRI," IEEE Transactions on Medical Imaging, vol. 17, pp. 653-662, 1998.
- [Stark, 1999] D. D. Stark and W. G. Bradley, "Magnetic resonance imaging," Mosby St. Louis, Mo, 1999.
- [Stoianovici, 2007] D. Stoianovici, A. Patriciu, D. Petrisor, D. Mazilu, and L. Kavoussi, "A New Type of Motor: Pneumatic Step Motor," Mechatronics, IEEE/ASME Transactions on Mechatronics, vol. 12, pp. 98-106, 2007.
- [Tada, 2002] M. Tada, S. Sasaki, and T. Ogasawara, "Development of an optical 2-axis force sensor usable in MRI environments," presented at Proceedings of The International Conference on Engineering in Medicine and Biology Society, San Francisco, CA, USA, 2002.
- [Tada, 2004] M. Tada and T. Kanade, "Development of an MR-compatible optical force sensor," presented at Proceedings of The International Conference on Engineering in Medicine and Biology Society, San Francisco, CA, USA, 2004.
- [Talwalkar, 2008] J. A. Talwalkar, M. Yin, J. L. Fidler, S. O. Sanderson, P. S. Kamath, and R. L. Ehman, "Magnetic resonance imaging of hepatic fibrosis: emerging clinical applications," Hepatology, vol. 47, pp. 332-342, 2008.
- [Tamiya, 2009] Tamiya, "Planetary Gearmotor-Tamiya 72001 ", 2009.

- [Taylor, 2003] J. L. Taylor, C. L. Wu, D. Cory, R. G. Gonzalez, A. Bielecki, and L. L. Cheng, "High-resolution magic angle spinning proton NMR analysis of human prostate tissue with slow spinning rates," Magnetic Resonance in Medicine, vol. 50, pp. 627-632, 2003.

- [Tenzer, 2008] Y. Tenzer, B. Davies, and F. Rodriguez y Baena, "Investigation into the Effectiveness of Vibrotactile Feedback to Improve the Haptic Realism of an Arthroscopy Training Simulator," presented at Proceedings of the International Conference on Medicine Meets Virtual Reality, Las Vegas, Nevada, USA, 2008.

- [Tse, 2008] Z. T. H. Tse, H. Elhawary, A. Zivanovic, M. Rea, M. Paley, B. Graham, B. L. Davies, I. Young, and M. U. Lamperth, "A 3 Degree Of Freedom MR Compatible Device for Magic Angle Related in Vivo Experiments," ASME/IEEE Transactions on Mechatronics, vol. 13, pp. 316-324, 2008.

- [Tse, 2009] Z. T. H. Tse, H. Elhawary, M. Rea, I. Young, B. L. Davies, and M. U. Lamperth, "A Haptic Unit designed for Magnetic-Resonance-Guided Biopsy," Proceedings of the IMECHE Part H Journal of Engineering in Medicine, vol. 223, pp. 159-172, 2009.

- [Tsekos, 2005] N. V. Tsekos, A. Ozcan, and E. Christoforou, "A prototype manipulator for magnetic resonance-guided interventions inside standard cylindrical magnetic resonance imaging scanners," Journal of Biomechanical Engineering, vol. 127, pp. 972-980, 2005.

- [Tsekos, 2007] N. V. Tsekos, A. Khanicheh, E. Christoforou, and C. Mavroidis, "Magnetic Resonance Compatible Robotic and Mechatronics Systems for Image-Guided Interventions and Rehabilitation: A Review Study," Annual Review of Biomedical Engineering, vol. 9, pp. 351-387, 2007.

- [Tseng, 2000] C. S. Tseng, "Image-guided robotic navigation system for neurosurgery," Journal of Robotic Systems, vol. 17, pp. 439-447, 2000.

- [Uffmann, 2002] K. Uffmann, "Design of an MR-compatible piezoelectric actuator for MR elastography," Concepts in Magnetic Resonance, vol. 15, pp. 239-254, 2002.

- [UKCancerResearch, 2008] UKCancerResearch, "Cancer research UK, Men's cancers factsheet," World Wide Web: http://info.cancerresearchuk.org/images/publicationspdfs/factsheetune2008.pdf, 2008.

- [Verrillo, 1963] R. T. Verrillo, "Effect of Contactor Area on the Vibrotactile Threshold," The Journal of the Acoustical Society of America, vol. 35, pp. 1962-1966, 1963.

- [Volpe, 1993] R. Volpe, "A theoretical and experimental investigation of explicit forcecontrol strategies for manipulators," IEEE Transactions on Automatic Control, vol. 38, pp. 1634-1650, 1993.

- [Wang, 2004] D. Wang, W. Strugnell, G. Cowin, D. M. Doddrell, and R. Slaughter, "Geometric distortion in clinical MRI systems: Part I: evaluation using a 3D phantom," Magnetic Resonance Imaging, vol. 22, pp. 1211-1221, 2004.

- [Weishaupt, 2003] D. Weishaupt, V. D. Kochli, and B. Marincek, “How Does MRI Work?,” Springer-Verlag, 2003.
- [Wolovich, 2007] W. A. Wolovich, “Robotics: Basic Analysis and Design,” CBS College Publishing,1987.
- [Xia, 2000] Y. Xia, Y, "Magic-angle effect in magnetic resonance imaging of articular cartilage: a review.," Investigative radiology, vol. 35, pp. 602-621, 2000.
- [Zhang, 2001] Q. Zhang, M. Wendt, A. J. Aschoff, J. S. Lewin, and J. L. Duerk, "A multielement RF coil for MRI guidance of interventional devices," Journal of Magnetic Resonance Imaging, vol. 14, pp. 56-62, 2001.